THE UNIVERSITY OF OKLAHOMA

GRADUATE COLLEGE

NEW APPLICATIONS OF MOLYBDENUM (VI) CATALYZED OXYGEN ATOM TRANSFER REACTIONS

A DISSERTATION

SUBMITTED TO THE GRADUATE FACULTY

in partial fulfillment of the requirements for the

Degree of

DOCTOR OF PHILOSOPY

By

THEO A H RUSMORE

Norman, Oklahoma

2022

NEW APPLICATIONS OF MOLYBDENUM (VI) CATALYZED OXYGEN ATOM TRANSFER REACTIONS

A DISSERTATION APPROVED FOR THE

DEPARTMENT OF CHEMISTRY AND BIOCHEMISTRY

BY THE COMMITTEE CONSISTING OF

Dr Daniel T Glatzhofer, Chair

Dr Kenneth M Nicholas, Co-chair

Dr Yihan Shao

Dr Yitong Dong

Dr Lance L Lobban

For Nana Jean, who lead the way

ACKNOWLEDGEMENTS

They say it takes a village to raise a child–and the same could be said of earning a PhD.

First, thank you to my family, for their unwavering support and encouragement, not only during grad school, but throughout my entire life: to Dad, for teaching me how to look at a perfectly good solution and then find a new problem to solve, and for showing me that the natural world is full of moving parts that can be watched and studied; to Mum, for helping me write everything that ever flowed off my pen, for teaching me how to frame ideas in language, and for the invaluable skill of deciphering any and all handwriting; to Nina, for being the coolest sister one could hope for and for having the same fire as I do for things both great and small (Congratulations on graduating from both undergrad and grad school in the time it took me to finish this PhD); to Margi, for her endless encouragement to push forward, commiserations on the stumbling blocks of academia, and solidarity in the long slog of writing; to Artie Sparke Hooper, for being the best dog (and the worst coworker), for dragging me along on walks, and for making sure I got more fresh air and sunshine than from walking between my car and lab.

Next, thanks to my advisors, Dr Kenneth Nicholas and Dr Daniel Glatzhofer, who coached me through experimental issues and apparent dead-ends, and without whom this PhD would have been entirely impossible. From the department at large, thanks to Dr Yihan Shao, for taking a clueless experimentalist and giving me the keys to the supercomputer; to Dr Ivan Yip and Dr Robyn Biggs, for making teaching less impossible; to Carol Jones, for her mastery in solving any and all bureaucratic problems; to Carl Van Buskirk, who always had a minute to chat and made me feel welcome every time I saw him, even when I had a T-Report in hand; to Jeff Jackson, who can seemingly fix anything; to Dr Susan Nimmo and Dr Stephen Foster, the bedrock of the department, keepers of the instruments and the deep wisdom, yet always with time to chat and solve a grad student's problems.

Last but certainly not least, thanks to my friends, near and far, old and new: Max Fefer, Jessica Trinh, Cori Malinky, Ross Kobe, Cole Carter, Rob Fogle, Matthew Swann, Marcee Olvera, David McIntosh, Marie Reynolds, Eric Gardner, Jessi Gardner, et al. Thank you for experimental advice, reasons to leave the house or lab, and good conversations that helped us vent our frustrations with the world–I couldn't have done this without you.

TABLE OF CONTENTS

LIST OF FIGURES

LIST OF SCHEMES

LIST OF TABLES

ABSTRACT

The chemistry of dioxomolybdenum coordination complexes has been deeply investigated as a model for molybdoenzyme structure and activity, as well as for non-biological chemical applications. In this work, we present investigation into new applications of dioxomolybdenum reactivity and the mechanisms thereof. Chapter 1 gives a brief summary of metal oxo bonding structure, the reactivity of molybdoenzymes and synthetic molybdenum complexes, oxidative kinetic resolutions, metal-dioxygen complexes, and catalytic oxidation of thiols.

Chapter 2 presents the use of a series of chiral dioxomolybdenum (VI) Schiff-base salen complexes as catalysts for the oxidative kinetic resolution of the *P*-chiral monophosphine, methylphenyl-*tert*-butyl phosphine. The studied complexes are shown to yield the chiral phosphine oxide in low to moderate enantiomeric excess (0-35% e.e.) employing pyridine *N*-oxide as the stoichiometric oxygen atom source. Use of a *para*-nitro substituent on the ligand salicylimine ring is found to increase catalyst activity, and enantioselectivity of the reaction is found to be controlled by steric bulk at the salen *ortho*-position. Density Functional Theory (DFT) study of the reaction finds the stereochemically-defining step is the *O*-transfer transition state involving nucleophilic attack of the phosphine on an oxo-group of the chiral $LMoO_2$ complex.

Chapter 3 reports the catalytic oxidation of phosphines by Schiff-base complexes of dioxomolybdenum under aerobic conditions. The activity of the complexes toward aerobic oxidation of phosphines is found to be the same as with pyridine *N*-oxide, with the presence of a *para*-nitro substituent greatly increasing the rate of oxidation. DFT studies are carried out to determine the mechanism of coordination and activation of dioxygen towards oxygen atom transfer, and to determine which of the available oxygen atom transfer pathways is most favorable for the oxidation of phosphines. Transfer of the oxo moiety is found to be most favorable, and the dioxo complex is regenerated through an unusual cleavage of the peroxo group. A computational investigation of oxygen atom transfer to sulfoxides and their lack of reactivity towards oxidation by dioxomolybdenum complexes is also reported.

Chapter 4 extends the reactivity of Schiff-base dioxomolybdenum complexes to include the oxidation of thiols to disulfides under base-free conditions. This reactivity is found to

encompass alkyl, benzyl, aryl, and amino acid-derived thiols. Alkyl and benzyl thiols are found to be oxidized to two primary products, of which the disulfide is the major (60-80% yield). The secondary products are found to differ due to substrate effects, with benzyl mercaptan oxidized to benzyl trisulfide and dodecane thiol oxidized to the previously unreported dodecane sulfenic anhydride. The selectivity of this oxidation toward formation of disulfide products is found to increase with addition of base, and variation of catalyst electronics (salen *para*-substituent = NO_2, H, OMe) shows significant rate and product distribution effects. DFT study of possible reaction intermediates suggest this oxidation proceeds initially *via* a hydrogen atom transfer process forming a thiyl radical and a molybdenum (V) oxo-hydroxyl species. Disproportionation of two molecules of the molybdenum (V) species forms one dioxomolybdenum (VI) complex, one oxomolybdenum (IV) complex, and a molecule of water. Mechanistic pathways are suggested for formation of disulfide, trisulfide, and sulfenic acid products.

CHAPTER 1

INTRODUCTION

1.1 Oxo group transfer and the electronic structure of metal oxo compounds

Oxygen transfer reactions are a class of oxidation/reduction reactions (*eq. 1*) in which the oxygen donor is reduced and the oxygen acceptor is oxidized. Our work focuses specifically on a class of oxygen transfer reactions, oxygen-atom transfer reactions (OAT) in which the formal gain or loss of an oxygen atom is mediated by a transition metal complex (*eq. 2*).

$$X + AO \rightarrow XO + A \qquad \textit{eq. 1}$$

$$M^nO_xL + X \rightleftharpoons M^{n-2}O_{x-1}L + XO \qquad \textit{eq. 2}$$

For these reactions, the transferred oxygen is: *i)* transferred as an oxygen atom, *ii)* atom transfer results in a change of oxidation state (*n±2*) of the metal results, and *iii)* the transferred oxo group is bound directly to the metal center. [1] These requirements mean that all oxo transfer reactions involve an oxo-metal species, with the number of terminal oxo groups ranging from one to four (Figure 1-1).

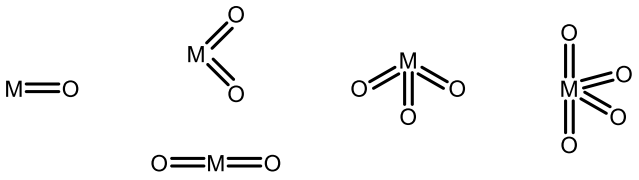

Figure 1-1. Geometries of known oxometal functional groups

Oxo-metal complexes are known to form with transition metals from groups 4-8, with the number of terminal oxo groups controlled by the oxidation state of the metal. Thus, group 4 titanium may only have one oxo ligand, while group 5 vanadium may have two, group 6 metals may have up to three, and rhenium and osmium complexes have up to four oxo ligands. The limitations on the number of oxo moieties comes down to the need for vacant or half-filled metal *d*-orbitals to accept π-electrons from the oxo group. Oxo ligands exhibit a strong *trans*-effect on the opposing ligand due to the electronic character of the M=O bond (Figure 1-2 b & c); that is, due to the strong M-O bond resulting from mixing of oxygen π-orbitals and metal *d*-orbitals removing electron density from the opposing metal-ligand bonding interactions. Metal dioxo

moieties are stabilized by the same orbital interactions as metal oxos, as shown in (Figure 1-2 d-h).

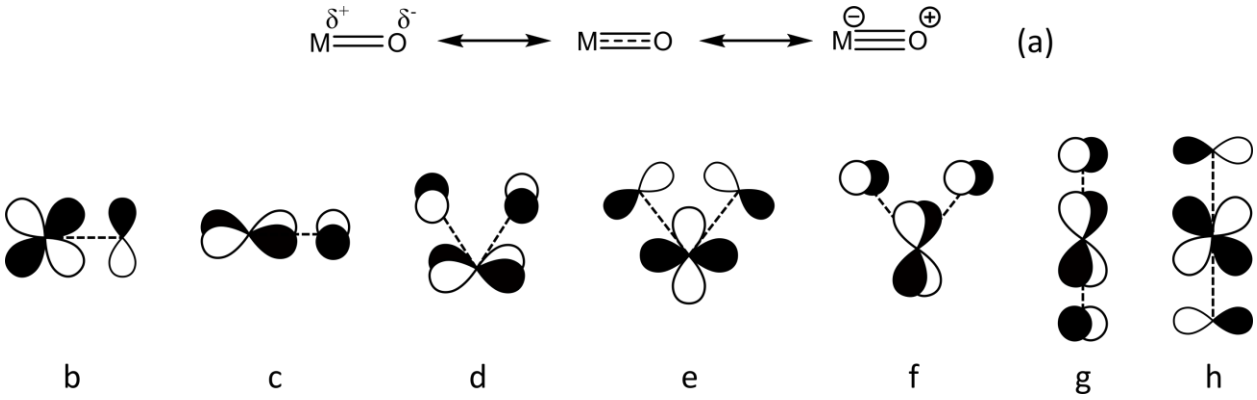

Figure 1-2. (a) Resonance structures for metal-oxo bonding. Bonding orbital alignments for metal oxo (b & c), d^0 metal *cis*-dioxo (d-f), and d^2 metal *trans*-dioxo (g & h) moieties

Due to the availability of two *d*-π bonding interactions in d^0-monooxo complexes, the strong metal oxo bond is sometimes described as a partial triple bond (Figure 1-2a). [2,3] For metal dioxo units, d^0 metal centers prefer the bent *cis*-dioxo geometry, while d^2 metal centers typically exhibit the linear *trans*-dioxo geometry. The linear geometry allows the valence electrons from the metal center to occupy a nonbonding *d*-orbital, which avoids destabilizing the π-bonding interactions between the metal and oxygen atom. Metal centers that are d^0 may also exhibit pyramidal geometry for MO_3 and *cis*-octahedral geometry for MO_4. These stoichiometries also exist as metal oxide ions, which will not be discussed here. The oxo group can also act as a bridging ligand, which results in metal center oxidation states one less than for the terminal oxo group (for $M_2[\mu^2\text{-}O]$) or the same as the terminal oxo-containing complex (for $M_2[\mu^2\text{-}O]_2$). Formation of these bridged species can be prevented by employing bulky ligand moieties, [4] allowing for stable monometallic oxo-metal species with terminal oxo groups that can act as oxygen transfer moieties.

1.2 Molybdoenzymes and OAT reactions of oxomolybdenum complexes

Catalytic oxygen atom transfer reactions can be promoted by both synthetic metal oxo complexes and by enzymatic oxometal centers. Both natural and synthetic oxygen atom transfer catalysts perform a metal-centered oxo transfer reaction (either the forward or reverse reaction given in eq. 2) and a coupled oxidation or reduction step that may or may not involve another oxo transfer reaction. The most prevalent metal oxo group in biological contexts is the iron heme oxo, which is an intermediate in many of the oxidation/reduction processes carried out by Cytochrome P450 and other iron heme enzymes. However, the bulk of experimental metal oxo species are molybdenum dioxo complexes. Molybdenum is the only second-row metal essential for biological function, and appears in more than 50 redox enzymes, including the xanthine oxidase, sulfite oxidase, and DMSO reductase families. [5] All molybdenum containing enzymes contain a conserved organic cofactor known as molybdopterin—or, more generally, pyranopterin—a bidentate, 4-electron dithiolate donor ligand. The structures of the molybdopterin cofactor and the molybdenum centers for each molybdoenzyme family are shown in Figure 1-3.

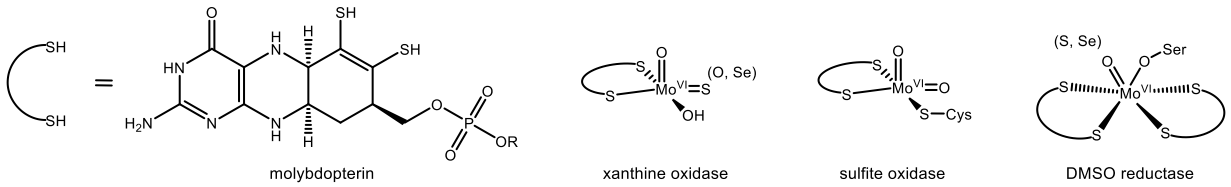

Figure 1-3. Structures of the molybdopterin cofactor and the coordination environment for each of the molybdoenzyme families. Each molybdenum (VI) center is represented in its most common coordination environment. Common ligand variations are given in parentheses.

The xanthine oxidase family of enzymes catalyzes the oxidative hydroxylation of their substrates, producing a carbonyl product from aromatic heterocyclic substrates (e.g. xanthine) and carboxylic acids from aldehydes. These reactions are not mechanistically oxygen atom transfers but involve instead a nucleophilic oxido moiety (generated by deprotonation of the hydroxyl group) attacking an electrophilic carbon on the substrate while the sulfide moiety acts as a hydride acceptor, generating a molybdenum (IV) thiolate complex. The product is then formed by elimination and protonation of the substrate, with association of free hydroxide (from water) regenerating the catalytic species (Figure 1-4).

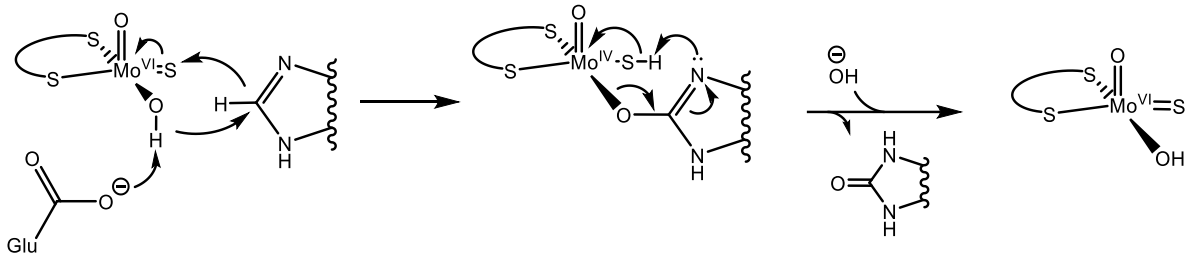

Figure 1-4. Mechanistic pathway for catalytic oxidation of xanthine by xanthine oxidase

Unlike xanthine oxidase, the molybdenum center of sulfite oxidase is a dioxomolybdenum (VI) center. One of the structural properties of this metal dioxo moiety is that only one of the oxo groups can be transferred, with the increase in metal-oxo bond strength leading to formation of a "spectator oxo." [5,6] The increase in Mo-O bonding character from formation of the molybdenum (IV) monooxo species contributes to the thermodynamic favorability of the oxo group transfer, counterbalancing the thermodynamic cost of cleaving the molybdenum-oxo double bond. The mechanism of oxo transfer with the sulfite oxidase dioxomolybdenum center differs from xanthine oxidase's oxo-sulfido center: absent the Mo=S moiety to act as a hydride acceptor, the transferred oxo group is electrophilic rather than nucleophilic, leading to the direct oxygen atom transfer (OAT) shown in Figure 1-5. The transferred oxygen atom again comes from water to regenerate the catalytic dioxomolybdenum species.

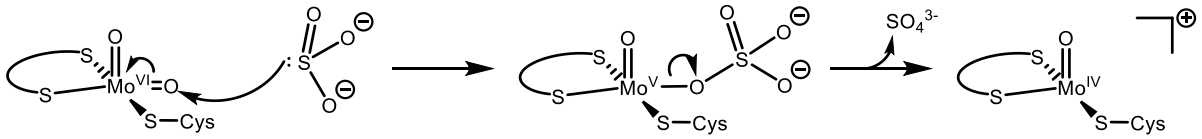

Figure 1-5. Mechanistic pathway for catalytic oxidation of sulfite by sulfite oxidase

The DMSO (dimethyl sulfoxide) reductase family, by contrast with the other molybdoenzyme families—which cycle between Mo (VI) and Mo (IV) by transferring a bound oxo moiety to the substrate molecule—cycles between Mo (IV) and Mo (VI) by abstracting an oxygen atom from the substrate molecule (Figure 1-6). The reduction of DMSO to DMS (dimethyl sulfide) is thought to occur through a concerted process, [1] where the cleaving S-O bond stabilizes the S-O π*-orbital, allowing for electron transfer from the metal center to the sulfur. The abstracted oxo group is then reduced to form water, reforming the Mo (VI) center.

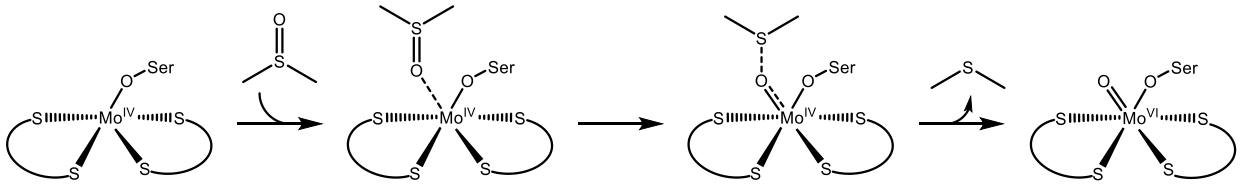

Figure 1-6. Mechanistic pathway for OAT reduction of DMSO by DMSO reductase

The chemistry of synthetic molybdenum complexes was developed with an eye to modeling the oxygen transfer chemistry of the molybdenum enzyme families. However, a significant amount of research on molybdenum-mediated oxo transfer was carried out prior to the determination of the structures of the molybdoenzyme active sites, so most early investigations focused on the $Mo^{IV}O/Mo^{VI}O_2$ redox couple due to its prevalence in conventional molybdenum chemistry. The eventual determination of the enzymatic coordination environments revealed that further investigation was needed to explore the $Mo^{IV}/Mo^{VI}O$ redox couple employed by DMSO reductase and presented the synthetic challenges of forming the $[Mo^{VI}OS]^{2+}$ center of xanthine oxidase and stabilizing the five-coordinate dioxomolybdenum (VI) center of sulfite oxidase. However, the early research with dioxomolybdenum complexes has made the atom transfer chemistry of molybdenum the best-understood of any element. [7–15]

Accurate structural synthetic analogues of the molybdoenzyme centers must necessarily employ dithiolene ligands (Figure 1-7). [16] However, a large range of ligands have been employed to make complexes that model the reactivity of the enzyme centers without regard to the specific atoms in the coordination sphere. [15] The vast majority of molybdenum (VI) complexes adopt the *cis*-dioxo geometry, with an overall octahedral coordination sphere. As described in Section 1.1, the *cis*-dioxo moiety is strongly preferred in d^0 complexes, and the strong σ- and π-donor influences of the oxo ligands have significant effects on the overall geometry of the complex. With both monodentate and bidentate ligands, where there is flexibility in the position of coordinating atoms, weaker π-bonding donor atoms occupy the coordination site *trans* to the oxo ligand. These *trans* position bonds are significantly longer than bonds with equivalent donor atoms in other coordination positions. [17]

Monodentate ligands of dioxomolybdenum complexes can either be monoanionic (X-type) or neutral (L-type). X-type ligands can be halides (most often chloride), cyano groups, [18]

alkyl or aryl groups directly bonded to the metal center, thiolates, [7,10] and -OR oxide groups (R = alkyl, aryl, silyl). L-type monodentate ligands can be donor-type solvent molecules (e.g. THF or DMF) or non-solvent O- or N-donor molecules, such as sulfoxides, phosphine oxides, and pyridine. Imido ligands, [19,20] while monodentate, are formally dianionic ligands, and share more properties with the oxo moiety than with the monoanionic ligands.

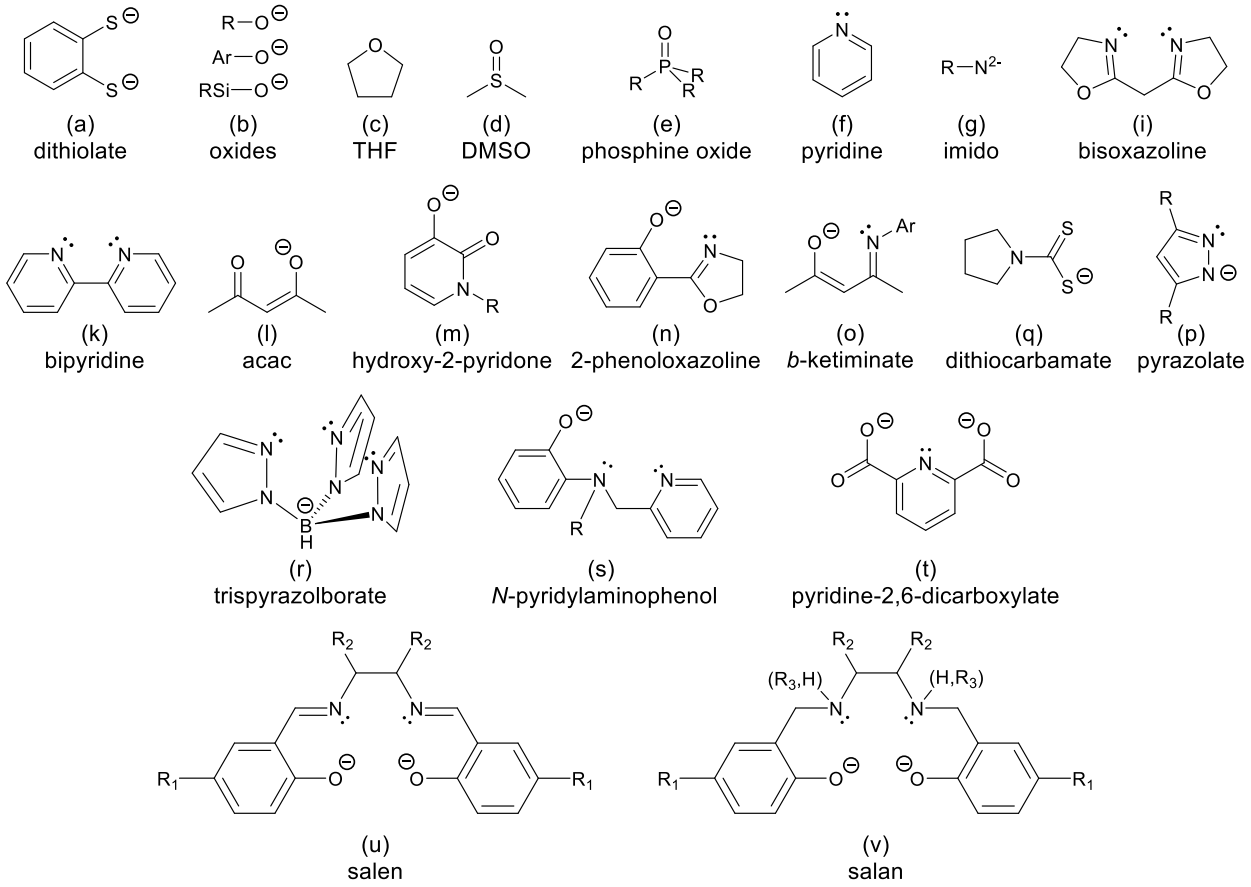

Figure 1-7. Common ligands of synthetic dioxomolybdenum (VI) complexes

Bidentate ligands can be neutral (generally N,N-donors, such as bis-oxazolines and bipyridine derivatives), [8,21] monoanionic O,O-, N,O-, N,N- or S,S-donor ligands (hydroxy-2-pyridinones, ketiminate Schiff bases, pyrazolates, and dithiocarbamates, respectively). Tridentate ligands can be monoanionic (trispyrazolylborate, [11] O,N,N-donors) or dianionic (O,N,O- or S,N,S-donors), and often have the octahedral molybdenum coordination sphere completed by a monodentate ligand. Finally, neutral complexes with the formula $[MoO_2L]$ can be

synthesized with tetradentate dianionic ligands, the most common of which are the O,N,N,O-donor Schiff base *salen* ligands, as well as their reduced *salan* form. [9,15]

The multidentate ligands are convenient for studies of dioxomolybdenum oxygen atom transfer due to their high formation constants and their steric bulk, which stabilizes the monomeric molybdenum (IV) oxo species by inhibiting dimerization to form μ-oxo molybdenum (V) species. The comproportionation[1] reactions forming these oxo-bridged dimeric complexes (Figure 1-8) may or may not be reversible, and the molybdenum (V) dimer is usually unreactive to OAT, meaning that irreversible dimerization will prevent catalytic activity. Of these multidentate ligands, Schiff-base and related O,N,N,O- and S,N,N,S- ligands [22] have particular utility for mechanistic investigations of dioxomolybdenum complexes due to their easy synthesis (Figure 1-9) and the ability to easily modify electronic and steric effects of the ligand by changing substituents on the starting materials. The electron-donating and -withdrawing effects of *para*-substitution in phenolic ligands on oxo transfer processes has been well demonstrated in both molybdenum and tungsten complexes [9,23] and can be used to probe mechanistic details of the OAT process.

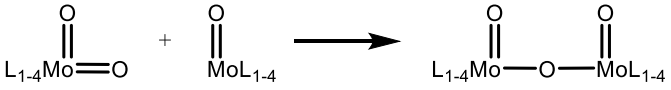

Figure 1-8. Comproportionation reaction of molybdenum (VI) dioxo and molybdenum (IV) monooxo to form molybdenum (V) μ-oxo

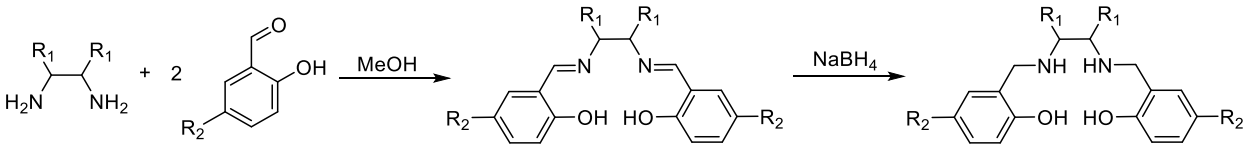

Figure 1-9. Synthesis of salen and salan ligands from diamines and salicylaldehydes

While the original source of the transferred oxygen atom for the oxidase enzymes and the product of molybdenum reductases is water, model molybdenum complexes and synthetic *O*-atom transfer catalysts employ a large range of oxygen atom donor and acceptor reagents (Figure 1-10). The enzymatic *O*-donor/acceptor natural substrates are DMSO, nitrate, sulfite, carbon

[1] A redox reaction where two reactants with different oxidation states react to form a single compound with an intermediate oxidation number. The opposite of a disproportionation reaction.

monoxide, formate and xanthine, while unnatural substrates have included sulfides, phosphines, amine oxides and alkenes (with peroxide oxidants). [5,17,24–26] It should be noted that the alkene/peroxide reactions are widely viewed to involve reactive metal peroxo intermediates, Mo(O-O) [8], whereas the others with non-peroxidic reagents involve reactive oxo-Mo (LMo=O) species.

Figure 1-10. General oxygen atom transfer reaction with molybdenum oxo species

Tertiary phosphines are widely used as model substrates for *O*-transfer mechanistic studies. [27] Phosphines are nucleophilic substrates, with the reactivity of the phosphine to oxidation dependent on its substituents (alkyl > aryl). A Hammett parameter study carried out by Whiteoak, et al. employing *para*-substituted salan dioxomolybdenum complexes determined that the oxygen atom transfer to phosphorus is accelerated by using strongly electron-withdrawing substituents (e.g. *para*-nitro), which act to dissipate the negative charge built up during nucleophilic attack by phosphine on the oxo moiety. [9] This effect is consistent with the initial nucleophilic attack being the rate-limiting step for phosphine oxidation, an experimental conclusion that has been supported by computational investigation. [6] Both phosphines and phosphine oxides have important uses in chiral form, particularly to confer chirality to metal complex catalysts for a variety of reactions. [28–33] Phosphine oxides are useful ligands for harder, higher oxidation state metal ions and chiral members can serve as ligands for metallic catalysts or as chiral organocatalysts for several classes of reactions. [28,29,34]

While phosphines are convenient unnatural substrates for investigating oxygen atom transfer from molybdenum oxo centers, natural sulfur-based substrates are also of significance. Both oxidation (sulfite-oxidase type reactivity) and deoxygenation (DMSO reductase-type reactivity) are of synthetic and industrial interest. Deoxygenation of sulfoxides to sulfides has been reported for a wide range of high oxidation state molybdenum complexes, catalyzing the general reaction shown in Figure 1-11, which is often coupled with OAT to phosphines in a catalytic setting. [15,35,36]

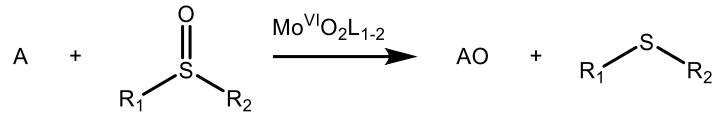

Figure 1-11. Catalytic deoxygenation of sulfoxides by dioxomolybdenum (VI) complexes

This reaction has been demonstrated with a wide variety of ligand types, including dichloride, dialkyldithiocarbamate, cyano, acetylacetonate, silyl-cyclopentadienyl, aminobisphenol, salan, and salen complexes of dioxomolybdenum. [9,18,24,25,37–41] The reverse (sulfite oxidase-type) reaction is less well-represented for synthetic dioxomolybdenum centers, with all known catalysts transferring not an oxo moiety to the substrate, but instead an oxygen atom from a peroxo or hydroperoxo group *via* electrophilic oxygen atom transfer. [42,43] These oxidoperoxido complexes, known as Mimoun complexes, [44] are also known to catalyze the epoxidation of olefins by an equivalent mechanism. In the presence of peroxidic reagents, peroxomolybdenum complexes can be formed from reduction of an organic peroxide or H_2O_2, co-producing an alcohol or water (Figure 1-12a). The peroxomolybdenum complex then transfers an oxygen atom from the peroxo group to the substrate *via* outer-shell nucleophilic attack of the substrate on the peroxo moiety. This mechanism, proposed by Sharpless, et al., is shown in Figure 1-12b. [45,46] It should be noted that the transfer of an oxygen atom to or from the molybdenum peroxo group is not a formal oxo transfer reaction, as the molybdenum remains in the +6 oxidation state throughout the process, and oxidation/reduction occurs at the peroxo ligand instead. [1]

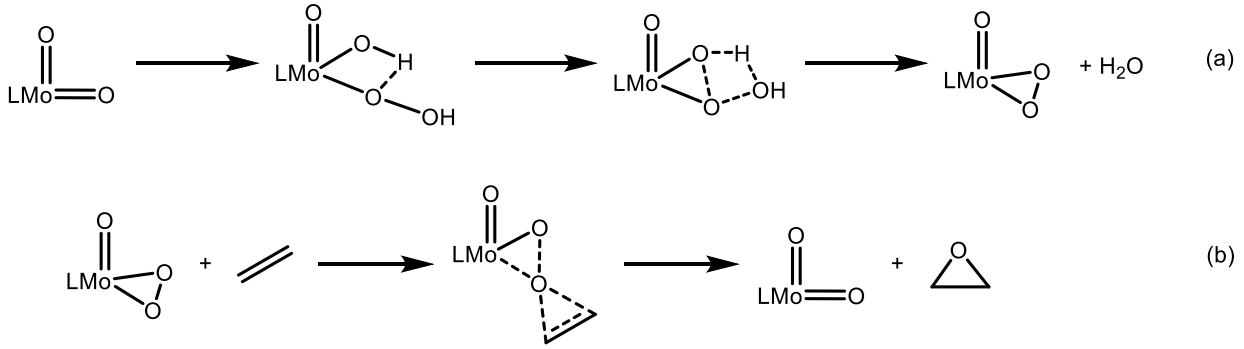

Figure 1-12. (a) Reaction of hydrogen peroxide with $LMoO_2$ to form a molybdenum (VI) oxoperoxo complex and (b) Sharpless mechanism for epoxidation of olefins by molybdenum peroxido species

1.2.1 Asymmetric synthesis and resolution processes involving molybdenum complexes

Like phosphine oxidation, sulfoxidation and epoxidation can be used to form valuable chiral products when a chiral oxo-transition metal catalyst is employed (Figure 1-13). These reactions, in which a prochiral sulfide is oxidized to the chiral sulfoxide or olefins are stereospecifically transformed to the epoxide, are a common application of chiral salen complexes. [47] The inclusion of a chiral diamine in the backbone of the ligand (Figure 1-9, R_1) induces an asymmetric environment around the dioxomolybdenum center and potentially allows for OAT catalysis to proceed stereoselectively.

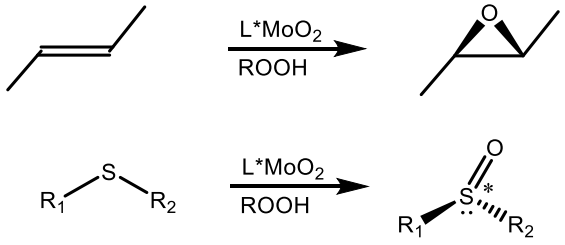

Figure 1-13. Molybdenum catalyzed enantioselective epoxidation and sulfoxidation

Enantioselective reactions with molybdenum complexes are well-represented in the literature, however most reports of high enantioselectivity are for C-C bond-forming reactions. Molybdenum carbonyl compounds with chiral bis(pyridyl-amide) and bis(oxazalinyl-amide) ligands have been demonstrated to catalyze allylic alkylation reactions with high regio- and enantioselectivities. [48,49] Investigations into this reactivity by Trost and coworkers reveal that molybdenum catalysts select for the more substituted allylic position, making these complexes more enantioselective than palladium-based catalysts. [50] Further studies show that the reaction proceeds *via* oxidative addition of the allylic substrate to the metal center, followed by nucleophilic attack to yield the substitution product. [51] Molybdenum catalysts have also been employed for asymmetric ring-opening and ring-closing reactions. The study of these reactions has been dominated by the work of Schrock, Hoyveda, and coworkers, using four- and five-coordinate molybdenum imido alkylidine complexes with chiral diolate ligands acting as the chirality-inducing scaffold. [52–55] Asymmetric synthesis with dioxomolybdenum complexes is also well-documented, though the selectivity of these systems towards epoxidation is often moderate-to-low. [56–60] The highest enantioselectivity for these reactions has been obtained

with bishydroxamic acid ligands (up to 96% e.e.), [61,62] as well as with phenoloxazaline ligands, for which the lability of the ligand and coordination of the olefin to the molybdenum center is involved in determining the reaction enantiospecificity. [63] High enantioselectivities have also been reported for the oxidation of sulfides to sulfoxides and sulfones, with the selectivity of the oxidation arising from a kinetic resolution effect for the oxidation of sulfoxide to sulfone. [64] Sulfoxidation of prochiral sulfides that have high selectivity to the sulfoxide product have not been demonstrated with high enantioselectivity. [65–67]

In the best-case scenario, asymmetric catalysis will result in full conversion of starting material to the desired enantiomeric product. For kinetic resolution reactions, in which a racemic mixture of substrate is enantiomerically enriched by reaction with a chiral reagent or catalyst, this result is possible only when the starting material can be isomerized by either coordination to the catalyst or a photochemical process. [68,69] However, when the interconversion of isomers is impractical or inaccessible, the maximum yield of an asymmetric resolution is 50% of the racemic starting material. That being said, kinetic resolution reactions have several advantages: *i)* the use of easily-accessible racemic substrates, *ii)* the option to select the enantiomer of the product by choosing the enantiomer of the chiral reagent or catalyst, and *iii)* the reduction of waste products typically associated with stoichiometric resolution processes. [70] There is a long list of criteria an ideal kinetic resolution process would meet, but the criteria for a practical kinetic resolution are simple: the racemate should be cheap and enantio-enriched sources unavailable, the employed catalyst is highly enantioselective, inexpensive, and effective at low loadings, and the product and the unreacted starting material are easily separated.

Enantioselectivity in kinetic resolutions arises from the difference in rate of reaction between the enantiomers of the racemic substrate, k_{rel}, with a homochiral reactant or catalyst. This selectivity is dictated by the difference in the activation energies of the enantiomeric transition state, $\Delta\Delta G^{\ddagger}$. Because the selectivity is a result of rate differences, the enantiomeric excess obtained changes over the course of the reaction, as opposed to enantioselective reactions of prochiral substrates, which yield products of constant e.e. throughout the reaction. This effect leads to differences in approach depending on whether the aim is to recover enantioenriched substrate or product. Obtaining highly enriched substrate is possible even with

relatively low selectivity, simply by allowing the reaction to proceed to higher conversion, which depletes the substrate of the faster-reacting enantiomer. Conversely obtaining highly enantioenriched products requires high selectivity, because after the first turnovers of the reaction, the e.e. of the product begins to decrease.

Oxidative kinetic resolutions have been established for secondary alcohols, [71–74], sulfoxides, [65,75] alkenes and allenes, [47,76]. There is, however, a scarcity of reports of kinetic resolutions for *P*-chiral phosphines, [77] and there have been, in fact, no reports of catalytic kinetic resolution of phosphines by oxidation of the phosphine prior to this study. [24,78–80] The oxidative catalytic resolution of phosphines is most comparable to that of sulfoxides, in which the chiral sulfur center is enantioselectively oxidized to the sulfone, leaving enantioenriched sulfoxide to be recovered from the reaction. Oxidative kinetic resolution of chiral phosphines, however, yields both an enantioenriched phosphine oxide product and recovered enantioenriched phosphine substrate, and could be catalyzed by metal oxo complexes rather than the metal peroxo complexes employed for oxidation of sulfoxides.

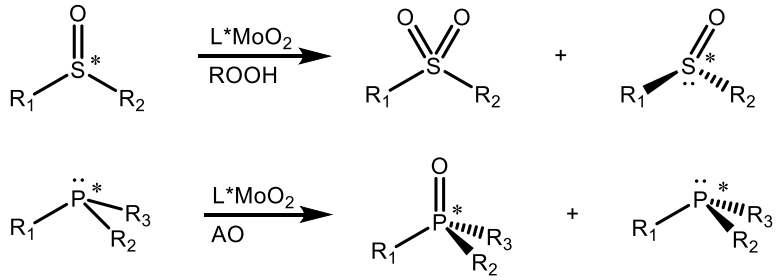

Figure 1-14. Molybdenum-catalyzed oxidative kinetic resolutions of sulfoxides and phosphines

1.3 Coordination and reaction of dioxygen with transition metal centers

As mentioned in the previous section, oxidation of electrophilic substrates by metal oxo complexes is usually carried out with stoichiometric peroxide reagents as an oxygen atom source, which generates a metal peroxo complex as the active catalyst. [8,45] Metal peroxo species can also be formed by reaction with dioxygen (Figure 1-15). The reaction/coordination of dioxygen to a metal center is very important for reactions that use dioxygen as a terminal oxidant. Ground-state (triplet) dioxygen is very slow to react with singlet substrates due to its weak electron-donor

properties and the spin-forbidden nature of the interaction. [18,81] Coordination of dioxygen to a metal produces an "activated" dioxygen molecule that can react more readily with singlet organic molecules. [82]

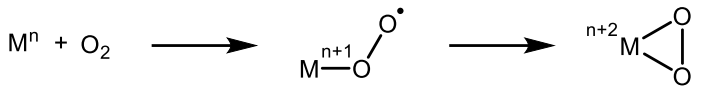

Figure 1-15. Stepwise 1-electron reductions of dioxygen to metal superoxo and metal peroxo

The stepwise reduction of dioxygen to form a peroxo ligand, however, is not the only possible fate for metal/dioxygen reactions, and the actual species formed can vary. The initial 1-electron reduction yields a metal superoxo complex, examples of which are known with copper, [83–85] cobalt, [86,87] and rhodium. [86,88] These complexes are paramagnetic and behave as free-radical initiators, reacting by 1-electron steps to catalyze oxidation of phenols and thiols. These complexes can also react with another metal center to form dioxygen-bridged dimers (Figure 1-16).

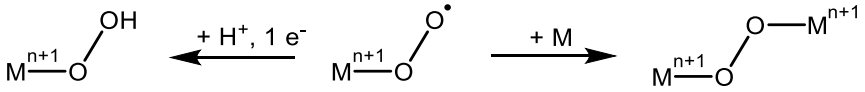

Figure 1-16. 1-electron reductions of metal superoxo to metal hydroperoxo and μ-O_2 dimer

The dioxygen-bridged dimer is a presumed intermediate in the formation of monooxo species from reactions of metals with dioxygen. The formally 2-electron reduced μ-O_2 species is further reduced to form two O^{2-} ligands, cleaving the O-O bond in the process (Figure 1-17). [82,89] The formed metal oxo species may then react as described in the previous section, with dioxygen coordination and splitting preceding (e.g. Fe^{II}) or following (e.g. V^{III}, Mo^{IV}) each substrate oxidation step.

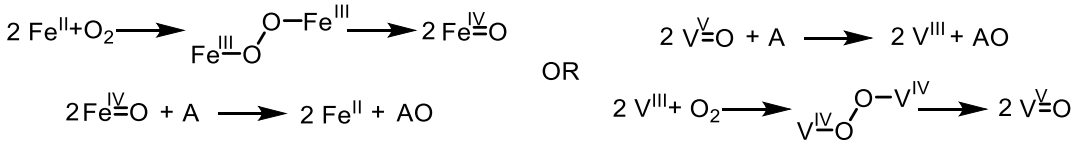

Figure 1-17. Mars-Van Krevelen mechanism for aerobic oxidation of substrates (A)

The 4-electron reduction of dioxygen to two oxo ligands rarely occurs at a single metal, as it involves increase the oxidation state of the metal by 4 in one reaction, though this transformation is accessible by metals with a large range of available oxidation states, such as ruthenium (Figure 1-18). [90]

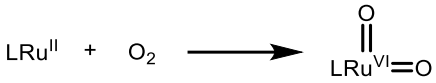

Figure 1-18. 4-electron reduction of dioxygen by ruthenium

Formation of side-on peroxo complexes is well-documented, but the mechanism of the coordination and reduction is not. Due to the changes in spin state of the dioxygen and of the reacting complex as the reaction proceeds, DFT investigations were unable to fully model the process prior to the development of methods for calculating the minimum energy crossing points (MECPs) between the high-spin and low-spin reaction surfaces. Yu and coworkers [91] were able to model the coordination of dioxygen with a series of ruthenium, osmium, cobalt, and iridium complexes. In all cases, they found that the 2-electron reduction of dioxygen to the peroxo ligand occurs in a stepwise fashion, beginning with end-on coordination of $^3O_2$ to the metal center, then forming a partially side-on peroxo before completing the reduction and η^2-coordination of the peroxo group, which may be a triplet or singlet, the latter requiring a spin-crossover step (Figure 1-19).

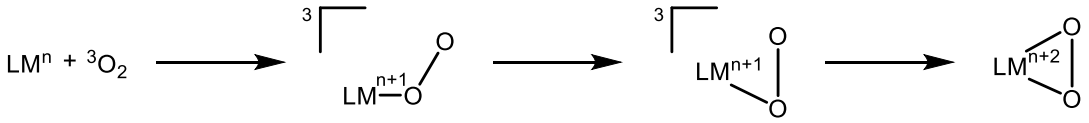

Figure 1-19. General scheme for oxygen coordination as described by Yu, et al. M=Ru, Os, Co, Ir

Perhaps the most famous transition metal peroxo-catalyzed reaction is the Sharpless epoxidation, [92] which represented the first practical method of asymmetric epoxidation. The titanium tartrate complex reacts selectively with secondary allylic alcohols, transferring an oxygen atom from *tert*-butyl hydroperoxide through the alcohol stabilized transition state shown in Figure 1-20. [93] The ligation of the substrate alcohol accounts for the substrate specificity of this enantioselective reaction. The Jacobsen-Katsuki epoxidation, by comparison, does not involve a transition state in which the substrate binds to the metal center and instead derives its

enantioselectivity from the steric environment of its cyclohexanediamine-derived salen ligand. [47]

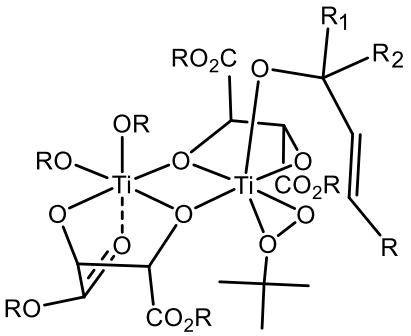

Figure 1-20. Coordinated intermediate structure for enantioselective epoxidation by Sharpless reagent [93]

Copper is known to form both superoxo and η^2-peroxo complexes, and is involved in enzymatic chemistry, including as a cofactor with molybdenum in CO dehydrogenase (a member of the xanthine oxidase family). [5,83,94] Copper is also involved in reversible binding of dioxygen, reduction of dioxygen to hydrogen peroxide or water, and mono- or deoxygenation of organic substrates. [95] Natural copper complexes for the transport of dioxygen are known as hemocyanins, and consist of a dinuclear μ-η^2,η^2-peroxo unit, which is far from the only Cu/O_2 binding mode or stoichiometry. Copper dioxygen complexes are known with stoichiometries varying from 1:1 to 4:1. (Figure 1-21) Synthetic complexes with copper centers have been employed to carry out hydroxylation of aryl and alkyl substrates, oxidation of alcohols to ketones, and oxidation of thiols to disulfides, among other transformations. [95–101]

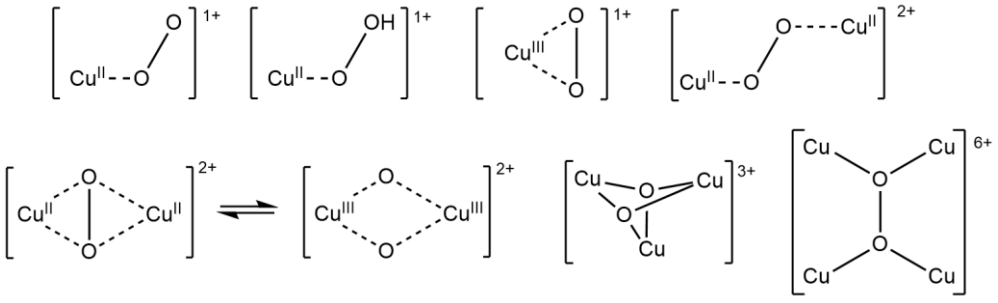

Figure 1-21. Coordination modes and stoichiometries of copper-dioxygen complexes

Cobalt has reactivity toward dioxygen similar to that of copper, although the majority of cobalt dioxygen complexes occur either as a mononuclear superoxo or as the dinuclear μ-η^2,η^2-

peroxo (Figure 1-22). [102] Significant work has been reported on aerobic oxidation catalyzed by cobalt (II) salen complexes, including oxidation of alcohols to ketones, epoxidation of alkenes, and OAT to phosphines and amines. These reactions have also been reported with a variety of other ligand systems.

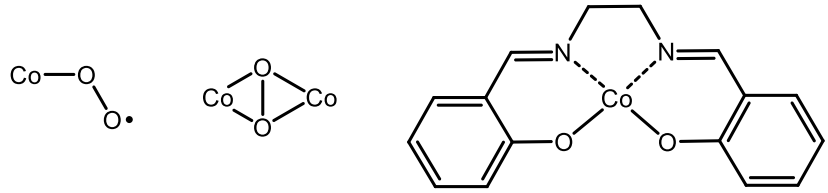

Figure 1-22. Coordination modes of cobalt-dioxygen complexes, structure of cobalt-salen complex

While the best-known and most well-studied molybdenum peroxo complexes are the Mimoun-type oxoperoxo complexes, which are usually generated using H_2O_2 or ROOH oxidation of an oxo moiety, [42,44,45,69,103–113] advances have recently been made in employing dioxygen as a source of oxygen atoms in molybdenum-catalyzed OAT. [19,114–121] This reactivity was first reported with a dithiocarbamate complex of oxomolybdenum (IV), which is suggested to form a molybdenum (V) binuclear species on reaction with molecular oxygen prior to generating the dioxomolybdenum (VI) species (Figure 1-23a). [122] Investigations of a cyano complex of molybdenum (IV), $[(CN)_5Mo^{IV}O]^{3-}$, found it oxidized 3 moles of triphenylphosphine per mole O_2 in a reaction proposed to involve 2 moles of the molybdenum complex. This activity was rationalized by the comproportionation of molybdenum (VI) dioxo species, leading to formation of an unreactive μ-oxo species following a final oxygen atom transfer to phosphine (Figure 1-23b). This differs from the previously reported dithiocarbamate complex, for which the unreactive molybdenum oxo-bridged dimer is in equilibrium with the dioxomolybdenum (VI) and oxomolybdenum (IV) species. More recent investigations by the group of Nadia Mösch-Zanetti have demonstrated the same aerobic phosphine oxidation for a stable monomeric complex, [117] and the authors propose based on ^{1}H and ^{31}P NMR data that both atoms of the peroxo group are transferred to phosphine. Later mechanistic investigations involving a related Schiff-base molybdenum (VI) complex suggest that the rate limiting step of the reaction is transfer of the first oxygen of the peroxo group, with transfer of the second oxygen atom quickly leading to formation of the monooxo molybdenum (IV) species (Figure 1-23c). [121] These ketiminato and

Schiff-base complexes are the first reported molybdenum complexes to catalytically oxidize phosphines with dioxygen as the terminal oxidant, and the intermediate species in the oxidation have yet to be studied in-depth either by experiment or *in silico*. The oxidation of sulfides to sulfoxides and sulfones is well-documented for Mimoun-type complexes formed by reaction with peroxidic reagents, but this activity is not reported for aerobic systems or for oxo-group transfer by dioxomolybdenum centers.

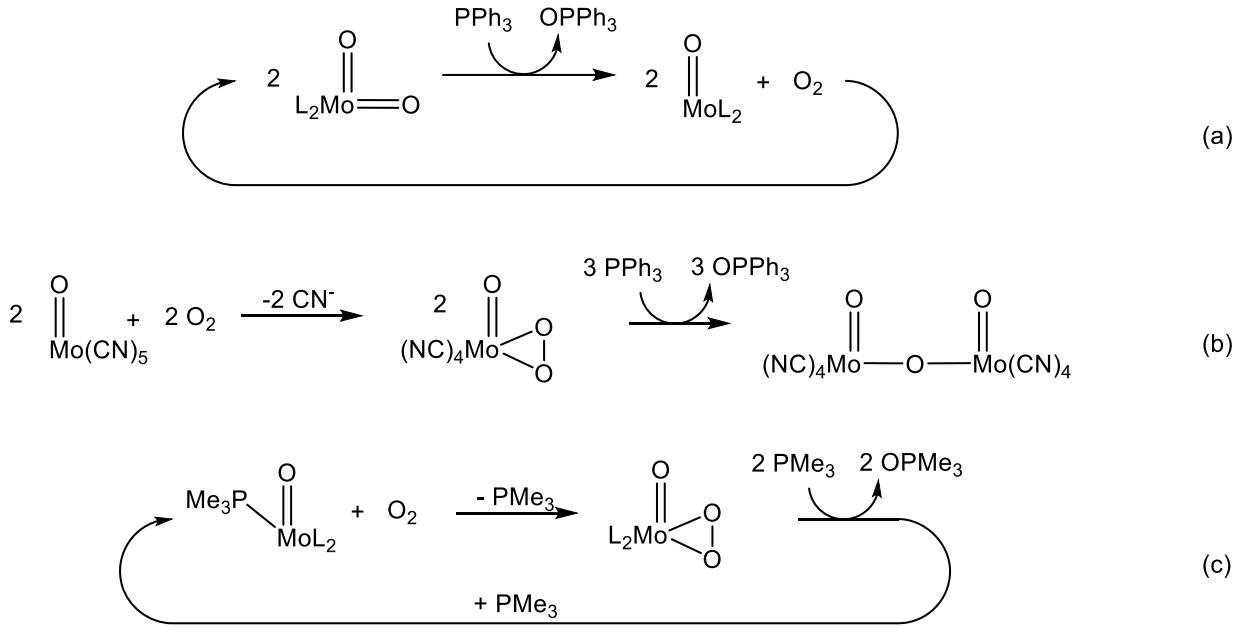

Figure 1-23. Catalytic aerobic oxygen atom transfer reported by Barral, et al. (a), aerobic oxygen atom transfer reported by Arzoumanian, et al. (b) and catalytic aerobic oxygen atom transfer reported by Dupé, et al. (c)

1.4 Oxidation of, and OAT to, thiols

Oxidation of thiols is an important reaction in the biological, synthetic, and industrial contexts. In cellular environments, cysteine thiol side chains are known to act as metabolic signaling switches, with their large variety of available reactions being selected for by their local environment (Figure 1-24), [122] and in the non-reducing extracellular environment, cysteine-disulfide bridges are a determining factor of protein structure.

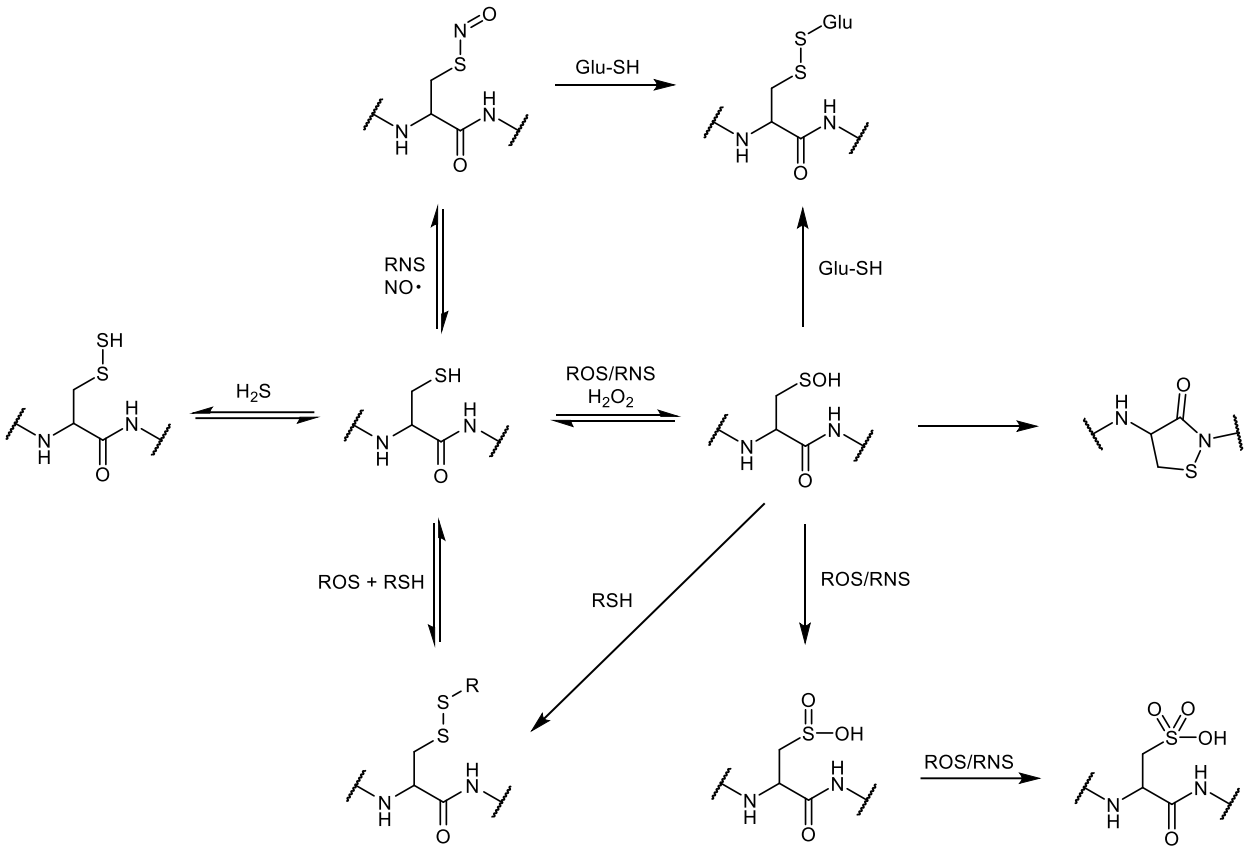

Figure 1-24. Oxidative reactions of cysteine with reactive oxygen species (ROS= $O_2^{\bullet-}$, $^{\bullet}OH$, H_2O_2), reactive nitrogen species (RNS= $^{\bullet}NO$, ^{+}NO, N_2O_3), and sulfur species

In industrial and synthetic contexts, the oxidation of thiols to disulfides is useful as a method of petroleum sweetening [123] and as thiolation, reduction, or thiol protection reagents. [124,125] Thiols are aerobically oxidized by a 1-electron process to thiyl radicals, which then homocouple to form disulfides (eq. 3), a process that can also proceed by an ionic pathway (eq. 4).

$$RSH + {}^{1}/_{2}\ O_2 \rightarrow 2RS^{\bullet} + H_2O \rightarrow RSSR \qquad \textit{eq. 3}$$

$$RSH + {}^{1}/_{2}\ O_2 \rightarrow RS^{+} + RSH \rightarrow RSSR + H_2O \qquad \textit{eq. 4}$$

This oxidation is often catalyzed by bases, which is proposed to be facilitated by the easier oxidation of the thiolate anion relative to that of the neutral thiol. [126] Metal oxide promoted coupling of thiols is demonstrated to proceed *via* the same mechanism as aerobic autooxidation, producing thiyl radicals and water as products of 1-electron oxidation processes. Catalytic systems employing both heterogeneous and homogeneous metal-containing catalysts have also

been well-documented, with vanadium, iron, cobalt, copper, molybdenum, rhodium, ruthenium, and gold catalysts represented in the literature. Previous molybdenum systems employed for this oxidation are scarce, with a two reports of thiols being used to stoichiometrically reduce dioxomolybdenum (VI) species to oxomolybdenum (IV), [25,127] a single report of aerobic oxidation by a molybdenum-containing heterogeneous catalyst, [128] and a report of catalytic oxidation employing a dimolybdenum (VI) DMSO complex (using DMSO as solvent and oxygen atom source, Figure 1-25). These few reports seem to suggest that, with an appropriate molybdenum complex, aerobic coupling of thiols to disulfides could be carried out under homogenous catalytic conditions.

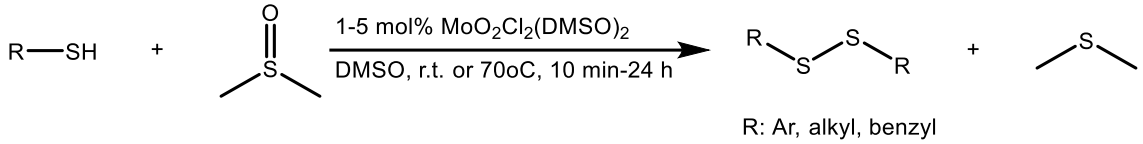

Figure 1-25. Oxidation of thiols to disulfides by $MoO_2Cl_2(DMSO)_2$ with dimethyl sulfoxide as solvent and oxygen atom source

1.5 Gaps in knowledge

The broad investigations of molybdenum-catalyzed oxygen atom transfer to this point have left few stones unturned. However, to the best of our knowledge, oxidative kinetic resolution of phosphines had not been examined, and the structural factors that may lead to the development of a practical catalyst for kinetic resolution of chiral monophosphines *via* oxygen atom transfer had not been elucidated. Using the easily-derivatized chiral cyclohexyl-salen ligand, we believed that a fast, enantioselective catalytic system could be developed for oxidative kinetic resolution of chiral phosphines. An accompanying computational study could establish whether DFT modeling of the enantioselective step can be used to screen potential catalysts. The recently re-emerged coordination chemistry of molybdenum dioxygen complexes is little developed, as is the possibility of catalytic oxygen atom transfer with dioxygen as the terminal oxygen atom source. The structural influences on differences in reactivity between nucleophilic and electrophilic substrates had also not been modeled. Using dioxomolybdenum (VI)

cyclohexylsalen complexes, we hoped to demonstrate the potential for aerobic oxidation of both nucleophilic and electrophilic substrates and to employ DFT methods to model previously unexplored features of the mechanism. Finally, literature reports of molybdenum-promoted oxidation of thiols remain scarce, as do examinations of the pathways and oxidation products of these reactions. The few existing reports suggest that a molybdenum-oxo catalyst should be able to carry out this oxidation under aerobic conditions, but the parameters for the reaction were yet to be established.

1.6 This work—Preview

In this dissertation, we present the results of catalytic investigations using dioxomolybdenum (VI) Schiff-base complexes for reactions and applications not previously examined for the system. Chapter 2 details the use of a chiral dioxomolybdenum catalyst for the enantiomeric enrichment of chiral phosphines and phosphine oxides by kinetic resolution, along with a computational investigation of the selectivity and mechanistic features. Small to moderate enantiomeric excesses of the product phosphine oxide (0-30%) are achieved, and we demonstrate strong correlation (R=0.99) between experimental selectivity and differences in activation energy calculated with DFT methods. Chapter 3 explores the mechanistic details of the aerobic oxidation of phosphines with these dioxomolybdenum species with an experimental and computational study of dioxygen coordination, activation, and transfer. DFT studies reveal spin-crossover processes in keeping with the literature for other transition metals for coordination of dioxygen, as well as a surprising oxygen atom transfer from the oxo group of the oxoperoxo complex and an unusual cleavage of the peroxo moiety to re-form the dioxomolybdenum complex. Finally, Chapter 4 reports the outcome of aerobic oxidation studies of thiols catalyzed by these oxo-molybdenum complexes. Oxidative homocoupling of thiols to disulfides is found to be general, with the catalytic reaction observed for alkyl, aryl, and amino acid-derived thiols. The oxidation of benzyl mercaptan to benzyl disulfide is found to be accompanied by C-S bond cleavage, resulting in the formation of benzyl trisulfide, and oxidation of dodecane thiol results in formation of a previously unreported oxidation product, the sulfenic anhydride, as a secondary product alongside the disulfide.

1.7 Works Cited

[1] R.H. Holm, Metal-centered oxygen atom transfer reactions, Chemical Reviews.87 (1987) 1401–1449.

[2] A.K. Rappe, W.A.I. Goddard, Hydrocarbon oxidation by high-valent Group VI oxides, J. Am. Chem. Soc. 104 (1982) 3287–3294.

[3] C.J. Ballhausen, H.B. Gray, The Electronic Structure of the Vanadyl Ion, Inorganic Chemistry. 1 (1962) 111–122.

[4] F. Basolo, Opening Remarks to Oxygen Complexes and Oxygen Activation by Transition metals, in: A.E. Martell, D.T. Sawyer (Eds.), Oxygen Complexes and Oxygen Activation by Transition Metals, Springer US, Boston, MA, 1988: pp. 1–2.

[5] R. Hille, J. Hall, P. Basu, The Mononuclear Molybdenum Enzymes, Chemical Reviews.114 (2014) 3963–4038.

[6] B.W. Kail, L.M. Pérez, S.D. Zarić, A.J. Millar, C.G. Young, M.B. Hall, P. Basu, Mechanistic Investigation of the Oxygen-Atom-Transfer Reactivity of Dioxo-molybdenum(VI) Complexes, Chemistry - A European Journal. 12 (2006) 7501–7509.

[7] B.E. Schultz, S.F. Gheller, M.C. Muetterties, M.J. Scott, R.H. Holm, Molybdenum-mediated oxygen-atom transfer: an improved analog reaction system of the molybdenum oxotransferases, J. Am. Chem. Soc. 115 (1993) 2714–2722.

[8] K. Ambroziak, New dioxomolybdenum(VI) complexes of tetradentate Schiff base as catalysts for epoxidation of olefins, Journal of Molecular Catalysis A: Chemical. 211 (2004) 9–16.

[9] C.J. Whiteoak, G.J.P. Britovsek, V.C. Gibson, A.J.P. White, Electronic effects in oxo transfer reactions catalysed by salan molybdenum(vi) cis-dioxo complexes, Dalton Transactions. (2009) 2337.

[10] K. Peariso, R.L. McNaughton, M.L. Kirk, Active-site stereochemical control of oxygen atom transfer reactivity in sulfite oxidase, J. Am. Chem. Soc. 124 (2002) 9006–9007.

[11] P. Basu, B.W. Kail, C.G. Young, Influence of the Oxygen Atom Acceptor on the Reaction Coordinate and Mechanism of Oxygen Atom Transfer from the Dioxo-Mo(VI) Complex, Tp i PrMoO2(OPh), to Tertiary Phosphines, Inorganic Chemistry. 49 (2010) 4895–4900.

[12] C. Lorber, M.R. Plutino, L.I. Elding, E. Nordlander, Kinetics of oxygen-atom transfer reactions involving molybdenum dithiolene complexes, Journal of the Chemical Society - Dalton Transactions. 2 (1997) 3997–4003.

[13] F.J. Arnaiz, R. Aguado, J.M. Martinez de Ilarduya, Dioxomolybdenum(VI) halides as oxotransfer catalysts, Polyhedron. 13 (1994) 3257–3259.

[14] B.E. Schultz, R.H. Holm, Kinetics of Oxygen Atom Transfer in an Analogue Reaction System of the Molybdenum Oxotransferases, Inorganic Chemistry. 32 (1993) 4244–4248.

[15] J.H. Enemark, J.J.A. Cooney, J.-J. Wang, R.H. Holm, Synthetic Analogues and Reaction Systems Relevant to the Molybdenum and Tungsten Oxotransferases, Chemical Reviews. 104 (2004) 1175–1200.

[16] P.P. Samuel, S. Horn, A. Döring, K.G.V. Havelius, S. Reschke, S. Leimkühler, M. Haumann, C. Schulzke, A crystallographic and Mo K-edge XAS study of molybdenum oxo bis-, mono-, and non-dithiolene complexes-first-sphere coordination geometry and noninnocence of ligands, European Journal of Inorganic Chemistry. (2011) 4387–4399.

[17] R. Sanz, M. Pedrosa, Applications of Dioxomolybdenum(VI) Complexes to Organic Synthesis, Current Organic Synthesis. 6 (2009) 239–263.

[18] H. Arzoumanian, D. Nuel, J. Sanchez, Oxygen atom transfer from dimethyl sulfoxide and N2O to triphenylphosphine mediated by a cyanooxomolybdate(IV) anion, Journal of Molecular Catalysis. 65 (1991) L9–L11.

[19] N. Zwettler, N. Grover, F. Belaj, K. Kirchner, N.C. Mösch-Zanetti, Activation of Molecular Oxygen by a Molybdenum(IV) Imido Compound, Inorganic Chemistry. 56 (2017) 10147–10150.

[20] M.J. Morris, 4. Molybdenum 1993, Coordination Chemistry Reviews. 146 (1995) 43–97.

[21] M. Bagherzadeh, S. Ataie, H. Mahmoudi, J. Janczak, Synthesis, structure characterization and study of a new molybdenum Schiff base complex as an epoxidation catalyst with very high turnover numbers, Inorganic Chemistry Communications. 84 (2017) 63–67.

[22] D. Dowerah, J.T. Spence, R. Singh, A.G. Wedd, G.L. Wilson, F. Farchione, J.H. Enemark, J. Kristofzski, M. Bruck, Molybdenum(VI) and molybdenum(V) complexes with N,N'-dimethyl-N,N'-bis(2-mercaptophenyl)ethylenediamine. Electrochemical and electron paramagnetic resonance models for the molybdenum(VI/V) centers of the molybdenum hydroxylases and related enzymes, J. Am. Chem. Soc. 109 (1987) 5655–5665.

[23] K.-M. Sung, R.H. Holm, Functional Analogue Reaction Systems of the DMSO Reductase Isoenzyme Family: Probable Mechanism of S-Oxide Reduction in Oxo Transfer Reactions Mediated by Bis(dithiolene)−Tungsten(IV,VI) Complexes, J. Am. Chem. Soc. 124 (2002) 4312–4320.

[24] T.A. Rusmore, M.J. Behlen, A. John, D.T. Glatzhofer, K.M. Nicholas, Oxidative kinetic resolution of P-chiral phosphines catalyzed by chiral (salen)dioxomolybdenum complexes, Molecular Catalysis. 513 (2021) 111776–111776.

[25] E.W. Harlan, J.M. Berg, R.H. Holm, Thermodynamic fitness of molybdenum(IV,VI) complexes for oxygen-atom transfer reactions, including those with enzymic substrates, J. Am. Chem. Soc. 108 (1986) 6992–7000.

[26] F. Choplin, G. Kaufmann, R. Rohmer, Vibrational spectra of new coordination complexes of molybdenum(VI) with trimethylamine and trimethylarsine oxides, C. R. Acad. Sc. Paris Serie C. 268 (1969) 333–336.

[27] V.N. Nemykin, P. Basu, Oxygen Atom Transfer Reactivity from a Dioxo-Mo(VI) Complex to Tertiary Phosphines: Synthesis, Characterization, and Structure of Phosphoryl Intermediate Complexes, (2005).

[28] E. Bergin, C.T. O'Connor, S.B. Robinson, E.M. McGarrigle, C.P. O'Mahony, D.G. Gilheany, Synthesis of P-Stereogenic Phosphorus Compounds. Asymmetric Oxidation of Phosphines under Appel Conditions, J. Am. Chem. Soc. 129 (2007) 9566–9567.

[29] A. Brandi, S. Cicchi, A. Goti, K.M. Pietrusiewicz, Chiral Vinyl Phosphine Oxides: Double Asymmetric Induction in the 1,3-Dipolar Cycloaddition to Chiral Nitrones. Kinetic Resolution of a Racemic Phospholene Oxide, Phosphorus, Sulfur, and Silicon and the Related Elements. 75 (1993) 155–158.

[30] D. Zhao, L. Mao, Y. Wang, D. Yang, Q. Zhang, R. Wang, Catalytic Asymmetric Hydrophosphinylation of α,β-Unsaturated N -Acylpyrroles: Application of Dialkyl Phosphine Oxides in Enantioselective Synthesis of Chiral Phosphine Oxides or Phosphines, Organic Letters. 12 (2010) 1880–1882.

[31] V. Bhat, S. Wang, B.M. Stoltz, S.C. Virgil, Asymmetric Synthesis of QUINAP via Dynamic Kinetic Resolution, J. Am. Chem. Soc. 135 (2013) 16829–16832.

[32] V.S. Chan, M. Chiu, R.G. Bergman, F.D. Toste, Development of Ruthenium Catalysts for the Enantioselective Synthesis of P-Stereogenic Phosphines via Nucleophilic Phosphido Intermediates, J. Am. Chem. Soc. 131 (2009) 6021–6032.

[33] C.E. Headley, S.P. Marsden, Synthesis and Application of P -Stereogenic Phosphines as Superior Reagents in the Asymmetric Aza-Wittig Reaction, The Journal of Organic Chemistry. 72 (2007) 7185–7189.

[34] Y.-N. Gao, F.-C. Shi, Q. Xu, M. Shi, Enantioselective Synthesis of Isoquinolines: Merging Chiral-Phosphine and Gold Catalysis, Chemistry - A European Journal. 22 (2016) 6803–6807.

[35] G. Lyashenko, G. Saischek, M.E. Judmaier, M. Volpe, J. Baumgartner, F. Belaj, V. Jancik, R. Herbst-Irmer, N.C. Mösch-Zanetti, Oxo-molybdenum and oxo-tungsten complexes of Schiff bases relevant to molybdoenzymes, Dalton Transactions. (2009) 5655–5665.

[36] C.J. Whiteoak, G.J.P. Britovsek, V.C. Gibson, A.J.P. White, Electronic effects in oxo transfer reactions catalysed by salan molybdenum(vi) cis-dioxo complexes, Dalton Transactions. (2009) 2337–2337.

[37] P.M. Reis, P.J. Costa, C.C. Romão, J.A. Fernandes, M.J. Calhorda, B. Royo, Hydrogen activation by high-valent oxo-molybdenum(VI) and -rhenium(VII) and -(V) compounds, Dalton Transactions. (2008) 1727–1733.

[38] A.C. Fernandes, C.C. Romão, A novel method for the reduction of sulfoxides and pyridine N-oxides with the system silane/MoO2Cl2, Tetrahedron. 62 (2006) 9650–9654.

[39] I. Cabrita, S.C.A. Sousa, A.C. Fernandes, Reduction of sulfoxides catalyzed by oxo-complexes, Tetrahedron Letters. 51 (2010) 6132–6135.

[40] F.E. Kühn, A.M. Santos, M. Abrantes, Mononuclear Organomolybdenum(VI) Dioxo Complexes: Synthesis, Reactivity, and Catalytic Applications, Chemical Reviews. 106 (2006) 2455–2475.

[41] A. Lehtonen, R. Sillanpää, Dioxomolybdenum(VI) complexes with tri- and tetradentate aminobis(phenolate)s, Polyhedron. 24 (2005) 257–265.

[42] O. Bortolini, S. Campestrini, F. Di Furia, G. Modena, Metal catalysis in oxidation by peroxides. 28. Kinetics and mechanism of the molybdenum-catalyzed oxidation of sulfoxides to sulfones with hydrogen peroxide, Journal of Organic Chemistry. 52 (1987) 5093–5095.

[43] V. Conte, O. Bortolini, Transition metal peroxides. Synthesis and role in oxidation reactions, in: The Chemistry of Peroxides, Volume 2, John Wiley & Sons, Ltd, n.d.

[44] M. Amini, M.M. Haghdoost, M. Bagherzadeh, Oxido-peroxido molybdenum(VI) complexes in catalytic and stoichiometric oxidations, Coordination Chemistry Reviews. 257 (2013) 1093–1121.

[45] L.F. Veiros, C.A. Gamelas, M.J. Calhorda, C.C. Romão, Chemoselective Sulfide and Sulfoxide Oxidations by CpMo(CO)3Cl/HOOR: a DFT Mechanistic Study, Organometallics. 30 (2011) 1454–1465.

[46] K.B. Sharpless, J.M. Townsend, D.R. Williams, Mechanism of epoxidation of olefins by covalent peroxides of molybdenum(VI), J. Am. Chem. Soc. 94 (1972) 295–296.

[47] E.N. Jacobsen, W. Zhang, A.R. Muci, J.R. Ecker, L. Deng, Highly enantioselective epoxidation catalysts derived from 1,2-diaminocyclohexane, J. Am. Chem. Soc. 113 (1991) 7063–7064.

[48] Jain, A., A.V. Gelatosb, T.T. Kodasa, Selective chemical vapor deposition of copper using (hfac) copper (I) vinyltrimethylsilane in the absence and presence of water, Thin Solid Films. 262 (1995) 52–59.

[49] O. Belda, C. Moberg, Molybdenum-Catalyzed Asymmetric Allylic Alkylations, Acc. Chem. Res. 37 (2004) 159–167.

[50] B.M. Trost, S. Hildbrand, K. Dogra, Regio- and Enantioselective Molybdenum-Catalyzed Alkylations of Polyenyl Esters, J. Am. Chem. Soc. 121 (1999) 10416–10417.

[51] D. Dvorak, I. Stary, P. Kocovsky, Stereochemistry of Molybdenum(0)-Catalyzed Allylic Substitution: The First Observation of a Syn-Syn Mechanism, J. Am. Chem. Soc. 117 (1995) 6130–6131.

[52] D.R. Cefalo, A.F. Kiely, M. Wuchrer, J.Y. Jamieson, R.R. Schrock, A.H. Hoveyda, Enantioselective Synthesis of Unsaturated Cyclic Tertiary Ethers By Mo-Catalyzed Olefin Metathesis, J. Am. Chem. Soc. 123 (2001) 3139–3140.

[53] S.J. Malcolmson, S.J. Meek, E.S. Sattely, R.R. Schrock, A.H. Hoveyda, Highly efficient molybdenum-based catalysts for enantioselective alkene metathesis, Nature. 456 (2008) 933–937.

[54] J.S. Harvey, S.J. Malcolmson, K.S. Dunne, S.J. Meek, A.L. Thompson, R.R. Schrock, A.H. Hoveyda, V. Gouverneur, Enantioselective Synthesis of P-Stereogenic Phosphinates and Phosphine Oxides by Molybdenum-Catalyzed Asymmetric Ring-Closing Metathesis, Angewandte Chemie International Edition. 48 (2009) 762–766.

[55] J.A. Brito, B. Royo, M. Gómez, An overview of chiral molybdenum complexes applied in enantioselective catalysis, Catal. Sci. Technol. 1 (2011) 1109–1118.

[56] R.J. Cross, P.D. Newman, R.D. Peacock, D. Stirling, Chiral phosphinoylalcohol complexes of monooxobis(peroxo)molybdenum(VI) and their use as asymmetric oxidants, Journal of Molecular Catalysis A: Chemical. 144 (1999) 273–284.

[57] H.-J. Hamann, E. Höft, D. Mostowicz, A. Mishnev, Z. Urbańczyk-Lipkowska, M. Chmielewski, New optically pure sugar hydroperoxides. Synhtesis and use for enantioselective oxygen transfer, Tetrahedron. 53 (1997) 185–192.

[58] V. Schurig, K. Hintzer, U. Leyrer, C. Mark, P. Pitchen, H.B. Kagan, Enantioselective epoxidation of unfunctionalized simple olefins by non-racemic molybdenum(VI)(oxo-diperoxo) complexes, Journal of Organometallic Chemistry. 370 (1989) 81–96.

[59] A.J. Burke, Chiral oxoperoxomolybdenum(VI) complexes for enantioselective olefin epoxidation: Some mechanistic and stereochemical reflections, Coordination Chemistry Reviews. 252 (2008) 170–175.

[60] F.E. Kühn, J. Zhao, W.A. Herrmann, Chiral monomeric organorhenium(VII) and organomolybdenum(VI) compounds as catalysts for chiral olefin epoxidation reactions, Tetrahedron: Asymmetry. 16 (2005) 3469–3479.

[61] A.U. Barlan, A. Basak, H. Yamamoto, Enantioselective Oxidation of Olefins Catalyzed by a Chiral Bishydroxamic Acid Complex of Molybdenum, Angewandte Chemie International Edition. 45 (2006) 5849–5852.

[62] S.U. Park, G.J. Kim, S.S. Yun, Studies on Enantioselective Epoxidation of Styrene Derivatives with Transition Metal(W, Mo and Re)-Peroxo Complexes, Bulletin of the Korean Chemical Society. 21 (2000) 446–448.

[63] C.I. Fernandes, M.S. Saraiva, T.G. Nunes, P.D. Vaz, C.D. Nunes, Highly enantioselective olefin epoxidation controlled by helical confined environments, Journal of Catalysis. 309 (2014) 21–32.

[64] A. Basak, A.U. Barlan, H. Yamamoto, Catalytic enantioselective oxidation of sulfides and disulfides by a chiral complex of bis-hydroxamic acid and molybdenum, Tetrahedron: Asymmetry. 17 (2006) 508–511.

[65] G. Romanowski, J. Kira, Chiral molybdenum(VI) complexes with tridentate Schiff bases derived from S(+)-1-amino-2-propanol: Synthesis, characterization and catalytic activity in the oxidation of prochiral sulfides and olefins, Polyhedron. 117 (2016) 352–358.

[66] M.M. Haghdoost, N. Zwettler, G. Golbaghi, F. Belaj, M. Bagherzadeh, J.A. Schachner, N.C. Mösch-Zanetti, Diastereoselective Synthesis and Catalytic Activity of Two Chiral cis -Dioxidomolybdenum(VI) Complexes, European Journal of Inorganic Chemistry. 2018 (2018) 2549–2556.

[67] M. Bonchio, T. Carofiglio, F. Di Furia, R. Fornasier, Supramolecular catalysis: enantioselective oxidation of thioanisole in water by hydrogen peroxide catalyzed by Mo(VI) in the presence of .beta.-cyclodextrin-based ligands, Journal of Organic Chemistry. 60 (1995) 5986–5988.

[68] J.S. Harvey, V. Gouverneur, Catalytic enantioselective synthesis of P-stereogenic compounds, Chemical Communications. 46 (2010) 7477–7485.

[69] C. Chien, T. Kawasaki, M. Sakamoto, Y. Tamura, Y. Kita, Stereospecific Epoxidation of cis-2-Butene-1, 4-diones to cis-2, 3-Epoxybutane-1, 4-diones with Oxodiperoxomolybdenum (VI), MoO5H2O·HMPA, Chemical & Pharmaceutical Bulletin. 33 (1985) 2743–2749.

[70] J.M. Keith, J.F. Larrow, E.N. Jacobsen, Practical Considerations in Kinetic Resolution Reactions, Advanced Synthesis & Catalysis. 343 (2001) 5–26.

[71] V.S. Martin, S.S. Woodard, T. Katsuki, Y. Yamada, M. Ikeda, K.B. Sharpless, Kinetic resolution of racemic allylic alcohols by enantioselective epoxidation. A route to substances of absolute enantiomeric purity?, J. Am. Chem. Soc. 103 (1981) 6237–6240.

[72] S. Hashiguchi, A. Fujii, K.-J. Haack, K. Matsumura, T. Ikariya, R. Noyori, Kinetic Resolution of Racemic Secondary Alcohols by RuII-Catalyzed Hydrogen Transfer, Angewandte Chemie International Edition in English. 36 (1997) 288–290.

[73] Y. Nishibayashi, I. Takei, S. Uemura, M. Hidai, Extremely High Enantioselective Redox Reaction of Ketones and Alcohols Catalyzed by RuCl2(PPh3)(oxazolinylferrocenylphosphine), Organometallics. 18 (1999) 2291–2293.

[74] H. Pellissier, Recent developments in non-enzymatic catalytic oxidative kinetic resolution of secondary alcohols, Tetrahedron. 74 (2018) 3459–3468.

[75] N. Komatsu, Y. Nishibayashi, T. Sugita, S. Uemura, Catalytic asymmetric oxidation of sulfides to sulfoxides using R-(+)-binaphthol, Tetrahedron Letters. 33 (1992) 5391–5394.

[76] Y. Noguchi, H. Takiyama, T. Katsuki, Kinetic Resolution of Racemic Allenes by Using Chiral (Salen)manganese(III) Complex as a Catalyst, Synlett. 1998 (1998) 543–545.

[77] O.I. Kolodiazhnyi, Recent developments in the asymmetric synthesis of P-chiral phosphorus compounds, Tetrahedron: Asymmetry. 23 (2012) 1–46.

[78] W. Perlikowska, M. Gouygou, J.-C. Daran, G. Balavoine, M. Mikołajczyk, Kinetic resolution of P-chiral tertiary phosphines and chlorophosphines: a new approach to optically active phosphoryl and thiophosphoryl compounds, Tetrahedron Letters. 42 (2001) 7841–7845.

[79] P. Le Maux, H. Bahri, G. Simonneaux, L. Toupet, Enantioselective Oxidation of Racemic Phosphines with Chiral Oxoruthenium Porphyrins and Crystal Structure of [5,10,15,20-Tetrakis[o-((2-methoxy-2-phenyl-3,3,3-trifluoropropanoyl)amino)phenyl]porphyrinato](carbonyl)(tetrahydrofuran) ruthenium(II) (α,β, α,β Isomer), Inorganic Chemistry. 34 (1995) 4691–4697.

[80] H. Pellissier, Catalytic Kinetic Resolution, in: Separation of Enantiomers, Wiley-VCH Verlag GmbH & Co. KGaA, Weinheim, Germany, 2014: pp. 75–122.

[81] D.T. Sawyer, Oxygen chemistry, Oxford University Press, New York, 1991.

[82] R.A. Sheldon, A History of Oxygen Activation: 1773–1993, in: D.H.R. Barton, A.E. Martell, D.T. Sawyer (Eds.), The Activation of Dioxygen and Homogeneous Catalytic Oxidation, Springer US, Boston, MA, 1993: pp. 9–30.

[83] K. Fujisawa, M. Tanaka, Y. Moro-oka, N. Kitajima, A Monomeric Side-On Superoxocopper(II) Complex: Cu(O2)(HB(3-tBu-5-iPrpz)3), J. Am. Chem. Soc. 116 (1994) 12079–12080.

[84] C. Würtele, E. Gaoutchenova, K. Harms, M.C. Holthausen, J. Sundermeyer, S. Schindler, Crystallographic Characterization of a Synthetic 1:1 End-On Copper Dioxygen Adduct Complex, Angewandte Chemie International Edition. 45 (2006) 3867–3869.

[85] A. Bakac, Oxygen Activation with Transition-Metal Complexes in Aqueous Solution, Inorganic Chemistry. 49 (2010) 3584–3593.

[86] R. Bakac, DIOXYGEN ACTIVATION BY TRANSITION METAL COMPLEXES. ATOM TRANSFER AND FREE RADICAL CHEMISTRY IN AQUEOUS MEDIA, in: Advances in Inorganic Chemistry, Elsevier, 2004: pp. 1–59.

[87] R.P. Hanzlik, D. Williamson, Oxygen activation by transition metal complexes. 2. Bis(acetylacetonato)cobalt(II)-catalyzed oxidation of tributylphosphine, J. Am. Chem. Soc. 98 (1976) 6570–6573.

[88] E. Szajna-Fuller, A. Bakac, Thermodynamics of Oxygen Activation by Macrocyclic Complexes of Rhodium, Inorganic Chemistry. 46 (2007) 10907–10912.

[89] P. Mars, D.W. van Krevelen, Oxidations carried out by means of vanadium oxide catalysts, Chemical Engineering Science. 3 (1954) 41–59.

[90] E.V. Rybak-Akimova, Mechanisms of Oxygen Binding and Activation at Transition Metal Centers, in: Physical Inorganic Chemistry, John Wiley & Sons, Ltd, 2010: pp. 109–188.

[91] H. Yu, Y. Fu, Q. Guo, Z. Lin, DFT Studies on Reactions of Transition Metal Complexes with O2, Organometallics. 28 (2009) 4443–4451.

[92] T. Katsuki, K.B. Sharpless, The first practical method for asymmetric epoxidation, J. Am. Chem. Soc. 102 (1980) 5974–5976.

[93] M.G. Finn, K.B. Sharpless, 8 - On the Mechanism of Asymmetric Epoxidation with Titanium—Tartrate Catalysts, in: J.D. Morrison (Ed.), Asymmetric Synthesis, Academic Press, San Diego, 1985: pp. 247–308.

[94] R. Mishra, R. Banerjee, S. Mukhopadhyay, Cu(II)-catalyzed oxidation of thiols by superoxide ligated to CoIII2, Journal of Physical Organic Chemistry. 25 (2012) 1193–1197.

[95] C.X. Zhang, H.-C. Liang, K.J. Humphreys, K.D. Karlin, Copper-dioxygen complexes and their roles in biomimetic oxidation reactions, in: L.I. Simándi (Ed.), Advances in Catalytic Activation of Dioxygen by Metal Complexes, Springer US, Boston, MA, 2002: pp. 79–121.

[96] E. Boring, Y.V. Geletii, C.L. Hill, A Homogeneous Catalyst for Selective O2 Oxidation at Ambient Temperature. Diversity-Based Discovery and Mechanistic Investigation of Thioether Oxidation by the Au(III)Cl2NO3(thioether)/O2 System, J. Am. Chem. Soc. 123 (2001) 1625–1635.

[97] A.D. Leu, D.A. Armstrong, Thiyl radical oxidation of copper(I): formation and spectra of oxidized copper thiolates, J. Phys. Chem. 90 (1986) 1449–1454.

[98] H. Firouzabadi, M. Naderi, A. Sardarian, B. Vessal, The Facile Oxidation of Thiols to Disulfides with Bis(2,2'-Bipyridyl) Copper-(II) Permanganate, Synthetic Communications. 13 (1983) 611–615.

[99] D. Kitko, BINUCLEAR COMPLEXES OF COBALT, NICKEL AND COPPER AND ACTIVATION OF MOLECULAR OXYGEN BY TRANSITION METAL COMPLEXES IN THE OXIDATION OF OLEFINIC SUBSTRATES, (1976) 168.

[100] A. John, K.M. Nicholas, Copper-Catalyzed Amidation of 2-Phenylpyridine with Oxygen as the Terminal Oxidant, Journal of Organic Chemistry. 76 (2011) 4158–4162.

[101] W. Buijs, P. Comba, D. Corneli, H. Pritzkow, Structural and mechanistic studies of the copper(II)-assisted ortho-hydroxylation of benzoates by trimethylamine N-oxide, Journal of Organometallic Chemistry. 641 (2002) 71–80.

[102] L.I. Simándi, Catalytic oxidations using cobalt(II) complexes, in: L.I. Simándi (Ed.), Advances in Catalytic Activation of Dioxygen by Metal Complexes, Springer US, Boston, MA, 2002: pp. 265–328.

[103] H. Arzoumanian, Oxygen Activation. Various Aspects of the Metal Oxo and Peroxo Function, Bulletin Des Sociétés Chimiques Belges. 100 (1991) 717–729.

[104] N. Gharah, S. Chakraborty, A.K. Mukherjee, R. Bhattacharyya, Oxoperoxo molybdenum(VI)- and tungsten(VI) complexes with 1-(2'-hydroxyphenyl) ethanone oxime: Synthesis, structure and catalytic uses in the oxidation of olefins, alcohols, sulfides and amines using H2O2 as a terminal oxidant, Inorganica Chimica Acta. 362 (2009) 1089–1100.

[105] M. Bagherzadeh, M.M. Haghdoost, M. Amini, P.G. Derakhshandeh, Molybdenum oxo–peroxo complex: A very fast catalyst for oxidation and reduction of sulfur-based compounds, Catalysis Communications. 23 (2012) 14–19.

[106] S.K. Maiti, K.M. Abdul Malik, R. Bhattacharyya, Oxoperoxo-molybdenum and -tungsten (VI) complexes: their synthesis, structure and catalytic uses in the peroxidic oxidation of alcohols to aldehydes and ketones, Inorganic Chemistry Communications. 7 (2004) 823–828.

[107] S. Campestrini, F. Di Furia, P. Rossi, A. Torboli, G. Valle, Comparison of the relative efficiency of peroxomolybdenum complexes as oxidants of the alcoholic function, Journal of Molecular Catalysis. 83 (1993) 95–105.

[108] N. Grover, F.E. Kuhn, Catalytic Olefin Epoxidation with η^5-Cyclopentadienyl Molybdenum Complexes, Current Organic Chemistry. 16 (n.d.) 16–32.

[109] L.J. Csányi, On the peroxomolybdate complexes as sources of singlet oxygen, Journal of Molecular Catalysis A: Chemical. 322 (2010) 1–6.

[110] M. Bagherzadeh, M. Amini, A. Ellern, L.K. Woo, Catalytic efficiency of a novel complex of oxoperoxo molybdenum(VI): Synthesis, X-ray structure and alkane oxidation, Inorganic Chemistry Communications. 15 (2012) 52–55.

[111] M. Bagherzadeh, M. Amini, H. Parastar, M. Jalali-Heravi, A. Ellern, L.K. Woo, Synthesis, X-ray structure and oxidation catalysis of a oxido–peroxido molybdenum(VI) complex with a tridentate Schiff base ligand, Inorganic Chemistry Communications. 20 (2012) 86–89.

[112] S. Das, T. Bhowmick, T. Punniyamurthy, D. Dey, J. Nath, M.K. Chaudhuri, Molybdenum(VI)-peroxo complex catalyzed oxidation of alkylbenzenes with hydrogen peroxide, Tetrahedron Letters. 44 (2003) 4915–4917.

[113] A. Jimtaisong, R.L. Luck, Synthesis and Catalytic Epoxidation Activity with TBHP and H2O2 of Dioxo-, Oxoperoxo-, and Oxodiperoxo Molybdenum(VI) and Tungsten(VI) Compounds Containing Monodentate or Bidentate Phosphine Oxide Ligands: Crystal Structures of WCl2(O)2(OPMePh2)2, WCl2(O)(O2)(OPMePh2)2, MoCl2(O)2dppmO2·C4H10O, WCl2(O)2dppmO2, Mo(O)(O2)2dppmO2, and W(O)(O2)2dppmO2, Inorganic Chemistry. 45 (2006) 10391–10402.

[114] H. Arzoumanian, Molybdenum-Oxo and Peroxo Complexes in Oxygen Atom Transfer Processes with O_2 as the Primary Oxidant, Current Inorganic Chemistry (Discontinued). 1 (2011) 140–145.

[115] T. Punniyamurthy, S. Velusamy, J. Iqbal, Recent Advances in Transition Metal Catalyzed Oxidation of Organic Substrates with Molecular Oxygen, Chemical Reviews. 105 (2005) 2329–2364.

[116] H. Arzoumanian, J.F. Petrignani, M. Pierrot, F. Ridouane, J. Sanchez, Preparation of an oxoperoxocyanomolybdate(VI) complex by dioxygen oxidation of an oxocyanomolybdate(IV) anion. Structure and reactivity toward phosphines and olefins, Inorganic Chemistry. 27 (1988) 3377–3381.

[117] G. Lyashenko, G. Saischek, A. Pal, R. Herbst-Irmer, N.C. Mösch-Zanetti, Molecular oxygen activation by a molybdenum(IV) monooxo bis(β-ketiminato) complex, Chemical Communications. (2007) 701–703.

[118] D. Matoga, J. Szklarzewicz, A. Samotus, K. Lewiński, Crystal structures of mixed-ligand oxocyano complexes of molybdenum(IV) and tungsten(IV) and their reactivity towards molecular oxygen studied by IR spectroscopy, J. Chem. Soc., Dalton Transactions. (2002) 3587–3592.

[119] D. Matoga, J. Szklarzewicz, A. Samotus, J. Burgess, J. Fawcett, D.R. Russell, Preparation and characterisation of [M(CN)4O(pz)]2− complexes (M=Mo or W) and their reactivity towards molecular oxygen, Polyhedron. 19 (2000) 1503–1509.

[120] N. Zwettler, M.E. Judmaier, L. Strohmeier, F. Belaj, N.C. Mösch-Zanetti, Oxygen activation and catalytic aerobic oxidation by Mo(iv)/(vi) complexes with functionalized iminophenolate ligands, Dalton Transactions. 45 (2016) 14549–14560.

[121] A. Dupé, M.E. Judmaier, F. Belaj, K. Zangger, N.C. Mösch-Zanetti, Activation of molecular oxygen by a molybdenum complex for catalytic oxidation, Dalton Transactions. 44 (2015) 20514–20522.

[122] R. Barral, C. Bocard, I.S. de Roch, L. Sajus, Activation de l'oxygene moleculaire en phase liquide homogene par des complexes oxo du molybdene oxydation catalytique selective des phosphines tertiaires, Tetrahedron Letters. 13 (1972) 1693–1696.

[123] L.J. Alcock, M.V. Perkins, J.M. Chalker, Chemical methods for mapping cysteine oxidation, Chem. Soc. Rev. 47 (2018) 231–268.

[124] G.F. Pavelko, Reactions of thiols and organic disulfides with iron and its oxides, Russ Chem Bull. 55 (2006) 1436–1439.

[125] A. Ogawa, Y. Nishiyama, N. Kambe, S. Murai, N. Sonoda, Selenium, carbon monoxide and water as a new reduction system: Reductive cleavage of disulfides and diselenides to thiols and selenols, Tetrahedron Letters. 28 (1987) 3271–3274.

[126] M. Kirihara, Y. Asai, S. Ogawa, T. Noguchi, A. Hatano, Y. Hirai, A Mild and Environmentally Benign Oxidation of Thiols to Disulfides, Synthesis. 2007 (2007) 3286–3289.

[127] T.J. Wallace, A. Schriesheim, The base-catalysed oxidation of aliphatic and aromatic thiols and disulphides to sulphonic acids, Tetrahedron. 21 (1965) 2271–2280.

[128] V. Sanz, T. Picher, P. Palanca, P. Gomez-Romero, E. Llopis, J.A. Ramirez, D. Beltran, A. Cervilla, Synthesis and structure of (Bu4N)[MoO(O2CC(S)Ph2)2]. The first mononuclear molybdenum(V) complex containing both coordinated thiolate and carboxylate groups, Inorganic Chemistry. 30 (1991) 3113–3115.

[129] A. Cervilla, A. Corma, V. Fornes, E. Llopis, P. Palanca, F. Rey, A. Ribera, Intercalation of [MoVIO2(O2CC(S)Ph2)2]2- in a Zn(II)-Al(III) Layered Double Hydroxide Host: A Strategy for the Heterogeneous Catalysis of the Air Oxidation of Thiols, J. Am. Chem. Soc. 116 (1994) 1595–1596.

CHAPTER 2

KINETIC RESOLUTION OF CHIRAL PHOSPHINES *VIA* OXYGEN ATOM TRANSFER FROM DIOXOMOLYBDENUM (VI) SALEN COMPLEXES

2.1 Introduction

A domain in which *O*-atom transfer reactions of dioxo-molybdenum complexes has received little attention is in their use for stereoselective reactions. *P*-Chiral phosphines are valuable for chiral catalysis, as they introduce a chiral environment in close proximity to the active site metal center [1,2]. The chemical resolution of chiral, racemic monophosphines, including *P*-stereogenic phosphines, typically involves the use of stoichiometric chiral resolving agents or chiral auxiliaries in a multistep reaction process. [3–13] More directly, the catalytic asymmetric synthesis of *P*-chiral phosphines from *sec*-phosphines *via* alkylation or hydrophosphination of alkenes with precious metal complexes has been achieved recently. [12,14,15] These asymmetric synthetic methods generally have limited scope and their enantioselectivities often vary according to the steric bulk of the phosphine. An approach to the enantiomeric enrichment of *P*-chiral phosphines and phosphine oxides that is unexplored is catalytic kinetic resolution (Figure 2-1). [16] Kinetic resolution exploits the differential reactivity of a pair of enantiomers towards a homochiral reagent or catalyst, leading to enantiomeric enrichment of both the remaining substrate and the forming product. [17,18] In a highly stereoselective transformation by kinetic resolution, the maximum enantiomeric enrichment (ee) of both substrate and product is obtained at 50 % conversion; higher ee's of reactant or product may be obtained at the sacrifice of conversion or yield. [18] A single investigation of a *stoichiometric* kinetic resolution of phosphines by Le Maux, et al. [19] employed a dioxoruthenium complex with a difficult to synthesize chiral porphyrin ligand. At 1:1 $LRuO_2$/phosphine, a 41% enantiomeric excess (ee) of the phosphine oxide product was obtained; at 1:10 $LRuO_2$/phosphine the ee fell to 12%. While demonstrating that a chiral oxo-metal species could show enantioselectivity in the oxidation of a racemic phosphine, the modest stereoselectivity and the stoichiometric use of this precious chiral reagent is impractical for the preparation of chiral phosphines or phosphine oxides.

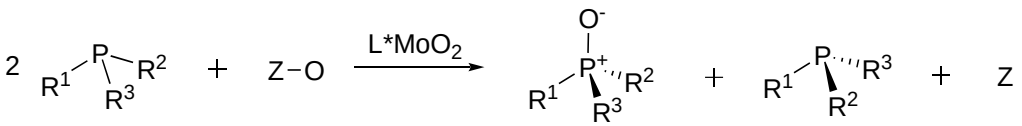

Z-O = R_3NO, R_2SO, ArIO; L* = chiral ligand

Figure 2-1**.** Concept of kinetic resolution of P-stereogenic phosphines by catalytic oxidation

An effective system for *catalytic* kinetic resolution should meet several conditions, most importantly: the chiral catalyst is economical, is easily prepared and its active site chirality is readily tuned structurally and electronically; the reactions are highly enantioselective, even at high substrate loading; and the stoichiometric reagent(s) is effective and inexpensive. [18] Complexes of Schiff-base (imine) ligands offer a versatile and convenient platform for testing structure/activity and selectivity effects, but (imine)MoO_2 complexes have received relatively little attention as catalysts for *O*-transfer reactions. [20–22] In this study we report the first examples of the *catalytic* kinetic resolution of a *P*-chiral monophosphine/phosphine oxide, which employ economical and customizable salen-type dioxo-molybdenum complexes. Also presented are the results of a DFT computational analysis of the catalytic mechanism and the origin of the reaction enantioselectivity.

This chapter largely consists of an article published in Molecular Catalysis in August 2021 [23], primarily written by Theo Rusmore.

2.2 Results and Discussion

2.2.1 Preparation and characterization of L*MoO_2 catalysts

The diimine-type salen-ligands **1-5** required for complexation were prepared by condensation of a salicylaldehyde derivative with an enantiopure ($\geq$ 98%) chiral diamine, either *trans*-(*R,R*)-1,2-diaminocyclohexane (in alcoholic solution) or (*S*)-1,1'-diamino-binaphthylene (in toluene) (Figure 2-2**,** Figure 2-3). The ligands were isolated as yellow powders and characterized spectroscopically. The corresponding LMoO_2 complexes **7-10** (L=CHD-salen) were prepared by refluxing a solution of the Schiff base ligand **1-5** with $MoO_2(acac)_2$ in a chlorinated solvent, 1,2-dichloroethane or chlorobenzene. Isolation by precipitation with a nonpolar solvent afforded the complexes as yellow/orange/brown powders. The BINAM-derived complex **12** was prepared

similarly from ligand **11** and $(DMF)_2MoO_2Cl_2$ (Figure 2-3). The measured optical rotations showed the complexes **7**-**10** to be optically active. It is assumed that configurational integrity is retained during preparation of the chiral ligand and its Mo-complex.

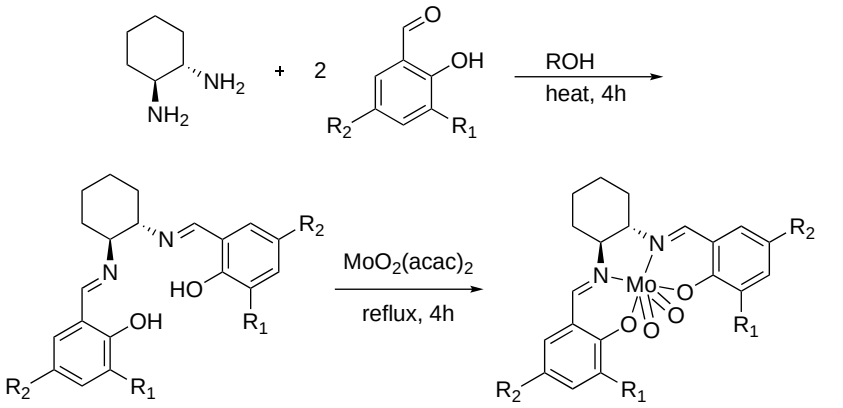

Ligand	Complex	R_1	R_2
1	**6**	H	H
2	**7**	H	NO_2
3	**8**	Br	NO_2
4	**9**	t-Bu	NO_2
5	**10**	t-Bu	t-Bu

Figure 2-2**.** Reaction scheme for the preparation of CHD-salen complexes **6**-**10;** (*S,S*)-configuration shown.

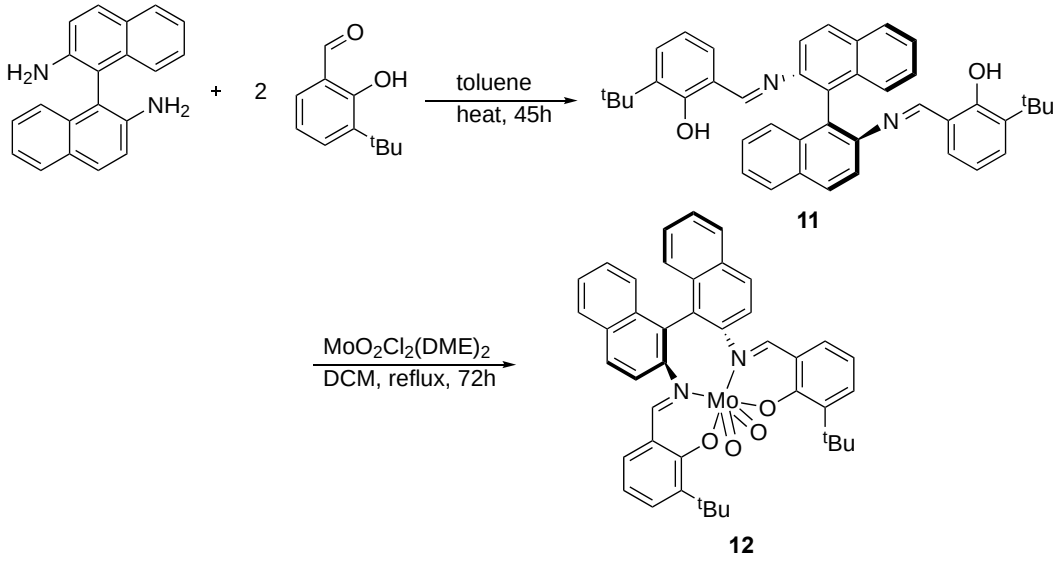

Figure 2-3. Reaction scheme for the synthesis of complex **12**; *S* configuration drawn

IR spectra of the ligands (LH_2, **1-5**) display characteristic imine stretching absorptions at 1582-1610 cm^{-1}, along with nearby aromatic C=C stretching absorptions (Figure A-1-Figure A-4). Ligation of the imine nitrogen to the MoO_2-center in complexes **7-10, 12** lowers the imine C=N stretching frequency noticeably (30-50 cm^{-1}). Two MoO_2 stretching absorptions are observed for all complexes in the range of 914-925 cm^{-1} and 877-898 cm^{-1}, typical of similar $LMoO_2$ complexes,

[20,24,25] ^{1}H-NMR spectra for the cyclohexyldiimine (CHD) ligands show characteristic splitting patterns for the aromatic ring and imine protons in the 7-10 ppm region. Dioxo-molybdenum coordination of these ligands causes an upfield shift of the aromatic and imine signals and a separation of the resonances for the aromatic protons, leading to a characteristic "doubled" ^{1}H-NMR pattern for the complexes **6-10**. This pattern points to a breaking of the symmetry of the ligand upon introduction of the oxo-molybdenum center, creating different electronic environments on the salicylimine rings and the oxo-Mo groups, indicative of a single compound with an unsymmetrical coordination geometry. These features may be compared to NMR data for a series of 1,2-diaminopropane-based salen-MoO_2 reported by Gullotti, et al. [24] and has also been noted by Schachner and coworkers. [26]

To further clarify what the preferred geometry is for the CHD-derived salen complexes, the structures of **6-10** were optimized using the B3LYP hybrid functional. Solvent phase free energies were obtained by single point energy calculation with the M06 functional and the SMD solvent model for 1,2-dichloroethane; with addition of entropy and temperature corrections from the corresponding B3LYP optimization. Two isomeric geometries were evaluated, a C_1 geometry that places two N's and one phenolate O in the equatorial plane, rendering the two oxo O's inequivalent, one trans to N and one trans to the phenolate-O. A second, C_2 geometry was also evaluated that places the two N's and two oxo groups in a plane and the two phenolate oxygen atoms in the *trans* diaxial positions (Figure 2-4). The respective C_1 and C_2 isomers, alternatively designated as *cis-*β and *cis-*α [26], both optimized to minima, but with different energies as listed in Table 1. For all of the CHD-salen derivatives, the unsymmetrical C_1 isomer was calculated to be significantly more stable than the C_2 symmetric isomer, both under B3LYP and with the M06/solvent functional. Among **6-10** the unsymmetrical (C_1) isomer was favored by 6.2-8.2 kcal/mol over the symmetric (C_2) isomers, consistent with the presence of two sets of salicylimine peaks in their ^{1}H NMR spectra. For these compounds the C_1 isomer is likely to be the exclusive form present under the catalytic reaction conditions used in this study.

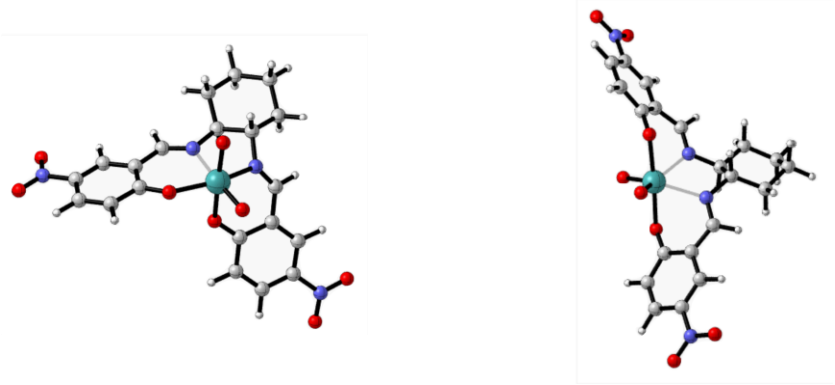

Figure 2-4. Calculated structures of the C_1 (left) and C_2 (right) coordination isomers of (*S,S*)-CHD-NO_2-salen)MoO_2 (7) [Mo- green, C- grey, H- white, O- red, N- blue)

Table 2-1. Energy differences for C_1 vs C_2 coordination isomers of modeled complexes

Complex	ΔG (B3LYP) from C_2 isomer, kcal/mol[a]	ΔG (M06) from C_2 isomer, solvent phase, kcal/mol[a]
7	-9.6	-11.1
8	-9.9	-11.3
9	-7.5	-8.8
10	-7.1	-6.7
12	+0.9	+1.0

[a] C_2 isomer is set at 0 kcal/mol to show favorability of C_1 isomer for (CHD-salen)MoO_2

As for the (BINAM-salen)MoO_2 complex **12**, the ^{1}H NMR spectrum of the reaction product was more complex (*vide* infra) than the distinctive pattern of inequivalent pairs of resonances found for the CHD derivatives **6-10**, suggesting that it did not have the same C_1 geometry. To clarify this issue definitively X-ray quality crystals of the **12** were obtained by vapor diffusion. The solved structure of **12** is shown in Figure 2-5; key bond lengths and angles are listed in Table 2 of the Experimental section.

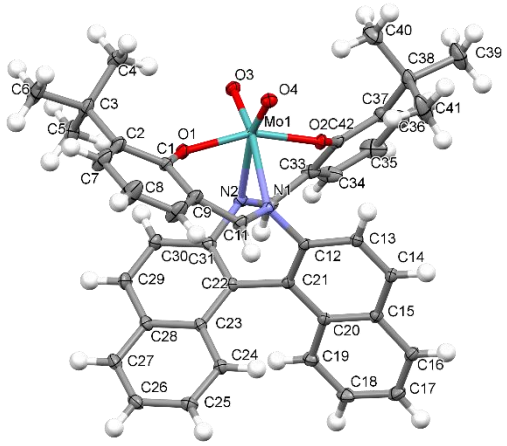

Figure 2-5. X-ray crystal structure of **12**

The X-ray-determined molecular structure of **12** (Figure 2-5) exhibits approximate C_2 symmetry with a distorted octahedral coordination sphere geometry. The two oxo groups occupy cis-positions, both trans to the imine N's and the two phenolate O-atoms are trans to each other. The O=Mo=O bond angle is nearly 110°, comparable to other cis-dioxomolybdenum complexes. [26,27] The trans-phenolate O-Mo-O angle is significantly non-linear at 158°, probably resulting from the constraints of the binaphthyl-diimine coordinating atoms (see Table 2 in Experimental). The dihedral "twist" angle as defined by the N-C-C-N atoms is 74° for **12** compared to 43° calculated for **7**.

We calculated optimized structures for the (BINAM-salen)MoO_2 **12** with the B3LYP hybrid functional (*in vacuo*) and solvated energies with the M06 functional (in 1,2-dichloroethane) (Figure 2-6). In this case it was found that the free energy difference between the C_1 unsymmetrical and C_2 symmetric structures was rather small, approximately 1.0 kcal/mole in favor of the C_2 geometry found in the X-ray structure of **12**. Careful re-analysis of the ^{1}H NMR spectrum of **12** prepared without purification showed partially overlapping patterns derived from the major symmetrical C_2 isomer and the minor unsymmetrical C_1 isomer (3:1 ratio; Figure A-23). Given the presence of both isomers and the small calculated energy difference between them it is possible that both isomers could play an active role in the *O*-transfer phosphine oxidation and its stereoselectivity.

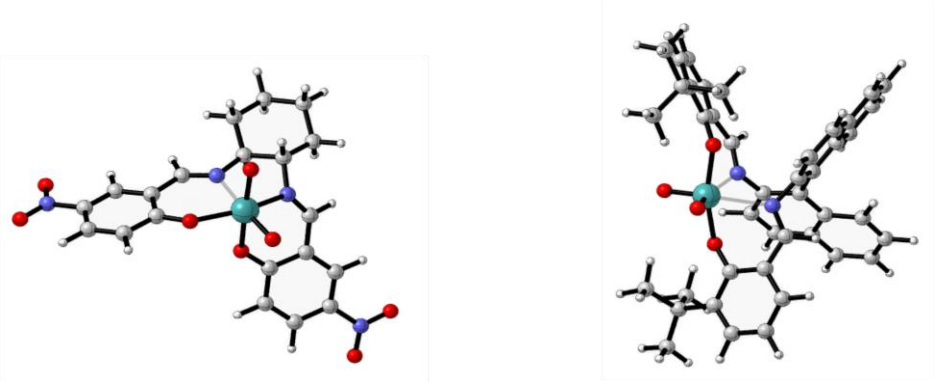

Figure 2-6. B3LYP-optimized structures of (*S,S*-CHD-NO_2-salen)MoO_2 **7** (left) and (*S*-BINAM-salen)MoO_2 **12** (right)

2.2.2 Experimental Reaction Studies

Stoichiometric oxygen atom transfer studies were carried out initially with the unsubstituted complex **6** in a 1:1 molar ratio with triphenylphosphine to establish reactivity and appropriate experimental conditions (Figure 2-7). The reaction was found to occur slowly at 70°C (92 h) in acetonitrile but resulted in complete oxidation of the phosphine. A comparative study of the stoichiometric reaction of triphenylphosphine with (CHD-NO_2-salen)MoO_2 (**7**) conducted at 25˚C in $CDCl_3$ showed a considerably faster conversion; the conversion rate for **7** at room temperature is comparable to that for **6** at 70°C. This result demonstrates acceleration of the *O*-atom transfer (OAT) reaction through the introduction of the *para*-NO_2 group on the salicylimine moiety, as observed in salan-type dioxomolybdenum complexes. [22,28]

$$PPh_3 + L^*MoO_2 \longrightarrow OPPh_3 + L^*MoO$$

Figure 2-7. Reaction of (salen)MoO_2 with PPh_3

Both DMSO and pyridine *N*-oxide were tested as possible oxygen donors for the catalytic oxidation reaction. Neither reagent was observed to oxidize phenylmethyl-*tert*-butylphosphine substrate in blank reactions (without catalyst). When triphenylphosphine and complex **12** (10 mol %) were heated in excess DMSO (solvent) at 65°C for 24-72 h, ^{31}P NMR monitoring showed gradual oxidation of the phosphine to $OPPh_3$. The corresponding reaction of an unsubstituted (2-H) analog of BINAM-derived complex **12** with pyridine *N*-oxide/PPh_3 (1:1; 40-65 ^oC) was

considerably more rapid (ca. 30% conversion in 3 h). Accordingly, subsequent kinetic resolution experiments with the catalysts **7-10** and **12** employed pyridine *N*-oxide as the stoichiometric oxidant (Figure 2-8).

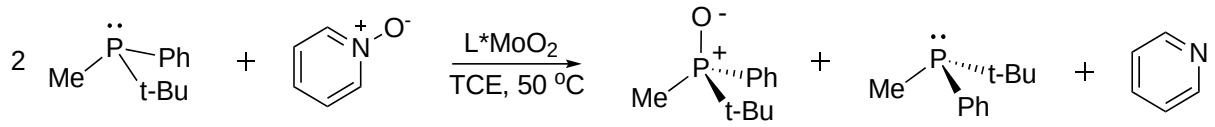

Figure 2-8. Scheme for catalytic oxidative kinetic resolution

The kinetic resolution studies were carried out using 0.5 equiv. of pyridine *N*-oxide relative to the racemic chiral phosphine PMePh^{t}Bu to control the conversion and with 0.3 - 2.0 mol % catalyst relative to the phosphine. Reactions were carried out under argon to prevent potential complications from aerobic oxidation. Reactions with the *p*-NO_2-substituted catalysts **7-9** were conducted at 50 °C in 1,1,2,2-tetrachloroethane, while reactions with the less activate non-nitrated catalysts **10** and **12** were run at 80 °C. Each reaction mixture started out as a yellow solution, turned brown-red after addition of phosphine and heating, and then turned to pale green after consumption of the pyridine *N*-oxide oxidant. The phosphine oxide was isolated from the reaction mixture after solvent evaporation and preparative TLC. The enantiomeric excess of the isolated phosphine oxide was determined by chiral HPLC and optical rotation.

The kinetic resolution results with the various catalysts are tabulated in Table 2-2. Among the set of (CHD-salen)MoO_2 complexes **7-10** the enantioselectivities range from negligible for the unsubstituted –NO_2 catalyst **7**, to 7% for the bromo-nitro compound **8**, to 16% for the ^{t}Bu-substituted derivative **9**. Thus, there is a trend of increasing selectivity with increasing size of the 2-substituent. A reaction employing the less active di-*t*-Bu catalyst **10** (lacking the *para*-NO_2 group), required higher temperature and longer reaction time, and afforded a lower (8%) ee. The binaphthyl-derived salen complex **12** gave a significant increase in the ee of the product but needed an 8 day reaction time at 80 °C with 10% catalyst loading to obtain a moderate yield of product (40% conversion). We note that the reactions could not be conducted under strictly identical conditions because of the differing catalyst solubilities and activities. Nonetheless, presuming that the stereo-defining step is first order in catalyst (supported by the calculations and prior experimental studies), then the stereoselectivity (% ee) should be independent of the

catalyst concentration. Therefore, the observed effects of substituents on activity and stereoselectivity are deemed valid.

Table 2-2. Experimentally determined enantioselectivities (ee) of the phosphine oxide

catalyst	catalyst loading (mol %)	ee	conversion	t_{rxn}	T_{rxn}
7	1.8	0 %[a]	42 %	6 h	50 °C
8	0.5	7 %[a]	42 %	6 h	50 °C
9	1.7	16 %[b]	40 %	74 h	50 °C
10	1.7	8 %[b]	18 %	16 d	80 °C
12	10	30 %[c]	40 %	8 d	80 °C

[a] repeated 2-3 times and give the same results, by HPLC and optical rotation. [b] obtained by multiple optical rotation measurements from the same experimental sample. [c] HPLC result

2.2.3 Computational analysis of the phosphine oxidation reaction

To map out the entire energy profile for the oxo-Mo catalyzed phosphine oxidation we employed the B3LYP hybrid functional for optimizations of stationary state species. Transition states were located using modredundant calculations to scan along the forming/dissociating bond and optimized to a Berny transition state using the B3LYP functional. All energies for solvated species were calculated using the M06 functional as single point energy calculations. The overall mechanistic pathway in Figure 2-9 was conceived to begin with attack by the phosphine on the electrophilic oxo-Mo center of $LMo(VI)O_2$ to produce the phosphine oxide adduct **B** in the stereo-defining step. Next the phosphine oxide dissociates to produce the reduced LMo(IV)O species **C**. To recycle the Mo-catalyst pyridine *N*-oxide coordinates with **C** to form the amine oxide adduct LMoO(OPyr) (**D**), which then dissociatively cleaves off pyridine to reform the original $LMoO_2$ species **A**.

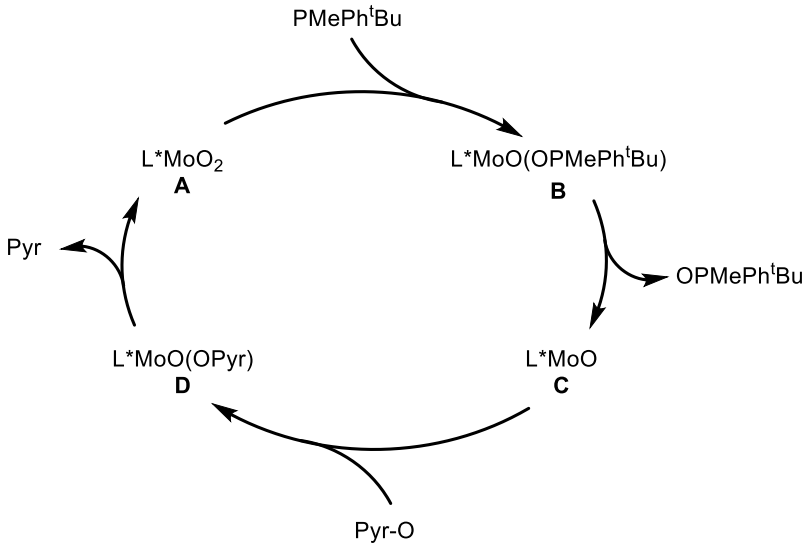

Figure 2-9. Putative pathway for Mo-catalyzed, *N*-oxide driven phosphine oxidation

We next analyzed each step of the suggested pathway, beginning with the interaction of the (CHD-NO$_2$-salen)MoO$_2$ complex **7** with the chiral phosphine PMePh^{t}Bu. For this and each subsequent step the reactant, product and, where possible, the transition state structures were optimized and the free energies were calculated. To address the stereoselectivity issue that arises in the phosphine reaction with L*MoO$_2$ complex **7-A** the diastereomeric phosphine oxide adducts **7**-**B** were first optimized to provide a starting point for the transition state searches (Figure 2-10). Note that since the two oxo-atoms are inequivalent, one (axial) being *trans* to the phenolate-*O*, the other (equatorial) *trans* to the imine-*N*, four isomeric adducts **7-B** (and transition states) are possible. While all four isomers could be optimized computationally, we found later that the activation energies for phosphine attack on the axial oxo-*O* of all the CHD-derived complexes are uniformly lower, e.g. $\Delta\Delta G^{\ddagger}_{ax/eq}$, 0.6 kcal/mol (**7-A/B)** < 0.8 kcal/mol (**8-A/B**) < 4 kcal/mol (**9-A/B**) < 10 kcal/mol (**10-A/B**). Therefore, we conclude that the stereoselectivity of the phosphine *O*-atom transfer for **7-10** is largely or exclusively the result of phosphine attack on the axial oxo group. As to why axial oxo attack is favored, this does not appear to result from the small differences in Mo=O atomic charges (Mulliken: ax -0.47, eq -0.45; APT: ax -0.78, eq -0.72) and Mo=O bond lengths (ax 1.73 Å, eq 1.72 Å for **7**), but instead from FMO populations and amplified by a steric effect as suggested by the trend in $\Delta\Delta G^{\ddagger}_{ax/eq}$ noted above. For the dioxo catalyst species, the LUMO is an orbital on the axial oxo group, while all unoccupied orbitals with

contribution on the equatorial oxo group also have contributions on the axial oxo group (LUMO+1 and above).

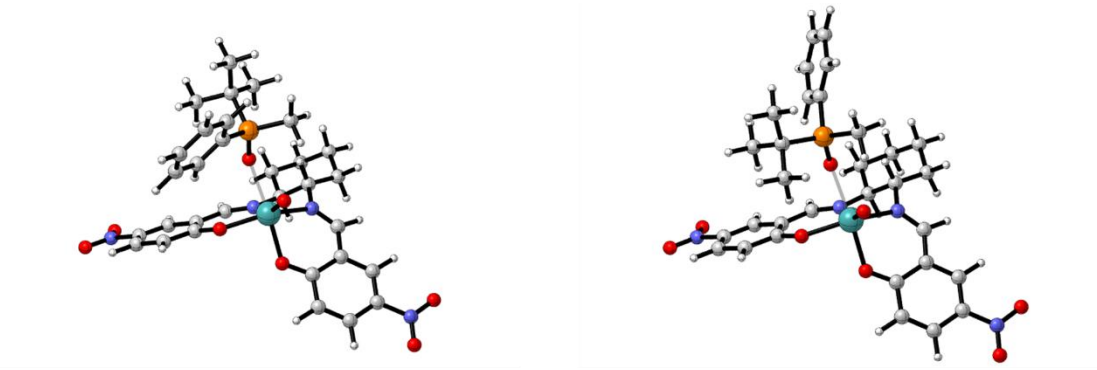

Figure 2-10. Optimized structures of (*S,S*-CHD-NO_2-salen)MoO(O-PMePh^{t}Bu) **7-B** diastereomers from attack on the axial oxo-*O*. The *S*-OPR_3 ternary complex (left) is more stable.

Transition states (TS) for phosphine attack on $LMoO_2$ were then located from the ternary phosphine oxide complex **7-B** using a relaxed coordinate scan (mod-redundant) along the P-O bond and then optimized *via* a Berny transition state calculation. In the diastereomeric transition states (Figure 2-11), one can see that the phosphine preferentially approaches the axial oxo-group from the more open (less hindered) quadrant away from the upward-projecting CHD ring. As the phosphine attacks the electrophilic oxo group, the Mo-O bond is lengthened (1.73 to 1.84 Å) from **7-A** and the forming P-O bond is much longer than in the ternary complex **7-B** (2.13 vs 1.52 Å). The calculated energy difference $\Delta\Delta G^{\ddagger}_{diast}$ for the stereoisomeric TSs is only 0.15 kcal/mol (Table 2-3), predicting a very low enantioselectivity in accordance with the undetectable experimental selectivity for this complex (Table 2-2).

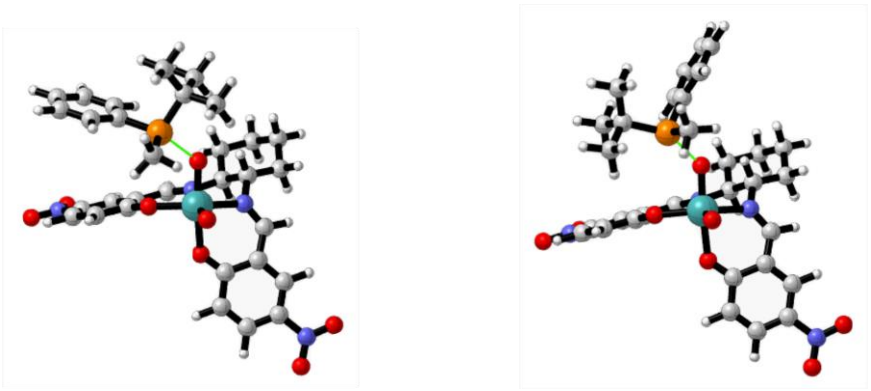

Figure 2-11. Representative structures for the associative P*R_3/L*MoO_2 transition states. left: $\mathbf{TS_{A\text{-}B}}$ **7-A/B** (pro-S OPR_3, favored TS); right: $\mathbf{TS_{A\text{-}B}}$ **7-A/B** (pro-R OPR_3)

Table 2-3. $\Delta G^{\ddagger}$ and $\Delta\Delta G^{\ddagger}_{diast}$ for diastereomeric transition states for L*MoO_2

	$\Delta G^{\ddagger}$ (kcal/mol)	$\Delta\Delta G^{\ddagger}$ of diastereomeric transition states (kcal/mol)	
complex	M06/solvent	calculated	experimental from % ee [c]
6[a]	24.4	0.9	- [d]
7[a]	20.9	0.15	0.00
8[a]	19.6	0.6	0.12
9[a]	23.0	1.4	0.26
10[b]	26.8	0.7	0.11
12[b]	27.5	3.5	0.59

[a] listed $\Delta G^{\ddagger}$ is calculated at 323.15 K; [b] listed $\Delta G^{\ddagger}$ is calculated at 353.15 K; [c] see eqn 1 (*vide infra*); [d] not determined

Diastereomeric transition states for phosphine attack on the various 2/4-substituted CHD-salen complexes **8-10** were similarly located and the energy differences between the diastereomeric transition states, $\Delta\Delta G^{\ddagger}_{diast}$, are listed in Table 3. An increase in calculated $\Delta\Delta G^{\ddagger}_{diast}$ can be seen as the 2-substituent increases in size from -H (**7**) to -Br (**8**) to –t-Bu (**9**). Among these, the diastereomeric transition states and activation energies for reaction of the phosphine enantiomers with the 2-t-Bu complex **9** (Figure 2-12) are the most differentiated energetically at 1.4 kcal/mol. Here, the lower activation energy transition state is the one that appears to minimize the steric interactions of the larger *P*-groups with the projecting cyclohexyl ring and left side salicyl aromatic ring. In considering the reaction of the enantiomeric phosphines with the C_2-symmetric, BINAM-derived **12-B** only one pair of diastereomeric phosphine oxide adducts and transition states are expected because of the geometrical and electronic equivalence of the two oxo-oxygens.

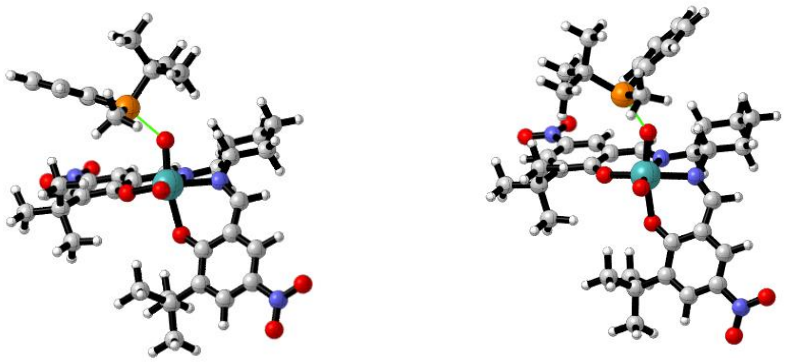

Figure 2-12. Diastereomeric transition states for reaction of enantiomeric PMePh^{t}Bu with **9**; left: **$TS_{A\text{-}B}$ 9-PR_3** (*pro*-*S*-OPR_3, favored TS); right: **$TS_{A\text{-}B}$ 9-PR_3** (*pro*-*R*-OPR_3)

The energy difference between the diastereomeric transition states leading to **12-B** (Figure 2-13) was calculated to be the largest among all the catalysts studied here at 3.5 kcal/mol. Curiously, the two TSs differ in the approach of the enantiomeric phosphines to the axial oxo unit. One (right) has the phosphine approaching the seemingly more hindered upward-projecting t-Bu group (with P-Me nearby), while the other (left) avoids the up t-Bu, but orients the larger *P*-substituents (Ph, t-Bu) in that direction. The increase in enantioselectivity with the BINAM-based complex **12** may arise from these interactions.

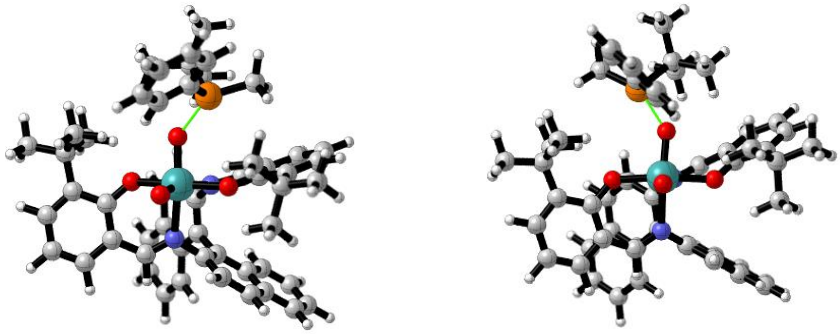

Figure 2-13. Diastereomeric transition states **$TS_{A\text{-}B}$** for **12-PR_3**. The pro-*S*-L*Mo(O)OPR_3 TS (left) is favored

Comparative 'experimental' $\Delta\Delta G^{\ddagger}_{diast}$ values can be calculated from the selectivity number, *s*, which is related to both the measured enantiomeric excess of the product and the conversion, *c*, using equation 1 [29]. The calculated values are thus independent of the changing enantiomeric excess of product as the reaction progresses. In comparing the experimental and

calculated enantioselectivities we first point out that the calculations predict that reactions of the *R*-phosphine enantiomer with **8-10**, **12** uniformly have lower activation energies, which would lead to faster formation of the *S*-phosphine oxide. However, in the computational modeling the enantiomeric (*S,S*)-configuration of the catalysts **6-10** was used, while the experimental structures were (*R,R*). Hence the *R*-phosphine oxide should be favored from the (*R,R*)-isomers, as observed experimentally. The computed values of $\Delta\Delta G^{\ddagger}_{diast}$ are consistently higher than those derived from the experimental results. However, the computational trend in $\Delta\Delta G^{\ddagger}$ for the studied complexes is roughly linear with respect to the experimental data (Figure 2-14). The linear relationship suggests a systematic origin of the discrepancy between calculation and experiment. It may arise in part from the limited ability of the DFT methods to determine very small differences in the TS energies, basis set selection and/or the solvent model.

$$s = e^{\Delta\Delta G^{\ddagger}/RT} = \frac{\ln[1-c(1+ee")]}{\ln[1-c(1-ee")]} \qquad \text{(eq. 1)}$$

s = selectivity, *c* = conversion, and *ee* = enantiomeric excess of the product

In Table 2-3 we also include the calculated activation free energies for the phosphine reaction with L*MoO_2 **6-10** and **12**, which range from 19.6 to 26.8 kcal/mol. Among the –NO_2 substituted complexes **7-9**, the activation barriers reflect composite electronic and steric effects of the 2-substituent, e.g. H/Br (**7**/**8**) and a steric effect H/t-Bu (**7**/**9**). Comparing the 4-NO_2-substituted catalysts (**7-9**) to those with or a 4-H (**6**, **12**) or a 4-t-Bu (**10**) group, one sees lower activation barriers of approximately 5 kcal/mol for the -NO_2 derivatives. The lower barriers for the more electron deficient (–NO_2 substituted) and the less hindered (2-substituted) complexes parallels what is observed experimentally in the relative reaction rates and suggests that the turnover-limiting step in the catalytic cycle is a nucleophilic phosphine-attack on the electrophile L*MoO_2. This conclusion is further supported by our analysis of the energetics for the remainder of the catalytic cycle.

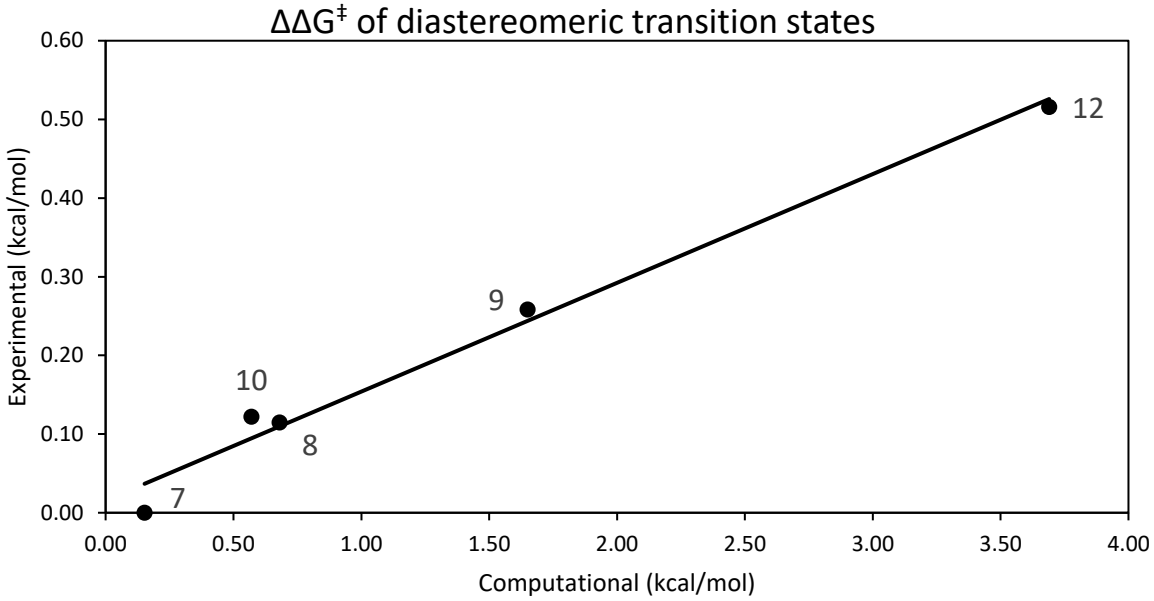

Figure 2-14. Comparison of DFT-computed and experimental $\Delta\Delta G^{‡}$ (R=0.99, x-intercept=0.01)

The next step of the catalytic *O*-transfer oxidation would involve dissociation of the phosphine oxide adduct to form LMo(IV)O + OPR_3. The release of the product phosphine oxide molecule appears to be a purely dissociative step, in contrast to the dissociative interchange (I_d) process described by Kail et al. This step is found to have a small activation barrier of +6.5 kcal/mol for the dissociation of the (*S*)-phosphine oxide and a +6.3 kcal/mol barrier for dissociation of the (*R*)-phosphine oxide. The transition state geometry for this dissociative step, $\mathbf{TS_{B\text{-}C}}$, is shown in Figure 2-15. Dissociation of the product phosphine oxide molecule lowers the coordination number of the metal, allowing the ligand to relax from the octahedral geometry toward the square pyramidal geometry observed for **7-C**. The overall free energy change for this dissociation step is practically thermoneutral for formation of the parent (CHD-sal)Mo(IV)O (**7-C**), with a ΔG of +0.3 kcal/mol for the (S)-phosphine oxide and +0.9 kcal/mol for the (R)-phosphine oxide.

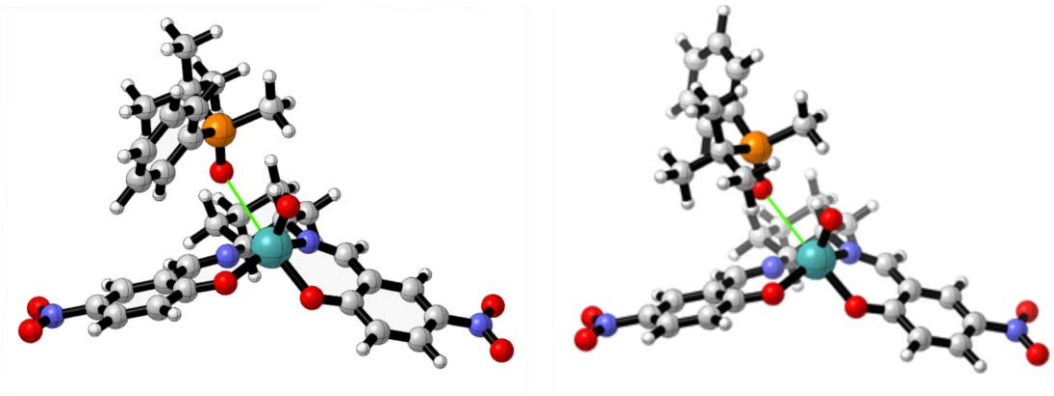

Figure 2-15. Transition state structure for the dissociation of the product phosphine oxide (*S*-OPR_3, left; *R*-OPR_3, right)

The optimized structure of **7-C** is square pyramidal and is calculated to be a ground state singlet (Figure 2-16). This geometry and spin state has been identified in other LMo(IV)O species [27], and is found to be stabilized by 11.3 kcal/mol versus the triplet state in our calculations.

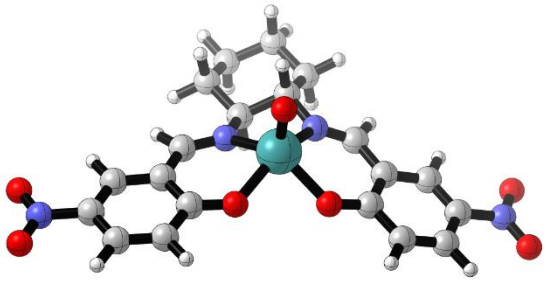

Figure 2-16. Optimized structure of (CHD-sal)Mo(IV)O (**7-C**)

Attack of pyridine *N*-oxide on five-coordinate LMo(IV)O (**7-C**) would produce the amine oxide adduct **7-D** (Figure 2-18) *via* an associative transition state $\mathbf{TS_{C\text{-}D}}$ (Figure 2-17). The reaction free energy for this association is +8.4 kcal/mol for the axial approach versus +8.5 kcal/mol for the equatorial approach, suggesting that neither approach is favored over the other. The Mo-O interaction in this transition state is such that the major geometry change occurs in the ligand coordination arrangement, with only a slight lengthening on the pyridine N-O bond (1.30 Å, axial approach, 1.28 Å, equatorial approach, 1.27 Å, free pyridine N-oxide). As shown in Figure 2-17, both approaches lead to reorganization of the ligand from square pyramidal **7C** to a distorted octahedral geometry more comparable to **7** and **7B**.

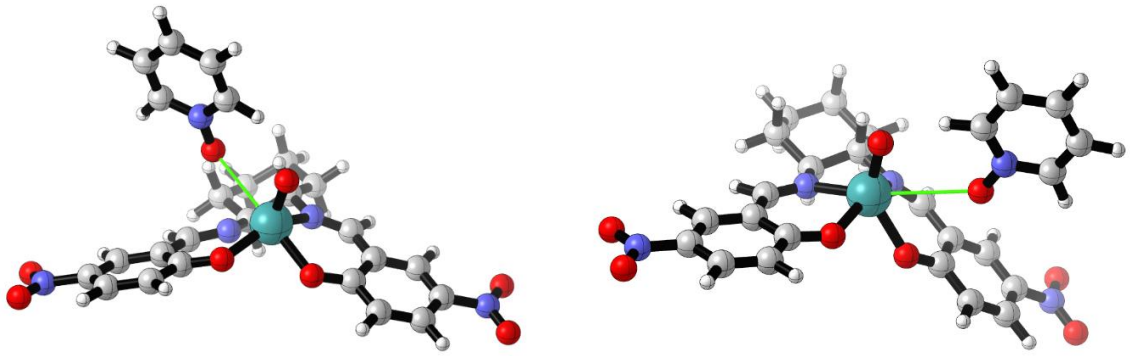

Figure 2-17**.** Transition states for **$TS_{C\text{-}D,\ ax}$**, left, and **$TS_{C\text{-}D,\ eq}$**, right

The geometry of the 6-coordinate amine oxide adduct (**7-D**, Figure 2-18) is slightly distorted octahedral with the Pyr-O ligand *cis* to Mo=O and the complex **7-D** may be compared to the structurally similar Mo(VI)-OPR_3 adduct **7-B**. In contrast to the transition states **$TS_{C\text{-}D,\ ax/eq}$**, the equatorial amine oxide adduct is stabilized by 2 kcal/mol relative to the axial adduct, likely due to the difference in steric confinement of the coordination site. Although amine oxides are known as ligands and reagents for TM-mediated oxidations [30–33], few structurally characterized metal complexes of amine oxides have been reported and, to the best of our knowledge, only one of Mo [34].

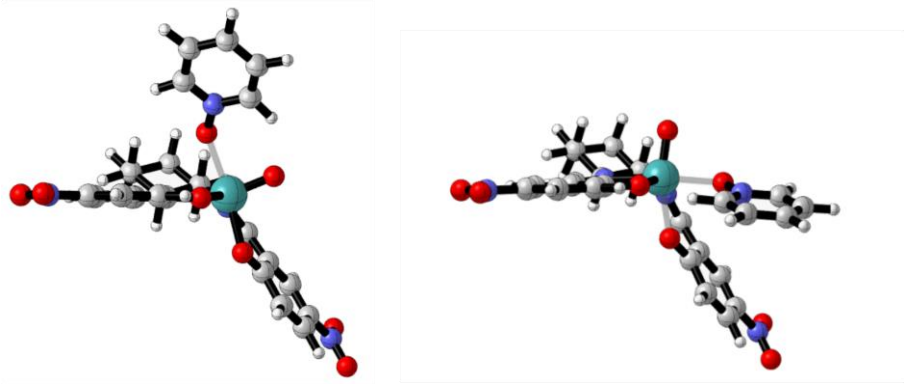

Figure 2-18. Optimized structures of (CHD-sal)Mo(IV)O(O-Pyr) (**$7\text{-}D_{ax}$,** left; **$7\text{-}D_{eq}$,** right)

The final step of the catalytic cycle is proposed to involve N-O cleavage and pyridine dissociation from the adduct LMo(IV)O(O-Pyr) (**7-D**). The thermodynamics for this step (-47 kcal/mol) are highly favorable. A TS for pyridine loss from **7-D** was also located (Figure 2-19). It has a modest $\Delta G^{\ddagger}$ of 11.4 kcal/mol (axial; 12.6 kcal/mol equatorial), resulting from compensating

N-O bond-breaking with Mo-O bond-making and a favorable dissociative entropy gain. Inspecting the bonding changes in the TS relative to the reactant **7-D**, one can see a considerably elongated N-O distance of 1.65 Å (vs 1.31 Å in **7D)** and a shortened Mo-O of 1.93 Å (vs 2.26 Å for **7-D**). It doesn't appear that such a TS has been modeled in other amine-oxide *O*-transfer reactions to metal centers.

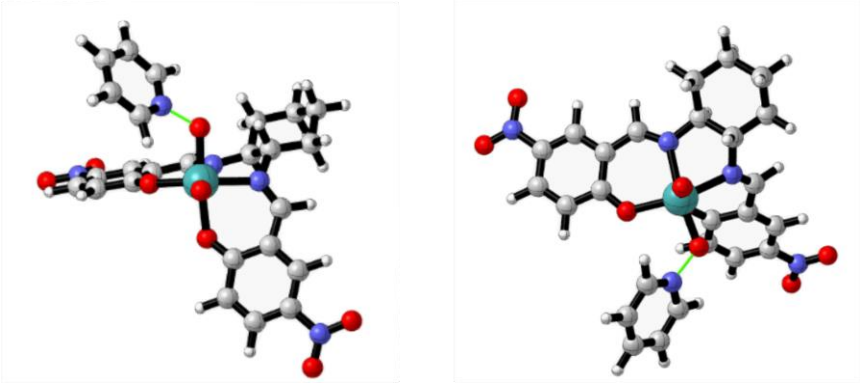

Figure 2-19. Optimized TS structures (axial, left; equatorial, right) for pyridine cleavage from **7-D/A**

A reaction coordinate energy profile based on the postulated mechanistic pathway is shown in Figure 2-20. Here it can be seen that the overall reaction PR_3 + Pyr-O → OPR_3 + Pyr is highly exergonic, -59 kcal/mol, and thus has a strong driving force. The turnover-limiting step for the catalytic reaction, with an activation energy of 22.2 kcal/mol, is phosphine attack on the catalyst L*MoO_2. This conclusion is also supported by the faster observed reactions of the nitro-substituted catalysts **7-9** relative to **10** and **12** and is consistent with prior experimental studies of other LMoO_2-promoted reactions with *O*-acceptors. [11,35] The energetic profile for the initial phosphine reaction with **7** (**A-C**) is quantitatively similar to that found by Thomson and Hall for PMe_3/$(SCH_2CHNH)_2$-MoO_2 [36] and by Kail and Basu for PEt_3/[hydrotris(3-isopropylpyrazol-1-yl)borate]MoO_2 [37].

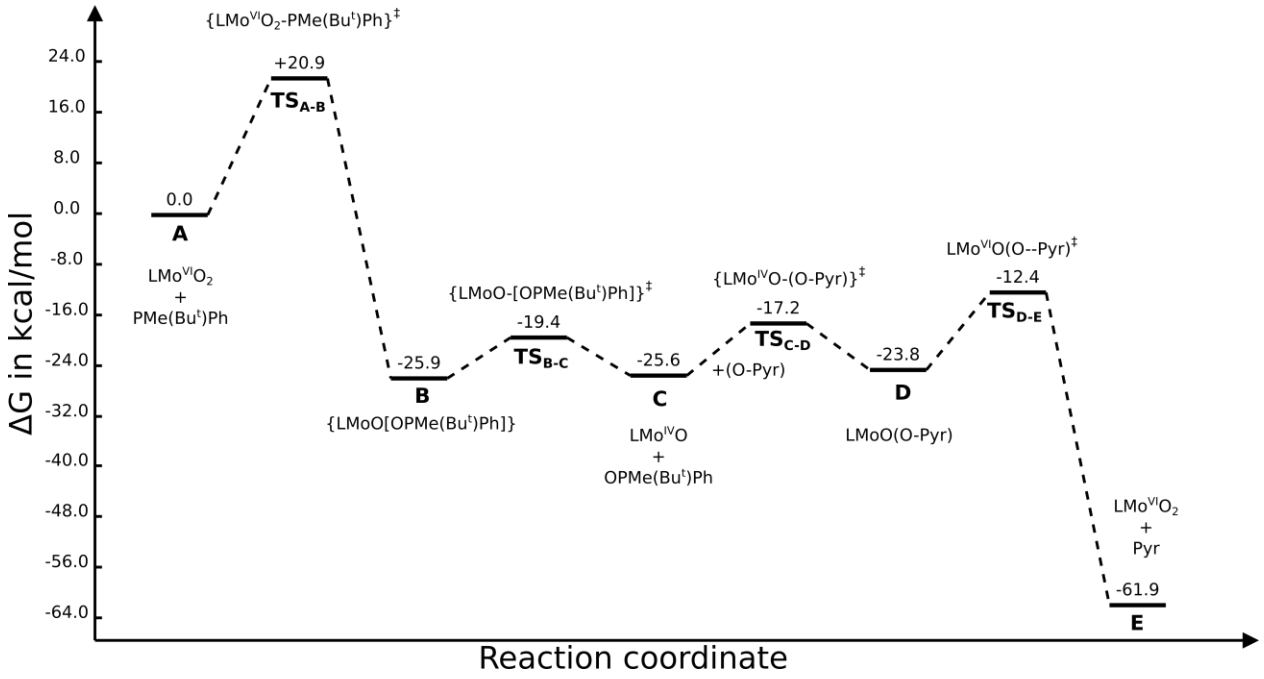

Figure 2-20. Free energy profile for the *O*-transfer reaction of **7** (L=NO_2-CHD-salen) with $PMePh^tBu$

2.3 Conclusions

A set of modular, chiral (salen)MoO_2 complexes derived from cyclohexyldiamine (CHD) and binapthyldiamine (BINAM) has been prepared and characterized. These compounds catalyze the efficient oxidation of a representative *P*-chiral *tert*-phosphine by pyridine *N*-oxide. The reactions proceed with low to moderate enantioselectivities, depending on the electronic and steric properties of the chiral ligand. The inclusion of an electron-withdrawing nitro group on the salicyl unit of the complexes is found to increase catalytic activity, while the presence of substituents at the 2-position increases enantioselectivity. The reaction pathway, including the stereo-defining phosphine/$LMoO_2$ reaction step, has been modeled by DFT methods, showing the energetic viability of various intermediates and features of the stereo-defining transition state. The DFT-calculated enantioselectivities with this set of catalysts linearly correlate with the experimental results.

Although modest enantioselectivities have been obtained in the kinetic resolution system studied here, the strong correlation between experimental and computational trends indicates

that computational methods could be used to design and pre-screen catalysts, reducing laboratory effort, and allowing for effective catalysts to be selected for specific substrates. By combining the lessons learned here from the steric and electronic effects of ligand substituents and conformation on the reaction stereoselectivity, we believe that dioxomolybdenum(VI) complexes are good catalyst candidates for other stereoselective *O*-atom transfer reactions.

2.4 Future and expanded research directions

In addition to the use of calculated $\Delta\Delta G^{\ddagger}$ for diastereomeric catalyst systems such as this, it may be possible to improve the efficiency of the search by using an approach similar to the design of transition state analogues for enzymatic catalysis. [38] For the purposes of this investigation and ones like it that may be conducted in future, we suggest using phosphine sulfides or selenides, as the larger atomic radius of the S atom will lead to increased M-E and E-P bond lengths. The crystallographically determined E-P bond lengths in tris(2-pyridyl)phosphine sulfide [39] is 1.93 Å, significantly longer than the analogous O=P bond length (1.48 Å [40]), and more similar to the O-P bond length in our calculated transition states, 2.13 Å. When ligated, it seems likely that the S-P bond will lengthen slightly, further approaching the calculated transition state geometry. The corresponding phosphine selenide has a Se=P bond length of 2.10 Å, making it another possible candidate for this transition state analogue. This transition state analogue approach may be useful for screening large libraries of catalyst structures *via* a single pair of calculations (pro-S and pro-R ternary complexes) for each possible catalyst, then following up encouraging results with transition state optimizations to determine the $\Delta\Delta G^{\ddagger}$ for the chiral phosphine oxidation step.

If pursuing ligand modification to improve the enantioselectivity of stereoselective *O*-atom transfer, there are several approaches that could be taken. Staying within the cyclohexylsalen ligand framework, the selectivity could be improved by increasing steric bulk at the salicylimine 3-position, such as substituting an adamantyl group. This substitution would be expected to be accompanied by a decrease in reaction rate, though the option to increase catalyst loading could likely be used to make up for this. Based on the results of this study, however, this modification would be expected to have limited impact on the enantioselectivity

due to the moderate increase in steric bulk on the reactive (axial) oxo group. Moving away from the CHD-salen, there are more options to be explored. One route to a more efficient kinetic resolution would be to increase the rate for OAT from the BINAM-salen complex by using the 4-NO_2 salicylaldehyde derivative. However, to improve the selectivity of the (BINAM-salen)MoO_2 catalyzed OAT reaction, one must first address the issue of coordination isomerism. One way to address this would be to add a steric element to the imine functionality by synthesizing the ligand from the 1-(2-hydroxyphenyl)ethanone or 1-(2-hydroxyphenyl)propanone derivatives. The steric encumbrance of the added methyl or ethyl groups may be enough to restrict the dioxomolybdenum complex to exclusively the C_2 coordination isomer. The added bulk at the α-imine position will not increase steric confinement of the transferred oxygen moiety, so if one were attempting to accomplish locking of the complex conformation and adding steric bulk to the active site with one modification, a 3,3'-modified binaphthyldiamine backbone would be a good starting point. A quick calculation of the structures of the C_1 and C_2 coordination isomers of the 3,3'-dimethylbinaphthyldiamine-derived salen complex (Figure 2-21) shows that the free energy difference for the two isomers is 3.5 kcal/mol, significantly larger than for the BINAM complex (1.0 kcal/mol), suggesting that this would indeed be a favorable approach for the synthesis of an exclusively C_2 BINAM-based OAT catalyst.

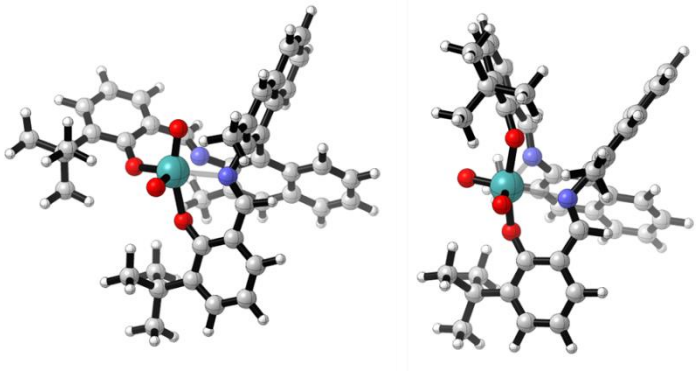

Figure 2-21. (3,3'-dimethyl-BINAM-salen)MoO_2, *C_1* (left) and *C_2* (right) coordination isomers

2.5 Experimental

2.5.1 General methods.

NMR spectra were obtained using Varian OXFORD 300, 400, and 500 MHz NMR spectrometers; IR spectra were obtained on a Shimadzu IRAffinity-1 FTIR; and optical rotations were measured using a Rudolph Research AUTOPOL III polarimeter. Reagent grade solvents were used as obtained. Chiral HPLC was carried out using a ChiraCel column with 3% isopropanol in hexanes as eluent at a flow rate of 1.0 mL/min. Compounds **1**, **2**, **4**, **5**, **6**, **11**, PMePh^{t}Bu and 3-t-Bu-5-nitro-salicylaldehyde were prepared as reported previously. [3,24,41–48] Complex **8** was prepared *via* a modification of the literature procedure [20].

2.5.2 Preparation of racemic phosphine and *p*-NO_2 salicylaldehydes

Preparation of racemic Phenylmethyl-tert-butylphosphine [3]

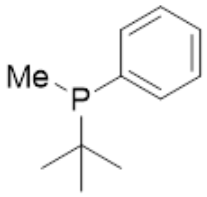

To a 50 mL round bottom flask under nitrogen flow was added 25 mL of newly opened anhydrous diethyl ether. The flask was placed in a -72^{o}C bath, and 2.5 g (12 mmol) of chlorophenyl-*tert*-butylphosphine was added by syringe. The flask was stoppered using a rubber septum and 12 mL of 1.6 M MeLi in diethyl ether was added by syringe. The reaction vessel was allowed to come to room temperature and stirred for 1.5 hours before stirring was stopped to allow salts to settle. The reaction was transferred to another 50 mL round bottom flask *via* cannula filter and concentrated under nitrogen flow. The first flask was rinsed with another 50 mL (2 x 25 mL) anhydrous diethyl ether, which was again transferred to the second flask by cannula filter. The impure product was an orange-brown semisolid and was distilled under vacuum (160-180 ^{o}C, 80 mtorr) to isolate the pure phosphine as a clear, viscous liquid (1.9 g, 87% yield). The phosphine was determined to be >95% pure by ^{31}P NMR. NMR: 1H NMR (300 MHz, $CDCl_3$) δ 7.48 (td, J = 6.7, 2.9 Hz, 2H), 7.38 – 7.31 (m, 3H), 1.32 (d, J = 3.7 Hz, 3H), 0.97 (d, J = 12.0 Hz, 9H). ^{31}P NMR (122 MHz, $CDCl_3$) δ -10.12.

Preparation of 3-tert-butyl-5-nitrosalicylaldehyde [41]

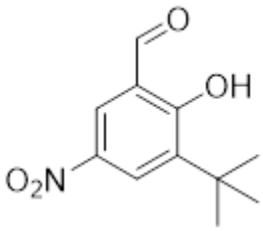

Into a 100 mL round bottom flask was placed 6.9 mmol (1.2 g) 3-*tert*-butyl-2-hydroxybenzaldehyde in 19 mL of glacial acetic acid. The flask was placed in a 0°C ice bath. Nitric acid (70%, 24 eq, 10.5 mL, 166 mmol) was added dropwise. The reaction was allowed to come to room temperature over 1 hour. The reaction was quenched by pouring the reaction mixture over ice in a 1 L beaker, and the product was isolated by filtration in 65% yield as a yellow powder, which was determined to be 90% pure by NMR. The nitrated salicylaldehyde was used for the ligand synthesis without purification. NMR: ^{1}H NMR (300 MHz, $CDCl_3$) δ 12.44 (s, 1H), 9.97 (s, 1H), 8.41 (s, 2H), 1.46 (s, 9H).

2.5.3 Preparation of ligands and dioxomolybdenum (VI) complexes

Preparation of diimine ligands. For the cyclohexylsalen ligand series, the ligands were prepared by combining 2 equivalents of the respective salicylaldehyde with the diamine in alcoholic solution and heating at reflux. Conditions for each prepared ligand are reported below.

*Preparation of (±)-trans-cyclohexylsalen ligand (**1**)*[42]

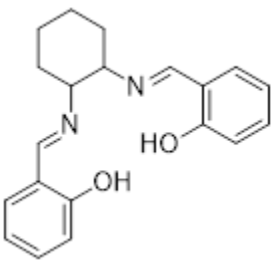

Salicylaldehyde (1.02 g, 8.33 mmol) was placed in a round-bottom flask with a stir bar. The aldehyde was dissolved in 5 mL distilled water, and (±)-trans-1,2-diaminocyclohexane (0.464 g, 3.90 mmol) in 5 ml water, dropwise with stirring. A yellow precipitate was visible immediately. The reaction mixture was refluxed for a few hours, extracted with CH_2Cl_2, and dried with sodium sulfate. The solvent was removed under vacuum, yielding 1.09 g (87%) of a yellow powder. NMR analysis confirmed that the aldehyde was consumed.^{1}H NMR (300 MHz, $CDCl_3$, δ) 13.32 (br s, 1H, -OH), 8.26 (s, 2H, N=CH), 7.24 (dt, 2H, Ar H), 7.15 (dd, 2H, Ar H), 6.88 (d, J=8.4Hz, 2H, Ar H), 6.79 (dt, J=7.5Hz, 2H, Ar H), 3.32 (m, 2H, CH-N), 1.91 (m, 4H, CH_2), 1.72 (m, 2H, CH_2), 1.47 (m, 2H, CH_2). IR (KBr) $\bar{\nu}_{max}$: 1630cm^{-1} (C=N).

*Preparation of (-)-trans-5-nitrocyclohexylsalen ligand (**2**)*[46]

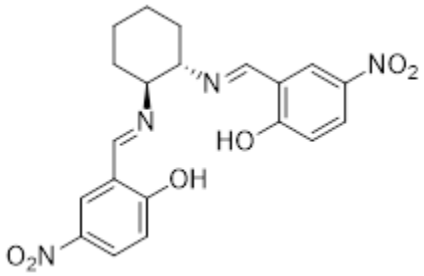

To a round bottom flask was added 20.0 mmol (3.34 g) of 5-nitrosalicylaldehyde and dissolved in 10 mL ethanol. The solution was stirred with a magnetic stir bar and (1R,2R)-(-)-cyclohexyl diamine (10.0 mmol, 1.14 g)) was added as an ethanolic solution (5 mL abs. ethanol). The reaction flask was attached to a Soxhlet extractor with a thimble of $MgSO_4$ as a drying agent and topped with a water condenser. The reaction flask was then heated to reflux for 6 hours. After cooling to room temperature, the precipitate was isolated by filtration and washed with cold absolute ethanol. The ligand was isolated as a bright yellow powder in 93% yield (9.35 mmol). NMR: ^{1}H NMR (400 MHz, DMSO-d6) δ 8.74 (s, 2H, HC=N), 8.40 (d, *J* = 3.0 Hz, 2H), 8.06 (dd, *J* = 9.5, 3.0 Hz, 2H), 6.77 (d, *J* = 9.4 Hz, 2H), 3.71 (d, *J* = 9.1 Hz, 2H, HC-N), 2.00 (d, *J* = 12.7 Hz, 2H), 1.80 (d, *J* = 8.7 Hz, 2H), 1.68 (d, *J* = 11.3 Hz, 2H), 1.43 (m, 2H). lit[46]: ^{1}H NMR (400 MHz, $CDCL_3$) δ 14.29 (OH), 8.35 (HC=N), 8.17, 8.14, 6.96, 3.46 (HC-N), 1.96, 1.75, 1.55. IR (KBr, cm^{-1}): 3097, 3064, 2960, 2933, 2860, 1635 (C=N), 1616 (C=C), 1483 (NO_2), 1332 (NO_2), 1298, 1095, 941, 916, 835, 754, 634

*Preparation of (-)-trans-3-bromo-5-nitrocyclohexylsalen ligand **3***

To a 200 mL round bottom flask was added 2.00 mmol (0.492 g) of 3-bromo-5-nitrosalicylaldehyde and 1.00 mmol (0.114 g) of (*1R,2R*)-(-)-cyclohexyldiamine under nitrogen. The reactants were dissolved in 80 mL of absolute ethanol, a magnetic stir bar was added, and the flask was connected to a Soxhlet extractor with a thimble containing $MgSO_4$ and topped with a water condenser. After 10 hours at reflux and cooling to room temperature, the precipitate was isolated by filtration (0.471 g, 0.825 mmol, 82.5% yield). NMR: ^{1}H NMR (300 MHz, Chloroform-*d*) δ 8.49 (d, *J* = 2.6 Hz, 1H, aryl), 8.30 (d, *J* = 3.2 Hz, 2H, HC=N), 8.16 (d, *J* = 2.7 Hz, 2H, aryl), 3.54 (dd, *J* = 6.7, 2.8 Hz, 2H, CH_2), 2.10 (d, *J* = 14.1 Hz, 1H, CH_2), 1.99 (d, *J* = 8.0 Hz, 1H, CH_2), 1.76 (m, 2H, CH_2), 1.53 (m, 2H, CH_2). ^{13}C NMR (126 MHz, $CDCl_4$) δ 167.0, 164.4, 138.4, 131.7, 127.8, 115.2, 114.0, 70.0, 32.6, 23.7. IR (KBr, cm^{-1}): 3080, 2935, 2864, 1637, 1602, 1541, 1338, 1220, 1093, 962, 904. MS (DCM, ESI+): 568.97 (50%), 570.96 (100%), 572.96 (50%); MS (calculated) 569 (50.3 %), 571 (100%), 573 (51.6%).

*Preparation of (-)-trans-3-tert-butyl-5-nitrocyclohexylsalen ligand (**4**)*[47]

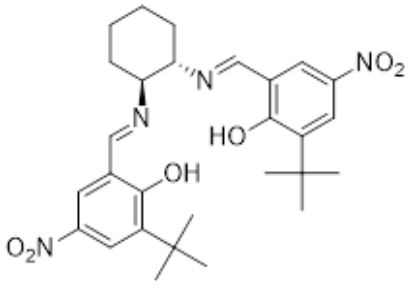

To a 100 mL round bottom flask was added crude 3-*tert*-butyl-5-nitrosalicylaldehyde (4.50 mmol) in 15 mL absolute ethanol and (-)-trans-cyclohexyldiamine (2.25 mmol) dissolved in 25 mL absolute ethanol. The reaction solution turn orange upon combining the two solutions. The reaction flask was attached to a Soxhlet extractor containing a thimble of $MgSO_4$ as a drying agent and the apparatus was topped with a water condenser. The reaction mixture was heated to reflux for 10 hours and allowed to cool to room temperature overnight. The product was precipitated by adding water dropwise and isolated by filtration. The isolated solid was found to be a mixture of products, approximately 95% pure target compound (0.99 g, 84% yield). The crude product was dissolved in a minimum of methanol and adsorbed onto celite. A dry column was prepared according to dry column vacuum chromatography procedures and neutralized with 4% triethylamine in hexane. Pure ligand was eluted with gradient mixtures of hexane/ethyl acetate and isolated from fractions with solvent mixtures between 91:9 hexane/ethyl acetate and 72:28 hexane/ethyl acetate. The product was recovered in 86% yield and was >99% pure by NMR. NMR: ^{1}H NMR (300 MHz, $CDCl_3$) δ 15.02 (s, 2H, OH), 8.35 (s, 2H, HC=N), 8.15 (d, *J* = 2.6 Hz, 2H), 7.99 (d, *J* = 2.6 Hz, 2H), 3.59 – 3.33 (m, 2H, HC-N), 2.06 (m, 2H), 1.97 (d, *J* = 8.0 Hz, 2H), 1.89 – 1.70 (m, 2H), 1.52 (m, 1H), 1.40 (s, 18H). lit[47]: δ_H (^{1}H 300 MHz, $CDCl_3$) 8.35 (2H, s), 8.15 (2H, d *J* 2.7 Hz), 8.00 (2H, d *J* 2.7 Hz), 3.5–3.4 (2H, m), 2.1–2.0 (2H, m), 2.0–1.9 (2H, m), 1.9–1.7 (2H, m), 1.40 (18H, s) 1.3–1.2 (2H, m). IR (KBr, cm^{-1}): 2949, 2864, 1610 (C=N), 1477 (NO_2), 1327 (NO_2), 1184, 1201, 1109 (C-O), 979, 927, 910, 746, 715.

*Preparation of (-)-trans-3,5-tert-butylcyclohexylsalen ligand (**5**)* [44]

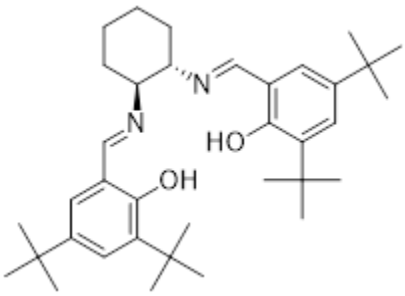

(1R,2R)-(-)-1,2-Diaminocyclohexane (0.253 g, 2.22 mmol) and 3,5-di-(tert-butyl)-salicylaldehyde (1.03 g, 4.44 mmol) were placed in a round-bottom flask with a stir bar and dissolved in 50 mL ethanol. A yellow precipitate was visible immediately. The flask was fitted with a condenser and heated to reflux for 18 h with stirring. The reaction mixture was allowed to cool. The resulting precipitate was isolated by filtration and washed sparingly with cold ethanol, yielding 1.18 g (92%) of yellow product. This product was judged to be sufficiently pure to be used in the complexation reaction without purification. Lit[45]: 1 H NMR ($CDCl_3$, 300 MHz): δ 12.90 (s, 2 H, OH), 8.60 (s, 2 H, CHN), 8.05 (d, 2 H, J = 8.80, Ph), 7.95 (d, 2 H, J = 8.15, aryl H), 7.58 (d, 2 H, J = 8.80, aryl H), 6.90–7.50 (m, 10 H, aryl H), 6.67 (t, 2 H, J = 7.62 Hz, aryl H), 1.2 (s, 18 H, Bu^t).

*Preparation of dioxomolybdenum (±)-trans-cyclohexylsalen complex **6.***

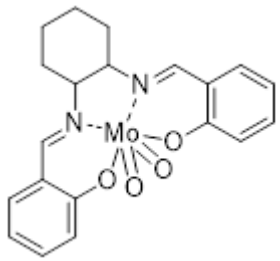

Complex **6** was prepared according to the literature.[24]. Bis-(acetylacetonato)-dioxomolybdenum (0.510 g, 1.56 mmol) was placed in a round-bottom flask with a stir bar and dissolved in 15mL anhydrous methanol, forming a suspension. Ligand **1** was added. The flask was fitted with a water condenser and heated to reflux for 90 minutes. The reaction mixture was allowed to cool. A yellow precipitate was visible at the bottom of the flask; the supernatant was clear and colorless. This precipitate was removed by filtration, yielding 0.56 g (80%) of a yellow powder. ^{1}H NMR (300MHz, $CDCl_3$, δ) 8.41 (s, 1H, N=CH), 8.40 (s, 1H, N=CH), 7.54 (dt, J=1.8Hz, 1H, Ar H), 7.40-7.49 (m, 3H, Ar H), 7.14 (d, J=8.4Hz, 1H, Ar H), 7.05 (dt, J=15, 1H, Ar H), 6.97 (d, J=8.4Hz, 1H, Ar H), 6.77 (dt, J=15Hz, 1H, Ar H), 4.25 (dt, J=10.5Hz, 1H, CH-N), 2.83 (t, 1H, CH-N), 2.57 (d, J=12.3Hz, 1H, CH_2), 2.40 (d, 1H, CH_2), 2.07 (d, J=12.3Hz, 2H, CH2), 1.65-1.75 (m, 2H, CH_2), 1.37-1.53 (m, 2H, CH_2). IR (KBr, cm^{-1}): 1614cm^{-1} (C=N), 914cm^{-1} (Mo=O), 883cm^{-1} (Mo=O). (lit[24]: Nujol mull, ν(Mo=O), 911 cm^{-1}, 884 cm^{-1})

*Preparation of dioxomolybdenum trans-5-nitrocyclohexylsalen complex **7*** [20]

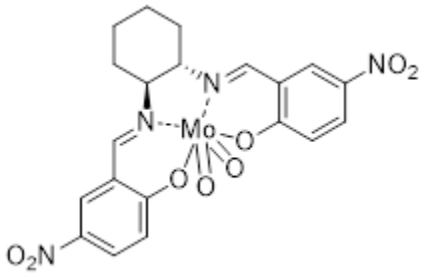

A 100 mL round bottom flask was charged with $MoO_2(acac)_2$ (1.85 mmol) and L^{3H} (1.85 mmol), along with a stir bar. 1,2-dichloroethane (40 mL) was added to the flask and the flask was attached to a Hickman still loaded with 4Å molecular sieves. The reaction mixture was heated to reflux for 10 hours, then allowed to cool to room temperature. The reaction solution was concentrated to 20 mL, and the yellow-brown precipitate isolated by filtration. After drying *in vacuo*, 0.23 g (0.43 mmol, 22% yield) of the complex was obtained. NMR: ^{1}H NMR (500 MHz, $CDCl_3$) δ 8.49 (d, *J* = 2.8 Hz, 1H), 8.48 (d, *J* = 2.9 Hz, 1H), 8.45 (dd, *J* = 9.1, 2.8 Hz, 1H), 8.31 (dd, *J* = 9.4, 2.9 Hz, 1H), 4.35 (t, *J* = 10.3 Hz, 1H), 2.99 (t, *J* = 11.3 Hz, 1H), 2.63 (d, *J* = 12.5 Hz, 1H), 2.49 (d, *J* = 11.6 Hz, 1H), 1.92 – 1.70 (m, 2H), 1.63 (t, *J* = 13.3 Hz, 1H), 1.53 – 1.42 (m, 1H). IR (KBr, cm^{-1}): 3066 (C-H), 2937 (C-H), 2862 (N=C-H), 1606 (C=N/C=C), 1512 (NO_2), 1338, 1323, 1301 (C-O), 1280, 1097 (C-O), 943 (C=N bend), 923 (MoO_2), 912 (C=N bend), 893 (MoO_2), 752, 719, 699, 650, 500 (MoO/MoN), 451 (MoO/MoN). $[\alpha]^D_{25}$ = +164° (PhCl, c=0.022).

*Preparation of dioxomolybdenum trans-3-bromo-5-nitrocyclohexylsalen complex **8***

To a round bottom flask was added $MoO_2(acac)_2$ (0.35 mmol, 0.114g**),** diimine **3** (1 eq, 0.200 g), 20 mL 1,2-dichloroethane, and a stir bar. The reaction flask was attached to a Hickman still loaded with 4Å molecular sieves and set to reflux for 5 hours. After cooling to room temperature, the bright yellow precipitate was isolated by filtration in 15.9 % yield. NMR: ^{1}H NMR (500 MHz, DMF-d_7) δ 9.04 (s, 1H, HC=N), 9.01 (s, 1H, HC=N), 8.51 (d, *J* = 3.0 Hz, 1H, aryl), 8.49 (d, *J* = 3.0 Hz, 1H, aryl), 8.47 (d, *J* = 2.9 Hz, 1H, aryl), 8.42 (d, *J* = 3.0 Hz, 1H, aryl), 4.05 (td, *J* = 10.9, 4.4 Hz, 1H, N-CH), 3.88 (td, *J* = 11.1, 4.2 Hz, 1H, N-CH), 2.32 (d, *J* = 12.7 Hz, 1H, chxn), 2.17 (d, *J* = 13.0 Hz, 1H, chxn), 1.92 (d, *J* = 10.8 Hz, 1H, chxn), 1.86 (d, *J* = 10.5 Hz, 2H, chxn), 1.69 (d, *J* = 10.8 Hz, 1H, chxn), 1.49 (dd, *J* = 9.2, 2.8 Hz, 2H, chxn). ^{13}C NMR (126 MHz, dmf) δ 173.9, 173.79, 172.99, 169.3, 168.9, 133.1, 132.5, 132.4, 118.2, 117.9, 114.1, 113.6, 66.4, 65.9, 54.5, 33.2, 32.4, 24.9, 24.8, 24.6. IR (KBr, cm^{-1}): 3078, 2935, 2864, 1641 (C=N), 1597, 1544, 1521, 1338, 1327, 1303, 1219, 1097, 950, 925 ($MoO_{2\ sym}$), 898 ($MoO_{2\ asym}$), 871, 744, 731, 709, 526, 472, 455. The low solubility of **8** prevented determination of its specific rotation.

*Preparation of dioxomolybdenum trans-3-tert-butyl-5-nitrocyclohexylsalen **9***

To a 25 mL round bottom flask was added L^{3tBu} **4** (0.337 mmol), 10 mL chlorobenzene, and 0.25 eq (0.084 mmol) of $MoO_2(acac)_2$. The reaction flask was attached to a Hickman still loaded with 4Å molecular sieves and set to reflux for 1 hour. Another 0.25 eq $MoO_2(acac)_2$ was added, and the mixture was again set to reflux for 1 hour. This process was repeated twice more, bringing the total equivalents of $MoO_2(acac)_2$ to 1 eq. The reaction solution was transferred to a centrifuge tube and concentrated to approximately 5 mL. n-Heptane was added dropwise to precipitate the complex as a bright yellow powder, and the solution was centrifuged to pellet the precipitate. After removing the supernatant by pipette and drying the solid under vacuum, the product was isolated in high purity (>95%) in 50% yield. NMR: ^{1}H NMR (500 MHz, Chloroform-*d*) δ 8.51 (m, 3H, HC=N, aryl), 8.37 – 8.33 (m, 2H, aryl), 8.29 (d, *J* = 2.8 Hz, 1H, aryl), 4.44 (ddd, *J* = 12.6, 10.5, 2.9 Hz, 1H, N-CH), 3.01 (tt, *J* = 11.0, 2.1 Hz, 1H, N-CH), 2.56 (dd, *J* = 12.6, 3.8 Hz, 2H, CH_2), 2.52 – 2.44 (m, 2H, CH_2), 1.81 (m, 4H, CH_2-CH_2), 1.50 (s, 9H, $C(CH_3)_3$), 1.25 (s, 9H, $C(CH_3)_3$). ^{13}C NMR (126 MHz, $CDCl_3$) δ 171.3, 162.23, 162.1, 142.8, 142.4, 140.6, 137.6, 128.9, 128.4, 127.9, 127.8, 121.5, 121.1, 73.6, 71.9, 35.9, 35.6, 30.8, 29.7, 29.2, 28.4, 24.5, 23.7. IR (KBr, cm^{-1}): 2954, 2988, 1597 (C=N), 1508, 1327, 1284, 1200, 1111, 950, 920 (MoO_2), 893 (MoO_2), 740, 721, 560, 520, 460, 420. MS (DCM, ESI+): 647.15 (49%), 649.12 (34%), 650.15 (64%), 651.315 (77%), 652.12 (55%), 653.15 (100%), 655.15 (39%); MS, calculated: 647 (52.1%), 649 (35.9%), 650 (66.9%), 651 (78.9%), 652 (56.6%), 653 (100%), 655 (39.8%). $[\alpha]^D_{25}$ = -245° (PhCl, extrapolated to infinite dilution).

*Preparation of dioxomolybdenum trans-3,5-tert-butylcyclohexylsalen complex **10***

Compound **5** (1.18 g, 2.16 mmol) and *bis*-(acetylacetonato)-dioxomolybdenum (0.700 g, 2.15 mmol) were placed in a round-bottom flask with a stir bar and dissolved in 40 mL acetonitrile. The flask was fitted with a condenser, and the reaction mixture was heated at reflux for 18 h. The reactants gradually went into solution over the course of the reaction, yielding a clear, orange solution. After cooling, the solvent was removed by vacuum, yielding a viscous orange material. The crude product was chromatographed over silica using CH_2Cl_2 as the eluent. Solvent was removed under vacuum and the resulting solid was washed with ether, yielding a spectroscopically pure microcrystalline orange product.

^{1}H NMR (300 MHz, $CDCl_3$, δ) 8.38 (s, 1H, -N=CH), 8.34 (d, J=1.2 Hz, 1H, -N=CH), 7.63 (d, J=2.4Hz, 1H, Ar H), 7.51 (d, J=2.4 Hz, 1H, Ar H), 7.24 (d, J=2.4 Hz, 1H, Ar H), 7.20 (d, J=2.4 Hz, 1H, Ar H), 4.33 (td, J=10.8, 3.1 Hz, 1H, CH-N), 2.74 (t, J=10.5 Hz, 1H, CH-N), 2.50 (d, J=11.1 Hz, 1H, CH_2), 2.37 (d, J=9.3 Hz, 1H, CH_2), 2.05 (d, J=11.4 Hz, 2H, CH_2), 1.70 (br s, 2H, CH_2), 1.47 (s, 9H, $C(CH_3)_3$), 1.34 (s, 9H, $C(CH_3)_3$), 1.28 (s, 9H, $C(CH_3)_3$), 1.25 (s, 9H, $C(CH_3)_3$). ^{13}C NMR (126 MHz, $CDCl_3$) δ 165.5, 162.2, 161.2, 157.3, 142.7, 140.3, 139.1, 138.5, 132.1, 130.1, 129.1, 126.2, 122.3, 121.1, 72.1, 71.2, 35.5, 35.4, 34.3, 34.1, 31.4, 31.2, 30.5, 30.2, 29.6, 28.5, 24.7, 23.9. IR (KBr, cm^{-1}): 2954, 2906, 2866, 1627, 1612, 1597, 1529, 1251, 921 ($MoO_{2\ sym}$), 877 ($MoO_{2\ asym}$), 561, 530. MS (DCM, ESI+): 669.31 (48%), 671.31 (34%), 672.31 (64%), 673.31 (79%), 674.31 (58%), 675.31 (100%), 677.31 (38%). MS, calculated: 669 (50%), 671 (35.6%), 672 (66.9%), 673 (80.8%), 674 (60.1%), 675 (100%), 677 (40.1%). $[\alpha]^{D}_{25}$ = -265˚ (PhCl, c=0.095)

*Preparation of 3-tertbutylbinaphthylsalen ligand (**11**)*[48]

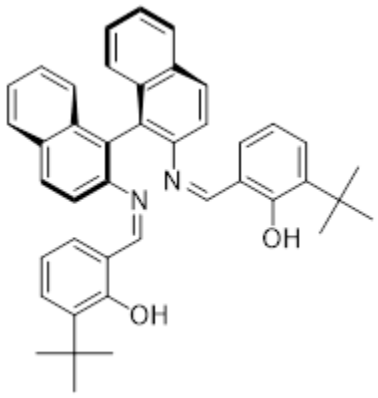

Optically pure *S*-(-)-2,2'-diaminobinapthyl camphorsulfonate (>95% ee, 3.07 g, 5.83 mmol) was placed in a round-bottom flask with a stir bar and dissolved in a biphasic water/DCM system with stirring. One gram of sodium carbonate was added to the system, and the mixture was left to stir for a few hours. The organic phase was separated, back-extracted with water two times, and dried, yielding 1.41g (85%) of the free diamine as a sticky tan powder. *S*-(-)-2,2'-Diaminobinapthyl (1.40 g, 4.93 mmol) was placed in a three-neck round-bottom flask with a stir bar. The flask is fitted with a dean-stark apparatus and flushed with nitrogen. 3-(tert-Butyl)-salicylaldehyde (1.55 g, 8.70 mmol) was added to the flask, the reactants were dissolved in dry toluene (50 mL) and the system was brought to reflux. Over the course of a few hours, the diamine dissolved, and the reaction mixture turned dark orange. After 45 hours at reflux, ~0.1 mL of water was evident in the Dean-Stark trap. The system was allowed to cool, and was stripped of solvent under vacuum, yielding about 3 g of a hygroscopic, sticky, golden-yellow solid that was difficult to dry completely, complicating the yield calculation. This solid was not isolated and was sufficiently pure for use in the complexation reaction without

isolation or purification. ^{1}H NMR (400 MHz, Benzene-d6) δ 13.26 (s, 2H), 8.21 (s, 2H), 7.82 (d, J = 8.8 Hz, 2H), 7.76 (d, J = 8.2 Hz, 2H), 7.46 (dd, J = 8.4, 1.1 Hz, 2H), 7.18 (d, J = 0.7 Hz, 1H), 7.17 (d, J = 1.3 Hz, 1H), 7.16 (d, J = 1.4 Hz, 1H), 7.15 (d, J = 1.2 Hz, 1H), 7.09 (dd, J = 7.8, 1.6 Hz, 2H), 6.98 (ddd, J = 8.3, 6.8, 1.3 Hz, 2H), 6.70 (dd, J = 7.6, 1.6 Hz, 2H), 6.53 (t, J = 7.6 Hz, 2H), 1.30 (s, 18H). Lit[48]: H NMR (CDCl3, 300 MHz): δ 12.9 (s, 2 H, OH), 8.6 (s, 2 H, CH=N), 8.05 (d, 2 H, J = 8.80, Ph), 7.95 (d, 2 H, J = 8.15, aryl H), 7.58 (d, 2 H, J = 8.80, aryl H), 6.90–7.5 (m, 10 H, aryl H), 6.67 (t, 2 H, J = 7.62 Hz, aryl H) and 1.2 (s, 18 H, Bu^t).

*Preparation of dioxomolybdenum 3-tertbutylbinaphthylsalen complex **12***

S-(-)-Ligand **11** (2.40 g, 3.98 mmol) was placed in a round-bottom side-arm flask with a stir bar followed by dioxo-molybdenum dichloride bis-dimethylformamide (1.52 g, 4.40 mmol). The flask was fitted with a reflux condenser, and the system was sealed, evacuated, and flushed with dry nitrogen several times. With the reaction apparatus under positive nitrogen pressure, dry CH_2Cl_2 was introduced *via* the side-arm port. The reaction was refluxed under nitrogen for 72 h. Initially, the reaction mixture was a clear, orange solution, which turned darker over the first few hours. The mixture was allowed to cool and stripped of solvent under vacuum. The crude product was dissolved in a small quantity of benzene and filtered through a filter cannula. The residual green solid was washed once with benzene and filtered. The filtrate was then concentrated under vacuum. The resulting gold solid was recrystallized from boiling ether to yield a gold, microcrystalline solid that was judged to be pure by ^{1}H NMR and HRMS. Crystallization by vapor diffusion from DCM to ether yielded crystals suitable for XRD structure determination. IR (KBr) $\bar{\nu}_{max}$: 2953, 2906, 1612 (C=N), 1587, 1558, 1419, 1259, 1190, 929 ($MoO_{2\ sym}$), 910, 867 ($MoO_{2\ asym}$), 831, 748, 669, 628, 489. ^{1}H NMR of C_2 coordination isomer in mixtures (500 MHz, $CDCl_3$) δ 8.06 (s, 2H, HC=N), 7.82 (dd, J = 8.7, 2.2 Hz, 4H, aryl), 7.66 (d, J = 8.6 Hz, 2H, aryl), 7.39 (ddd, J = 8.2, 6.7, 1.2 Hz, 2H, aryl), 7.36 (dd, J = 7.7, 1.7 Hz, 2H, aryl), 7.25 (dt, J = 6.7, 1.6 Hz, 2H, aryl), 7.20 (dd, J = 8.6, 1.2 Hz, 2H, aryl), 6.97 (dd, J = 7.7, 1.7 Hz, 2H, aryl), 6.70 (t, J = 7.6 Hz, 2H, aryl), 1.43 (s, 18H, $C(CH_3)_3$). ^{1}H NMR of C_1 coordination isomer (500 MHz, Benzene-d6) δ 7.89 (s, 1H, HC=N), 7.60 (d, J = 8.7 Hz, 1H, aryl), 7.60 (s, 1H, HC=N), 7.55 (d, J = 8.6 Hz, 1H, aryl), 7.36 (d, J = 8.6 Hz, 1H, aryl), 7.29 (d, J = 8.1 Hz, 1H, aryl), 7.26 (dd, J = 7.8, 1.7 Hz, 2H, aryl), 7.16 (dd, J = 7.4,

1.8 Hz, 2H, aryl), 7.11 (t, J = 7.5 Hz, 2H, aryl), 7.07 (d, J = 7.5 Hz, 1H, aryl), 7.00 (d, J = 7.6 Hz, 2H, aryl), 6.73 (d, J = 8.6 Hz, 1H, aryl), 6.46 (t, J = 7.7 Hz, 1H, aryl), 6.37 (dd, J = 7.8, 1.6 Hz, 1H, aryl), 6.18 (dd, J = 7.9, 1.7 Hz, 1H, aryl), 6.12 (t, J = 7.6 Hz, 1H, aryl), 1.63 (s, 9H, $C(CH_3)_3$), 1.55 (s, 9H, $C(CH_3)_3$). MS (DCM, ESI+): 727.20 (46%), 729.20 (34%), 730.20 (65%), 731.20 (81%), 732.20 (61%), 733.20 (100%), 735.20 (40%). MS (calculated): 727 (48.1%), 729 (35.5%), 730 (66.6%), 731 (81.8%), 732 (62.8%), 733 (100%), 735 (41%).

2.5.4 Kinetic resolution procedure

For each run of the kinetic resolution reaction, a Schlenk tube was charged with catalyst (~1% loading, see Table 2-4), 15.4 mg of pyridine *N*-oxide (0.162 mmol), and 5 mL of 1,1,2,2-tetrachloroethane. The reaction solution was deoxygenated by performing three freeze-pump-thaw cycles under vacuum, followed by backfilling the Schlenk tube with argon. Methylphenyl-*tert*-butylphosphine (70 mg, 0.39 mmol) was then added by pipette, the Schlenk tube was again evacuated, and two additional freeze-pump-thaw cycles were performed. The reaction tube was backfilled with argon and placed in a 50°C oil bath overnight. The reaction mixtures were observed to darken from the initial yellow to a brown or red-brown color; the reactions involving **7** and **8** were observed to further change color until they were a nearly pale green. The phosphine oxide was isolated from the reaction solution in a nitrogen-filled glove bag by preparative TLC. The plate was developed using 90:10 CH_2Cl_2/MeOH, and the phosphine oxide band at R_f=0.3 was scraped off the plate, and washed with several portions of iPrOH, followed by solvent evaporation from the washings. Optical rotation measurements of the phosphine oxide were recorded in $CHCl_3$ solution and calculated % ee was confirmed using chiral HPLC.

2.5.5 Computational methods

All calculations were carried out using Gaussian 09. Structures were optimized using the B3LYP hybrid functional and the basis sets: Mo, LANL2DZ; P, Br, 6-311++ G(d,p); C, H, O, N, 6-311 G(d) using Gaussian 09's ultrafine integration grid. Solvent phase energies were obtained as a single point energy calculation using the M06 functional (basis sets: Mo, SDD; P, Br, C, H, O, N, 6-311++G(d,p) in conjunction with the SMD solvent model for 1,2-dichloroethane. The free energy

correction to the energy was taken from the B3LYP frequency calculation. Relaxed coordinate scans were employed to focus Berny saddle point searches. For transition states $TS_{B\text{-}C}$ and $TS_{C\text{-}D}$, starting points for the Berny optimizations were located by running a series of single-point optimizations with the M-OA bond length frozen. Transition states were verified by the existence of a single imaginary frequency along the reaction coordinate involving bond making/breaking. Reaction profiles were generated using the mechaSVG program. [49]

2.5.6 Supplemental Data

Spectral data for characterization of reported compounds can be found in Appendix A (pg 168).

Table 2-4: Reaction conditions for kinetic resolution studies

catalyst	**Catalyst loading (mol %)**	**Loading of pyr-O (mol %)**	t_{rxn}	T_{rxn}
7	1.8%	42 %	6 h	50 °C
8	0.5%	42 %	6 h	50 °C
9	1.7%	40 %	74 h	50 °C
10	1.7%	40%	16 d	80 °C
12	10%	40 %	8 d	80 °C

Table 2-5: Tabulated bond parameters for Mo-coordination sphere from X-ray structure of complex **12***

Bond	Length (Å)	Bond Angle	angle (°)
Mo(1)-O(4)	1.7050(14)	O(3)-Mo(1)-O(1)	96.74(6)
Mo(1)-O(3)	1.7106(13)	O(2)-Mo(1)-O(1)	158.31(6)
Mo(1)-O(2)	1.9539(13)	O(4)-Mo(1)-N(1)	88.12(6)
Mo(1)-O(1)	1.9594(13)	O(3)-Mo(1)-N(1)	163.94(6)
Mo(1)-N(1)	2.3226(15)	O(2)-Mo(1)-N(1)	84.59(6)
Mo(1)-N(2)	2.3600(17)	O(1)-Mo(1)-N(1)	78.72(5)
Bond Angle	angle (°)	O(4)-Mo(1)-N(2)	160.06(6)
O(4)-Mo(1)-O(3)	107.79(7)	O(3)-Mo(1)-N(2)	91.82(6)
O(4)-Mo(1)-O(2)	96.39(6)	O(2)-Mo(1)-N(2)	77.68(6)
O(3)-Mo(1)-O(2)	95.52(6)	O(1)-Mo(1)-N(2)	84.09(6)
O(4)-Mo(1)-O(1)	96.81(6)	N(1)-Mo(1)-N(2)	72.47(5)

*complete X-ray data for **12** can be obtained from the corresponding cif file in the Cambridge database

Computational SI

CITATION FOR GAUSSIAN 09

Gaussian 09, Frisch, M. J.; Trucks, G. W.; Schlegel, H. B.; Scuseria, G. E.; Robb, M. A.; Cheeseman, J. R.; Scalmani, G.; Barone, V.; Mennucci, B.; Petersson, G. A.; Nakatsuji, H.; Caricato, M.; Li, X.; Hratchian, H. P.; Izmaylov, A. F.; Bloino, J.; Zheng, G.; Sonnenberg, J. L.; Hada, M.; Ehara, M.; Toyota, K.; Fukuda, R.; Hasegawa, J.; Ishida, M.; Nakajima, T.; Honda, Y.; Kitao, O.; Nakai, H.; Vreven, T.; Montgomery, Jr., J. A.; Peralta, J. E.; Ogliaro, F.; Bearpark, M.; Heyd, J. J.; Brothers, E.; Kudin, K. N.; Staroverov, V. N.; Kobayashi, R.; Normand, J.; Raghavachari, K.; Rendell, A.; Burant, J. C.; Iyengar, S. S.; Tomasi, J.; Cossi, M.; Rega, N.; Millam, J. M.; Klene, M.; Knox, J. E.; Cross, J. B.; Bakken, V.; Adamo, C.; Jaramillo, J.; Gomperts, R.; Stratmann, R. E.; Yazyev, O.; Austin, A. J.; Cammi, R.; Pomelli, C.; Ochterski, J. W.; Martin, R. L.; Morokuma, K.; Zakrzewski, V. G.; Voth, G. A.; Salvador, P.; Dannenberg, J. J.; Dapprich, S.; Daniels, A. D.; Farkas, Ö.; Foresman, J. B.; Ortiz, J. V.; Cioslowski, J.; Fox, D. J. Gaussian, Inc., Wallingford CT, 2009.

Table 2-6: M06 calculated energies (solvent phase, Hartrees) for B3LYP optimized structures of C_1 and C_2 isomers of complexes **7-10, 12**

Species	G
6	-1252.09849
6-C_2	-1252.08671
7	-1661.05061
7-C_2	-1661.03287
8	-6807.91045
8-C_2	-6807.89244
9	-1975.17748
9-C_2	-1975.16346
10	-1880.35343
10-C_2	-1880.34271
12-C_1	-2100.56528
12	-2101.18883

Table 2-7: M06 calculated energies (solvent phase, Hartrees) for B3LYP optimized structures of species in **Figure** 2-20

7-A	-1661.36670
PPhtBuMe	-770.53182
7-B (pro-S-OPR3)	-2431.96280
TS_{A-B} 7-A/B (pro-S-OPR3)	-2431.88635
7-B (pro-R-OPR3)	-2431.96196
TS_{A-B} 7-A/B (pro-R-OPR3)	-2431.88598
TS_{B-C} 7-B/C (pro-S-OPR3)	-2432.53951
TS_{B-C} 7-B/C (pro-R-OPR3)	-2432.54013
7-C	-1585.40510
OPPhtBuMe	-845.79032
pyridine N-oxide	-323.32243
TS_{C-D} 7-C/D_{eq}	-1909.90180
TS_{C-D} 7-C/D_{ax}	-1909.90566
7-D_{eq}	-1909.49459
7-D_{ax}	-1909.91043
TS_{D-E} 7-D/E_{eq}	-1909.47199
TS_{D-E} 7-D/E_{ax}	-1909.89042
Pyridine	-248.16349

2.6 Works Cited

[1] K.M. Pietrusiewicz, M. Zablocka, Preparation of Scalemic P-Chiral Phosphines and Their Derivatives, Chemical Reviews. 94 (1994) 1375–1411.

[2] J. Bayardon, S. Jugé, P-Chiral Ligands, in: Phosphorus(III) Ligands in Homogeneous Catalysis: Design and Synthesis, John Wiley & Sons, Ltd, Chichester, UK, 2012: pp. 355–389.

[3] E. Bergin, C.T. O'Connor, S.B. Robinson, E.M. McGarrigle, C.P. O'Mahony, D.G. Gilheany, Synthesis of P-Stereogenic Phosphorus Compounds. Asymmetric Oxidation of Phosphines under Appel Conditions, J. Am. Chem. Soc. 129 (2007) 9566–9567.

[4] A. Brandi, S. Cicchi, A. Goti, K.M. Pietrusiewicz, Chiral Vinyl Phosphine Oxides: Double Asymmetric Induction in the 1,3-Dipolar Cycloaddition to Chiral Nitrones. Kinetic Resolution of a Racemic Phospholene Oxide, Phosphorus, Sulfur, and Silicon and the Related Elements. 75 (1993) 155–158.

[5] Y.-N. Gao, F.-C. Shi, Q. Xu, M. Shi, Enantioselective Synthesis of Isoquinolines: Merging Chiral-Phosphine and Gold Catalysis, Chemistry - A European Journal. 22 (2016) 6803–6807.

[6] D. Zhao, L. Mao, Y. Wang, D. Yang, Q. Zhang, R. Wang, Catalytic Asymmetric Hydrophosphinylation of α,β-Unsaturated N -Acylpyrroles: Application of Dialkyl Phosphine Oxides in Enantioselective Synthesis of Chiral Phosphine Oxides or Phosphines, Organic Letters. 12 (2010) 1880–1882.

[7] V. Bhat, S. Wang, B.M. Stoltz, S.C. Virgil, Asymmetric Synthesis of QUINAP via Dynamic Kinetic Resolution, J. Am. Chem. Soc. 135 (2013) 16829–16832.

[8] V.S. Chan, M. Chiu, R.G. Bergman, F.D. Toste, Development of Ruthenium Catalysts for the Enantioselective Synthesis of P-Stereogenic Phosphines via Nucleophilic Phosphido Intermediates, J. Am. Chem. Soc. 131 (2009) 6021–6032.

[9] K. Nikitin, K. V. Rajendran, H. Müller-Bunz, D.G. Gilheany, Turning Regioselectivity into Stereoselectivity: Efficient Dual Resolution of P-Stereogenic Phosphine Oxides through Bifurcation of the Reaction Pathway of a Common Intermediate, Angewandte Chemie International Edition. 53 (2014) 1906–1909.

[10] W. Perlikowska, M. Gouygou, J.-C. Daran, G. Balavoine, M. Mikołajczyk, Kinetic resolution of P-chiral tertiary phosphines and chlorophosphines: a new approach to optically active phosphoryl and thiophosphoryl compounds, Tetrahedron Letters. 42 (2001) 7841–7845.

[11] S. Kikuchi, H. Konishi, Y. Hashimoto, The deoxygenation of sulfoxide mediated by the Ph3P/Lewis acid combination and the application to the kinetic resolution of racemic phosphines using optically active sulfoxide, Tetrahedron. 61 (2005) 3587–3591.

[12] C. Scriban, D.S. Glueck, Platinum-Catalyzed Asymmetric Alkylation of Secondary Phosphines: Enantioselective Synthesis of P-Stereogenic Phosphines, J. Am. Chem. Soc. 128 (2006) 2788–2789.

[13] J.S. Harvey, V. Gouverneur, Catalytic enantioselective synthesis of P-stereogenic compounds, Chemical Communications. 46 (2010) 7477–7485.

[14] J.S. Harvey, V. Gouverneur, Catalytic enantioselective synthesis of P-stereogenic compounds, Chemical Communications. 46 (2010) 7477–7485.

[15] A. Grabulosa, J. Granell, G. Muller, Preparation of optically pure P-stereogenic trivalent phosphorus compounds, Coordination Chemistry Reviews. 251 (2007) 25–90.

[16] H. Pellissier, Catalytic Kinetic Resolution, in: Separation of Enantiomers, Wiley-VCH Verlag GmbH & Co. KGaA, Weinheim, Germany, 2014: pp. 75–122.

[17] H. Pellissier, Recent developments in non-enzymatic catalytic oxidative kinetic resolution of secondary alcohols, Tetrahedron. 74 (2018) 3459–3468.

[18] J.M. Keith, J.F. Larrow, E.N. Jacobsen, Practical Considerations in Kinetic Resolution Reactions, Advanced Synthesis & Catalysis. 343 (2001) 5–26.

[19] P. Le Maux, H. Bahri, G. Simonneaux, L. Toupet, Enantioselective Oxidation of Racemic Phosphines with Chiral Oxoruthenium Porphyrins and Crystal Structure of [5,10,15,20-Tetrakis[o-((2-methoxy-2-phenyl-3,3,3-trifluoropropanoyl)amino)phenyl]porphyrinato](carbonyl)(tetrahydrofuran) ruthenium(II) (α,β, α,β Isomer), Inorganic Chemistry. 34 (1995) 4691–4697.

[20] K. Ambroziak, New dioxomolybdenum(VI) complexes of tetradentate Schiff base as catalysts for epoxidation of olefins, Journal of Molecular Catalysis A: Chemical. 211 (2004) 9–16.

[21] N.R. Pramanik, S. Ghosh, T.K. Raychaudhuri, S. Ray, R.J. Butcher, S.S. Mandal, Synthesis, characterization and crystal structure of oxomolybdenum (VI) and (IV) complexes of some tridentate ONS donor ligands, Polyhedron. 23 (2004) 1595–1603.

[22] C.J. Whiteoak, G.J.P. Britovsek, V.C. Gibson, A.J.P. White, Electronic effects in oxo transfer reactions catalysed by salan molybdenum(vi) cis-dioxo complexes, Dalton Transactions. (2009) 2337.

[23] T.A. Rusmore, M.J. Behlen, A. John, D.T. Glatzhofer, K.M. Nicholas, Oxidative kinetic resolution of P-chiral phosphines catalyzed by chiral (salen)dioxomolybdenum complexes, Molecular Catalysis. 513 (2021) 111776–111776.

[24] M. Gullotti, A. Pasini, G.M. Zanderighi, G. Ciani, A. Sironi, Dioxomolybdenum(VI) complexes of quadridentate chiral Schiff bases and the crystal and molecular structure of

dioxo[(2R)-propane-1,2-diylbis(salicylideneiminato)]molybdenum(VI), Journal of the Chemical Society, Dalton Transactions. (1981) 902.

[25] M. Karman, G. Romanowski, Cis-dioxidomolybdenum(VI) complexes with chiral tetradentate Schiff bases: Synthesis, spectroscopic characterization and catalytic activity in sulfoxidation and epoxidation, Inorganica Chimica Acta. 511 (2020) 119832.

[26] M.M. Haghdoost, N. Zwettler, G. Golbaghi, F. Belaj, M. Bagherzadeh, J.A. Schachner, N.C. Mösch-Zanetti, Diastereoselective Synthesis and Catalytic Activity of Two Chiral cis -Dioxidomolybdenum(VI) Complexes, European Journal of Inorganic Chemistry. 2018 (2018) 2549–2556.

[27] H. Sugimoto, S. Tatemoto, K. Suyama, H. Miyake, S. Itoh, C. Dong, J. Yang, M.L. Kirk, Dioxomolybdenum(VI) Complexes with Ene-1,2-dithiolate Ligands: Synthesis, Spectroscopy, and Oxygen Atom Transfer Reactivity, Inorganic Chemistry. 48 (2009) 10581–10590.

[28] M. Kamal Hossain, J.A. Schachner, M. Haukka, M.G. Richmond, N.C. Mösch-Zanetti, A. Lehtonen, E. Nordlander, Oxygen atom transfer catalysis by dioxidomolybdenum(VI) complexes of pyridyl aminophenolate ligands, Polyhedron. 205 (2021) 115234.

[29] M.D. Greenhalgh, J.E. Taylor, A.D. Smith, Best practice considerations for using the selectivity factor, s, as a metric for the efficiency of kinetic resolutions, Tetrahedron. 74 (2018) 5554–5560.

[30] W. Buijs, P. Comba, D. Corneli, H. Pritzkow, Structural and mechanistic studies of the copper(II)-assisted ortho-hydroxylation of benzoates by trimethylamine N-oxide, Journal of Organometallic Chemistry. 641 (2002) 71–80.

[31] S. CHRISTIE, M. CLERK, M. ZAWOROTKO, Trimethylamine-N-oxide induced disproportionation of Re, Journal of Crystallographic and Spectroscopic Research. 23 (1993) 591–594.

[32] J.-K. Cheng, Y.-G. Yao, J. Zhang, Z.-J. Li, Z.-W. Cai, X.-Y. Zhang, Z.-N. Chen, Y.-B. Chen, Y. Kang, Y.-Y. Qin, Y.-H. Wen, A Simultaneous Redox, Alkylation, Self-Assembly Reaction under Solvothermal Conditions Afforded a Luminescent Copper(I) Chain Polymer Constructed of Cu3I4- and EtS-4-C5H4N+Et Components (Et = CH3CH2), J. Am. Chem. Soc. 126 (2004) 7796–7797.

[33] S. Polanc, B. Stanovnik, M. Tišler, Selective Deoxygenation of N -Oxides and Reduction of Nitro Compounds by Molybdenum(III) Species, Synthesis. 1980 (1980) 129–131.

[34] F. Choplin, G. Kaufmann, R. Rohmer, Vibrational spectra of new coordination complexes of molybdenum(VI) with trimethylamine and trimethylarsine oxides, C. R. Acad. Sc. Paris Serie C. 268 (1969) 333–336.

[35] V.N. Nemykin, P. Basu, Oxygen Atom Transfer Reactivity from a Dioxo-Mo(VI) Complex to Tertiary Phosphines: Synthesis, Characterization, and Structure of Phosphoryl Intermediate Complexes, (2005).

[36] L.M. Thomson, M.B. Hall, A Theoretical Study of the Primary Oxo Transfer Reaction of a Dioxo Molybdenum(VI) Compound with Imine Thiolate Chelating Ligands: A Molybdenum Oxotransferase Analogue, J. Am. Chem. Soc. 123 (2001) 3995–4002.

[37] B.W. Kail, L.M. Pérez, S.D. Zarić, A.J. Millar, C.G. Young, M.B. Hall, P. Basu, Mechanistic Investigation of the Oxygen-Atom-Transfer Reactivity of Dioxo-molybdenum(VI) Complexes, Chemistry - A European Journal. 12 (2006) 7501–7509.

[38] V.L. Schramm, ENZYMATIC TRANSITION STATES AND TRANSITION STATE ANALOG DESIGN, Annu. Rev. Biochem. 67 (1998) 693–720.

[39] A.N. Kharat, A. Bakhoda, T. Hajiashrafi, A. Abbasi, Synthesis, Characterization, and Crystal Structures of Tris(2-pyridyl)phosphine Sulfide and Selenide, Phosphorus, Sulfur, and Silicon and the Related Elements. 185 (2010) 2341–2347.

[40] R.J. Bowen, M.A. Fernandes, P.W. Gitari, M. Layh, Tris(2-pyridyl)-phosphine oxide: how C—H···O and C—H···N interactions can affect crystal packing efficiency, Acta Cryst C. 60 (2004) o258–o260.

[41] Y.A. Rulev, Z. Gugkaeva, V.I. Maleev, M. North, Y.N. Belokon, Robust bifunctional aluminium–salen catalysts for the preparation of cyclic carbonates from carbon dioxide and epoxides, Beilstein Journal of Organic Chemistry. 11 (2015) 1614–1623.

[42] R.S. Downing, F.L. Urbach, Circular dichroism of square-planar, tetradentate Schiff base chelates of copper(II), J. Am. Chem. Soc. 91 (1969) 5977–5983.

[43] J.P. Duxbury, J.N.D. Warne, R. Mushtaq, C. Ward, M. Thornton-Pett, M. Jiang, R. Greatrex, T.P. Kee, Phospho-Aldol Catalysis via Chiral Schiff Base Complexes of Aluminum †, Organometallics. 19 (2000) 4445–4457.

[44] E.N. Jacobsen, W. Zhang, A.R. Muci, J.R. Ecker, L. Deng, Highly enantioselective epoxidation catalysts derived from 1,2-diaminocyclohexane, J. Am. Chem. Soc. 113 (1991) 7063–7064.

[45] X.-G. Zhou, J.-S. Huang, P.-H. Ko, K.-K. Cheung, C.-M. Che, Titanium and ruthenium binaphthyl Schiff base complexes as catalysts for asymmetric trimethylsilylcyanation of aldehydes, Journal of the Chemical Society, Dalton Transactions. (1999) 3303–3309.

[46] K. Ambroziak, Z. Rozwadowski, T. Dziembowska, B. Bieg, Synthesis and spectroscopic study of Schiff bases derived from trans-1,2-diaminocyclohexane. Deuterium isotope effect on 13C chemical shift, Journal of Molecular Structure. 615 (2002) 109–120.

[47] Y.N. Belokon, W. Clegg, R.W. Harrington, M. North, C. Young, In Situ Formation of Heterobimetallic Salen Complexes Containing Titanium and/or Vanadium Ions, Inorganic Chemistry. 47 (2008) 3801–3814.

[48] A. Soriente, M. De Rosa, M. Lamberti, C. Tedesco, A. Scettri, C. Pellecchia, Synthesis, crystal structure and application in regio- and stereoselective epoxidation of allylic alcohols of a titanium binaphthyl-bridged Schiff base complex, Journal of Molecular Catalysis A: Chemical. 235 (2005) 253–259.

[49] Angnes, R. A. mechaSVG, GitHub repository, 2020, doi: 10.5281/zenodo.3970267.

CHAPTER 3

DIOXYGEN ACTIVATION AND SUBSTRATE OXIDATION BY OXOMOLYBDENUM SALEN SPECIES

3.1 Introduction

In the laboratory and industrially, molybdenum catalysts are applied for production of epoxides from alkenes, using either hydrogen peroxide or *tert*-butyl hydrogen peroxide, [1] reactions which are believed to proceed through metal peroxo intermediates [2]. The existence of these metal peroxo intermediates has led to interest in using dioxygen to form the molybdenum peroxo species directly in an atom-economical fashion. [3] Oxygen coordination and reactivity has been well explored for other metals, including iron [4,5], copper [5–9], chromium [10], manganese [11], rhenium [12], and rhodium [10], for which formation of metal superoxo and metal hydroperoxo species are observed and hydrogen atom transfer (HAT) reactivity through the radical pathway is favored [10]. Reactivity involving presumed coordination of dioxygen to a molybdenum center and oxygen transfer from the formed peroxo unit was first reported in 1988 by Arzoumanian, et al. [13] and has been further explored by other groups in the following decades. [11,14–19] While the existence of these compounds and their reactivity for oxygen atom transfer (OAT) reactions has been well established, we are not aware of any work exploring the mechanism of dioxygen coordination, activation, and O-transfer reactivity for the intermediate Mo(IV) complexes. Reports exist that demonstrate the necessity of increased ligand steric bulk to prevent the disproportionation of molybdenum (VI) peroxo species to molybdenum (VI) oxo species *via* the Mars-Van Krevelen mechanism (Figure 3-1). [13,20,21]

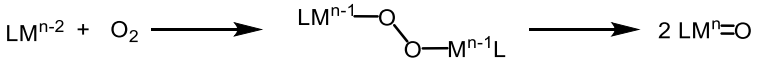

Figure 3-1. Mars-Van Krevelen mechanism for transition metal splitting of dioxygen

The literature for production and reactions of molybdenum peroxo complexes includes reports of epoxidation reactions, [22] oxidations to alcohols and ketones, [23] and sulfoxidation reactions. [24] Many of these catalysts are formed by reaction of MoO_3 with their chosen ligand and aqueous peroxides (commonly *tert*-butylhydroperoxide) and employ hydrogen peroxide as the oxygen atom source for catalytic oxidations. As a consequence of this synthetic approach,

much of the literature on molybdenum peroxo catalysis is based on oxobisperoxo molybdenum (VI) species. Epoxidations by these species are found to proceed *via* direct transfer of a peroxo group oxygen to the olefin double bond, rather than *via* olefin coordination to the metal center. [25] Under basic conditions, this single-atom transfer mechanism can break down and triperoxomolybdate species can lead to peroxidation of olefins by evolution and transfer of singlet dioxygen, $^1O_2$. [26] Computational studies of these epoxidation reactions show that the bis- and tris- peroxo complexes are more active for the epoxidation of olefins than the oxo-monoperoxo counterparts, which can sometimes be inactive as epoxidation catalysts even when the respective dioxomolybdenum species is an effective oxygen atom transfer catalyst. [27–29] This observation notably rules out the molybdenum (VI) oxoperoxo species as an intermediate in olefin epoxidation reactions with organic hydroperoxides. Oxidation of alcohols to ketones has been reported for molybdenum oxoperoxo complexes with various ligands, including picolinate and cyclopentadienyl complexes, [1] each of which employs an organic peroxide or hydrogen peroxide as the stoichiometric oxidant for catalytic oxidation, although there is a report of dioxygen being used as a co-oxidant. [30] Molybdenum (VI) oxoperoxo species are also reported for the oxidation of alkanes to alcohols and ketones, especially at benzylic positions. [23] Activity for this oxidation is seemingly dependent on the strength of the C-H bond to be oxidized rather than on the catalyst, and the catalytic cycle may depend partially on the presence of dioxygen. Further investigations of these complexes revealed that molybdenum (VI) peroxo complexes are capable of catalyzing the oxidation of sulfides to sulfoxides and sulfones, again using organic peroxides as the oxygen atom source. [31–34] Selectivity of the reaction for sulfoxide or sulfone products seemingly depends on electronic characteristics of the substrate. [31]

Reports from the group of Nadia Mösch-Zanetti [3,14,35,36] give evidence for the presence of an Mo(η^2-peroxo) complex generated from reaction with dioxygen (including an XRD structure of an imido-peroxo complex [35]) and OAT reactivity with triphenylphosphine for the oxoperoxo complex [14,36]). Based on these studies, the best comparison for the dioxygen coordination activity of the molybdenum (IV) monooxo sal-CHXD complex comes from a computational study of the coordination of dioxygen to a series of transition metal complexes, including ruthenium and iridium. [37] This DFT study closely examines the reaction profile for

coordination of dioxygen, producing detailed reaction surfaces and examining the spin-crossover processes involved. The study by Yu, et al. does not, however, examine the oxygen atom transfer properties of the resulting metal peroxo complexes, and to the best of our knowledge, computational studies have not been carried out on metal oxoperoxo complexes for OAT to phosphines or any other substrate.

3.2 Results

3.2.1 Observation of oxygen coordination activity

While optimizing the conditions for the molybdenum-catalyzed kinetic resolution of phosphine (Chapter 2), we found that, if exposed to air, the reaction would proceed beyond the conversion of the phosphine expected based on the loading of pyridine N-oxide (Scheme 3-1), suggesting that oxygen in the air could be acting as an oxidation reagent for the reaction. This prompted us to investigate the use of air/dioxygen as the oxygen atom donor for the phosphine oxidation process.

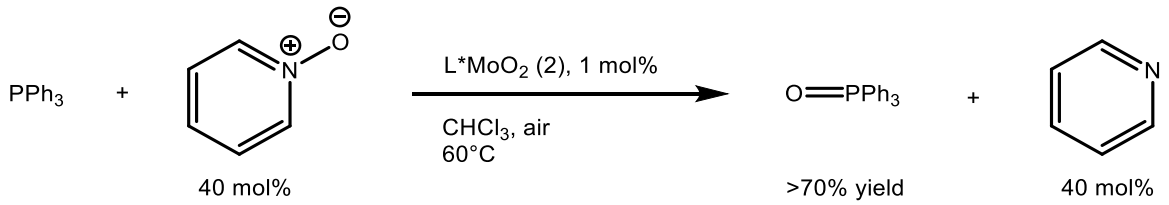

Scheme 3-1: Conditions for observed overconversion (by *o*-bromo-*p*-nitro-salCHXD MoO_2 complex **2**) of phosphine substrate with respect to available organic oxygen donor

To explore the use of dioxygen as an oxygen atom donor, a phosphine oxidation reaction was set up under air with no organic oxygen donor added (Scheme 3-2). The overall conversion of the reaction proceeded at roughly the same rate observed for reactions involving pyridine N-oxide as the oxygen atom donor.

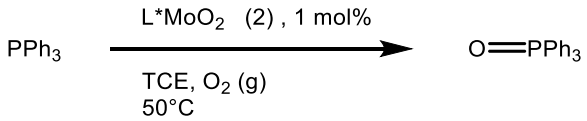

Scheme 3-2. Catalytic phosphine oxidation under dioxygen atmosphere

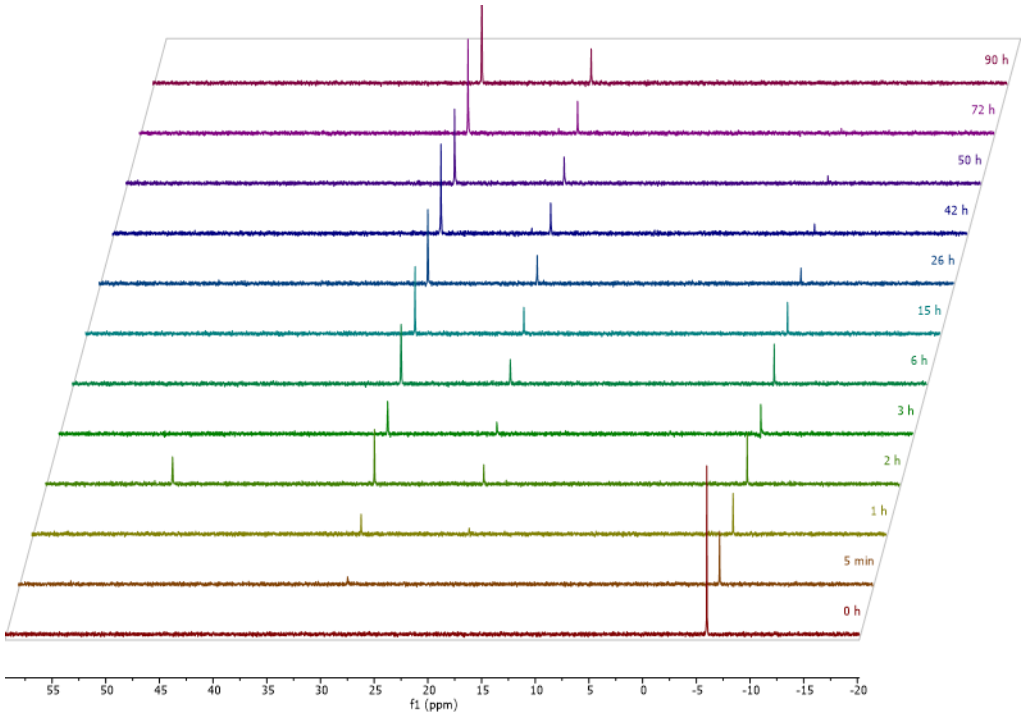

Figure 3-2. NMR study of phosphine oxidation by complex **2** under dioxygen (Scheme 3-2)

Monitoring of this reaction by ^{31}P NMR (Figure 3-2) appears to show the formation of two phosphorus-containing products, which are assigned as triphenylphosphine oxide (δ=29.7 ppm) and the molybdenum-bound triphenylphosphine oxide ternary complex, L*MoO($OPPh_3$) (δ=20.3 ppm). An intermediate species (δ=48.1 ppm) is tentatively assigned as the triphenylphosphine monooxo complex, L*$Mo^{IV}O(PPh_3)$. Catalytic phosphine oxidation under air was further studied, revealing that complex **2** has a TON in excess of 950, with a TOF of 1 eq/3.9 min up to 50% conversion and an average TOF of 1 eq/10 min over the full course of the reaction.

To determine the scope of the dioxygen coordination and activation, further studies were carried out with other molybdenum dioxo catalysts, including the molybdenum dioxo bis-acetylacetonate metal precursor **3,** and a series of *para*- or *ortho*-substituted dioxomolybdenum sal-CHXD complexes (*p*-nitro sal-CHXD **1**, sal-CHXD **4**, *o*-ethyl sal-CHXD **5,** 3,5-*tert*-butyl sal-CHXD **6**, and *p*-chloro sal-CHXD **7**).

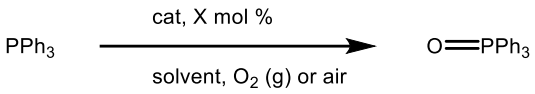

catalyst	mol %	solvent	T	atm	t	conversion
3	22	TCE	60 °C	air	5h	30%
4	1	PhCl	50 °C	O_2	13h	4%
5	1	PhCl	50 °C	O_2	13h	4%
6	1	PhCl	50 °C	O_2	13h	4%
7	1	PhCl	50 °C	O_2	13h	6%
1	1	PhCl	50 °C	O_2	13h	10%

Scheme 3-3. Studies of phosphine oxidation by dioxomolybdenum complexes with dioxygen as the oxygen atom source

The oxidation reaction for triphenyl phosphine is found to proceed with all studied dioxomolybdenum complexes (Scheme 3-3), with all sal-CHXD complexes (**1, 4-7**) showing catalytic activity at 1 mol % loading. $MoO_2(acac)_2$ (**3**), was found to have lower activity, but the oxygen atom transfer from dioxygen at atmospheric pressure was found to proceed at 60°C.

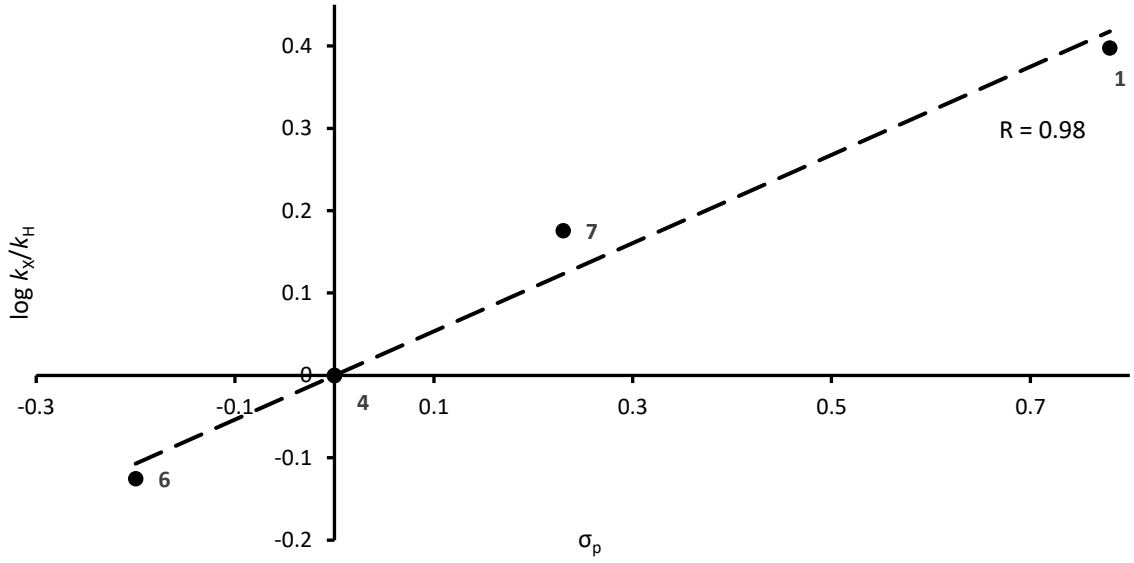

Figure 3-3. Relative rate constants log k_X/k_H versus Hammett parameter σ_p for the OAT reaction between dioxygen and PPh_3, catalyzed by sal-CHXD Mo complexes

Examination of relative rates for the salCHXD-based catalysts **1**, **4-7** shows that there is a linear Hammett relationship for rate of oxidation by these catalysts. *Para*-substitution of the salicylimine ring has significant effect on the rate of conversion, with addition of electron-withdrawing groups ($\sigma_p > 0$) significantly accelerating the reaction. By comparison with the Hammett relationship established by Whiteoak et al. for the analogous salan-type dioxomolybdenum series with OAT from DMSO, [38] the presence of a *para*-position electron

withdrawing group has a lesser effect on the rate of reaction, though this study does not make clear whether this decrease in effect is due to a change in the rate-limiting step or a decrease in the rate of reoxidation of the molybdenum (IV) monooxo species. The Hammett correlation (R=0.98) for this reaction suggests that the rate-limiting step is again the oxygen atom transfer step from the molybdenum (IV) center to the phosphine.

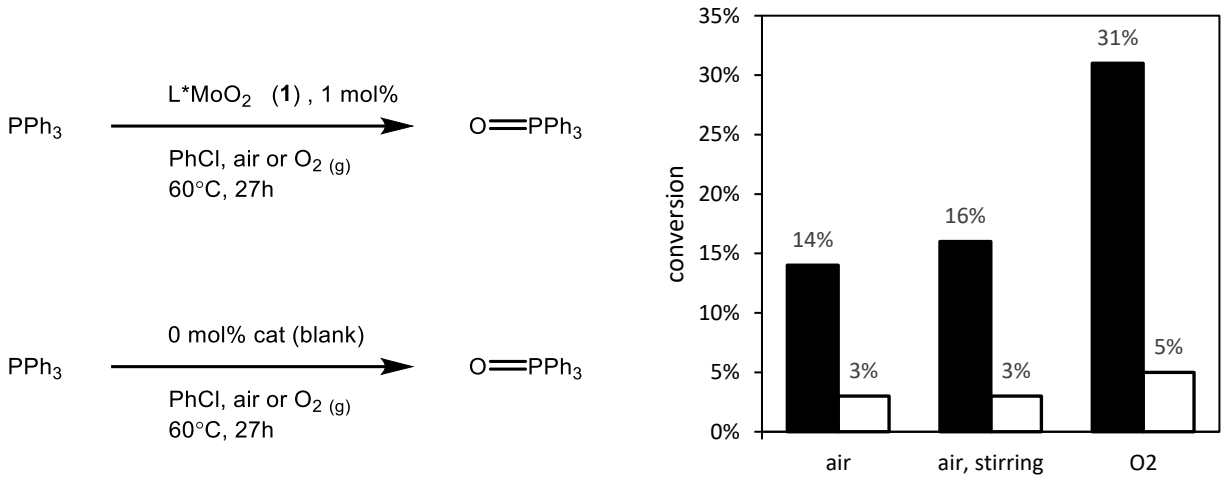

Figure 3-4. Comparison of conversion for catalyzed (solid bar) and blank (empty bar) phosphine oxidation reactions with complex **1**

The effects of pO_2 were also studied (Figure 3-4), and it was found that an increase of dioxygen concentration in solution does increase the rate of reaction, with a small effect observed by maintaining a steady partial pressure of air (pO_2 = 0.21 atm) over the course of the reaction, and a large (approximately 3x) increase in rate observed when running the reaction under dioxygen only (pO_2=1 atm). Under both conditions, there is autooxidation of triphenylphosphine (conversion for blank reactions can be seen in Figure 3-4), but the catalyzed reaction is observed to be approximately five times faster than that that of the uncatalyzed reaction.

3.2.2 Effect on enantioselectivity of chiral phosphine oxidation with chiral salicylimine catalysts

One of the opportunities presented by this dioxygen coordination and activation capability is the possibility of carrying out kinetic resolution reactions without the use of an organic oxygen atom donor. The oxoperoxo complex is reported to have different steric and

chiral character from the dioxomolybdenum complex, [3] suggesting that use of dioxygen as an oxygen atom source may alter the enantioselectivity of the reaction. To explore this effect, we took the complex with the best enantioselectivity (**8**, MoO_2(5-NO_2-3-^{t}Bu-sal-CHXD) and repeated the kinetic resolution reaction under aerobic conditions (Scheme 3-4). The enantiomeric excess of the product phosphine oxide was found to decrease to 6% e.e. from the 16% e.e. for the reaction involving pyridine N-oxide as the oxygen atom source. The reduction of enantiomeric excess by approximately one half represents a decrease in selectivity from *s*=1.49 to *s*=1.17, suggesting that the oxidation does not proceed exclusively through the dioxomolybdenum complex. The oxidation may instead proceed *via* two catalytic oxygen atom transfers from the molybdenum complex, the initial from the dioxo complex and the second from a complex with coordinated dioxygen having different steric parameters for the oxygen atom transfer step.

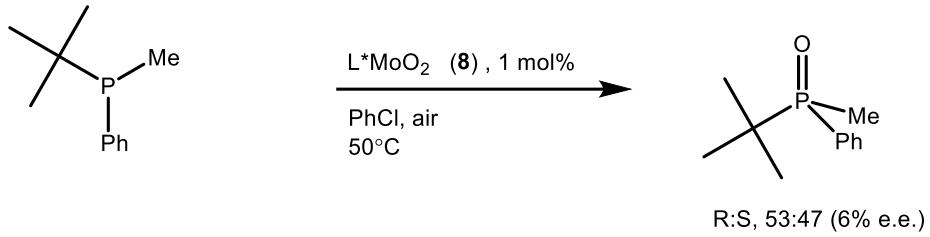

Scheme 3-4: Reaction scheme and enantioselectivity of kinetic resolution under aerobic oxidation conditions

This result may rule out a Mars-Van Krevelen mechanism for reoxidation, because if the activated dioxygen were being split between two molecules of catalyst, the kinetic resolution process would result in the same enantioselectivity as with an organic oxygen donor, as the dioxo pathway is the only one available.

3.3 Modeling of LMo(O2)O Oxygen Atom Transfer

To the best of our knowledge, computational studies of Mo-catalyzed OAT have not been expanded to include dioxygen as an OA donor, possibly due to the small body of literature reporting molybdenum oxo-monoperoxo complexes. [14,16,17,31,35,36,39–41] This leads to a similar absence in the literature of computational studies of OAT from oxoperoxo complexes. Because we have an experimental system shown to demonstrate good activity for this reaction,

it seemed pertinent to expand the computational study of this OAT reaction cycle to account for generation of a peroxo moiety *via* activation of dioxygen, rather than the previously investigated disproportionation of organic peroxide species. [34]

To determine the likely pathway of this reaction series, potential stationary state species were optimized using the B3LYP hybrid functional in the gas phase. Transition states were located using loose modredundant scans along the forming/breaking bond and optimized to a Berny transition state using the B3LYP functional. Minimum energy crossing points were located by Chance Lander using the sobMECP program. All energies for solvated species were calculated using the M06 functional. In the following text, reported ΔEs are B3LYP electronic energies in the gas phase, and ΔGs are solvent-phase M06 free energies.

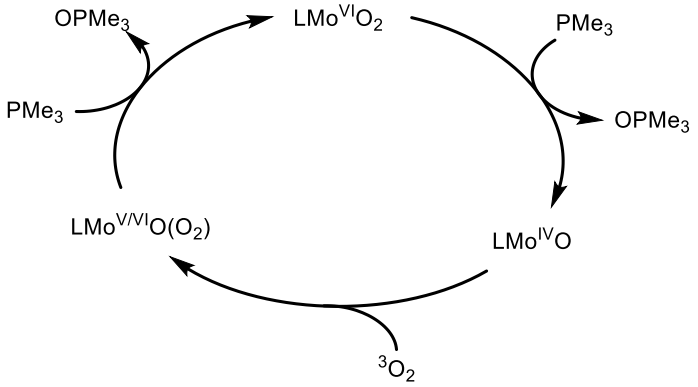

Figure 3-5: Overall putative catalytic process for trimethylphosphine oxidation by the Mo(NO_2-CHD-salen) complex under O_2

Based on the experimental study carried out in section 3.2, we propose that the catalytic cycle involves OAT from the dioxo species (as studied in chapter 2), reoxidation of the monooxo Mo(IV) complex by dioxygen, and finally OAT from the Mo(VI)O(O_2) species to regenerate the dioxo catalyst (Figure 3-5). The coordination of dioxygen to the metal center could form either the molybdenum (V) oxo-superoxo species (Figure 3-6a) or the molybdenum (VI) oxoperoxo species (Figure 3-6b), both of which are potential candidates for oxygen atom transfer to the substrate molecule.

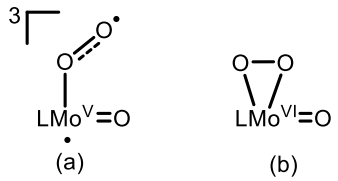

Figure 3-6. Molybdenum oxo-dioxygen cores, molybdenum (V) oxo-superoxo (a), molybdenum (VI) oxoperoxo (b)

Of greatest interest for this study are the species involved in the dioxygen coordination and those involved in subsequent oxygen atom transfer reactions. Available crystal structures of molybdenum peroxo complexes exclusively show the η^2-coordinated molybdenum peroxo, [13,14,39], rather than the η^1-superoxo structure commonly observed in other metal complexes. [6] The coordination of dioxygen, however, presumably proceeds though an η^1-superoxo intermediate which transitions to the oxo-η^2-peroxo species. [37] The intermediates, coordination transition states, and spin crossover events involved in this process are all of interest.

In the similar catalytic system reported by Mösch-Zanetti's group [3], it is reported that 2 equivalents of phosphine are oxidized per equivalent of dioxygen, but the pathway of this OAT has not been determined. While the oxo-η^2-peroxo species is presumed to be the stable structure of the $MoO(O_2)$salen complex, literature on oxidations involving metal-dioxygen complexes suggest that the radical-involving oxidation pathway from the metal superoxo species is a concern for the selectivity of the reaction, and necessary to investigate. [42] To fully characterize the catalytic mechanism, we need to model oxygen transfer pathways starting from both oxo-superoxo and oxoperoxo molybdenum species, and model the transfer of oxygen atoms from both the molybdenum oxo and dioxygen moieties.

3.3.1 Modeling phosphine oxidation of PMe_3 by dioxo complex **1**

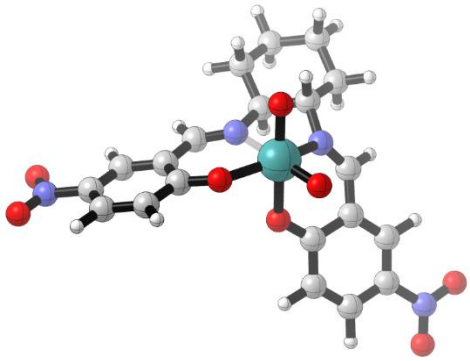

Figure 3-7. Dioxomolybdenum sal-CHXD complex **1A**

The optimized geometry of the dioxomolybdenum complex is the same as that described in Chapter 1. The C_1 cis-dioxo species (Figure 3-7) has inequivalent oxo groups, one trans to one of the imine N-donor ligand atoms, and the axial oxo group trans to the phenolate moiety. Examining the reactive axial oxo group, the FMOs involved in the reaction are the HOMO-1, which contains the oxo-group lone pair and the LUMO, which contains the π* orbital for the Mo-O moiety (Figure 3-8).

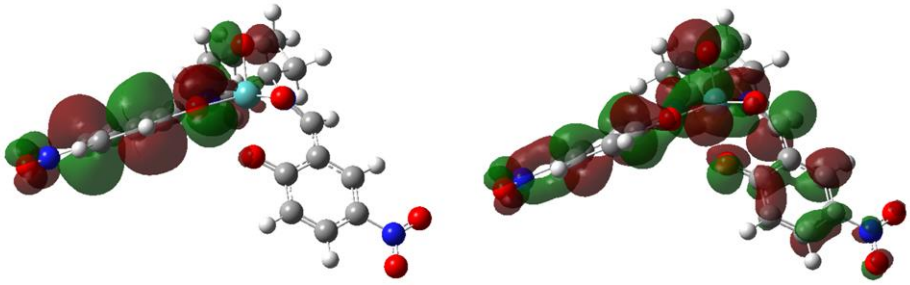

Figure 3-8. HOMO-1 (left) and LUMO (right) for the dioxo complex

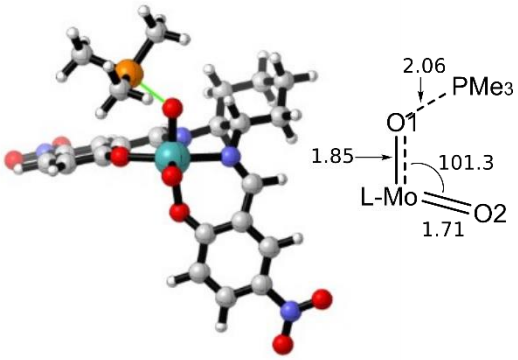

Figure 3-9. $\mathbf{TS_{A\text{-}B}}$ for phosphine oxidation by dioxomolybdenum catalyst **1**

Based on the computational study discussed in Chapter 2, only the axial approach of phosphine was considered. In this transition state (Figure 3-9), which is 20.1 kcal/mol uphill from the starting materials, we observe a slight decrease in the O-Mo-O bond angle from the dioxo species (101.3° from 103.0°). This approach is supported by the orbital analysis of complex **1A**, which shows that any orbitals with contribution on the equatorial oxygen are either significantly stabilized (oxo lone pair) or higher in energy (Mo-O π* orbital). As the phosphine substrate approaches, we see a reduction in the bond order of the axial Mo-oxo moiety, with the Mo-O bond length increasing from 1.72 Å to 1.85 Å. The HOMO is observed to have an orbital contribution in the forming O-P σ-bond, whose bond distance is 2.06 Å, representing a bond order much lower than that in the product ternary complex **1B** and the free phosphine oxide.

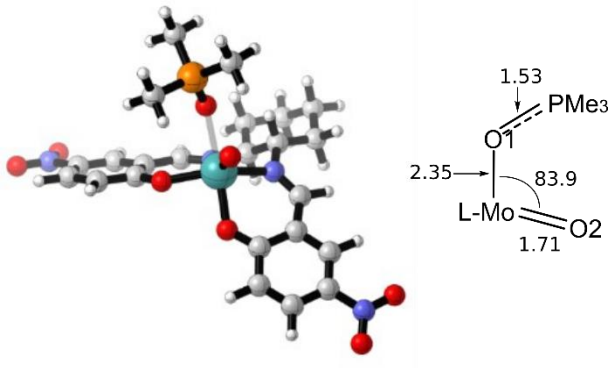

Figure 3-10. Ternary complex **1B**, with Mo-ligated $OPMe_3$

The energetic driving force of the oxygen atom transfer reaction is the formation of the ternary complex **1B** (Figure 3-10), 27.6 kcal/mol downhill from the starting materials. The P-O bond order has increased to nearly the full double bond (1.53 Å) of the free phosphine oxide (1.50 Å), while the Mo-O bond has reduced to a weak dative bond (2.35 Å). The molybdenum complex has begun reorganizing to the square pyramidal coordination environment of the monooxo complex **1C**, with the dissociation of the phosphine oxide allowing the O-Mo-O angle to decrease to 83.9°.

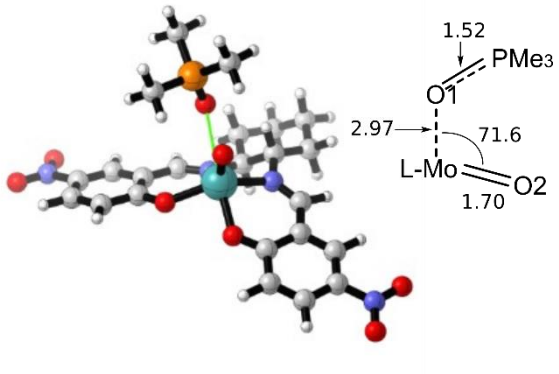

Figure 3-11. $\mathbf{TS_{B\text{-}C}}$, dissociation of $OPMe_3$ from ternary complex **1B**

As the phosphine oxide dissociates from the metal center (Figure 3-11, $\Delta G^{\ddagger} = 6.7$ kcal/mol), the complex continues to reorganize to square pyramidal **1C** (Figure 3-12), with the Mo-O bond nearly cleaved at 2.97 Å. The P-O bond continues to increase as the back-bonding contribution from the molybdenum center decreases. The weak back-bonding interaction between the metal center and product leads to the P-O bond remaining slightly lengthened compared to the free phosphine oxide.

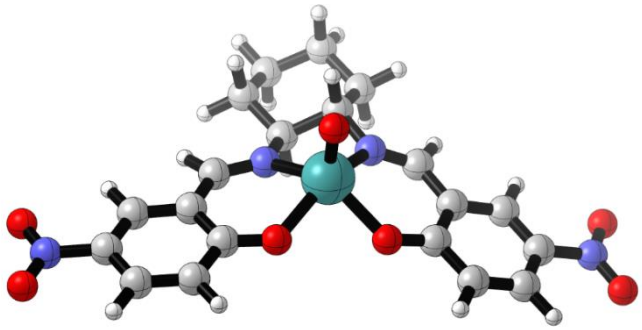

Figure 3-12. Monooxo molybdenum^{IV} complex **1C**

Following dissociation of the product phosphine oxide, reorganization of the coordinated salen ligand has completed, and the bond order for the remaining Mo-oxo moiety has increased, with the bond length contracting to 1.69 Å (from 1.72 Å in the dioxo species). The molybdenum (IV) monooxo complex and product phosphine oxide are stabilized by 27.3 kcal/mol versus the reactant dioxomolybdenum and trimethylphosphine, and nearly thermoneutral (+0.3 kcal/mol) with the ternary complex. The triplet state is predicted not to be involved in the catalytic pathway, as it is destabilized by 11.3 kcal/mol versus the singlet.

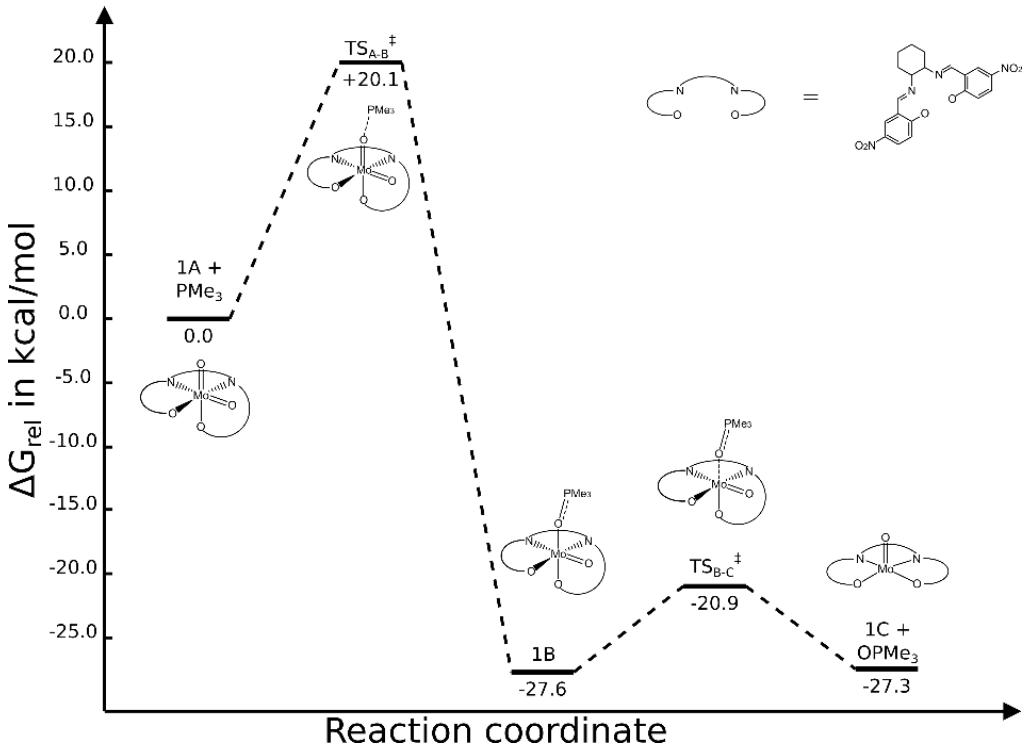

Figure 3-13: reaction profile for OAT from complex **1** to trimethylphosphine

The reaction profile for oxidation of trimethyl phosphine (Figure 3-13) is very similar to the profile determined for the phosphine oxidation of PMePh^{t}Bu (Ch 1). We see that the activation energy for the oxygen atom transfer step is slightly lower (PMePh^{t}Bu: +22.9 kcal/mol) due to the decrease in steric interactions and increased nucleophilicity of the smaller trimethyl phosphine modeled in this profile. The ternary complex, dissociative transition state, and products all have relative energies nearly identical to the PMePh^{t}Bu derivative once adjusted for the difference in activation energy for the OAT step. The formation of the strong P-O bond is once again found to be the driving force of the reaction.

3.3.2 Coordination of triplet dioxygen ($^3O_2$) by monooxo Mo(IV) complex

The coordination of dioxygen to molybdenum centers has been reasonably well described in the literature [3,13,14,21], but the mechanism of dioxygen coordination and reactivity to OAT of the resulting oxoperoxo molybdenum (VI) has not been explored *via* detailed computational study. Based on the experimental results presented in section 3.2, the reoxidation of the complex

to a molybdenum (VI) oxoperoxo species is presumed to occur in a single-centered process (Scheme 3-5), analogous to the coordination of dioxygen to a ruthenium center examined by Yu, et al. [37], rather than a biomolecular process, as in the Mars-Van Krevelen mechanism, bis-metallic, or other disproportionation processes. [13,21,43]

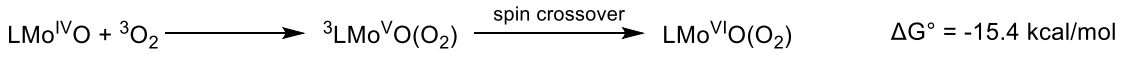

Scheme 3-5. Reoxidation of **1C** by dioxygen

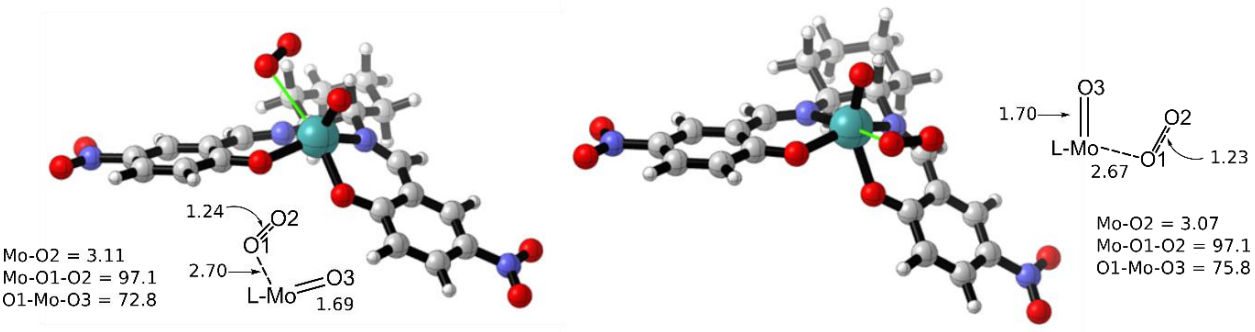

Figure 3-14: Calculated structures for ligation of dioxygen, **$TS_{C\text{-}D\ ax}$** (left) and **$TS_{C\text{-}D\ eq}$** (right)

Reoxidation of the metal complex is shown to begin with an interaction of triplet dioxygen ($^3O_2$) with the ground state singlet molybdenum (IV) species. Two possible coordinative approaches were considered, with the equatorial approach being preferred ($\Delta G^{\ddagger}$ = 5.8 kcal/mol) versus the axial ($\Delta G^{\ddagger}$ = 7.1 kcal/mol). The structures for these transition states (Figure 3-14) were located by scanning the distance between the molybdenum center and the O-O bond centroid, starting from the superoxo complexes ^{3}1D (Figure 3-16). The ligand is seen to begin reorganizing to an octahedral geometry as the dioxygen molecule approaches the metal center, which is accompanied by a reduction of the O-O bond order (O-O bond length increases from 1.21 Å to 1.23 Å), representing a contribution to the side-on bonding interaction of the metal $d_{x^2-y^2}$ orbital with the dioxygen π* orbital. This interaction is observed in the HOMO-2 orbital, which is the highest energy doubly occupied molecular orbital, while the SOMO orbitals are the dioxygen π* (HOMO-1) and a delocalized molecular orbital with mostly ligand character (HOMO).

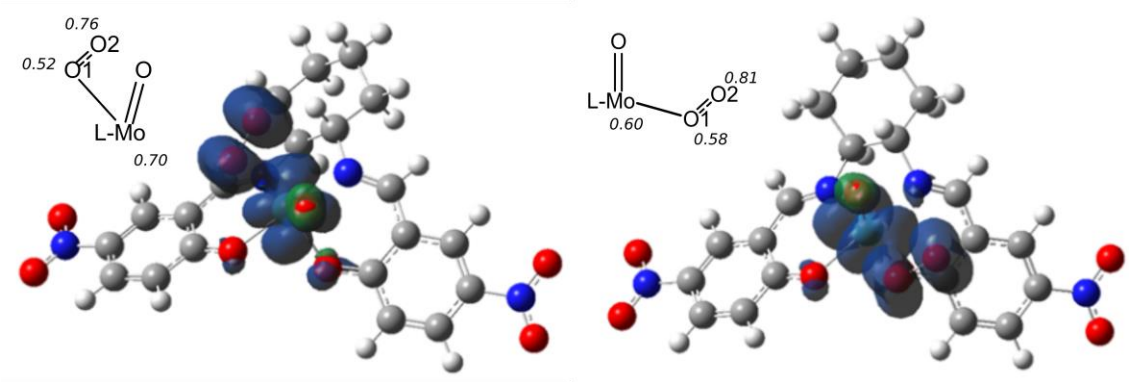

Figure 3-15. Spin density surfaces for $TS_{C\text{-}D\ ax}$ (left) and $TS_{C\text{-}D\ eq}$ (right). Labels in italics are spin densities.

Each of the approaches results in a triplet species, with the activation barrier for the equatorial approach 1.3 kcal/mol lower than the axial. The dioxygen moiety has a diradical character in this transition state (Figure 3-15), with spin density largely concentrated in the occupied orbitals with dioxygen π* character (SOMO 2), showing this transition state to maintain the spin state of unbound triplet dioxygen with a minor delocalization of radical character over the forming O-Mo bond.

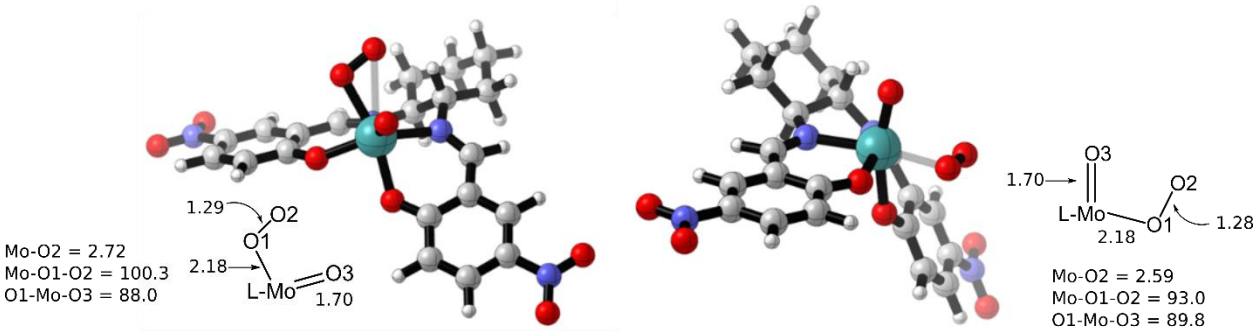

Figure 3-16: calculated structures for ^{3}1D$_{ax}$ (left) and ^{3}1D$_{eq}$ (right)

Following the associative transition state, a stable structure for the triplet oxo-superoxo species is located for both coordination isomers (Figure 3-16, ΔG_{ax} = -4.5 kcal/mol. ΔG_{eq} = -4.6 kcal/mol). Bonding to the metal center leads to a small increase in the O-O bond length, and the Mo-O1 bond is observed in the SOMO orbitals as interactions between the d_{yz} orbital (axial) and d_{xz} orbital (equatorial). η^2-bonding interactions are observed in the HOMO-2 doubly occupied orbital, involving alignment between the molybdenum d-orbitals (d_{xz} axial, $d_{x^2-y^2}$ equatorial)

and the dioxygen π* orbital. The spin densities for the superoxo complex (Figure 3-17) indicate that coordination of dioxygen has led to a partially oxidized metal species (formally Mo^{V}), with spin densities concentrated on Mo and O2, though the molybdenum radical remains delocalized through the bond with O1.

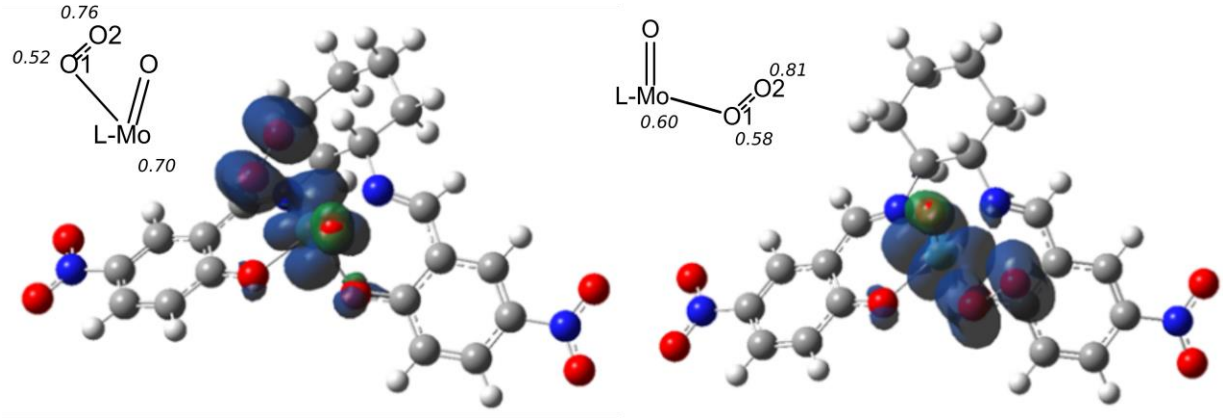

Figure 3-17. Spin density maps for $^{3}1D_{ax}$ (left) and $^{3}1D_{eq}$ (right). Labels in italics are spin densities.

The next step in the reoxidation process involves a spin-crossover process. Spin crossover events occur when a reaction proceeds across more than one potential energy surface, [44] in this case a triplet surface and a singlet surface. The minimum energy crossing point (MECP) is the lowest energy point along the intersection of the two involved potential energy surfaces, and can be located using gradient-based optimizations, for which we employed the sobMECP algorithm. [45] MECPs were calculated by Chance Lander and were located from either reactant/product pairs or points from the internal reaction coordinate calculations.

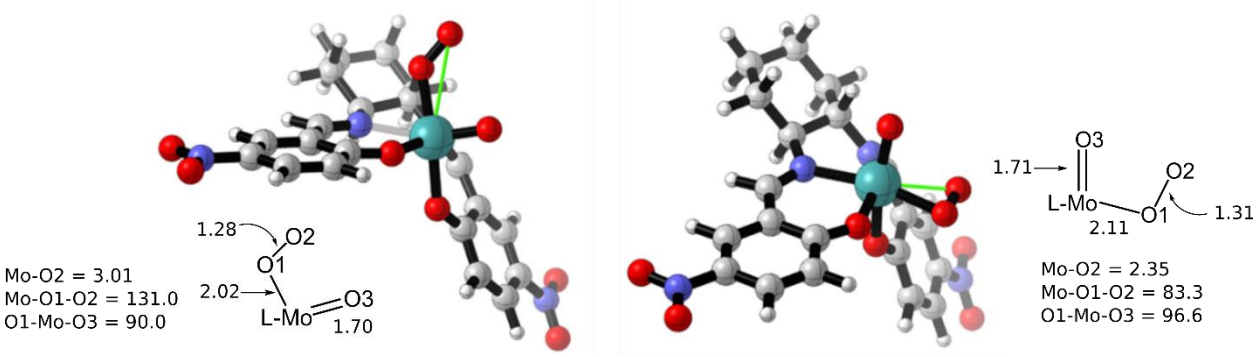

Figure 3-18. Calculated structures for oxo-superoxo triplet to singlet oxoperoxo MECP 1D (axial, left; equatorial, right)

The calculated structures for the triplet-to-singlet MECP in the dioxygen coordination process (Figure 3-18) display some notable differences between the axial and equatorial coordination isomers. While the overall coordination spheres are very similar, the coordination mode of the dioxygen moieties are inequivalent. The equatorial coordination isomer shows an increase in symmetry of the coordination, displaying significantly more η^2-like binding (Mo-O1 = 2.11 Å, Mo-O2 = 2.35 Å, Mo-O1-O2 = 83.3°) and a related decrease in O-O bond order, with the O-O bond length increasing to 1.31 Å. Meanwhile, the Mo-O distances for the axial coordination isomer display a decrease in symmetry, making the binding mode of the dioxygen unit more end-bound in character (Mo-O1 = 2.02 Å, Mo-O2 = 3.01 Å, Mo-O1-O2 = 131°) and resulting in a slight increase in bond order, from 1.29 Å to 1.28 Å. The activation barrier to this crossover is also quite different between the two isomers, with $\Delta G^{\ddagger}$ for the equatorial peroxo only 0.1 kcal/mol and $\Delta G\ddagger$ for the axial +6.2 kcal/mol. This difference in activation energies may indicate that the dioxygen coordination process contains two triplet minima, as observed by Yu et al. [37], for which our study located the first, less symmetric species for the axial approach and the second, higher symmetry species for the equatorial approach, and the difference in energy of activation arises from the increased distance on the energy surface from the crossing point.

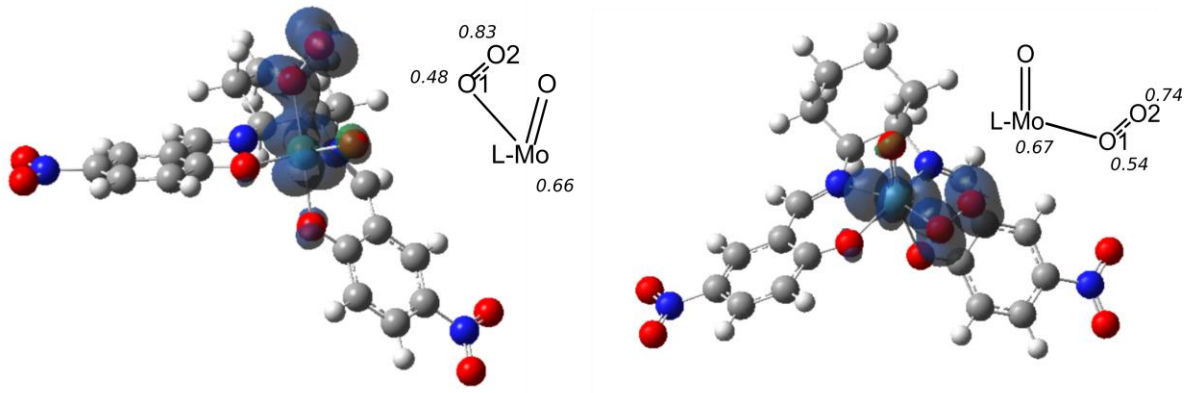

Figure 3-19. Spin density surfaces for triplet-calculated MECP 1D. Atomic spin densities are labeled in italics.

Spin densities for the MECP were calculated for the triplet spin state (Figure 3-19). The change in atomic spin density from the superoxo complex is consistent with the differences in symmetry between the two isomers, with the axial dioxygen moiety showing a greater free

radical character on O2 than the triplet and the equatorial showing a decrease in free radical character. Both isomers demonstrate a delocalization of an unpaired electron between the Mo center and O1, presumably through the Mo-O σ-bonding interaction.

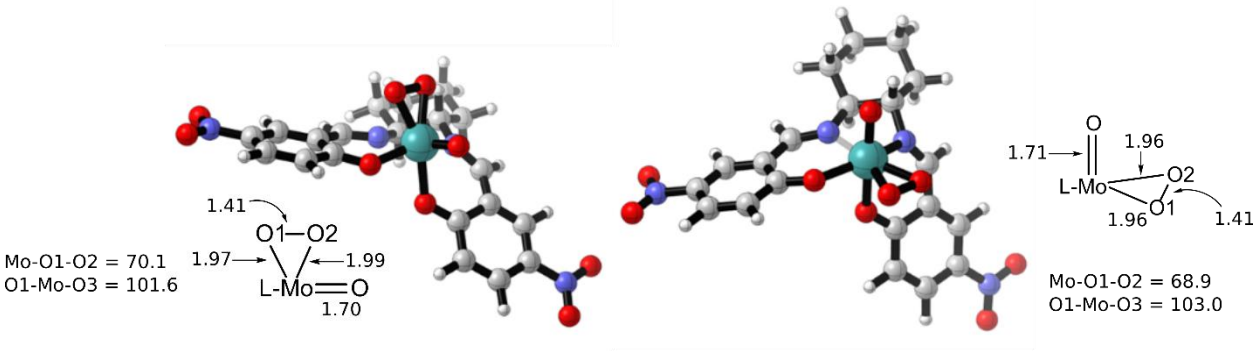

Figure 3-20. Singlet oxoperoxo Mo(VI) complexes $1D_{ax}$ and $1D_{eq}$

The singlet oxoperoxo species (Figure 3-20) is stabilized relative to MECP 1D by 24.1 kcal/mol for the axial species and 19.2 kcal/mol for the equatorial. Each species shows the expected symmetrically bound η^2-dioxygen moiety, and the side-on binding mode leads to significant decrease in the O-O bond order. Interestingly, the O-Mo-(O_2) bond angles are nearly equivalent to the O-Mo-O bond angle in the dioxo species.

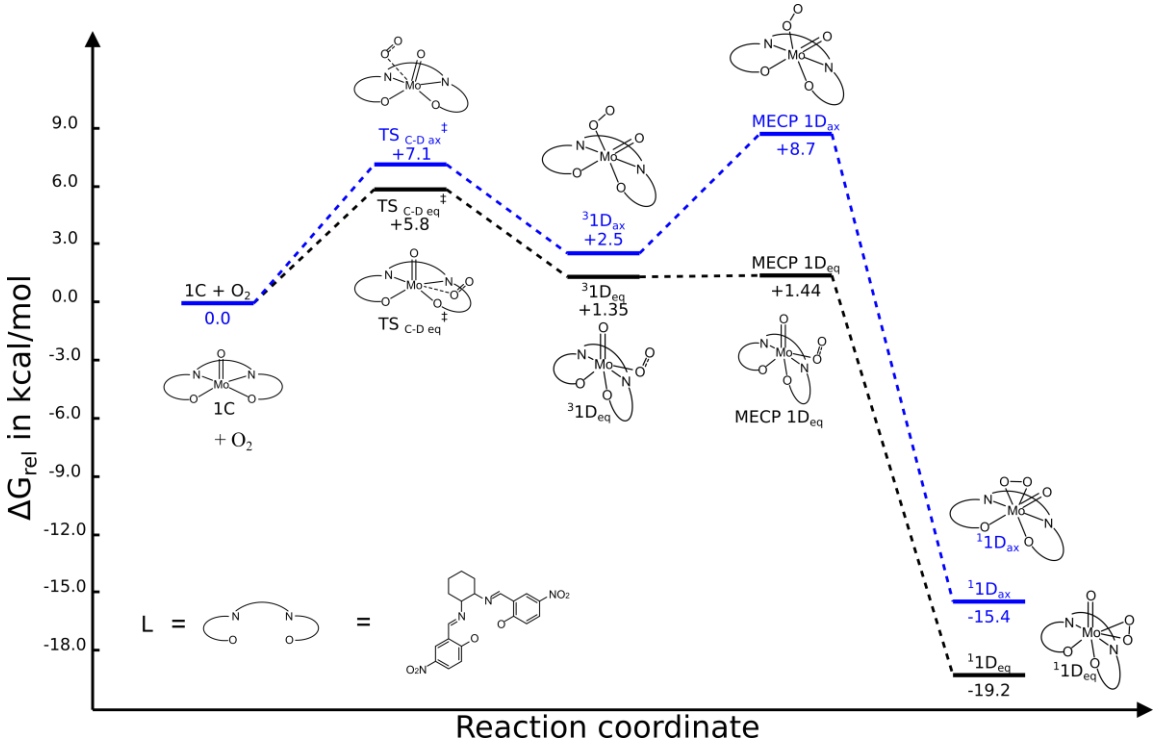

Figure 3-21: Reaction profile for dioxygen activation by monooxo Mo(IV) complex **1C**

The reaction profile for coordination of dioxygen to the molybdenum (IV) complex 1C (Figure 3-21) is shown to be overall exergonic, with the formation of the singlet, η^2-peroxo species ^{1}1D serving as the driving force for the oxygen coordination steps. The located transition state for initial coordination of triplet dioxygen, $TS_{C\text{-}D}$, has a moderate energetic barrier, as does the spin-crossover step for the axial complex, MECP $1D_{ax}$. The triplet superoxo complexes, ^{3}1D, are moderately destabilized relative to the starting materials, but the modest (+8.7 kcal/mol) barrier for spin-crossover from the axial complex and near barrier-less (+0.09 kcal/mol) crossover from the equatorial complex indicates a facile conversion to the greatly stabilized singlet oxoperoxo molybdenum (VI) species ^{1}1D.

Computed structures resemble those studied for the comparable coordination of dioxygen to other metal complexes [37], however the overall energetics are quite different. None of the complexes studied by Yu, at al. exhibit the large exothermic step following the spin-crossover event to form the peroxo species, and all intermediate species (with the exception of the iridium complex) are found to be stabilized relative to the reactants. However, we do observe qualitative agreement between the two profiles, with similar structures for calculated triplet (superoxo) species and MECP structures, as well as similar activation energy for the MECP. Our study did not locate secondary stable triplet structures, nor any associated transition states, however, the difference between the structures of ^{3}1D_{ax} and ^{3}1D_{eq}, specifically the differences between the Mo-O2 bond lengths, may suggest that similar structures may be located. This difference may also account for the difference in $\Delta G^{\ddagger}$ for the axial and equatorial spin-crossover steps.

Within the context of the experimental results reported in Section 3.1.1, the low barrier for dioxygen coordination may provide some explanation for the rate effects observed with changing pO_2 (Figure 3-4). It is still possible that the overall rate of reoxidation for the molybdenum (IV) monooxo complex is limited by the concentration of dioxygen in the solvent, but the initial association of dioxygen to form the molybdenum (V) oxo-superoxo complex has a low reverse barrier (+4.4 kcal/mol), indicating that an equilibrium between the monooxo and oxo-superoxo species may precede the formation of the active molybdenum (VI) oxoperoxo complex.

3.3.3 Oxygen Atom Transfer from molybdenum oxo-dioxygen (peroxo) complexes

The next step of the catalytic cycle is presumed to be an oxygen atom transfer reaction involving either the triplet oxo-superoxo molybdenum (V) species, ^{3}**1D**, or the oxoperoxo molybdenum (VI) species, ^{1}**1D**. The superoxo and peroxo moieties are typically thought to be more reactive than an oxo moiety, [25] leading to the reaction shown in Scheme 3-6, with regeneration of the dioxomolybdenum catalyst by transfer of one of the dioxygen moiety oxygen atoms.

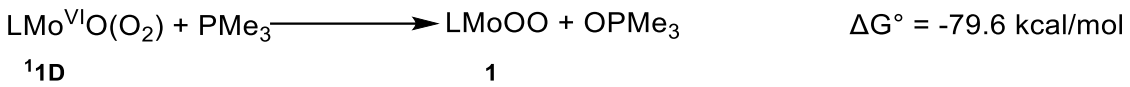

Scheme 3-6. Oxidation of trimethyl phosphine by Mo(VI) oxoperoxo complex

One of the common concerns with use of dioxygen as an oxygen source is the propensity for free radical reactions with either the superoxo complex or the dioxygen molecule itself [21]. For triphenylphosphine oxidation under our experimental conditions, auto-oxidation is of low concern. [46] However, studies with other metal-dioxygen systems have posited selective formation of the phosphine oxide from reaction with a metal-superoxide moiety, [42] so investigation of this possible pathway is necessary despite the oxo-superoxo species (^{3}**1D**) being more than 15 kcal/mol destabilized relative to the singlet oxoperoxo species ^{1}**1D**.

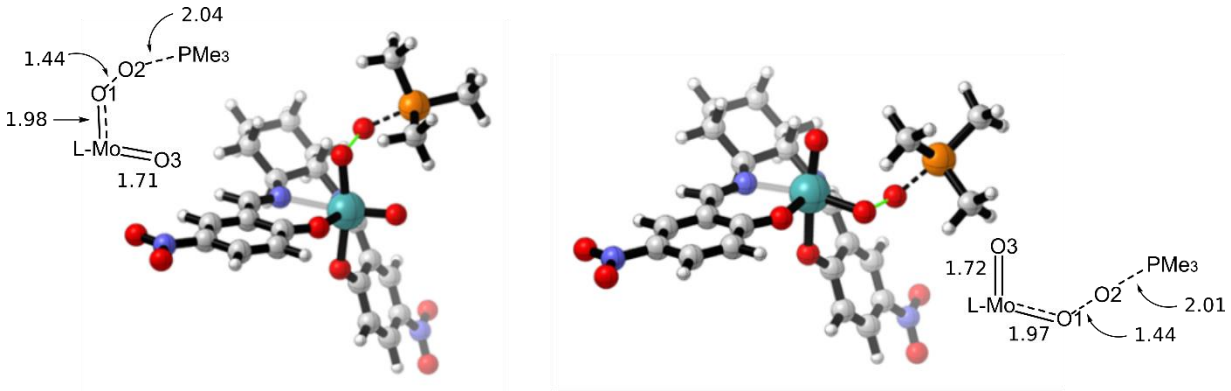

Figure 3-22. Oxygen atom transfer transition states for LMo(V)oxo-superoxo complexes $^{3}TS_{D\text{-}F\ ax}$ (left) and $^{3}TS_{D\text{-}F\ eq}$ (right)

Starting from the oxo-superoxo complex ^{3}1D (Figure 3-16), the oxygen atom transfer reaction is found to occur *via* a single transition state involving concerted formation of the O-P

bond and cleavage of the O-O bond (Figure 3-22). OAT from the equatorial superoxo group is seen to have a slightly higher free energy of activation (+16.0 kcal/mol) than the axial (+13.7 kcal/mol), though both activation barriers are smaller than that for OAT from the dioxomolybdenum complex **1A** (+20.1 kcal/mol), perhaps due the higher reactivities associated with radical reaction pathways. The forming O-P bond has similar character to that found for the oxo group OAT transition state (TS_{A-B}, O-P 2.06 Å), and the O-O bond length increases as the phosphorus lone pair electron density is added to the O-O π* antibonding orbital.

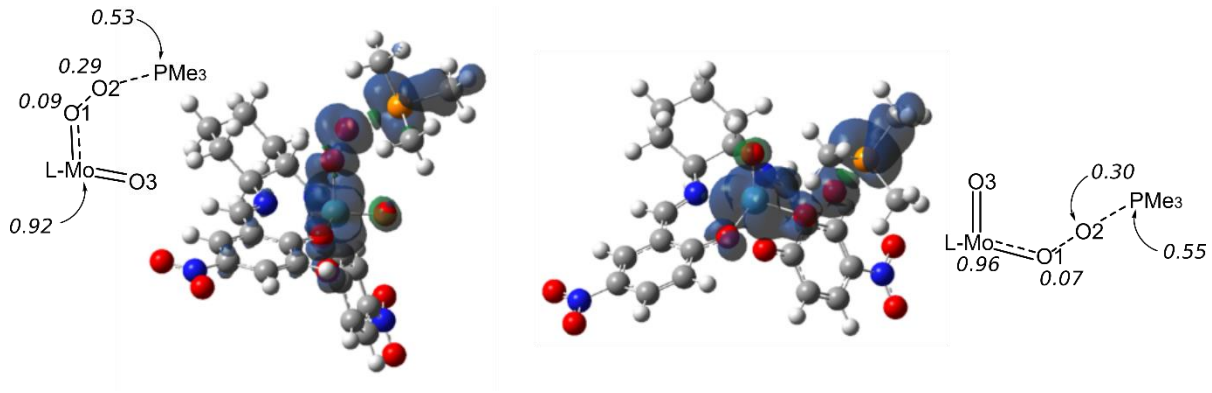

Figure 3-23. Spin densities for $^3TS_{D\text{-}F\ ax}$ (left) and $^3TS_{D\text{-}F\ eq}$ (right)

The atomic spin densities are noted to change significantly from the complex ^{3}1D following the phosphine attack on the superoxo oxygen (Figure 3-23). Spin density for the unpaired electron previously shared between Mo and O1 is now concentrated on the molybdenum center, while the superoxo spin character is shared between the oxygen and phosphorus atoms. Interestingly, the character of this shared unpaired electron is not present in the O-P σ-bonding interaction, which has a plane of opposite spin density along the forming axis, but is instead shared *via* π-bonding interactions, analogous to those observed for forming O-P bonds *via* oxo group transfer [47].

Further examination of atomic spin densities (given in Table 3-1), shows that the unpaired electron character in this oxygen atom transfer step is further delocalized over the P-C bond interacting with the oxygen SOMO *via* interaction of the oxygen orbital with the P-C σ* orbital.

Table 3-1. Spin density values for OAT-involved atoms

Atom	Spin densities	
O_{44}=Mo-$O_{51/45}$-O_{52}-P_{53}-C_{56}	Axial superoxo $TS_{D\text{-}G}$	Equatorial superoxo $TS_{D\text{-}G}$
Mo	0.9223	0.9581
O_{44}	-0.0453	-0.0453
M-O-	O_{51}: 0.0908	O_{45}: 0.0660
O_{52}	0.2891	0.2956
P_{53}	0.5298	0.5468
C_{56}	0.0865	0.1020

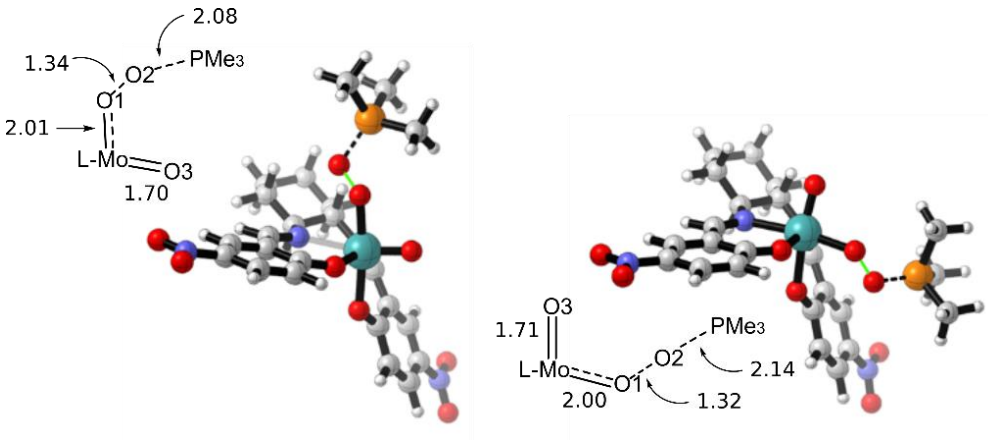

Figure 3-24. Geometries of singlet OAT transitions states for $^1TS_{D\text{-}A\ ax}$ (left) and $^1TS_{D\text{-}A\ eq}$ (right)

A second option for OAT from the $MoO(O_2)$salen complexes proceeds through the molybdenum (VI) oxoperoxo complex *via* transfer of an oxygen atom from the peroxo moiety (Figure 3-24). These singlet transition states ($\Delta G^{\ddagger}_{ax}$ = 34.0 kcal/mol, $\Delta G^{\ddagger}_{eq}$ = 35.2 kcal/mol) were located by a two-dimensional scan along the forming P-O bond and the dissociating O-O bond. As compared to the superoxo OAT step, this atom transfer occurs with a significant change in the coordination geometry of the peroxo group, with the Mo-O2 bond length increasing dramatically and leading to an η^1-end-on coordination of the dioxygen moiety. This change in hapticity of the peroxo group leads to an increase in the O-O bond character despite the formation of the O-P bond in this transition state. The forming O-P bond is reduced in bonding character relative to that of the transition state for the dioxo atom transfer transition state (**$TS_{A\text{-}B}$**, 2.06 Å) and the

superoxo atom transfer transition states (^{3}**TS$_{D\text{-}G}$**, 2.01 Å axial, 2.04 Å equatorial). Even taking the decreased bond character into consideration, this is a relatively late transition state, with concerted formation of the O-P bond and dissociation of the O-O bond resulting in product phosphine oxide and regenerated dioxomolybdenum (VI) complex (ΔG = -103.7 kcal/mol, Figure 3-32).

The imaginary frequencies for these OAT transition states show only O-P and O-O bond stretching and are absent of any Mo-O2 bonding character. This suggests that there may be a transition state for the cleavage of the Mo-O2 bond and a metastable η^1-peroxo intermediate prior to the transfer of the oxygen atom to the phosphine substrate. However, neither the Mo-O bond cleavage transition state nor the metastable intermediate has been located computationally.

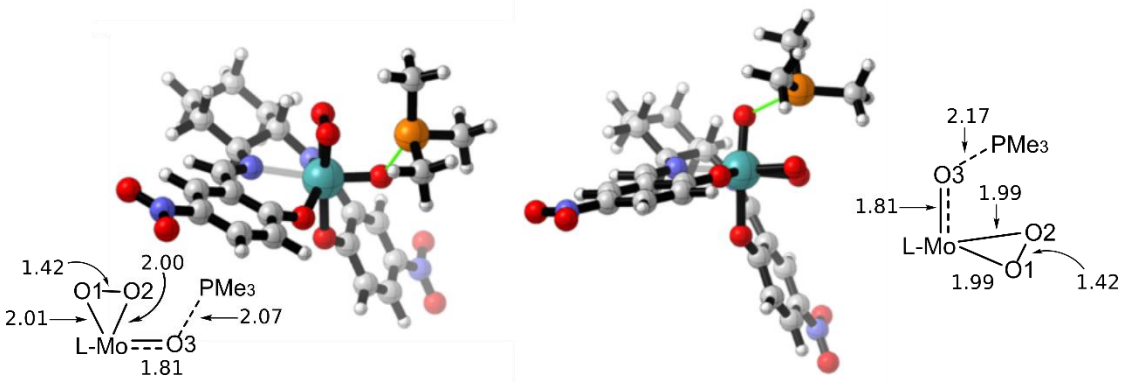

Figure 3-25. OAT transition state geometries for oxo moiety OAT TS$_{D\text{-}E}$

The final possible pathway for OAT from the oxoperoxo complex is for the oxygen atom of the oxo group to be transferred (Figure 3-25), in a process analogous to the transfer from the oxo moiety in the dioxo complex. Compared to the other studied OAT reactions, this is the earliest transition state, with increased bond order for the Mo=O and decreased P-O bonding character. Despite the earlier transition state, the $\Delta G^{\ddagger}$ for this OAT reaction (+20.2 kcal/mol axial oxo, +21.0 kcal/mol equatorial oxo) is nearly the same as for the dioxo OAT step (+20.1 kcal/mol axial). The transfer of electron density into the forming O-P bond additionally leads to an increase in the back-bonding interaction with the peroxo moiety, leading to a slight increase in the O-O bond distance.

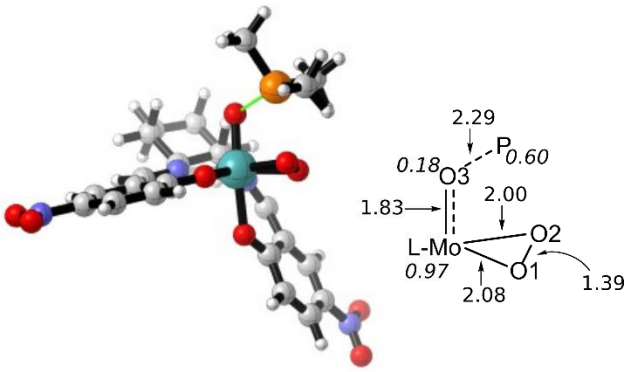

Figure 3-26. OAT transition state geometry for triplet-surface oxo moiety OAT $^{3}TS_{D\text{-}E}$. Atomic spin densities are labeled in italics.

The transition state for the triplet oxygen atom transfer from the axial oxo group was also located (Figure 3-26). The triplet oxygen atom transfer transition state is significantly higher in energy than the singlet and is 16.8 kcal/mol uphill from the triplet oxo-superoxo molybdenum (V) species that would ostensibly be the active complex for this atom transfer process. Consequently, there are significant differences between $^{1}TS_{D\text{-}E}$ and $^{3}TS_{D\text{-}E}$, and a few notable structural and electronic changes from ^{3}1D. The peroxo group has greater O-O bonding character in this triplet species than in the singlet OAT transition state but is also much more symmetrical than is observed for the superoxo moiety in ^{3}1D, instead bearing more resemblance to the peroxo moiety in the monoperoxo species ^{3}1G (Figure 3-30). This transition state is also seemingly more reactant-like than observed on the singlet profile, with a greatly increased O-P bond length. However, there is also a small increase in the length of the Mo-O bond for the transferred oxygen atom, though this may be attributed to the species having a molybdenum (V) oxyl character rather than the transferred atom behaving as an oxo group. This comparison is supported also by the atomic spin densities, which show that the radical character is again concentrated in the reacting Mo-O moiety, though for this pathway, that is apparently through the higher-energy oxyl structure rather than the superoxo structure shown in Figure 3-22.

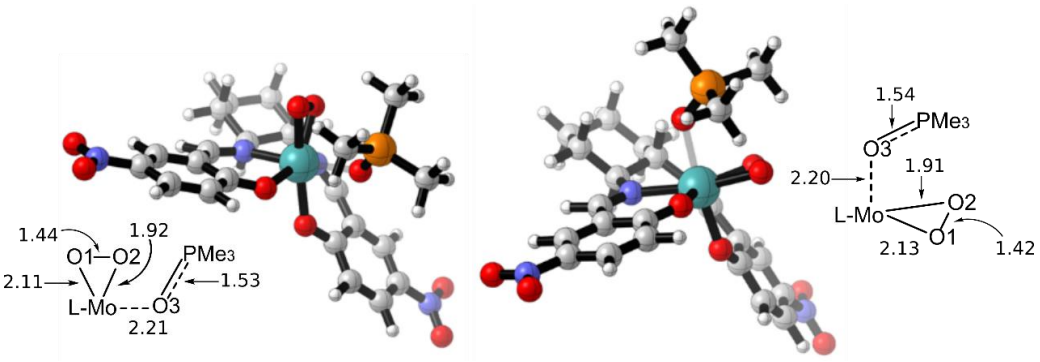

Figure 3-27. ternary complexes for singlet oxo moiety OAT, ^{1}1E$_{eq}$ (left) and ^{1}1E$_{ax}$ (right)

Unlike the superoxo and peroxo OAT reactions, oxygen atom transfer from the oxo group proceeds through a ternary complex (Figure 3-27, ΔG_{eq} = -39.3 kcal/mol, ΔG_{ax} = -38.9 kcal/mol). Similar to the transition state, the Mo-O bond for this complex is shorter than observed in the dioxo complex (2.35 Å), while the O-P bond is not affected much by the change in electronic character. The peroxo group begins to shift from the symmetric coordination observed in the oxoperoxo complex toward the distorted η^2-ligation present in the singlet monoperoxo complex **1G** (Figure 3-30).

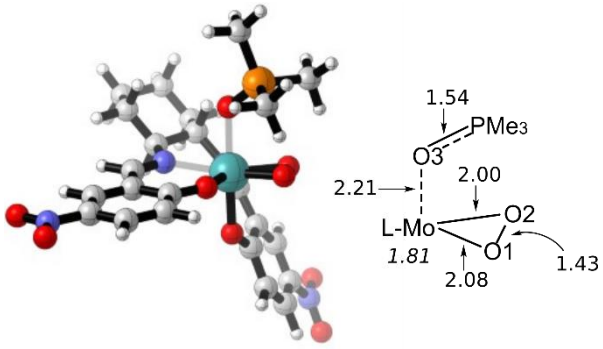

Figure 3-28. Ternary complex for triplet oxo moiety OAT, ^{3}1E$_{ax}$. Atomic spin densities are labeled in italics.

The ternary complex for the triplet surface (Figure 3-28) is stabilized by 11.0 kcal/mol compared to the singlet structure, indicating that there is possibly a spin-crossover event on the reaction profile between the atom-transfer transition state and the ternary complex (-67.3 kcal/mol). The structure of the MECP for this process has not been located, but one might expect to observe changes in the coordination of the peroxo group, as that moiety has the most pronounced differences in the transition state structures and ternary complexes. ^{3}1E$_{ax}$ shows

little difference in the geometry around the transferred oxo/oxyl group from $^{1}1E_{ax}$, but the peroxo group displays an increase in symmetry and back-bonding interaction with the metal, as indicated by the increase in the O-O bond length. Interestingly, the spin density of the triplet ternary complex is nearly entirely on the molybdenum center, indicating that the datively bound product molecule has little influence on the electronic configuration of the high spin monoperoxo complex $^{3}1G$.

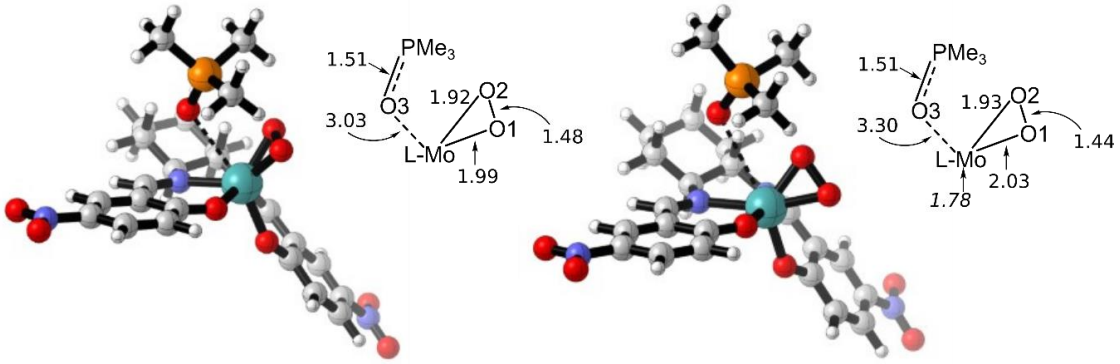

Figure 3-29. Dissociation of $OPMe_3$ from $^{1}1E_{ax}$, $^{1}TS_{E\text{-}G\ ax}$ (left) and from $^{3}1E_{ax}$, $^{3}TS_{E\text{-}G\ ax}$ (right). Atomic spin densities are labeled in italics.

The release of phosphine oxide from the ternary complex was studied for the favored transfer of an oxygen atom from the axial oxo group (Figure 3-29, singlet $\Delta G^{\ddagger}$ = 16.8 kcal/mol, triplet $\Delta G^{\ddagger}$ = 22.7 kcal/mol). The changes in geometry for the complex as the product molecule dissociates are quite similar to those observed for $TS_{B\text{-}C}$, with the peroxo ligand shifting toward the axial position and the axially ligated salicylimine ligand unit relaxing toward a square pyramidal geometry. The reduction of the molybdenum center leads to increased back-bonding from the metal to the peroxo unit and a significant increase in the O-O bond length for the singlet species (1.47 Å), and a small increase in the triplet species. The peroxo moiety is also observed to have decreased symmetry in the triplet species, perhaps due to differences in orbital alignment based on the different orientation of the peroxo moiety. The spin density of the triplet complex is again concentrated on the molybdenum (IV) center, with little contribution from ligand atomic spin densities.

Dissociation of phosphine oxide from the molybdenum center yields a distorted square pyramidal monoperoxo molybdenum (IV) complex (Figure 3-30, singlet ΔG=-3.2 kcal/mol, triplet ΔG=-7.5 kcal/mol). These complexes have reduced symmetry compared to the monooxo

molybdenum (IV) complex **1C**, with the ligand not quite achieving the planar coordination observed in **1C**, perhaps due to the increased coordinative space occupied by the peroxo group. The bonding character of the peroxo unit increases again as its alignment with occupied metal orbitals decreases.

Examination of the triplet spin state for the monoperoxo species reveals that it is stabilized relative to the singlet by 8.8 kcal/mol. The triplet species (Figure 3-30) further assumes the square pyramidal coordination observed in **1C**. The peroxo group is less tightly bound than the oxoperoxo species ^{1}**1D**, with a more symmetrical μ^2-coordination mode as compared to the singlet species.

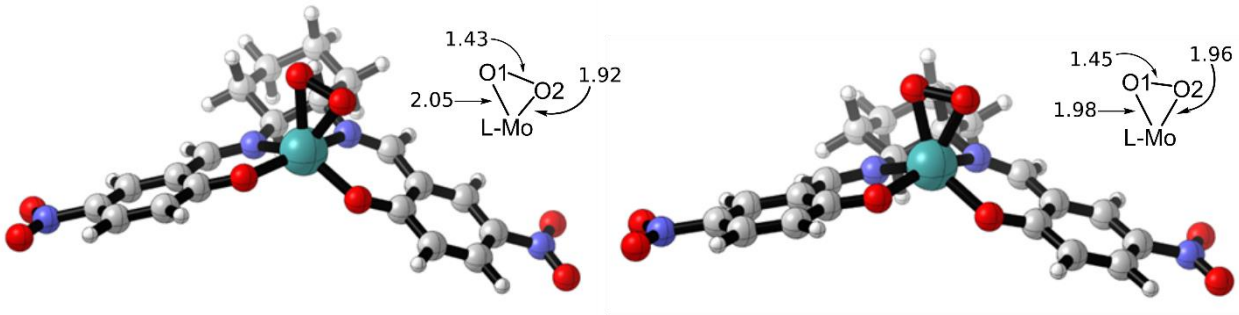

Figure 3-30. B3LYP-optimized structures of the singlet (left) and triplet (right) monoperoxo Mo (IV) complex **1G**.

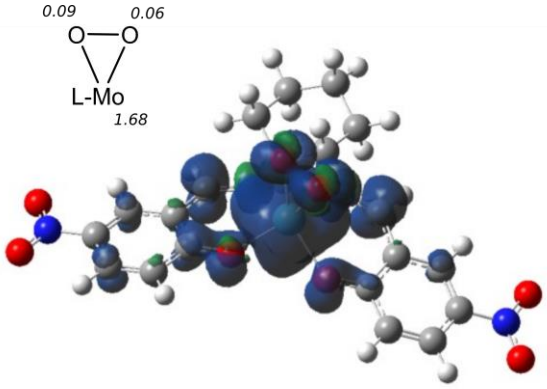

Figure 3-31. Spin density on the triplet monoperoxo **1G**. surface at density = 0.0009

Radical character in the triplet monoperoxo is concentrated on the molybdenum center (Figure 3-31, spin density = 1.68). Among the ligated O atoms, the axially oriented atom of the peroxo group has the highest spin density (0.09), while the other oxygen in the peroxo group has a spin density of 0.06, comparable to the imine carbons and the more z-oriented salicylimine phenol.

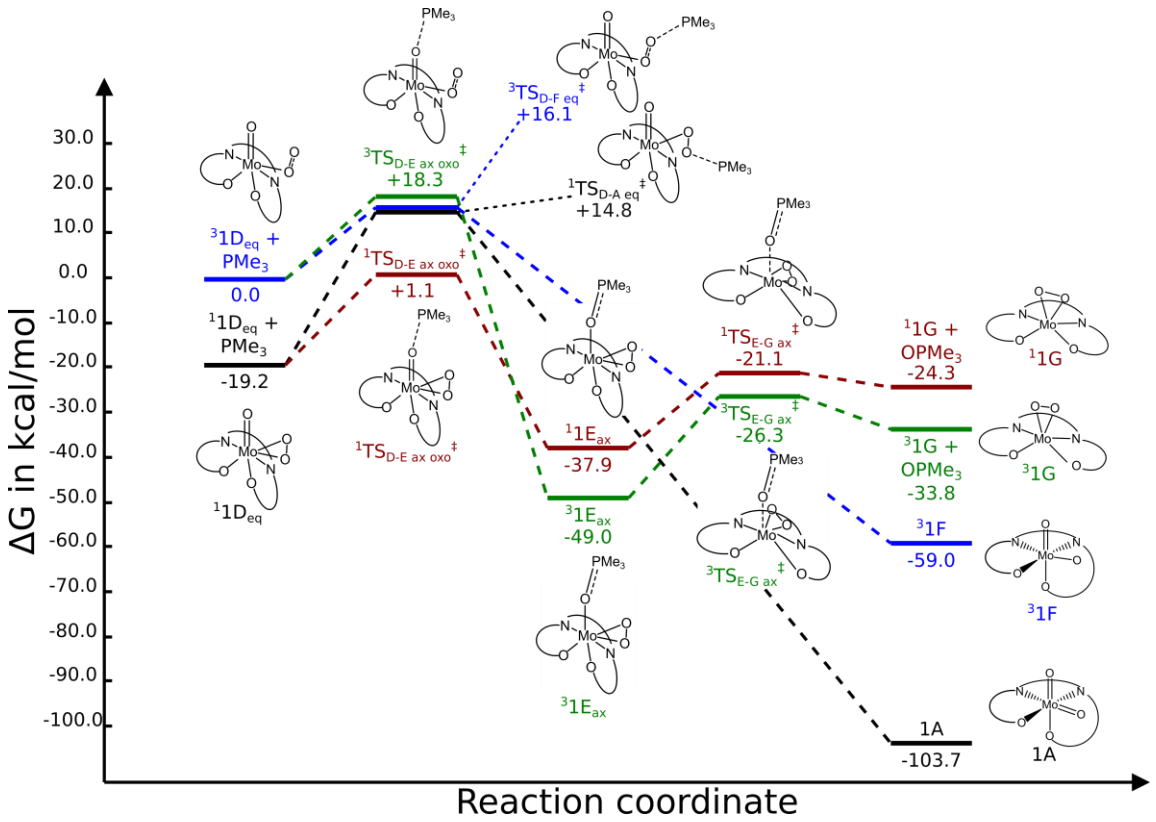

Figure 3-32. Relative reaction pathways for OAT from superoxo (blue), peroxo (black), oxoperoxo oxo (dark red), and oxosuperoxo oxo (green) groups. Free energies are relative to the starting materials for the superoxo OAT pathway.

For each of the possible pathways for OAT (Figure 3-32), the axial and equatorial coordination isomers have very similar activation barriers (superoxo $\Delta\Delta G^{‡}$ = 0.75 kcal/mol, peroxo $\Delta\Delta G^{‡}$ = 1.1 kcal/mol, oxo $\Delta\Delta G^{‡}$ = 0.8 kcal/mol). The lowest energy barriers are for OAT from the superoxo species **^{3}1D**, both for transfer of an oxygen atom from the superoxo moiety (+16.1 kcal/mol) and from the oxyl moiety (+18.3 kcal/mol), but the OAT steps have a much higher free energy barrier than the spin crossover from the superoxo to peroxo complex (MECP 1D$_{ax}$: +8.7 kcal/mol, MECP 1D$_{eq}$: +1.44 kcal/mol), suggesting that the oxygen atom transfer step occurs by reaction with the oxoperoxo Mo(VI) complex **^{1}1D** rather than the superoxo Mo(V) complex **^{3}1D**. Between the peroxo- and oxo-group transfer pathways, atom transfer from the oxo-group is, unexpectedly, the more favorable pathway, with an activation barrier 13.7 kcal/mol lower than atom transfer from the peroxo group. The peroxo groups are typically considered to be a more reactive moiety for OAT reactions, [3,25] but for this phosphine oxidation, it appears

that the electron demand favors OAT from the oxo group over OAT from the peroxo group, an observation that may be in line with previous reactivity studies. [2,38]

3.3.4 Regeneration of LMo(VI)dioxo complex from LMoO(O_2) OAT products

The favorability of the oxo-group transfer from the oxoperoxo complex leads to the consideration of an unexpected reaction process—the splitting of the peroxo group to regenerate the dioxomolybdenum (VI) complex, completing the catalytic cycle. A similar process has been examined by the Nicholas lab in recent years (Herndon, Lander, Shao, Nicholas, unpublished work), which has revealed a stepwise process involving multiple spin-crossover events involved in the conversion of the molybdenum-bound peroxo unit into a cis-dioxo moiety.

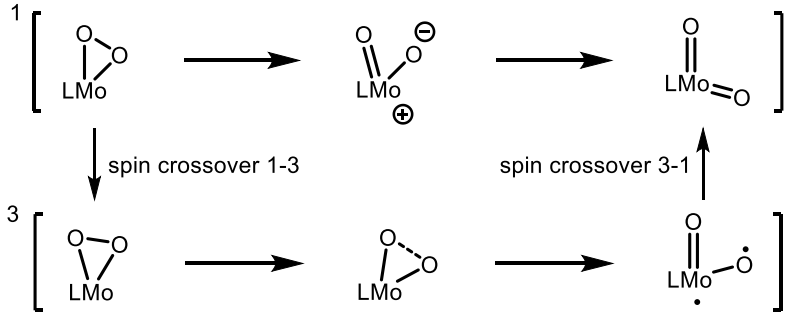

Scheme 3-7. (top) Singlet reaction surface for regeneration of LMo(VI)O_2
(bottom) Triplet pathway for regeneration of Mo(VI)O_2

To explore the full profile (Scheme 3-7) for regeneration of the dioxo complex from the monoperoxo species, both singlet and triplet surfaces need to be modeled. The porphyrin molybdenum peroxo splitting process examined by Herndon, et al. suggest that the singlet surface for peroxo cleavage proceeds *via* an oxo-oxyl transition state (Scheme 3-7, top middle), while the triplet transition state (Scheme 3-7, bottom middle) has not been located.

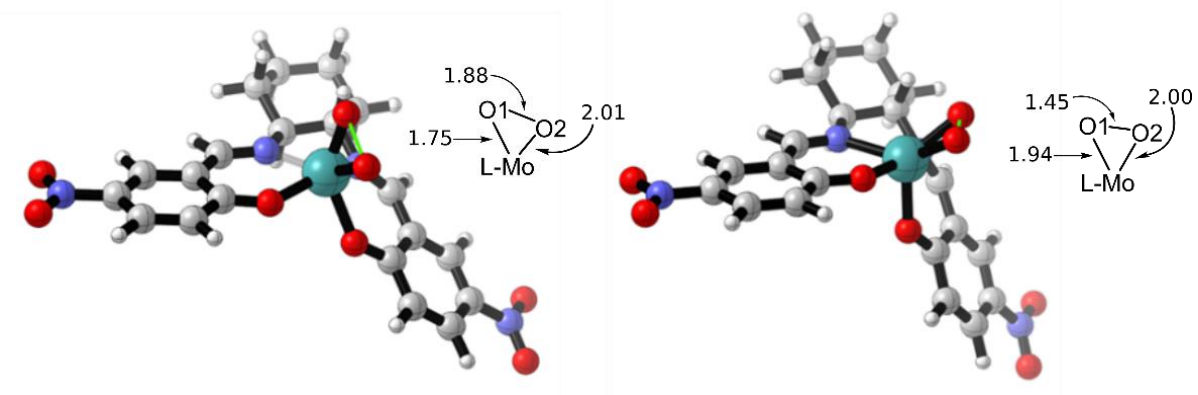

Figure 3-33. Peroxo splitting transition states $^{1}TS_{G\text{-}A}$ (left) and $^{3}TS_{G\text{-}F}$ (right)

Transition states for peroxo splitting by the salen-molybdenum complex (Figure 3-33) were located by scanning along the dissociating O-O bond on the singlet surface, then optimizing to a Berny transition state for both singlet and triplet spin states. $^{1}TS_{G\text{-}A}$ exhibits a pronounced difference in Mulliken charges between the peroxo group atoms, with the axial oxygen atom δ+ and essentially a moly-oxo moiety (Mo-O 1.75 Å, only slightly longer than in the dioxomolybdenum(VI) species, 1.72 Å) while the oxygen approaching the equatorial position carries a significant δ- charge and has a Mo-O bond length of 2.01 Å. This singlet transition state exhibits a solvent stabilization effect ($\Delta E^{\ddagger}$ = 17.5 kcal/mol, $\Delta G^{\ddagger}$ = 10.5 kcal/mol), which is explained by the difference in Mulliken atomic charges between the oxo groups. This difference, along with the difference in Mo-O bond lengths suggests the development of an oxo-oxido structure as the O-Mo-O bond angle increases to 60°, with the O-O bond length having much lower bonding character than the singlet monoperoxo (O-O bond length 1.88 Å).

The triplet transition state $^{3}TS_{G\text{-}F}$, like the singlet transition state, has the bis-salicylimine ligand adopting the geometry seen in the octahedral dioxo complex. The peroxo group, however, occupies a position between axial and equatorial, splitting the difference between the two planes of the ligand salicylimine rings. Interestingly, and unlike the singlet transition state, the imaginary frequency displays a “rocking” motion, where the outer O atom pivots around the mostly stationary inner O atom. The triplet transition state does not exhibit the polarization of oxo groups or difference in Mo-O bond lengths observed in the singlet transition state, indicating that this transition state maintains peroxo character rather than oxo-oxyl. As the $\Delta G^{\ddagger}$ for this triplet

step (+6.0 kcal/mol) is lower than that for the singlet profile and the triplet monoperoxo is stabilized relative to the singlet, the spin crossover step becomes a process of interest.

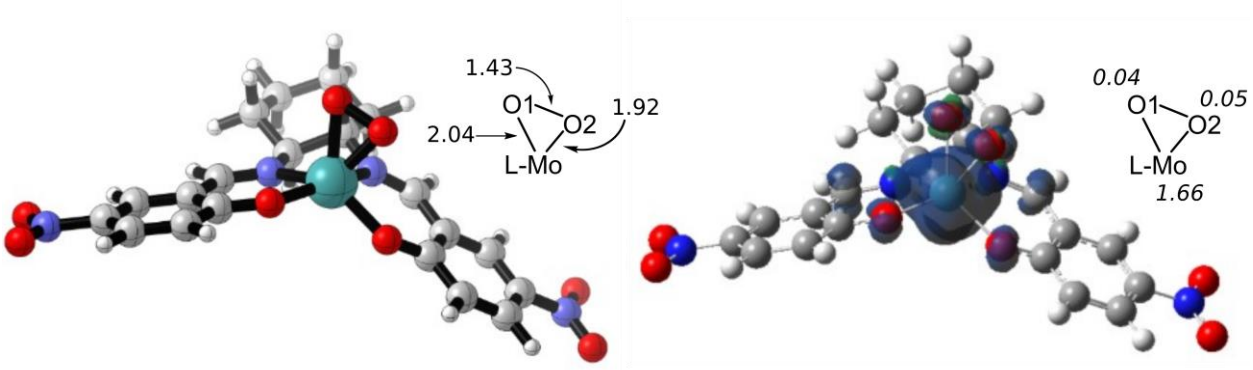

Figure 3-34. Monoperoxo singlet-triplet MECP 1F. Atomic spin densities are labeled in italics.

The minimum energy crossing point for spin-crossover between singlet and triplet monoperoxo species (Figure 3-34) has a $\Delta G^{\ddagger}$ of only 1.2 kcal/mol from the singlet monoperoxo and is strikingly similar to the singlet species. The peroxo group exhibits a slight decrease in O-O bond character which does not have significant associated change in the Mo-O bond lengths. As in the triplet monoperoxo, the atomic spin density is concentrated on the molybdenum center, representing the spin-unpaired Mo (IV) oxidation state.

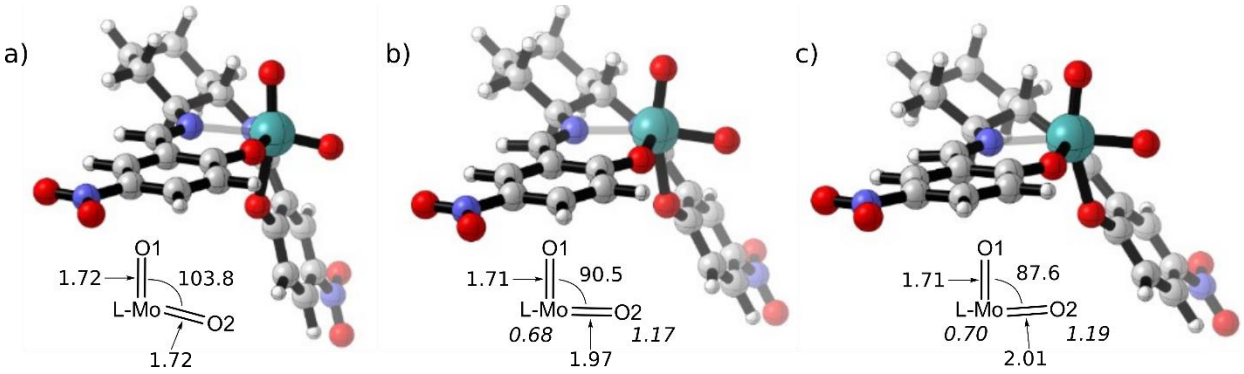

Figure 3-35: Computed structures of MoO_2sal-CHXD singlet 1A (a), triplet 1F (b), and MECP (c). Atomic spin densities for 1F and the MECP are given in italics.

To reform the singlet dioxo complex (Figure 3-35a) and complete the catalytic cycle, there needs to be another spin crossover event, occurring either between the triplet Mo^{V} oxo-oxyl complex (Figure 3-35b) and the singlet dioxo or between the peroxo cleavage transition state ($^{3}TS_{G\text{-}F}$, Figure 3-33) and the singlet dioxo. The structural parameters of this MECP (Figure 3-35c)

indicate that it is at an earlier reaction coordinate than the triplet oxo-oxyl complex, making it likely that the crossover event occurs prior to the formation of the triplet oxo-oxyl species.

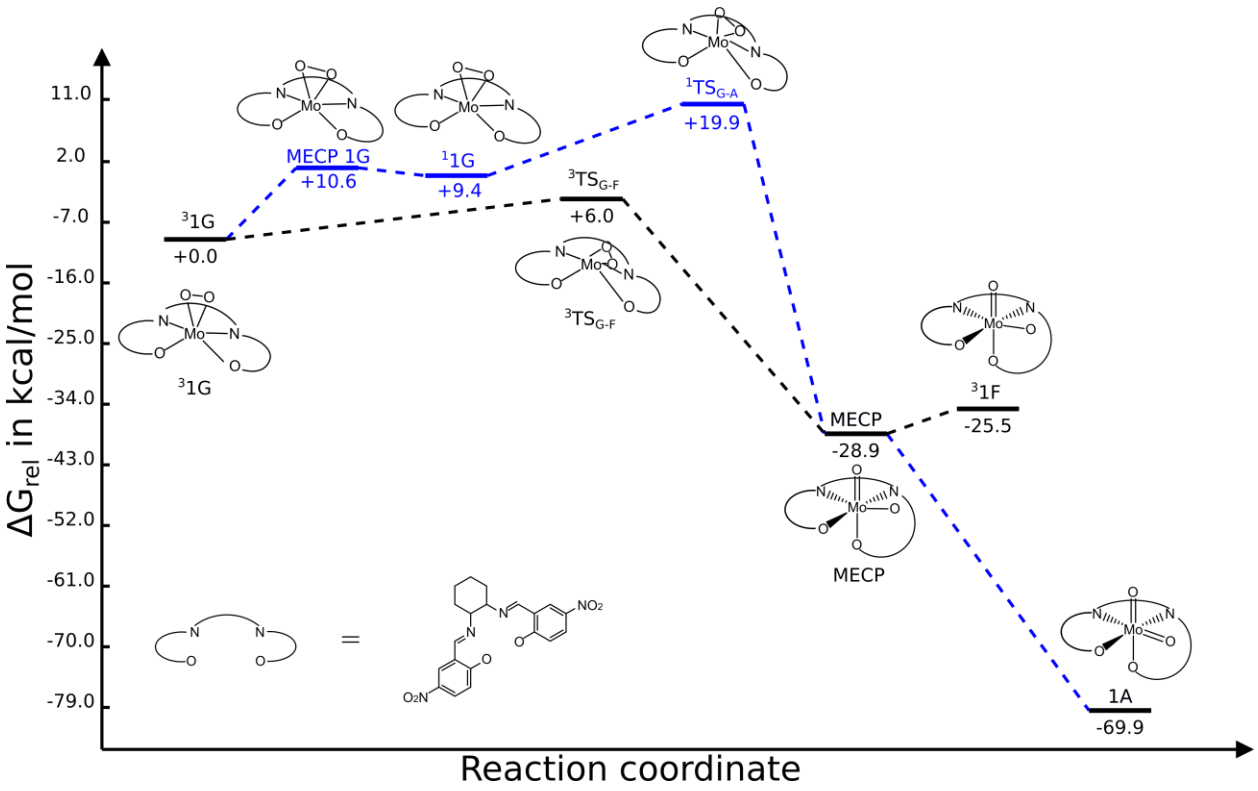

Figure 3-36. Reaction profile for peroxo splitting reaction

The higher activation energy for the spin crossover step between singlet and triplet peroxo complexes as compared to the triplet peroxo splitting step ($\Delta G^{\ddagger}$ = +10.6 kcal/mol vs $\Delta G^{\ddagger}$ = +6.0 kcal/mol) suggests that the triplet reaction profile is dominant in the splitting of the peroxo group to the dioxo species (Figure 3-36). The triplet transition state for cleavage of the peroxo group, ^{3}**TS$_{G\text{-}F}$**, is at an earlier reaction coordinate than the singlet transition state ^{1}**TS$_{G\text{-}A}$**, with greater peroxo character present in the dioxo moiety, while the singlet transition state is more indicative of an oxo-oxyl structure. While the spin crossover structure (**MECP$_{G\text{-}A}$**) is shown on the free energy diagram to be stabilized relative to the triplet oxo-oxyl ^{3}**1F**, this is due to the sobMECP optimization algorithm working based on electronic energies rather than free energies, which can result in a change in apparent energetic ordering of species when calculated free energy corrections are added. The reformation of the dioxo species **1A** and relaxation of the triplet to singlet dioxo are the thermodynamic driving forces for this step. While many oxo-metal systems

reoxidized by dioxygen undergo a two-centered Mars-Van Krevelen type reoxidation, leading to one atom of oxygen added to each participating metal center, [48] there are also several experimentally reported and computationally suggested systems for which dioxygen cleavage occurs at a single metal center. Monometallic peroxo-group splitting has been considered for both chromium [49] and molybdenum complexes [50,51], and photochemical dioxygen evolution has been studied for the permanganate ion. [52] The cleavage of the peroxo group to two oxo groups on a single center is a spin-forbidden process, but spin-crossover processes may be favorable enough to counterbalance the spin-conservation "rules" often invoked to rule out spin-forbidden processes. The splitting of the peroxo moiety by a chromium trispyrazolylborate is fast and found to be quite favorable by computational study, with a product-like MECP, and experimental reports of dioxygen/peroxo group splitting show this to be a favorable process despite as well. Computational study by Herndon, et al. of the molybdo-porphyrin system (unpublished work) reveal a reaction profile for the peroxo splitting process that is very similar to the profile reported in this section.

Looking at the overall reaction profile (Figure 3-37), it becomes apparent that the turnover limiting steps for phosphine oxidation are the OAT steps for transfer of oxo group to the phosphine substrate, which is in line with the experimental result reported in Section 3.1.1. The driving thermodynamic force for each regime of the reaction is the formation of oxygen-containing double-bonded moieties, including both phosphine oxide and the regenerated dioxomolybdenum complex. The intermediate regimes are fairly thermoneutral, with the spin crossovers to stabilized triplet species as the next largest thermodynamic sinks.

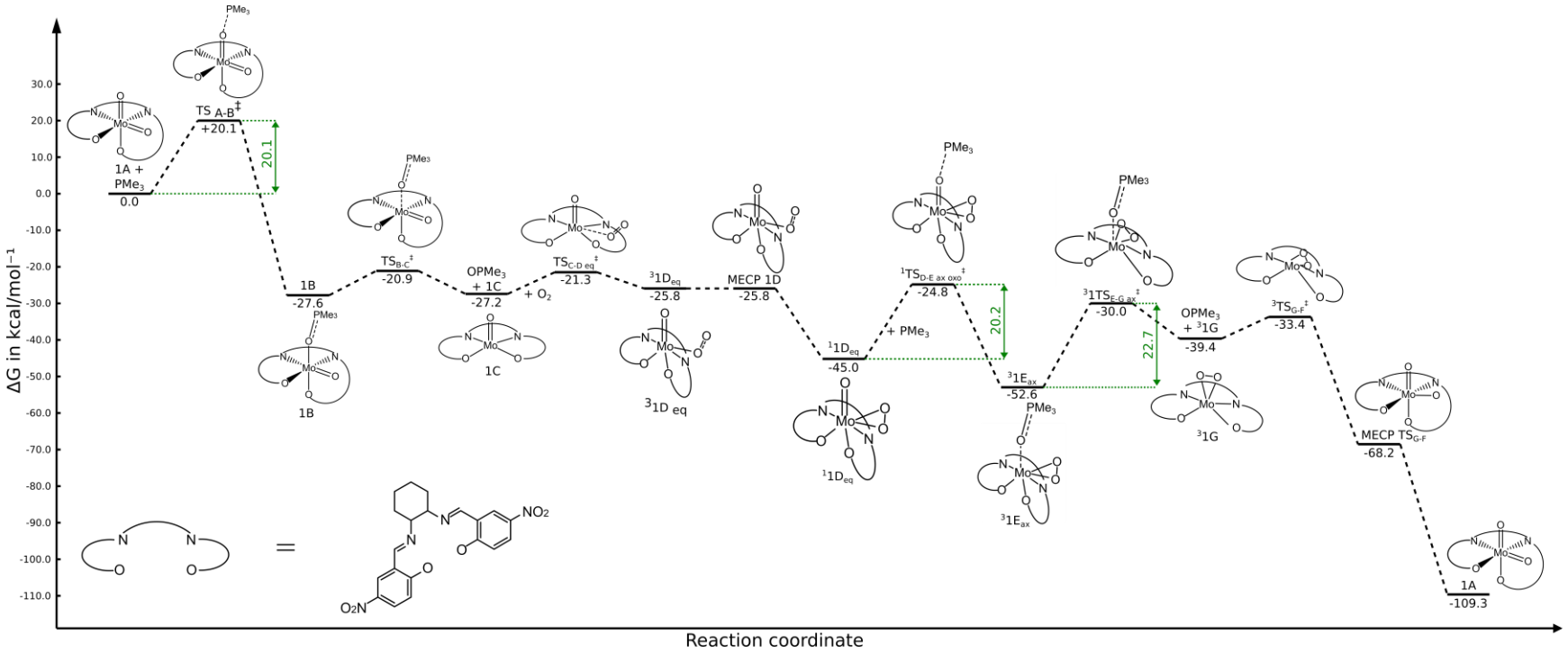

Figure 3-37. Overall reaction profile for phosphine oxidation

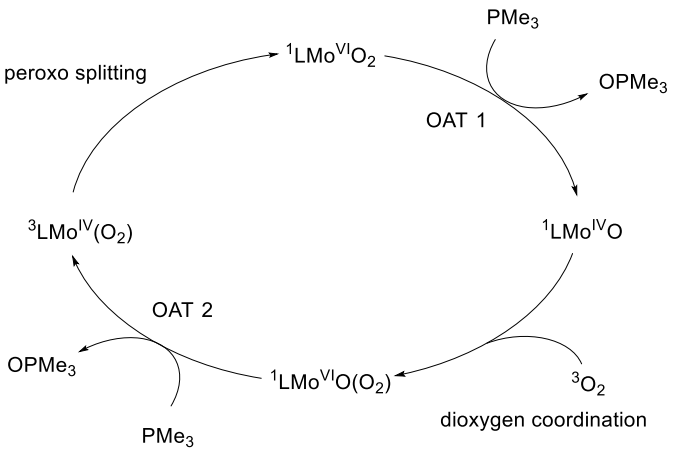

Figure 3-38. Overall catalytic cycle for phosphine oxidation by LMo(VI)O_2 complex under air

Our computational study reveals that the second oxidation step does not proceed *via* OAT from the peroxo group, as reported by Sharpless, et al. for oxidation of phosphines by oxodiperoxo molybdenum complexes, [25] but through oxygen atom transfer from the oxo group in the oxoperoxo species. This means that the overall reaction proceeds through OAT from a dioxomolybdenum species, followed by coordination of dioxygen to form an oxo-superoxo species and its crossover-stabilized singlet oxoperoxo sibling. The second oxygen atom transfer of the catalytic cycle proceeds *via* phosphine attack on the remaining oxo group, and the product monoperoxo molybdenum (IV) complex then splits the peroxo moiety, rearranging to form the dioxo catalyst.

3.3.5 Sulfoxidation

Due to the possibility of using the chiral MoO_2sal-CHXD platform for other enantioselective OAT reactions, we chose to investigate their potential for catalytic oxidation of sulfoxides to sulfones. Oxidation could theoretically occur either *via* a disproportionation of the sulfoxide to sulfide and sulfone (Table 3-2) or through OAT from an external oxygen atom donor, for which we wished to investigate the use of dioxygen as an oxygen atom source (Table 3-3).

Table 3-2: DFT-calculated thermodynamic values for catalyzed disproportionation of DMSO to DMS and dimethyl sulfone

Reaction	ΔG° (kcal/mol)
$LMo^{VI}O_2 + SOMe_2 \longrightarrow LMo^{IV}O + SO_2Me_2$	+2.8
$LMo^{IV}O + SOMe_2 \longrightarrow LMo^{VI}O_2 + SMe_2$	-23.3
$2\ SOMe_2 \xrightarrow{LMo^{VI}O_2} SO_2Me_2 + SMe_2$	-20.5

Table 3-3. DFT-calculated thermodynamic values for catalyzed oxidation of DMSO to dimethyl sulfone with dioxygen as the oxygen atom source

Reaction	ΔG° (kcal/mol)
$LMo^{VI}O_2 + SOMe_2 \longrightarrow LMo^{IV}O + SO_2Me_2$	+2.8
$LMo^{IV}O + O_2 \longrightarrow LMo^{VI}O(O_2)$	-39.5
$LMo^{VI}O(O_2) + SOMe_2 \longrightarrow LMo^{VI}O_2 + SO_2Me_2$	-50.2
$2\ SOMe_2 + O_2 \xrightarrow{LMo^{VI}O_2} 2\ SO_2Me_2$	-86.9

For oxygen atom transfer from the dioxomolybdenum species, the formation of the sulfone product is an endergonic process (+2.8 kcal/mol), with reoxidation to Mo(VI) species is the thermodynamic driving force for the overall exergonic reaction (oxidation by OAT from sulfoxide, Table 3-2, -23.3 kcal/mol; oxidation by reaction with dioxygen, Table 3-3, -39.5 kcal/mol). In comparison, the oxidation of dimethyl sulfide to dimethyl sulfoxide by the dioxomolybdenum catalyst is calculated to have ΔG° = +23.3 kcal/mol.

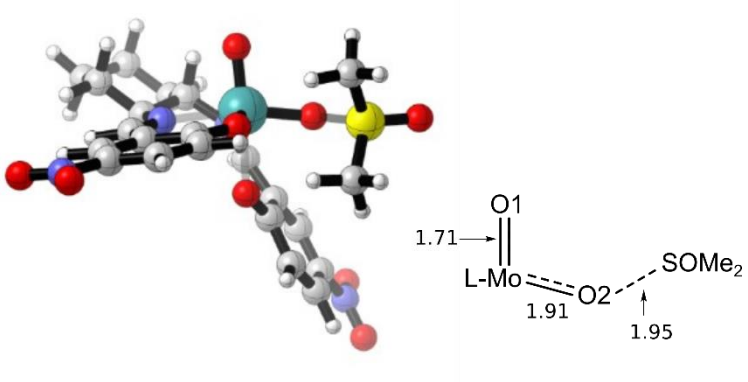

Figure 3-39. OAT transition state for sulfoxidation TS_{A-B}

The sulfoxidation OAT transition state (Figure 3-39) was located by scanning along the reaction coordinate for the forming O-S bond, starting from the optimized ternary complex geometry. Compared to the oxygen atom transfer transition state modeled for the phosphine oxidation, the sulfoxidation TS_{A-B} is a much later transition state, with significantly reduced Mo-O bonding character in the transferred oxo group. The forming S-O bond also has reduced bond character compared to the product S-O double bond, having a bond length nearly equal to that of the Mo-O bond. One of the other notable changes in geometry occurs in the existing S-O double bond, which contracts from the sulfoxide reactant to 1.48 Å.

For this atom-transfer step, only the transition state for equatorial approach of substrate was located. The dramatic increase in activation energy ($\Delta G^{\ddagger}$ = 39.4 kcal/mol, 19.3 kcal/mol increase over phosphine oxidation), suggests that the sulfoxide substrate is much more resistant to oxidation by the Mo^{VI} complex than the phosphine substrate.

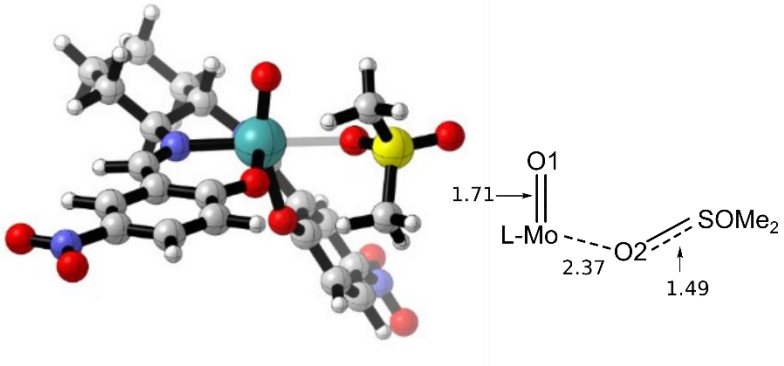

Figure 3-40. Ternary complex 1B with Mo-bound molecule of dimethyl sulfone

The ternary complex for the sulfoxidation (Figure 3-40) is structurally very similar to that determined for the dioxo phosphine oxidation. The datively bound product molecule has a slightly elongated S-O bond for the ligated oxygen atom, and the Mo-O bond has only partial bonding character (2.37 Å). The ternary complex is destabilized relative to the reactants by 8.3 kcal/mol, showing that the forming S=O bond is not as strong of a thermodynamic sink as the P=O bond formation examined in Section 3.2.1, despite the similarities in electronic structure of the substrate. The products (following sulfone dissociation) are also destabilized relative to the reactants (ΔG = +7.4 kcal/mol).

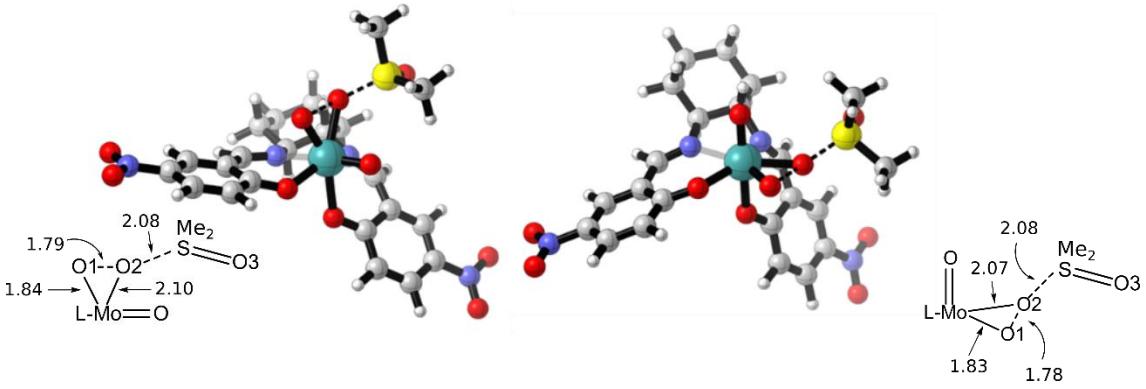

Figure 3-41. OAT from peroxo moiety of the oxoperoxo Mo(VI) species, $^{1}TS_{D\text{-}A\ ax}$ (left) and $^{1}TS_{D\text{-}A\ eq}$ (right)

Unlike the dioxo atom transfer step, transition states for atom transfer from the oxoperoxo complex were located for both the axial peroxo and equatorial complexes. These transition states (Figure 3-41) are much later than those observed in the phosphine oxidation transition states ($^{1}TS_{D\text{-}A}$, Figure 3-24), with their imaginary frequencies demonstrating a concerted breaking of Mo-O and O-O bonds as the O-S bond is forming. The alignment of substrate with the peroxo group also contrasts the phosphine oxidation reaction, [47] exhibiting a near-linear relationship of the donating sulfur lone pair with the dissociating O-O bond. This step is significantly more favorable than the dioxo-catalyzed OAT step, with a $\Delta G^{\ddagger}$ of +28.9 kcal/mol (equatorial, +29.6 kcal/mol axial), comparable to the *para*-hydro complexes discussed in Chapter 2.

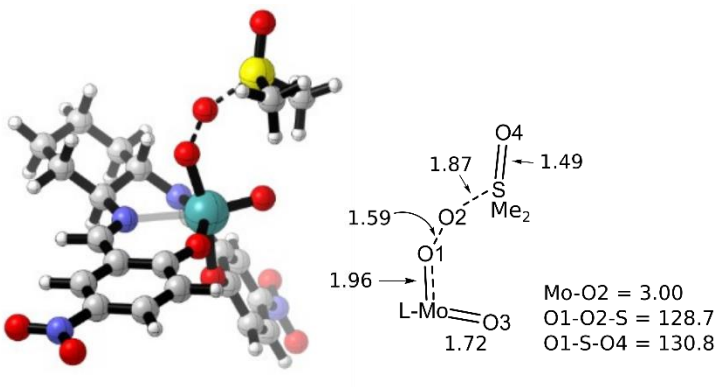

Figure 3-42. OAT TS for the oxo-superoxo Mo(V) species, $^{3}TS_{D\text{-}F}$

For the OAT transition state from the triplet superoxo complex, only the axial isomer was located (Figure 3-42). The geometry of this transition state is very similar to that of the phosphine oxidation $^{3}TS_{D\text{-}F}$ (Figure 3-22), with side-on interaction of the superoxo unit and sulfur center. This transition state ($\Delta G^{\ddagger}$ = +35.4 kcal/mol) is later than that observed for the singlet OAT step, with a greatly reduced S-O bond distance and the O-O bond in the superoxo unit much longer than for the singlet transition state (S-O: 2.08 Å, O-O: 1.79 Å).

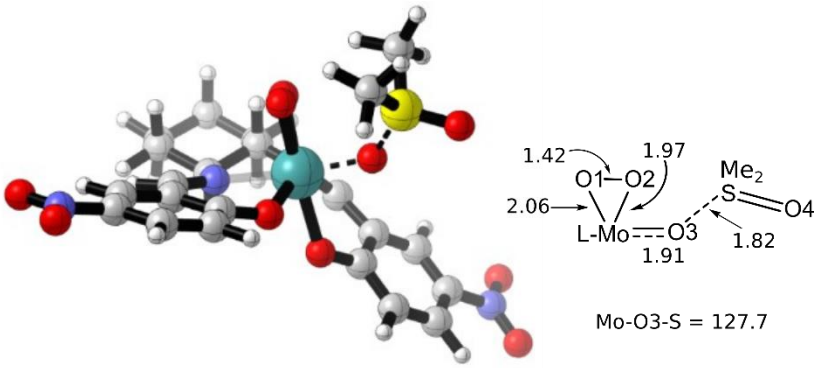

Figure 3-43. Transition state for Mo=O OAT from Mo(IV) oxoperoxo complex, $TS_{D\text{-}E}$

The oxo-group atom transfer from the oxoperoxo complex (Figure 3-43) is very similar to that observed in the OAT transfer from the dioxo complex, with an apparent late transition state. The Mo-O bond has single bond character, and the forming O-S bond has increased bonding character compared to the dioxo transition state. Supporting the discussion of reversed favorability for OAT from the dioxo complex, this OAT step is the least favorable of the three possible pathways, with a $\Delta G^{\ddagger}$ of +46 kcal/mol.

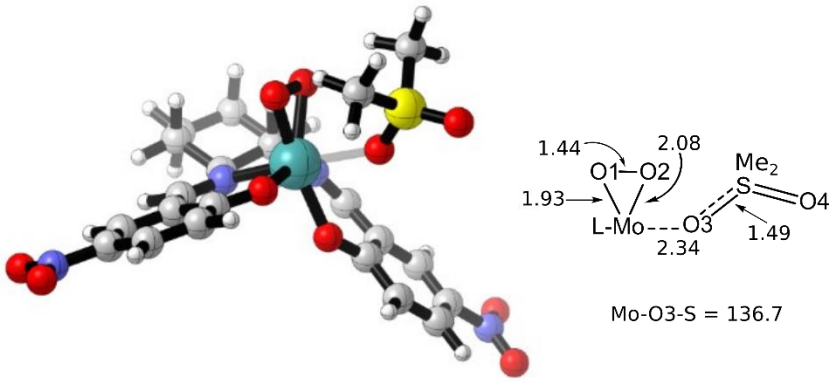

Figure 3-44. Ternary complex for OAT from oxo moiety of singlet oxoperoxo molybdenum (VI) species

The ternary complex (Figure 3-44) formed by this process is also very similar to that in the dioxo OAT step, with a datively bound sulfone having only a small effect on the bonding interactions around the metal center, but largely maintaining the octahedral geometry. The peroxo group/phenolate coordination angle has begun to collapse, and the peroxo group has reduced symmetry.

In contrast to the phosphine oxidation, transfer of an oxygen atom from the peroxo moiety is the most favorable pathway for sulfoxidation (Figure 3-45). This peroxo OAT barrier is nearly 7 kcal/mol less than that for the superoxo OAT and 16 kcal/mol less than that of the oxo group transfer. As the spin crossover barrier from triplet oxo-superoxo Mo(V) to singlet oxoperoxo Mo(VI) is much smaller than the activation barrier for the OAT step associated with the oxo-superoxo species, it is likely that OAT from the peroxo group of the oxoperoxo species is the exclusive pathway for this oxidation step, consistent with the Sharpless mechanism. [25,34]

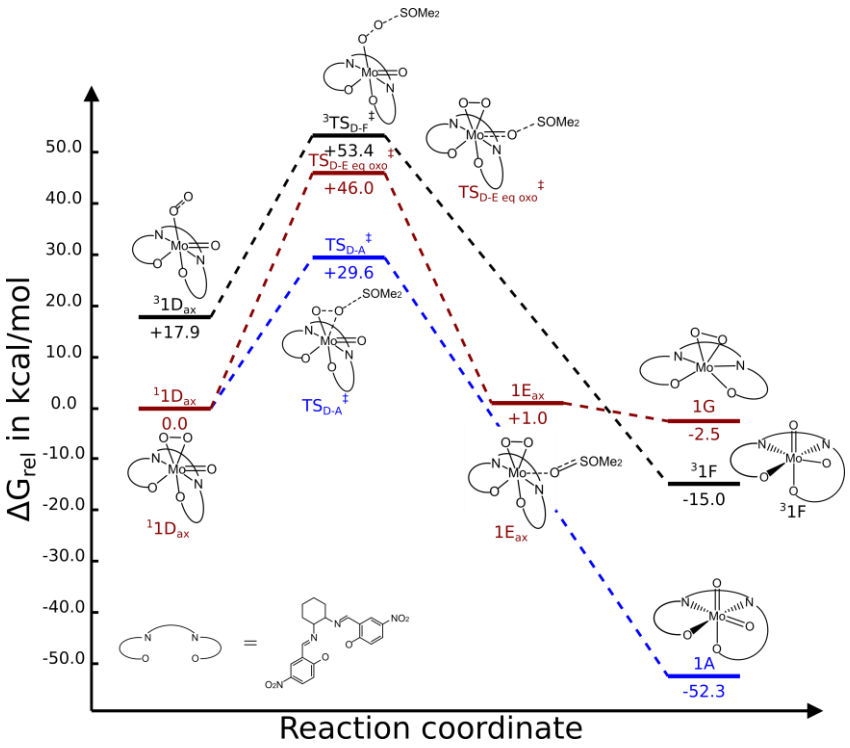

Figure 3-45. Comparison of reaction profiles for sulfoxidation by the $LMoO(O_2)$ complexes; superoxo OAT (black), oxoperoxo oxo OAT (dark red), and peroxo (blue)

Out of curiosity regarding the electron demand of the oxygen atom transfer reactions for sulfoxidation, the *para*-methoxy MoO_2 sal-CHXD complex **9** was also modeled (Figure 3-46). Analysis of the differences between dioxo OAT and peroxo OAT with complex **1** suggested that an increase in electron density of the transferred oxygen would favor oxidation of the sulfoxide species, in a reversal of the electronic character favoring phosphine oxidation [38].

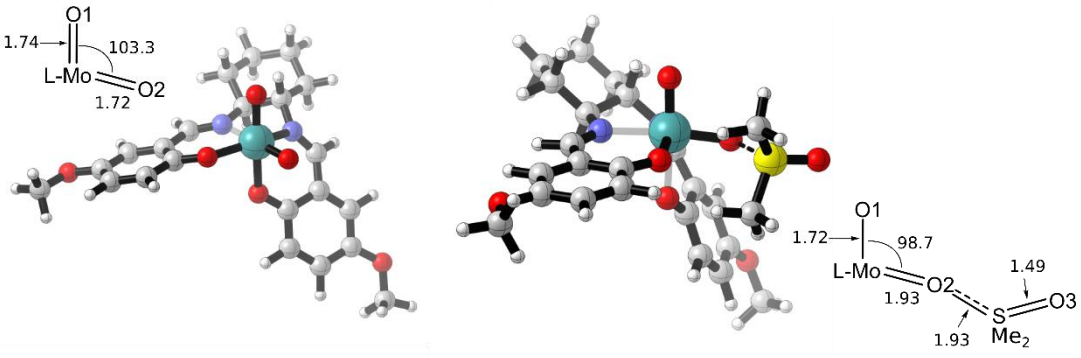

Figure 3-46. *p*-OMe-salCHXD complex **9** (left) and oxygen atom transfer transition state 9 TS_{A-B} (right)

The oxygen atom transfer step from complex **9** is found to have a $\Delta G^{\ddagger}$ of 44.2 kcal/mol, 5 kcal/mol higher than the calculated barrier for complex **1**. The transition state structure for this sulfoxidation step shows that it is a slightly later transition state than occurs with complex **1**, with the Mo-O2 and O2-S bonds equal in length, displaying a slight decrease in the Mo-O bond order and increase in S-O bond order compared to the phosphine oxidation.

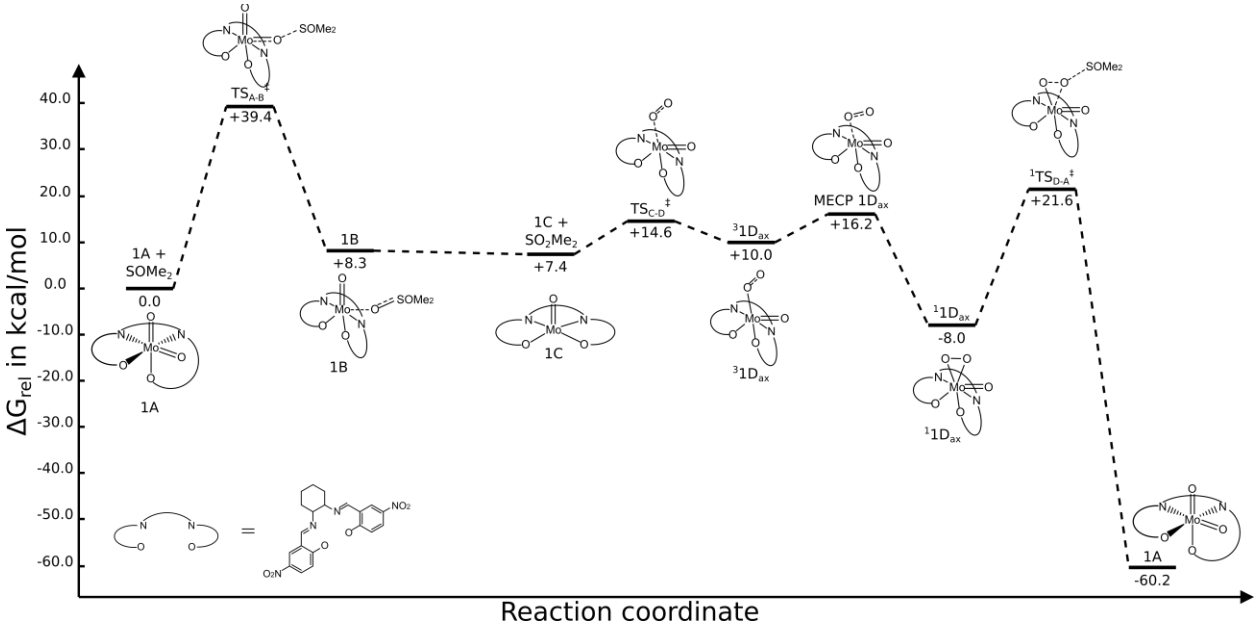

Figure 3-47. Overall reaction profile for sulfoxidation reaction

The overall catalytic cycle for sulfoxidation by complex **1** (Figure 3-47) is exergonic, with the formation of bonds with oxygen serving as the primary thermodynamic sinks. The formation of the sulfone product is not as strong a driving forces as the formation of phosphine oxide, but the reformation of the dioxo catalyst *via* OAT from the oxoperoxo complex goes some way to making up for this decreased thermodynamic favorability. Both catalytic cycles have the initial OAT as their rate-limiting step, though the sulfoxidation reaction is tremendously less favorable. This increase in free energy of activation between substrates is perhaps unsurprising, as the sulfoxide is less oxidizable than the phosphine.

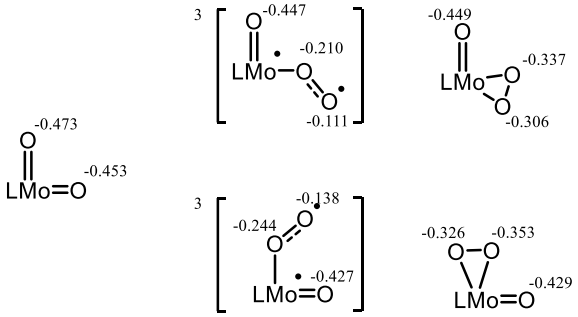

Figure 3-48. Mulliken charges for transferable oxygen atoms

Differences in electrostatic interactions could be invoked to explain the difference in reactivity, but examination of calculated atomic Mulliken charges on the oxygen atoms (Figure 3-48) reveals that this analysis would suggest reactivity trends opposite of that revealed by the computational study. Mulliken charges for the studied species show that the oxo moieties are more electron-rich (more negative) in character than the peroxo groups. However, Mulliken charges are well-known to be unreliable as representatives of physical charge distributions, especially as the size of the basis set increases. [53] For the studied reactions, the phosphine behaves as a nucleophilic substrate, with increases in reactivity correlated with decreased electron-density on the oxo group, while the sulfoxide behaves as an electrophilic substrate, favoring reaction with electron-rich oxygen moieties. The Mulliken charges show that the phosphine reacts most favorably with the most electronegative oxygen, while OAT to sulfoxide is favored by a more electropositive oxygen atom. This reversal suggests that an electrostatic explanation, as modeled by Mulliken atomic populations, cannot be satisfactorily linked to the reactivity of the catalyst. What is more likely is that orbital energy matching is responsible for discrimination between the possible pathways. Both phosphine and sulfoxide substrates have frontier orbitals consisting of a lone pair and X-C σ-bonding orbitals (HOMO) and π non-bonding orbitals, which react *via* the former donating density into the antibonding orbitals of the transferred oxygen atom and the latter accepting density from the oxygen atom lone pair.

3.3.6 Experimental study of sulfoxidation

Despite the large activation barrier calculated for the sulfoxidation, we wanted to experimentally determine whether the reaction (Scheme 3-8) could occur.

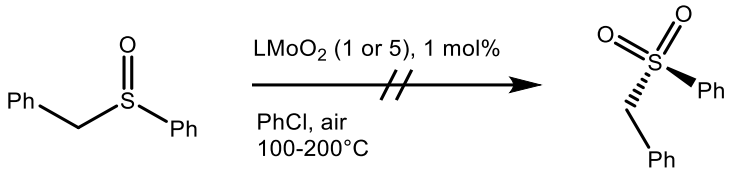

Scheme 3-8. Experimental study of sulfoxidation by complex 1

Benzylphenyl sulfoxide was selected as a substrate for the oxidation due to the presence of an easily-observable methylene group for ^{1}H NMR monitoring of the reaction. The experimental investigation revealed that even under more severe conditions (up to 220°C, 1 mol % catalyst in chlorobenzene under air atmosphere), no formation of the sulfoxide was observed. This lack of reactivity aligns well with the high activation barrier and the lack of a thermodynamic driving force for the initial oxygen atom transfer step from the dioxo complex. The reaction in question has been demonstrated with a molybdenum (IV) oxoperoxo bis-hydroxyphenyloxazaline, with urea hydrogen peroxide as the oxidant, producing methylphenyl sulfone as a double-oxidation product of methylphenyl sulfide, [31] suggesting that this lack of reactivity is due to a difference in the catalyst properties or a change in mechanism as a consequence of the hydroperoxide oxidant, rather than an intrinsic limitation of molybdenum (VI) oxoperoxo catalysts.

3.3.7 Future work

Further computational work on this study will involve locating all triplet and open-shell singlet species to elucidate what reaction coordinates are involved in the minimum energy crossing events. As there appear to be many crossover events throughout the catalytic profile, this system is a promising one for examining spin-crossing reactions in molybdenum. Similarly, as the dioxygen coordination activity appears to be conserved within the broader molybdenum salen family, computational study of other derivatives than complex **1** could reveal further information about the electronic properties and mechanistic demands of the dioxygen

coordination process. Experimentally, there is a significant body of work that could be done to show whether our computational analysis of the system is possible to validate. The initial experimental result reported in Section 3.1.1 seemingly contradicts the computational results outlined in Section 3.2.3, as computational study shows that the oxygen atom transfer steps occur exclusively *via* the molybdenum oxo moiety, which would maintain the selectivity of the dioxo complex toward the chiral phosphine. Further investigation of this reaction could determine whether the change in selectivity of the kinetic resolution arises from an autooxidation process or from a change in reaction mechanism due to steric or electronic effects of the *tert*-butyl groups present on complex **8**. Proceeding through the studied mechanism, the next opportunity for experimental confirmation is to conduct trapping or spectroscopic detection experiments for the metal oxo-superoxo and oxoperoxo catalytic intermediates. *In-situ* IR detection of the molybdenum peroxo moiety may be possible (O-O stretching frequency expected at ~860 cm^{-1} [17]), and studies on thiooxidase model complexes have employed nitrone spin traps to study the iron superoxo intermediate, [54] suggest that this may be a possibility for study of the unstable molybdenum (V) intermediates. It is also possible that the triplet species involved in peroxo group splitting could be detected by EPR experiments. Finally, isotopic labeling studies could be carried out to determine which oxygen atoms are transferred during the catalytic process. This labeling study could be conducted by running a two-turnover catalytic oxidation with labeled dioxygen, which would produce solely unlabeled phosphine oxide and a doubly-labeled dioxomolybdenum center if the catalytic cycle proceeds *via* the peroxo group splitting pathway described in Section 3.2.4.

3.4 Experimental Section

3.4.1 General methods.

NMR spectra were obtained using Varian OXFORD 300, 400, and 500 MHz NMR spectrometers; IR spectra were obtained on a Shimadzu IRAffinity-1 FTIR; and optical rotations were measured using a Rudolph Research AUTOPOL III polarimeter. Reagent grade solvents were used as obtained. Dioxomolybdenum compounds and PMePh^{t}Bu were prepared as reported in Chapter 1.

3.4.2 Reactions under O_2

Kinetic Resolution under dioxygen atmosphere

To a 25 mL round bottom flask was added a stir bar, 10 mL 1,1,2,2-tetrachloroethane, 10.8 mg catalyst **8** (0.02 mmol), and 79 mg methylphenyl-*tert*-butylphosphine (0.4 mmol). The reaction vessel was fitted with a water-cooled condenser and placed in an oil bath at 50°C. Conversion was monitored by NMR, and the reaction vessel was removed from heat after 4 hours (40% conversion). The phosphine oxide was isolated from the reaction solution in a nitrogen-filled glove bag by preparative TLC. The plate was developed using 90:10 CH_2Cl_2/MeOH, and the phosphine oxide band at R_f=0.3 was scraped off the plate and washed with several portions of iPrOH, followed by solvent evaporation from the washings. Optical rotation measurements on the phosphine oxide were recorded in $CHCl_3$ solution.

Catalyst Variation study

To a vial was added $MoO_2(acac)_2$ (3.26 mg, 0.01 mmol), triphenylphosphine (12.0 mg, (0.05 mmol), and 1 mL 1,1,2,2-tetrachloroethane. The reaction mixture was observed to turn blue-purple upon addition of triphenylphosphine. The reaction vial was fitted with a condenser and placed in a 60°C oil bath for 5 hours while open to the air. Conversion of triphenylphosphine to triphenylphosphine oxide was determined by ^{31}P NMR.

To a round bottom flask was added 183.2 mg (0.7 mmol) triphenylphosphine, 10 mL chlorobenzene, and approximately 1 mol% catalyst (5.3 mg **1**, 98 μmol; 3.1 mg **4**, 69 μmol; 3.8 mg **5**, 70 μmol; 4.7 mg **6**, 70 μmol; or 3.6 mg **7**, 70 μmol), along with a stir bar. The reaction flasks

were then purged with O_2 before being sealed and placed in a 50°C oil bath for 4 hours. Aliquots were taken of each reaction mixture and conversion was assessed by ^{31}P NMR.

Turnover study under dioxygen atmosphere

To a round bottom flask was added chlorobenzene (20 mL), 2.5 mg complex **2** (3.5 µmol), and triphenylphosphine (671.5 mg, 2.5 mmol). The flask was evacuated and backfilled with O_2 before being placed in an oil bath at 50°C. Aliquots were taken for NMR analysis and progress of the reaction was determined by ^{31}P NMR.

Dioxygen concentration study

To each of eight 13 mm culture tubes was added 12.0 mg triphenylphosphine (0.05 mmol) and 0.7 mL chlorobenzene. Half the tubes were then charged with a small portion (~0.2 mg, 0.5 µmol) of complex **1**, the other tubes serving as blank reactions. The catalyzed and blank reactions were then capped with a septum and assigned pairwise to one of four conditions: 1) no added atmosphere, 2) atmospheric pressure of air maintained by way of a balloon, 3) atmospheric pressure of air maintained by a balloon, with stirring, and 4) 1 atmosphere of O_2 maintained by balloon. For condition 4, the culture tube was sparged with oxygen gas prior to capping with a septum. All reactions were then placed in a 60°C oil bath and incubated overnight. Conversion was determined by ^{31}P NMR.

Sulfoxidation study

To a pressure tube was added 172.5 mg methylphenylsulfoxide (1.2 mmol), 5 mL chlorobenzene, and 5 mg catalyst (complex **1** or **5**). The reaction vessel was then purged with O_2, capped, and placed in an oil bath (T = 150-220°C). After 24 hours, the reaction vessel was removed from the oil bath, and allowed to cool to room temperature. Aliquots were taken for ^{1}H NMR analysis.

3.4.3 Computational methods

All calculations were carried out using Gaussian 09. Structures were optimized using the B3LYP hybrid functional and the basis sets: Mo, LANL2DZ; P, S, 6-311++ G(d,p); C, H, O, N, 6-311 G(d) using Gaussian 09's ultrafine integration grid. Solvent phase energies were obtained as a single point energy calculation using the M06 functional (basis sets: Mo, SDD; P, S, C, H, O, N, 6-311++G(d,p) in conjunction with the SMD solvent model for 1,2-dichloroethane. The free energy correction to the energy was taken from the B3LYP frequency calculation. Relaxed coordinate scans were employed to focus Berny saddle point searches. For transition states $TS_{B\text{-}C}$ and $TS_{C\text{-}D}$, starting points for the Berny optimizations were located by running a series of single-point optimizations with the M-OA bond length frozen. Transition states were verified by the existence of a single imaginary frequency along the reaction coordinate involving bond making/breaking. Minimum-Energy Crossing Point structures were calculated using the B3LYP optimized singlet and triplet structures as inputs for the sobMECP optimization algorithm and free energies for these structures were computed from Gaussian frequency calculation outputs. Reaction profiles were generated using the mechaSVG program. [55]

3.5 Computational SI

CITATION FOR GAUSSIAN 09

Gaussian 09, Frisch, M. J.; Trucks, G. W.; Schlegel, H. B.; Scuseria, G. E.; Robb, M. A.; Cheeseman, J. R.; Scalmani, G.; Barone, V.; Mennucci, B.; Petersson, G. A.; Nakatsuji, H.; Caricato, M.; Li, X.; Hratchian, H. P.; Izmaylov, A. F.; Bloino, J.; Zheng, G.; Sonnenberg, J. L.; Hada, M.; Ehara, M.; Toyota, K.; Fukuda, R.; Hasegawa, J.; Ishida, M.; Nakajima, T.; Honda, Y.; Kitao, O.; Nakai, H.; Vreven, T.; Montgomery, Jr., J. A.; Peralta, J. E.; Ogliaro, F.; Bearpark, M.; Heyd, J. J.; Brothers, E.; Kudin, K. N.; Staroverov, V. N.; Kobayashi, R.; Normand, J.; Raghavachari, K.; Rendell, A.; Burant, J. C.; Iyengar, S. S.; Tomasi, J.; Cossi, M.; Rega, N.; Millam, J. M.; Klene, M.; Knox, J. E.; Cross, J. B.; Bakken, V.; Adamo, C.; Jaramillo, J.; Gomperts, R.; Stratmann, R. E.; Yazyev, O.; Austin, A. J.; Cammi, R.; Pomelli, C.; Ochterski, J. W.; Martin, R. L.; Morokuma, K.; Zakrzewski, V. G.; Voth, G. A.; Salvador, P.; Dannenberg, J. J.; Dapprich, S.; Daniels, A. D.; Farkas, Ö.; Foresman, J. B.; Ortiz, J. V.; Cioslowski, J.; Fox, D. J. Gaussian, Inc., Wallingford CT, 2009.

Table 3-4. M06 calculated energies (solvent phase, Hartrees) for B3LYP optimized structures of phosphine oxidation pathway complexes

Species	G
1A	-1661.05061
PMe_3	-460.93676
TS_{A-B}	-2121.95532
1B	-2122.03133
TS_{B-C}	-2122.02065
1C	-1585.83666
$OPMe_3$	-536.19404
$^3O_2$	-150.30816
$TS_{C-D\ ax}$	-1736.13345
$TS_{C-D\ eq}$	-1736.13549
^{3}1D$_{ax}$	-1736.14079
^{3}1D$_{eq}$	-1736.14266
MECP 1D$_{ax}$	-1736.13091
MECP 1D$_{eq}$	-1736.14252
^{1}1D$_{ax}$	-1736.16937
^{1}1D$_{eq}$	-1736.17319
$^3TS_{D-F\ ax}$	-2197.05563
$^3TS_{D-F\ eq}$	-2197.05384
$^1TS_{D-A\ ax}$	-2197.05009
$^1TS_{D-A\ eq}$	-2197.05576
$^1TS_{D-E\ ax}$	-2197.07775
$^1TS_{D-E\ eq}$	-2197.07265
$^3TS_{D-E\ ax}$	-2197.05020
^{1}1E$_{ax}$	-2197.13988
^{1}1E$_{eq}$	-2197.13448
^{3}1E$_{ax}$	-2197.15748
$^1TS_{E-G\ ax}$	-2197.11309
$^3TS_{E-G\ ax}$	-2197.12135
^{1}1G	-1660.92418
MECP 1G	-1660.92231
^{3}1G	-1660.93921
$^1TS_{G-A}$	-1660.90739
$^3TS_{G-F}$	-1660.92967
MECP 1F	-1660.98515
^{3}1F	-1660.97937

Table 3-5. M06 calculated energies (solvent phase, Hartrees) for B3LYP optimized structures of species in sulfoxidation pathway

Species	G
1A	-1661.05061
$SOMe_2$	-553.08277
TS_{A-B}	-2214.07053
1B	-2214.12008
1C	-1585.83666
SO_2Me_2	-628.28485
$^1D_{ax}$	-1736.16937
$^1D_{eq}$	-1736.17319
$^3D_{eq}$	-1736.14079
$^3O_2$	-150.30816
$^1TS_{D-A\ ax}$	-2289.20503
$^1TS_{D-A\ eq}$	-2289.20990
$^3TS_{D-F}$	-2289.16707
$^1TS_{D-E}$	-2289.17891
$^1E_{ax}$	-2289.20342
^1G	-1660.92418
^3F	-1660.97937
9	-1481.20750
9 TS_{A-B}	-2034.34669

3.6 Works Cited

[1] M. Amini, M.M. Haghdoost, M. Bagherzadeh, Oxido-peroxido molybdenum(VI) complexes in catalytic and stoichiometric oxidations, Coordination Chemistry Reviews. 257 (2013) 1093–1121.

[2] K. Ambroziak, New dioxomolybdenum(VI) complexes of tetradentate Schiff base as catalysts for epoxidation of olefins, Journal of Molecular Catalysis A: Chemical. 211 (2004) 9–16.

[3] A. Dupé, M.E. Judmaier, F. Belaj, K. Zangger, N.C. Mösch-Zanetti, Activation of molecular oxygen by a molybdenum complex for catalytic oxidation, Dalton Transactions. 44 (2015) 20514–20522.

[4] A. Hazell, C.J. McKenzie, L.P. Nielsen, S. Schindler, M. Weitzer, Mononuclear non-heme iron(III) peroxide complexes: syntheses, characterisation, mass spectrometric and kinetic studies, J. Chem. Soc., Dalton Transactions. (2002) 310–317.

[5] G.M. Yee, W.B. Tolman, Transition Metal Complexes and the Activation of Dioxygen, in: P.M.H. Kroneck, M.E. Torres (Eds.), Sustaining Life on Planet Earth: Metalloenzymes Mastering Dioxygen and Other Chewy Gases, Springer International Publishing, Cham, 2015: pp. 131–204.

[6] C. Würtele, E. Gaoutchenova, K. Harms, M.C. Holthausen, J. Sundermeyer, S. Schindler, Crystallographic Characterization of a Synthetic 1:1 End-On Copper Dioxygen Adduct Complex, Angewandte Chemie International Edition. 45 (2006) 3867–3869.

[7] K. Fujisawa, M. Tanaka, Y. Moro-oka, N. Kitajima, A Monomeric Side-On Superoxocopper(II) Complex: Cu(O2)(HB(3-tBu-5-iPrpz)3), J. Am. Chem. Soc. 116 (1994) 12079–12080.

[8] A.M. Reynolds, B.F. Gherman, C.J. Cramer, W.B. Tolman, Characterization of a 1:1 Cu−O2 Adduct Supported by an Anilido Imine Ligand, Inorganic Chemistry. 44 (2005) 6989–6997.

[9] E.A. Lewis, W.B. Tolman, Reactivity of Dioxygen−Copper Systems, Chemical Reviews.104 (2004) 1047–1076.

[10] A. Bakac, Oxygen Activation with Transition-Metal Complexes in Aqueous Solution, Inorganic Chemistry. 49 (2010) 3584–3593.

[11] T. Punniyamurthy, S. Velusamy, J. Iqbal, Recent Advances in Transition Metal Catalyzed Oxidation of Organic Substrates with Molecular Oxygen, Chemical Reviews. 105 (2005) 2329–2364.

[12] Z. Zhu, J.H. Espenson, Methylrhenium trioxide as a catalyst for oxidations with molecular oxygen and for oxygen transfer, Journal of Molecular Catalysis A: Chemical. 103 (1995) 87–94.

[13] H. Arzoumanian, J.F. Petrignani, M. Pierrot, F. Ridouane, J. Sanchez, Preparation of an oxoperoxocyanomolybdate(VI) complex by dioxygen oxidation of an oxocyanomolybdate(IV) anion. Structure and reactivity toward phosphines and olefins, Inorganic Chemistry. 27 (1988) 3377–3381.

[14] G. Lyashenko, G. Saischek, M.E. Judmaier, M. Volpe, J. Baumgartner, F. Belaj, V. Jancik, R. Herbst-Irmer, N.C. Mösch-Zanetti, Oxo-molybdenum and oxo-tungsten complexes of Schiff bases relevant to molybdoenzymes, Dalton Transactions. (2009) 5655–5665.

[15] V.N. Nemykin, J. Laskin, P. Basu, Isolation, Characterization of an Intermediate in an Oxygen Atom-Transfer Reaction, and the Determination of the Bond Dissociation Energy, J. Am. Chem. Soc. 126 (2004) 8604–8605.

[16] N. Ueyama, N. Yoshinaga, A. Nakamura, Catalytic air and amine N-oxide oxidation of p-substituted benzoin by molybdenum(VI) complexes. Identification of the deactivation process by dioxygen, J. Chem. Soc., Dalton Transactions. (1990) 387–394.

[17] G. Lyashenko, G. Saischek, A. Pal, R. Herbst-Irmer, N.C. Mösch-Zanetti, Molecular oxygen activation by a molybdenum(IV) monooxo bis(β-ketiminato) complex, Chemical Communications. (2007) 701–703.

[18] D. Matoga, J. Szklarzewicz, A. Samotus, K. Lewiński, Crystal structures of mixed-ligand oxocyano complexes of molybdenum(IV) and tungsten(IV) and their reactivity towards molecular oxygen studied by IR spectroscopy, J. Chem. Soc., Dalton Transactions. (2002) 3587–3592.

[19] D. Matoga, J. Szklarzewicz, A. Samotus, J. Burgess, J. Fawcett, D.R. Russell, Preparation and characterisation of [M(CN)4O(pz)]2− complexes (M=Mo or W) and their reactivity towards molecular oxygen, Polyhedron. 19 (2000) 1503–1509.

[20] R.A. Sheldon, A History of Oxygen Activation: 1773–1993, in: D.H.R. Barton, A.E. Martell, D.T. Sawyer (Eds.), The Activation of Dioxygen and Homogeneous Catalytic Oxidation, Springer US, Boston, MA, 1993: pp. 9–30.

[21] H. Arzoumanian, Molybdenum-Oxo and Peroxo Complexes in Oxygen Atom Transfer Processes with O_2 as the Primary Oxidant, Current Inorganic Chemistry (Discontinued). 1 (n.d.) 140–145.

[22] D.V. Deubel, J. Sundermeyer, G. Frenking, Theoretical Studies of Molybdenum Peroxo Complexes [MoOn(O2)3-n(OPH3)] as Catalysts for Olefin Epoxidation†, Inorganic Chemistry. 39 (2000) 2314–2320.

[23] S. Das, T. Bhowmick, T. Punniyamurthy, D. Dey, J. Nath, M.K. Chaudhuri, Molybdenum(VI)-peroxo complex catalyzed oxidation of alkylbenzenes with hydrogen peroxide, Tetrahedron Letters. 44 (2003) 4915–4917.

[24] Oxidation of sulfides in aqueous media catalyzed by pyrazole-oxidoperoxido-molybdenum(VI) complexes, Inorganica Chimica Acta. 511 (2020) 119814.

[25] K.B. Sharpless, J.M. Townsend, D.R. Williams, Mechanism of epoxidation of olefins by covalent peroxides of molybdenum(VI), J. Am. Chem. Soc. 94 (1972) 295–296.

[26] L.J. Csányi, On the peroxomolybdate complexes as sources of singlet oxygen, Journal of Molecular Catalysis A: Chemical. 322 (2010) 1–6.

[27] I.V. Yudanov, C. Di Valentin, P. Gisdakis, N. Rösch, Olefin epoxidation by mono and bisperoxo complexes of Mo(VI): a density functional model study, Journal of Molecular Catalysis A: Chemical. 158 (2000) 189–197.

[28] F.E. Kühn, A.M. Santos, M. Abrantes, Mononuclear Organomolybdenum(VI) Dioxo Complexes: Synthesis, Reactivity, and Catalytic Applications, Chemical Reviews.106 (2006) 2455–2475.

[29] N. Grover, F.E. Kuhn, Catalytic Olefin Epoxidation with η^5-Cyclopentadienyl Molybdenum Complexes, Current Organic Chemistry. 16 (n.d.) 16–32.

[30] S. Campestrini, F. Di Furia, P. Rossi, A. Torboli, G. Valle, Comparison of the relative efficiency of peroxomolybdenum complexes as oxidants of the alcoholic function, Journal of Molecular Catalysis. 83 (1993) 95–105.

[31] M. Bagherzadeh, M.M. Haghdoost, M. Amini, P.G. Derakhshandeh, Molybdenum oxo–peroxo complex: A very fast catalyst for oxidation and reduction of sulfur-based compounds, Catalysis Communications. 23 (2012) 14–19.

[32] N. Gharah, S. Chakraborty, A.K. Mukherjee, R. Bhattacharyya, Oxoperoxo molybdenum(VI)- and tungsten(VI) complexes with 1-(2′-hydroxyphenyl) ethanone oxime: Synthesis, structure and catalytic uses in the oxidation of olefins, alcohols, sulfides and amines using H2O2 as a terminal oxidant, Inorganica Chimica Acta. 362 (2009) 1089–1100.

[33] S.K. Maiti, K.M. Abdul Malik, R. Bhattacharyya, Oxoperoxo-molybdenum and -tungsten (VI) complexes: their synthesis, structure and catalytic uses in the peroxidic oxidation of alcohols to aldehydes and ketones, Inorganic Chemistry Communications. 7 (2004) 823–828.

[34] L.F. Veiros, C.A. Gamelas, M.J. Calhorda, C.C. Romão, Chemoselective Sulfide and Sulfoxide Oxidations by CpMo(CO)3Cl/HOOR: a DFT Mechanistic Study, Organometallics. 30 (2011) 1454–1465.

[35] N. Zwettler, N. Grover, F. Belaj, K. Kirchner, N.C. Mösch-Zanetti, Activation of Molecular Oxygen by a Molybdenum(IV) Imido Compound, Inorganic Chemistry. 56 (2017) 10147–10150.

[36] N. Zwettler, M.E. Judmaier, L. Strohmeier, F. Belaj, N.C. Mösch-Zanetti, Oxygen activation and catalytic aerobic oxidation by Mo(iv)/(vi) complexes with functionalized iminophenolate ligands, Dalton Transactions. 45 (2016) 14549–14560.

[37] H. Yu, Y. Fu, Q. Guo, Z. Lin, DFT Studies on Reactions of Transition Metal Complexes with O2, Organometallics. 28 (2009) 4443–4451.

[38] C.J. Whiteoak, G.J.P. Britovsek, V.C. Gibson, A.J.P. White, Electronic effects in oxo transfer reactions catalysed by salan molybdenum(vi) cis-dioxo complexes, Dalton Transactions. (2009) 2337–2337.

[39] J. Tachibana, T. Imamura, New Dioxygen Complex of Molybdenum Porphyrin. Reactions of Oxomolybdenum(IV) Porphyrins with Molecular Oxygen, Chemistry Letters. 19 (1990) 2085–2088.

[40] F.R. Fronczek, R.L. Luck, G. Wang, Synthesis, characterization and reactivity of MoCl2(O)(O2)(OPR3)2, OPR3=OPMePh2, OPPh3; an isomerization catalyst for some allylic alcohols, Inorganic Chemistry Communications. 5 (2002) 384–387.

[41] A. Jimtaisong, R.L. Luck, Synthesis and Catalytic Epoxidation Activity with TBHP and H2O2 of Dioxo-, Oxoperoxo-, and Oxodiperoxo Molybdenum(VI) and Tungsten(VI) Compounds Containing Monodentate or Bidentate Phosphine Oxide Ligands: Crystal Structures of WCl2(O)2(OPMePh2)2, WCl2(O)(O2)(OPMePh2)2, MoCl2(O)2dppmO2·C4H10O, WCl2(O)2dppmO2, Mo(O)(O2)2dppmO2, and W(O)(O2)2dppmO2, Inorganic Chemistry. 45 (2006) 10391–10402.

[42] R.P. Hanzlik, D. Williamson, Oxygen activation by transition metal complexes. 2. Bis(acetylacetonato)cobalt(II)-catalyzed oxidation of tributylphosphine, J. Am. Chem. Soc. 98 (1976) 6570–6573.

[43] H. Arzoumanian, J. Sanchez, G. Strukul, R. Zennaro, Dioxygen Ligand Transfer from Platinum to Molybdenum. Isolation of a Highly Reactive Molybdenum(VI) Oxoperoxo Dimer, in: D.H.R. Barton, A.E. Martell, D.T. Sawyer (Eds.), The Activation of Dioxygen and Homogeneous Catalytic Oxidation, Springer US, Boston, MA, 1993: pp. 443–443.

[44] J.N. Harvey, Spin-forbidden reactions: computational insight into mechanisms and kinetics, WIREs Computational Molecular Science. 4 (2014) 1–14.

[45] Using the sobMECP program combined with the Gaussian program to search for the minimum energy intersection, (n.d.).

[46] T.E. Barder, S.L. Buchwald, Rationale Behind the Resistance of Dialkylbiaryl Phosphines toward Oxidation by Molecular Oxygen, J. Am. Chem. Soc. 129 (2007) 5096–5101.

[47] B.W. Kail, L.M. Pérez, S.D. Zarić, A.J. Millar, C.G. Young, M.B. Hall, P. Basu, Mechanistic Investigation of the Oxygen-Atom-Transfer Reactivity of Dioxo-molybdenum(VI) Complexes, Chemistry - A European Journal. 12 (2006) 7501–7509.

[48] S.N. Brown, J.M. Mayer, Photochemical generation of a reactive rhenium(III) oxo complex and its curious mode of cleavage of dioxygen, Inorganic Chemistry. 31 (1992) 4091–4100.

[49] E.S. Akturk, G.P.A. Yap, K.H. Theopold, Dioxygen Activation by Non-Adiabatic Oxidative Addition to a Single Metal Center, Angewandte Chemie International Edition. 54 (2015) 14974–14977.

[50] M.H. Chisholm, K. Folting, J.C. Huffman, C.C. Kirkpatrick, Reactions of metal-metal multiple bonds. 10. Reactions of Mo2(OR)6 (M.tplbond.M) and [Mo(OR)4]x compounds with molecular oxygen. Preparation and characterization of oxo alkoxides of molybdenum: MoO2(OR)2, MoO2(OR)2(bpy), MoO(OR)4, Mo3O(OR)10, Mo4O8(OR)4(py)4, and Mo6O10(OR)12, Inorganic Chemistry. 23 (1984) 1021–1037.

[51] H. Ledon, M. Bonnet, J.-Y. Lallemand, Photoejection of a dioxygen ligand during the photolysis of bisperoxomolybdenum(VI) porphyrin. Synthesis and characterisation of cis-dioxo-molybdenum(VI) tetra-p-tolylporphyrin, J. Chem. Soc., Chemical Communications. (1979) 702–704.

[52] W.A. Thornley, T.E. Bitterwolf, Photochemistry of the Permanganate Ion in Low-Temperature Frozen Matrices, Inorganic Chemistry. 54 (2015) 3370–3375.

[53] A.E. Reed, R.B. Weinstock, F. Weinhold, Natural population analysis, J. Chem. Phys. 83 (1985) 735–746.

[54] S. Thierbach, N. Bui, J. Zapp, S.R. Chhabra, R. Kappl, S. Fetzner, Substrate-Assisted O2 Activation in a Cofactor-Independent Dioxygenase, Chemistry & Biology. 21 (2014) 217–225.

[55] Angnes, R. A. mechaSVG, GitHub repository, 2020, doi: 10.5281/zenodo.3970267.

CHAPTER 4

CATALYTIC AEROBIC OXIDATION OF THIOLS CATALYZED BY SCHIFF-BASE OXOMOLYBDENUM COMPOUNDS

Although our prior experimental work did not provide evidence for molybdenum-promoted oxygen atom transfer reactivity with sulfides and sulfoxides, we wished to explore the potential for other sulfur oxidase-type reactivity of the dioxomolybdenum (IV) sal-CHXD complexes. As the results described in Chapter 3 demonstrate, the activity of the dioxomolybdenum (IV) *para*-nitro-salen complex **1** as a thioether/sulfide oxidation catalyst is limited and seemingly not experimentally accessible, so we chose to explore whether it could be applied to catalyze the oxidation of thiols to disulfides. This oxidation reaction was chosen as a more likely target for this reaction due to the possibility of a lower barrier to oxidation of thiol compounds as compared to sulfides and sulfoxides. [1]

Disulfides can be formed from thiols by either 1-electron reduction or 2-electron reduction pathways, by reaction with various oxidants. For the purposes of this chapter, we will focus on dioxygen, oxo-metal complexes, [2–4] and hydroperoxides as the oxidizing species, with generalized pathways for each of these under aqueous conditions shown in Figure 4-1. [2] All reactions of thiols are shown to start from the deprotonated thiolate (formed under basic conditions), with the oxidizing agent **A** acting to convert thiolate to thiyl radical. In the cellular environment, the common metal oxo oxidants are hemeperoxidases, which employ H_2O_2 as the stoichiometric oxidant for this reaction. [5] The generated thiyl radical can react with available thiolate to form the disulfide radical anion, which can be oxidized to the neutral disulfide by dioxygen. [2,6,7] The two-electron pathway generates sulfenate/sulfenic acids *via* a pseudo-S_N2 mechanism involving a proton migration following the oxygen atom transfer transition state, [8] generating water or the protonated alcohol as side products of the reaction. Reaction with a molecule of thiolate produces disulfide by elimination of hydroxide ion to form the disulfide product.

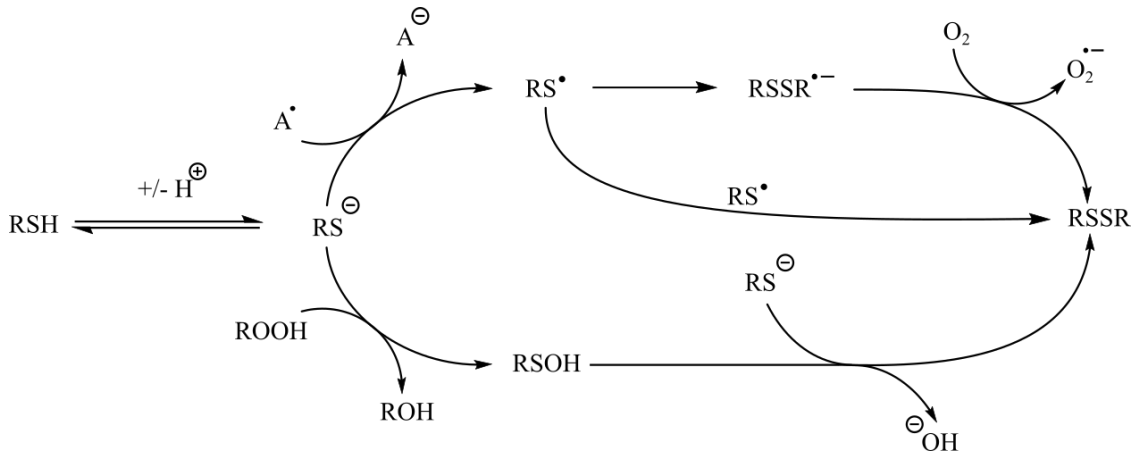

Figure 4-1. One- and two-electron reduction pathways of thiols to form disulfides

Catalytic thiol oxidations have been reported by molecular oxygen with a large variety of species as catalysts, [9] including bases, [10,11] metal ions, [12,13] transition metal species, [11,14–18] and even basic alumina. [3] The most relevant of these are metal oxo and metal oxide species, which are believed to react with thiols *via* similar pathways to produce disulfides. Metal oxides (MnO_2, Fe_2O_3, Co_2O_3, CuO [15]) have been employed as stoichiometric oxidants for the coupling of thiols to disulfides. The oxidation of the thiol substrate is demonstrated to proceed by a diffusion-controlled 1-electron process, leading to the formation a reduced metal species, two molecules of the thiyl radical, and water through a two-step oxidation process in which the acidity of the thiol has no influence. Later investigations with a heterogenous gold catalyst [17] also demonstrated that oxidation of the thiol proceeded *via* a thiyl radical intermediate, and that for the studied system, addition of base inhibits the oxidation, excluding the 1-electron reduction of a thiolate species as part of the reaction mechanism. A heterogenous iron-catalyzed system has also been reported, employing a metal-organic framework [14] to form the disulfide product *via* self-coupling of the reduced thiol substrate, followed by reoxidation of the metal center with molecular oxygen. Complexes of vanadium (V), [19] iron (III), [20], cobalt (II), [21] copper (II), [22,23], rhodium (I), [24] and ruthenium (II) [11] have been reported as homogenous catalysts for thiol oxidation. Each of these systems couples thiols to disulfides by generating the thiyl radical, though the mechanism of the reduction step changes depending on solvent. The cobalt (II) phthalocyanine catalyzed oxidation [21] was carried out in ionic liquid solvent, leading to a 1-electron oxidation of the thiolate anion to thiyl radical rather than hydrogen atom transfer (HAT)

from the thiol. The iron and copper-catalyzed systems, by comparison, generate the thiyl radical from the protonated thiol, as observed for the heterogeneous catalysts. The rhodium and ruthenium catalysts, however, are demonstrated to proceed by dehydrogenation of the substrate, allowing these reactions to proceed without added oxidant by coupling the oxidation of thiol with formation of hydrogen gas [24] or by employing a base to regenerate the active catalyst. [11]

There are a few literature reports of thiol oxidation by molybdenum species [25–28], though there has not been a detailed examination of the mechanism for formation of disulfides by these species. In each case, the formation of disulfide is demonstrated to be accompanied by reduction of the molybdenum center from molybdenum (VI) to molybdenum (IV), generating water as a byproduct of the reaction. Stoichiometric reaction of aryl thiols with a dioxomolybdenum (IV) S-N-S pincer complex was reported to form disulfide, water, and the reduced monooxomolybdenum (IV) complex as products. [25] Catalytic oxidation of thiols to disulfides has been reported using a $MoO_2Cl_2(DMSO)_2$ catalyst, run in DMSO solvent [26], which also acts as the oxygen atom donor for reoxidation of the molybdenum center to the active dioxomolybdenum (VI) species (Figure 4-2).

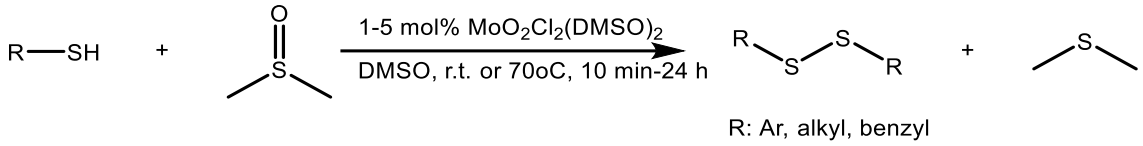

Figure 4-2. Oxidation of thiols to disulfides by $MoO_2Cl_2(DMSO)_2$ with dimethyl sulfoxide as solvent and oxygen atom source

4.1 Results

4.1.1 Synthesis of alkyl disulfides by aerobic oxidation with *p*-nitro-salCHXD MoO_2 (**1**) complex

The initial exploration of this reaction used dodecane thiol as a substrate due to its low volatility, less intense odor, and ease of handling relative to lower-molecular weight mercaptans. Additionally, this substrate had previously been found to react in good (86%) yield at a relatively slow rate using the $MoO_2Cl_2(DMSO)_2$ catalyst and dimethyl sulfoxide oxidant reported by Sanz, et al [26]. We hoped to not only replicate the previously reported reactivity, but also determine the viability of dioxygen as the oxidant, to observe ligand effects on the reaction efficiency and to identify mechanistic features in the generation of the disulfide product.

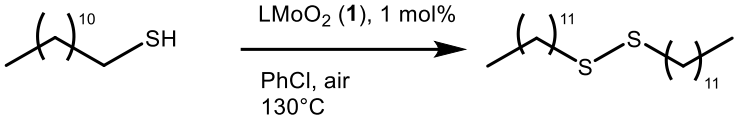

Scheme 4-1. Targeted oxidation of dodecane thiol to dodecyl disulfide by complex **1**

The catalyzed aerobic oxidation of dodecane thiol (Scheme 4-1) was found to proceed at an average rate of 1 mol/mol_{cat} h^{-1} (~100 eq of thiol over the course of 96h) when the reaction was conducted at 130°C in chlorobenzene under air in the presence of 1 mol% of **1**. The disulfide product **2a** was formed in 80% yield, as determined by ^{1}H NMR integration of the α-methylene protons ($CDCl_3$, δ = 2.69 ppm, t, 4H), and was isolated by preparatory-scale TLC. The remainder of the product mixture was determined to be composed of dodecanal (**2b**, ~1% yield, α-CH δ = 9.32 ppm) and ~15% of an unknown secondary product, **2c**. This secondary product was assumed to also be an oxidation product of the dodecane thiol, but the product is spectroscopically distinct from the disulfide and could be isolated from the product mixture using chromatography (3% EtOAc/hexane on silica, R_f=0.80, disulfide R_f=0.75). A blank (0 mol% catalyst **1**) reaction was conducted on the same scale and with the same concentration of dodecane thiol at 130°C for 48 hours, for which no conversion of thiol was observed.

The secondary product has a single methylene resonance in the proton NMR spectrum (PhCl, δ = 2.16 ppm, t, Figure 4-3), strongly suggesting that it is a symmetric species likely with a stronger electron-withdrawing group than dodecane disulfide (α-methylene, δ = 2.0 ppm) with equivalent, non-chiral α-methylene positions on either side of the sulfur-containing linkage.

Further characterization and study showed that this species is distinct from any thiol oxidation product described in the literature. ESI-MS gives the molecular weight of the compound to be 418 g/mol ($[M+H]^+ = 419$ m/z, 16 m/z higher than the disulfide and 16 m/z lower than the trisulfide [29], which has nearly identical ^1H and ^{13}C NMR spectra to those of the putative sulfenic anhydride. Based on this molecular mass, the product is identified as an oxygen atom transfer product of the thiol oxidation with the formula $(C_{12}H_{25})S_2O$. The IR spectrum of the isolated compound lacks a vibrational absorption near 1100 cm^{-1}, which would represent an S=O stretching frequency, ruling out didodecyl thiolsulfinate $[C_{12}H_{25}S(S=O)C_{12}H_{25}]$ as its identity. Based on this data, we have tentatively identified the product as dodecyl sulfenic anhydride (Scheme 4-2, **2c**). Compounds containing the sulfenic anhydride functional group have not been previously isolated. Previous literature suggesting formation of sulfenic anhydrides, along with a suggested mechanism for forming them from reaction with molybdenum (VI) oxoperoxo complexes, is discussed in Section 4.2.1.

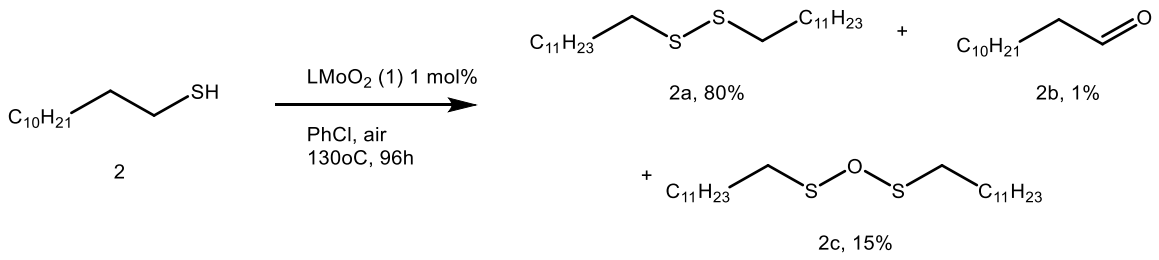

Scheme 4-2. Oxidation of dodecane thiol to product mixture

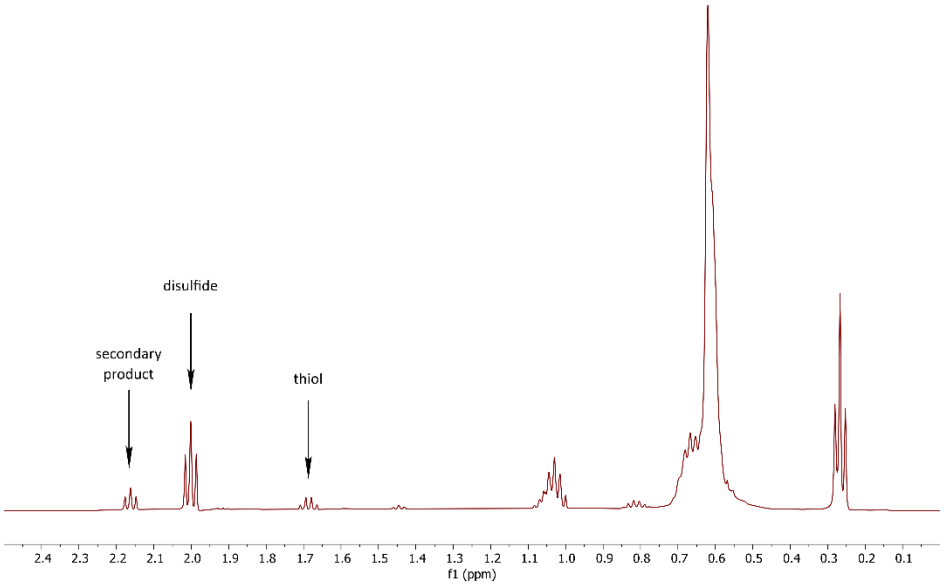

Figure 4-3. ^{1}H NMR spectrum of the reaction mixture for the dodecane thiol reaction shown in Scheme 4-2, shown at 85% conversion. The α-CH_2 signals are labeled for each species present.

4.1.2 Substrate scope

Of immediate interest was whether formation of the putative sulfenic anhydride was an exclusive property of the dodecane thiol, or whether the secondary product would be observed with other thiols. Harlan, et al. [25] established that dioxomolybdenum complexes could be reduced to molybdenum (IV) oxo complexes by thiophenol species, and the oxidation of thiophenols to disulfides by a dioxomolybdenum complex was reported by Sanz, et al. [26] *Para*-nitrothiophenol and *para*-chlorothiophenol were selected as appropriate aryl substrates (Scheme 4-3) for study of the reaction with complex **1**.

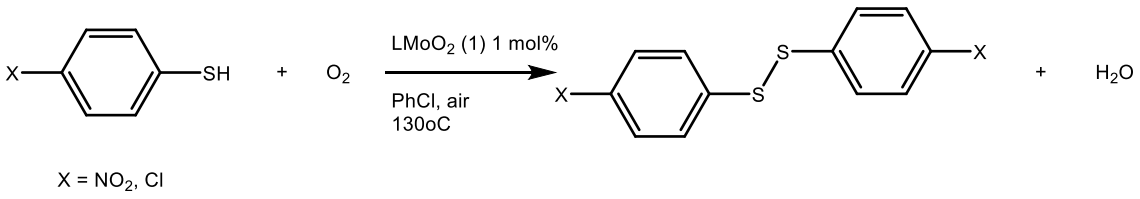

Scheme 4-3. Catalytic oxidation of *para*-substituted thiophenols by complex **1**

In the experimental test, oxidation of *p*-chlorothiophenol (Scheme 4-3) was observed to proceed much faster than the dodecanethiol substrate, with a rate of 4 mol/mol_{cat} h^{-1} under

aerobic conditions at 130°C. The product of the *para*-chlorothiophenol oxidation appears to be a mixture based on analytical HPLC analysis—with two distinct peaks eluting at 28.25 and 28.96 minutes, having a 2:1 ratio of peak area—and a decrease in melting point relative to literature values for bis-*para*-chlorophenyl disulfide (product mixture 67-70°C, lit 73°C), but the components of the mixture are not easily differentiated by ^{1}H NMR or ^{13}C NMR, and only the *para*-chlorophenyl disulfide was observed by GCMS ($[M]^{+}$ = 286 m/z). As the secondary product again appears to be a symmetric species with properties very similar to the disulfide, we propose that this product is a sulfenic anhydride, employing the same reasoning as for dodecane sulfenic anhydride. The product(s) of the *para*-nitrothiophenol oxidation was characterized only by melting point, which was recorded as 165-170°C (lit 188-189°C [30]). The low solubility and similarity of starting material and product ^{1}H NMR ($CDCl_3$, δ 8.20, d, *J* = 9.0 Hz, 7.63, d, *J* = 8.9 Hz for both starting material and product) prevented monitoring and quantitation of the reaction rate for the oxidation of *para*-nitrothiophenol. Formation of product in the oxidation of *para*-chlorothiophenol was possible to measure by ^{1}H NMR due to the disappearance of the single aromatic resonance for the thiol at 7.21 ppm (400 MHz, $CDCl_3$) and appearance of product doublets at 7.40 ppm (400 MHz, $CDCl_3$, *J* = 8.9 Hz) and 7.28 ppm (400 MHz, $CDCl_3$, *J* = 8.9 Hz). Preparative separation of the product(s) of these thiophenol oxidations was not performed due to lack of separation on silica and a lack of significant yield of the secondary product.

To better monitor reaction conversion and product distribution and to further evaluate the reaction scope, another alkyl substrate was selected, benzyl mercaptan, this time with the added goal of producing crystallizable product(s) (Scheme 4-4).

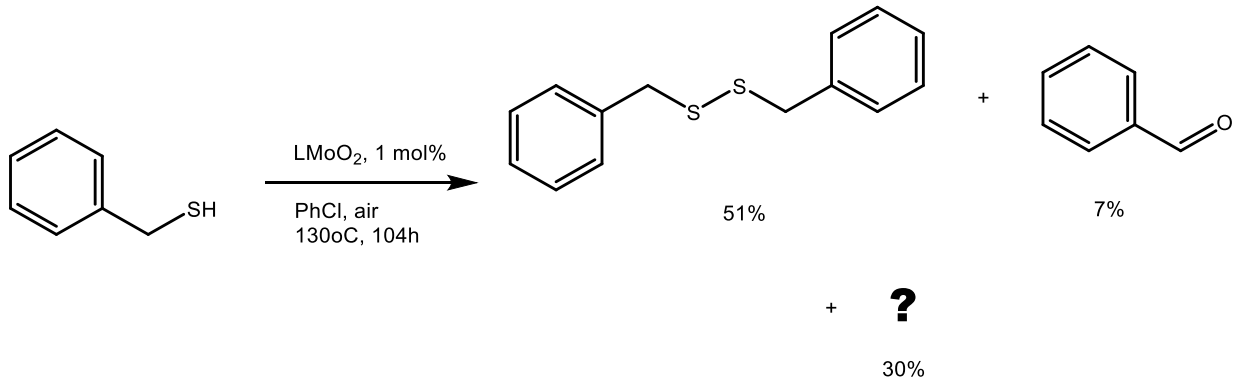

Scheme 4-4. Oxidation of benzyl mercaptan by **1**, percent yield at >95% conversion

Benzyl mercaptan was found to have an average catalyzed reaction rate nearly identical to that of dodecane thiol, at 1.03 mol/mol_{cat} h^{-1} (Scheme 4-4) under the standard reaction conditions. Conversion of the mercaptan was monitored by integration of its α-CH_2 peaks for the mercaptan and each product species. A secondary product (30% yield by NMR) is formed in a 1:2.25 ratio with the expected disulfide. A blank reaction (0 mol% **1**) run under the same condition resulted in no conversion of thiol after 48 hours.

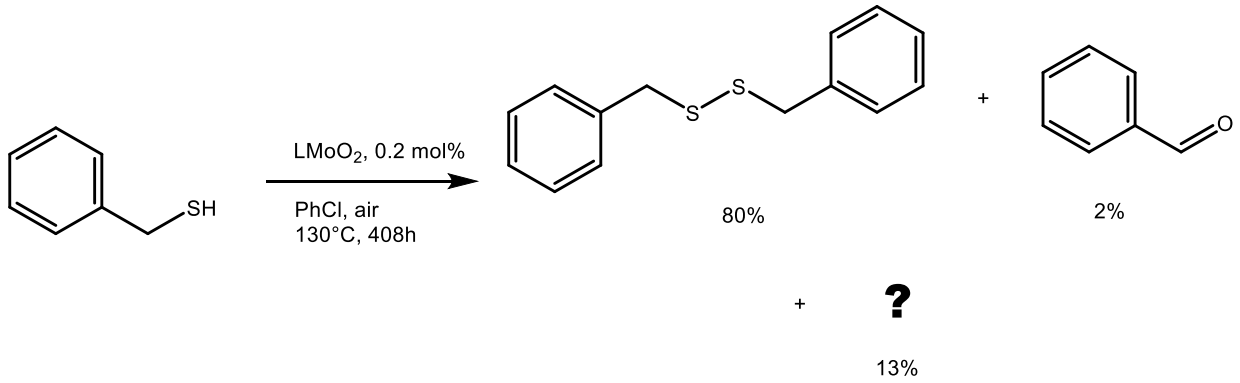

Scheme 4-5. Oxidation of benzyl mercaptan with 0.2 mol % loading of **1**, percent yield at >95% conversion

This increase in relative yield (selectivity) toward the secondary product led to further studies with benzyl mercaptan as a substrate, the first of which involved approximately doubling the substrate concentration (from 0.062 M to 0.155 M) while maintaining the same concentration of the catalyst. This reaction (Scheme 4-5) proceeded at the same rate observed for the reactions with 1 mol % catalyst, demonstrating that the overall reaction is zero-order in the mercaptan. This increase in thiol concentration leads to a decrease in the selectivity for the benzyl secondary product from 30% to 13% (from 3:1 to 5:1), perhaps due to the increased concentration of thiol substrate scavenging an intermediate in the secondary product forming mechanism to form the disulfide instead. This product was initially identified as benzyl sulfenic anhydride, in keeping with the logic used to assign the secondary product of the dodecane thiol oxidation, but was later confirmed to be benzyl trisulfide (*vide infra*, Section 4.1.3)

To further examine the substrate scope of disulfide formation, derivatives of cysteine were tested for reactivity (Scheme 4-6). Cysteine (**6**) was found to have limited solubility in chlorobenzene, preventing NMR monitoring of the reaction. N-acetyl-cysteine (**7**) was also found

to have limited solubility in chlorobenzene at 130°C, but determination of conversion was possible by NMR measurement of the cysteine S-S dimer, **7a** (N,N'-diacetylcystine, Scheme 4-6) peaks. The conversion rate was 15.4 mol/mol$_{cat}$ h^{-1} —at least twice as fast as the uncatalyzed reaction (0 mol % **1**)—and seemed to form a single product by ^{1}H NMR analysis. Conversion of the substrate was tracked using the acetyl methyl resonance (PhCl, δ=1.31 ppm), which shifts downfield upon oxidation to the N-acetyl cystine (PhCl, δ = 1.53 ppm). Conversion can also be observed by changes to the splitting patterns and chemical shift of the α-methylene signals (500 MHz, PhCl, 2.47, dd *J*= 45.7 Hz, 13.5 Hz). Contrary to our other studied substrates, N-acetyl cysteine is observed by NMR to be converted solely to the cystine product.

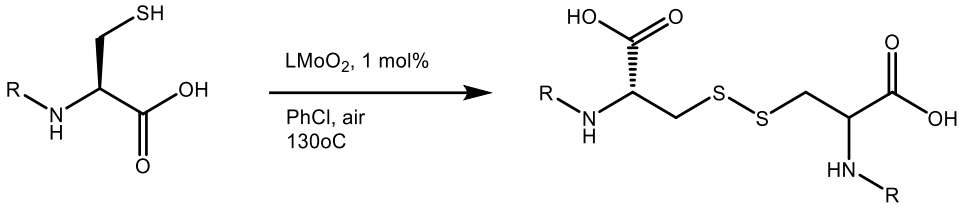

6 (cysteine): R=H **6a**: R=H

7 (NAC): R=Ac **7a**: R=Ac

Scheme 4-6. Catalyzed oxidation of cysteine derivatives **6** and **7**

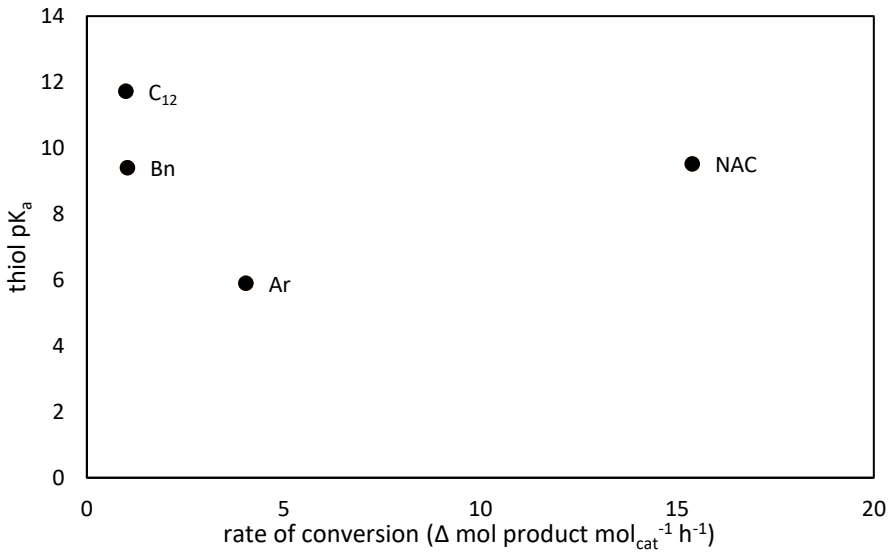

Figure 4-4. Rate of thiol substrate conversion versus pKa of the thiol species

The reactivity trends of the substrates seem not to reflect a relationship between conversion rate and the acidity of the thiol (Figure 4-4). For the studied substrates the rate of conversion is not linearly related to pKa, with no observed increase in rate between dodecanethiol (pKa = 11.72) and benzyl mercaptan (pKa = 9.4). Rate of conversion increases for chlorothiophenol (pKa = 5.9), but the cysteine derivative (pKa = 9.52) converts at a much higher rate than the more acidic thiophenol. These results support the idea that Mo-catalyzed disulfide formation proceeds though a hydrogen atom transfer (HAT) pathway. This increase in reactivity of the cysteine substrate is suggested to be due to intramolecular charge-assisted hydrogen bonding (CAHB), [31] in which the carboxyl group acts to polarize the thiol moiety, making the thiol moiety more reactive to HAT.

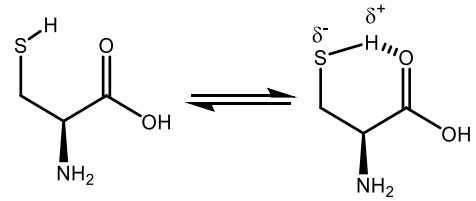

Figure 4-5. Intermolecular hydrogen bonding interaction responsible for activation of cysteine thiols toward oxidation

4.1.3 Identification and characterization of the secondary product from benzyl thiol

Formation of secondary products from the oxidation of the thiol substrate were easily identified from ^{1}H NMRs of the crude mixture for the oxidation of dodecane thiol and benzyl mercaptan and was suggested for other substrates (*p*-nitrothiophenol, *p*-chlorothiophenol) based on melting point data or ^{1}H NMR data. Additionally, analytical HPLC of the *p*-chlorothiophenol oxidation product shows two distinct peaks with similar elution times. The higher selectivity for a secondary product in the oxidation of benzyl mercaptan led to this reaction being used for preparation and purification studies of the secondary product.

The products of the catalytic aerobic oxidation of benzyl mercaptan (Scheme 4-4) were purified using reverse-phase HPLC (C18, MeCN/water). The secondary product species is observed to be reasonably stable in chloroform and acetonitrile solution, with a sample

contained in an NMR tube decaying from >98% purity to approximately 80% purity over the course of a month. Decay of the sample results in formation of disulfide (10%), an unidentified species that was also observed as an oxidation product of the catalyzed reaction (^{1}H NMR, α-CH_2, δ 4.15 ppm, 8.7%), and a third species that appears as a very minor product in the initial reaction but cannot be definitively assigned (apparently 3 peaks, at 4.16, 4.19 and 4.23 ppm); we tentatively assign this compound to be benzyl thiosulfinate, $PhCH_2S(O)$-SCH_2Ph.

After isolating approximately 20 mg of the secondary product from the benzyl mercaptan oxidation, the product was compared to authentic commercial benzyl trisulfide, fortuitously located in the lab inventory. It was found to be identical by ^{1}H and ^{13}C NMR using a sample spiking experiment and to have the same melting point (45-47°C) as the commercial sample, and C,H elemental analysis gives composition of the sample as 60.39% C, 5.03 % H (calculated 60.39% C, 5.07% H). Thus, we concluded that the secondary product from the benzyl thiol oxidation is in fact benzyl trisulfide, $PhCH_2S$-S-SCH_2Ph (Figure 4-6). Confirmation of this assignment was attempted though ESI-MS, but the molecular ion was observed for neither the experimental nor the commercial sample.

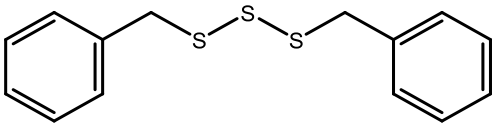

Figure 4-6. Secondary product of benzyl mercaptan oxidation, benzyl trisulfide

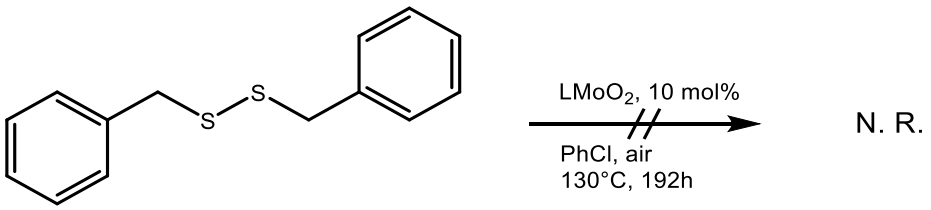

Scheme 4-7. Oxidation study of benzyl disulfide

To determine the origin of the trisulfide product and demonstrate that the disulfide product is stable to further reaction or reduction, we attempted to oxidize benzyl disulfide under the same conditions used for the thiol oxidation (Scheme 4-7). Under these conditions, no reaction was observed for the disulfide, indicating that the disulfide is stable to both oxidation and reduction by catalyst **1**, and that the trisulfide is not produced from the disulfide.

4.1.4 Effects of added base

Taking a cue from the literature for increasing rate of disulfide by formation of the more-easily oxidized thiolate ion, [9–11] we looked to determine if addition of base would have an effect on the rate and selectivity of the molybdenum-catalyzed oxidation reaction (Scheme 4-8). For a blank reaction under base-promoted conditions (5 mol% iPr_2Net, 0 mol% **1**), disulfide was formed in only 5% yield over 48 hours.

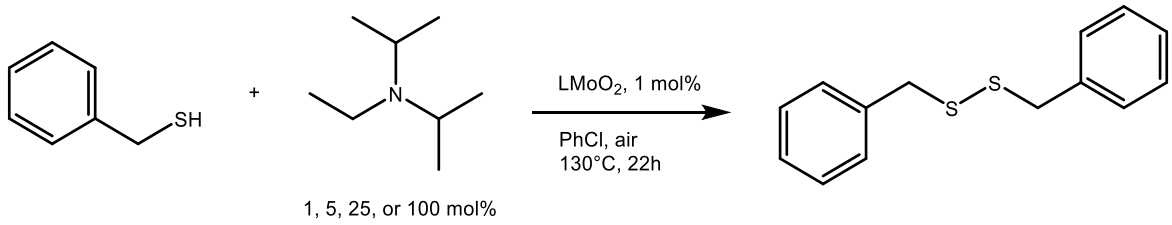

Scheme 4-8: Base-inclusive oxidation of benzyl mercaptan by complex **1**

Table 4-1. Effects of addition of base on rate of conversion and product ratio for oxidation of benzyl mercaptan

mol% of $N(^iPr)_2Et$	conversion at 22h	disulfide/trisulfide ratio
0%	20%	2.25
1%	76%	3.52
5%	81%	4.33
25%	52%	5.89
100%	47%	28.50

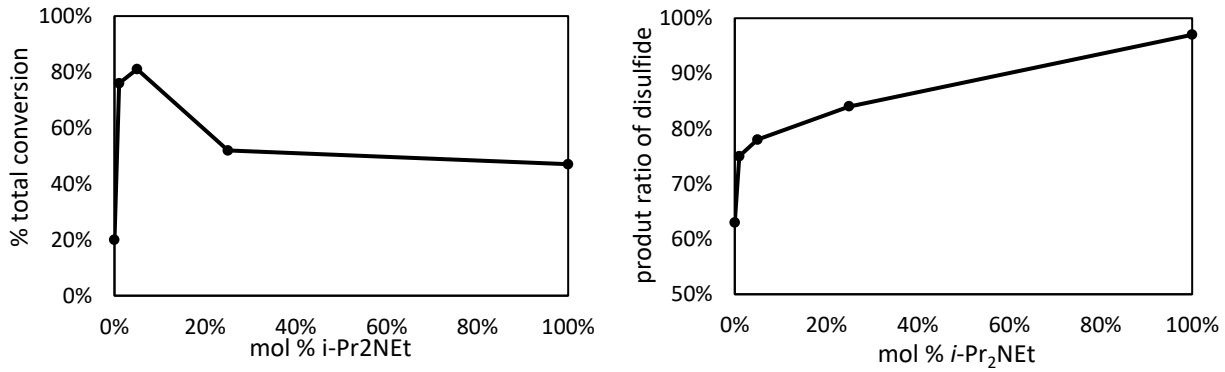

Figure 4-7. Effects of base addition on overall rate of reaction (left) and on product distribution (right)

Addition of diisopropylethylamine to the **1**-catalyzed oxidation reaction of benzyl mercaptan under standard conditions (Scheme 4-8, results reported in Table 4-1) initially causes

a large effect on the rate of reaction, with 1 mol % added base leading to nearly four times greater conversion over the observed 22-hour period. Conversion over the same period increases with 5 mol% added base, but then decreases to approximately 2.5 times the conversion of the base-free reaction as added base is increased to 25 mol% and 100 mol% relative to the thiol substrate (Figure 4-7, left). Addition of base to the reaction mix also has the effect of increasing selectivity of the reaction toward the disulfide product, (Figure 4-7, right) with 1% added base increasing disulfide from 64% to 75% of the product mixture. With 100 mol% added base, disulfide makes up 96% of the product, however the decrease in rate of conversion means that 5 mol% added base has the highest yield of disulfide product, with a 68% yield of disulfide over the observed 22 hour period. Overall, addition of base favors the formation of benzyl disulfide as the product of the oxidation, improving both rate and selectivity toward the product. A mechanistic interpretation of these results is presented in Section 4.2.3.

4.1.5 Stoichiometric and oxygen-free reactions

To elucidate some of the mechanistic details of this oxidation process, oxidation reactions of dodecane thiol and benzyl mercaptan were carried out under several different atmospheric conditions. Each reaction was initially held at R.T. for 24h to monitor for stoichiometric reaction or non-oxidative reactivity. Under nitrogen gas with dodecane thiol, only a single turnover of the oxidation catalyst was observed, resulting in 1 evolved equivalent of dodecyl disulfide (1% yield) and no apparent formation of the secondary product. However, upon heating and air exposure, the reaction resumed and eventually proceeded to the 20% yield of the secondary product and 75% yield of the disulfide observed for the reaction as carried out under air. This result was replicated under both standard (1 mol% catalyst) and low-equivalency (25 mol% catalyst) conditions. A room temperature reaction study with benzyl mercaptan as the substrate and 1 mol% catalyst loading resulted in no observed conversion of substrate, and the catalyst was observed to dissociate, with the only free ligand and substrate peaks observed in the NMR. No peaks associated with ligation of the thiol substrate to the metal center appeared. After being heated to 130°C, complex **1** was observed to reform and, the reaction already having been exposed to air, oxidation of benzyl thiol proceeded as previously reported in Section 4.2.2

(Scheme 4-4). In the absence of dioxygen, complex **1** reacts stoichiometrically with dodecane thiol to form disulfide at room temperature, while oxidation of benzyl mercaptan is only accessible at elevated temperature.

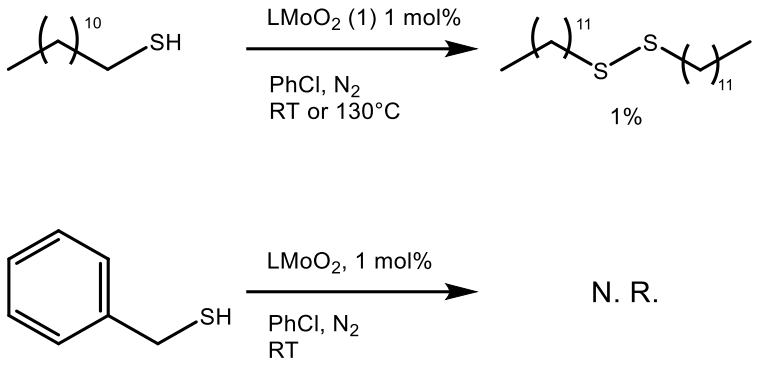

Scheme 4-9. Reactions of dodecane thiol and benzyl mercaptan with complex **1** under inert (N_2) atmosphere

4.1.6 Effects of the oxygen atom source on the benzyl mercaptan oxidation

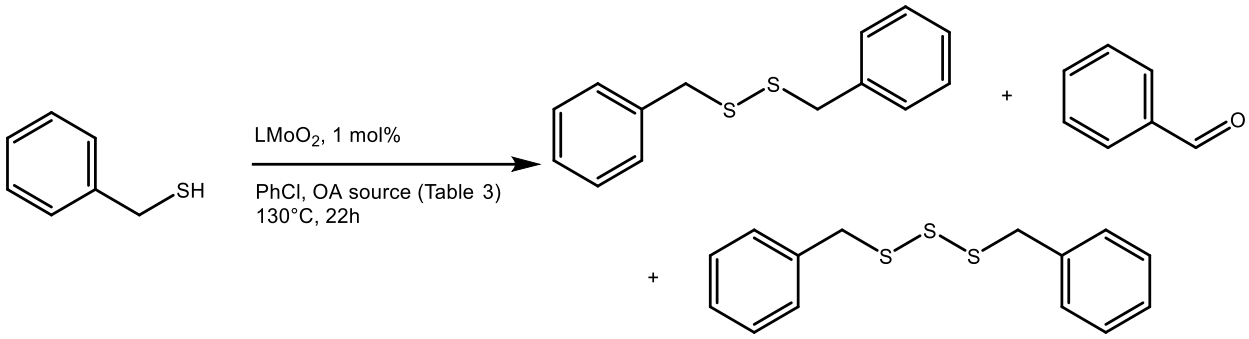

Scheme 4-10. Oxidation of benzyl mercaptan by catalyst **1** with variation of atmosphere/gaseous oxygen atom source

Table 4-2. Effects of oxygen atom source/atmosphere on conversion and product ratio for oxidation of benzyl mercaptan (Scheme 4-10)

O atom source	[thiol]	conversion at 22h	disulfide/trisulfide ratio
N_2	58 mM	1%	1/0
Air (21% O_2)	58 mM	20%	2.25
O_2 (1 atm)	58 mM	14%	3.75
N_2O (1 atm)	58 mM	31%	5.4

With an interest in the possible effects of different oxygen atom donors on the oxidation reaction, we carried out a series of experiments varying the atmosphere of the reaction (Scheme 4-10). The results of the reactions under inert atmosphere (N_2) are discussed in Section 4.2.5, and the results for these variations are reported in Table 4-2. The standard reaction conditions referenced so far in this chapter employ air as the dioxygen source (P_{O_2}= 0.21 atm), so pure O_2 was used with the aim of increasing the concentration of dissolved dioxygen in the reaction mixture. N_2O was employed as a convenient gaseous single-atom oxygen donor. Switching to an oxygen atmosphere had an unexpected effect on both rate of conversion and the yield of the benzyl trisulfide. The formation of the secondary product species had, to this point, been considered to proceed by oxidation by the activated oxoperoxo Mo(VI) species, which would be expected to increase in concentration due to the increase in P_{O_2}. Instead, the yield of secondary product was observed to decrease, suggesting that the pathway leading to the secondary product is inhibited by the coordination of dioxygen to the Mo(IV) center. This experiment does not clarify the relationship between the overall rate and the individual rates of disulfide and trisulfide formation, so the decrease in rate (14% conversion over 22h) could arise either from inhibition of the secondary product evolution or from quenching of a radical species involved in the formation of the disulfide.

Nitrous oxide was established as an oxygen atom source for molybdenum-catalyzed oxygen atom transfer reactions in 1991, when Arzoumanian, et al. reported oxidation of triphenyl phosphine by $[Mo^{IV}O(CN)_5][PPh_4]$ under a N_2O atmosphere. [32] Our own experiments confirm this activity for MoO_2sal-CHXD catalyst **1**. However, there are fewer examples in the literature than one might expect using this oxygen atom source. A limited number of catalytic oxygen atom transfer reactions have been reported with N_2O for complexes of first- (Fe, Co, Ni) and second-row (Mo, Ru) metals, despite several reports of other transition metal complexes forming terminal oxo groups by reaction with N_2O. [33] Using N_2O as an oxidant in a catalytic system has several potential benefits over using dioxygen: first, there is no need for a spin-crossover process, as observed in dioxygen-coordination systems (Chapter 3), second, that N_2O transfers only one oxygen atom, generating an oxo group directly rather than forming superoxo or peroxo species, and third, that the oxidant and reoxidized species do not have the potential for creating a radical

mechanism in competition with the target mechanistic pathway. [23] In the case of our system, switching the atmosphere to N_2O should restrict the catalytic cycle to the dioxo Mo(VI) form of the catalyst. In the experiment, reaction of benzyl mercaptan under an N_2O atmosphere (Scheme 4-10) and catalyst **1** results in an increase of both conversion (31% over 22h) and selectivity for the disulfide product (5.4:1).

Since the dioxomolybdenum species catalyzes formation of the disulfide product, the trisulfide must be formed by either the molybdenum oxoperoxo or by interaction of the thiol substrate with the Mo(IV) monooxo species. The increase in selectivity for the disulfide from an increase in P_{O_2} suggests that the trisulfide may form from a catalytic cycle involving the molybdenum (IV) monooxo complex.

4.1.7 Catalyst Variation

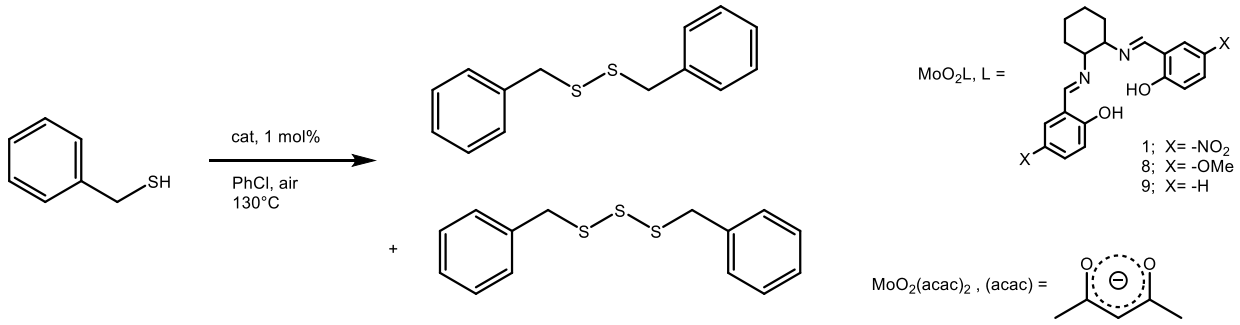

Scheme 4-11. Catalyst variation study for oxidation of benzyl mercaptan

Given the unexpected formation of trisulfide by reaction with complex **1** as a catalyst, we wished to investigate whether changes to the electronic character of the catalyst would change the reaction rate or the product distribution of the oxidation. All reactions for this study were carried at 1 mol % catalyst (0.58 mM), 58 mM benzyl mercaptan, and heated to 130°C in chlorobenzene (Scheme 4-11). Previous studies with triphenyl phosphine (Chapter 3, Section 3.1.1) had established that dioxygen coordination and transfer activity was exhibited by the *o*-OMe sal-CHXN (**8**) and sal-CHXD (**9**) derivatives of catalyst **1**, as well as the molybdenum-containing precursor, $MoO_2(acac)_2$, **10**. The reactivity of the *o*-OMe catalyst was presumed to be

transferrable to the *p*-OMe catalyst **8**, which was selected for the more direct electronic effect and absence of possible steric interference of the *para*-located electron donating group.

Table 4-3. Effects of catalyst variation on rate of conversion and product ratio for oxidation of benzyl mercaptan (Scheme 4-11).

catalyst	conversion at 22h	disulfide/trisulfide ratio
1	20%	2.25
8	63%	5.67
9	35%	22.00
10	46%	33.33

1 = MoO_2-*p*-NO_2-salCHXD, **8** = MoO_2-*p*-OMe-salCHXD, **9** = MoO_2-salCHXD, **10** = $MoO_2(acac)_2$

The variation in catalyst structure has a dramatic effect on conversion and product distribution of the thiol oxidation (Table 4-3). In the studied series of catalysts, the electron-poor catalyst **1** has the lowest activity for the oxidation of thiols, with increases in ligand electron-donating character giving greater conversion. The reaction with catalyst **8** was observed to have the highest conversion and an increased selectivity for the disulfide product (5.67:1 over the trisulfide) as compared to the *para*-nitro catalyst **1**, though the less active **9** shows much greater selectivity for the disulfide, and $MoO_2(acac)_2$ **10** forms the disulfide in much higher proportion, though a large number of side products are observed, amounting to nearly 20% of formed product. Many of the side products formed in the reaction with **10** are also produced by the Schiff-base complexes, but these catalysts seem to select for disulfide and trisulfide over all other possible oxidation products. Overall, formation of disulfide is disfavored by the presence of the strongly electron-withdrawing *para*-nitro groups (**1**) compared to the other molybdenum Schiff-base complexes (**8** & **9**), leading to a relative increase in yield for the trisulfide product.

4.2 Discussion

4.2.1 Sulfenic anhydride formation

We have assigned the structure of the secondary product of the oxidation of dodecane thiol as a sulfenic anhydride based on spectroscopic and mass data. This oxygen atom transfer

product stands in contrast to the formation of trisulfide from the benzylic substrate, which we suggest is a consequence of the reduced ease of oxidation for non-benzylic aliphatic carbon positions. In comparison with the benzyl disulfide reactions, the formation of stoichiometric dodecanal is not observed, nor is the formation of dodecane trisulfide.

Sulfenic anhydrides were first discussed in the literature as a potential intermediate in the formation of disulfides from thionyl chloride in 1915 and first reported in 1918 as an oxidation product of sulfinyl chlorides (Figure 4-8) [34].

Figure 4-8. Synthesis of 'sulfenic anhydrides' reported by Zincke and Baemer, 1918 [34]

Later evidence published by E. Vinkler [35] established that the previous synthetic routes to the “sulfenic anhydrides” produced only the isomeric thiosulfinate RS(S=O)R species. In concurrence with the observation that the thiolsulfinate species can be formed by oxidation of the corresponding disulfide [35,36]—and that the formation of a symmetric species by oxygen atom insertion into the S-S bond is not observed experimentally—we suggest that the sulfenic anhydride product is formed by a two-step HAT process from the thiol substrate to the oxoperoxo molybdenum (VI) catalyst. The HAT process generates a hydro- or hydroperoxo- molybdenum (IV) sulfenyl complex (Figure 4-9) followed by reaction with another molecule of thiol to produce the sulfenic anhydride, water, and the molybdenum (IV) monooxo species. We consider forming the sulfenic anhydride *via* a radical pathway (Figure 4-10) to be less likely based on the expected low concentration of the reactive radical intermediates.

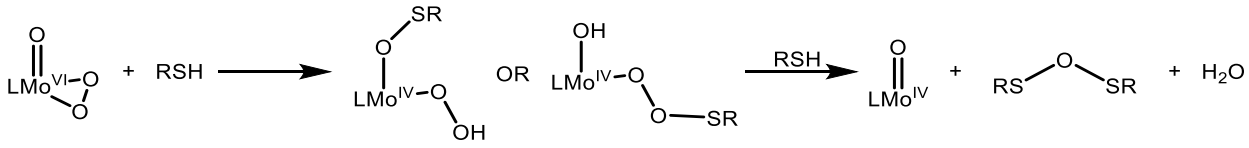

Figure 4-9. Possible reaction and intermediates for formation of sulfenic anhydride product

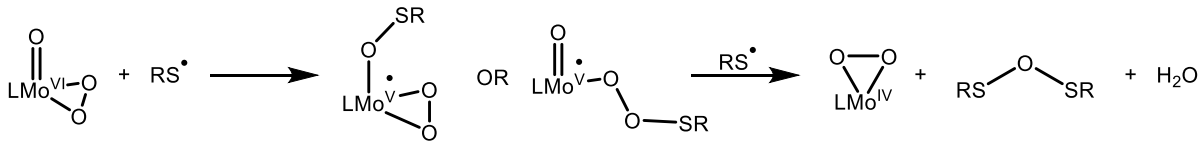

Figure 4-10. Possible radical-involved pathway for formation of sulfenic anhydride product

4.2.2 Computational investigation of initial reaction steps of thiol oxidation by $LMoO_2$

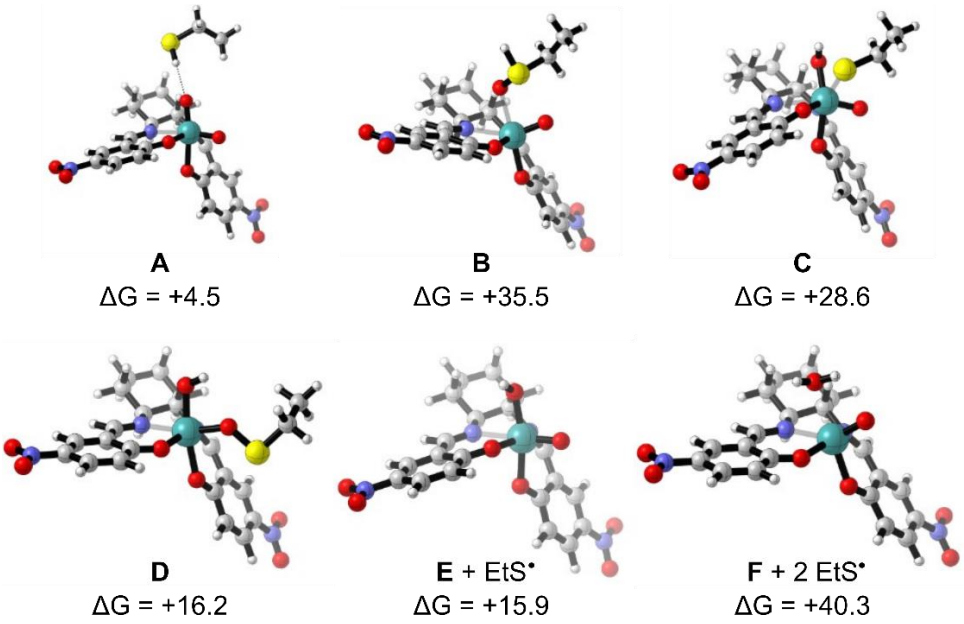

Figure 4-11. Optimized structures for suggested reaction intermediates for 1-electron oxidation of thiol by complex **1**. ΔG is given in kcal/mol relative to the starting materials (ethane thiol and complex **1**)

The structures represented in Figure 4-11 and Figure 4-12 were obtained by optimization of isomeric products of ethyl mercaptan interacting with complex **1**, using both the semi-empirical pm6 method and the DFT b3lyp functional as necessary to generate the target isomeric species (**A-D**, **G**, **H**). The structures for complexes **E** and **F** were obtained by optimization of the dioxomolybdenum (VI) complex with one (**E**) and two (**F**) added hydrogen atoms, using the b3lyp functional. The reaction mechanism is proposed to begin with structure **A** (+4.5 kcal/mol uphill from starting materials), having a hydrogen-bonding interaction between the axial oxo moiety and thiol. Nucleophilic attack on the oxo moiety by the thiol sulfur lone pair, producing an O-bonded zwitterionic moiety with an anionic oxygen and cationic, protonated sulfur, is disfavored, with the intermediate structure **B** +35.5 kcal/mol uphill from the starting materials, suggesting that a HAT pathway would be preferred (structures **C** and **D**). These structures both contain a formally 1-electron reduced sulfur center, though 7-coordinate structure **C**, with an axial hydroxy ligand and the thiyl/thiolate bound to the Mo center, is 12.5 kcal/mol less stable than the diradical triplet structure **D**, in which the thiyl radical is bonded to the equatorial oxo moiety.

Homolytic cleavage of the O-S bond present in **D** generates the molybdenum (V) hydroxy-monooxo species **E** and a thiyl radical (ΔG = -0.3 kcal/mol from **D**). A second hydrogen atom transfer from another molecule of thiol gives the hydrated molybdenum (IV) monooxo complex **F**, in which a water molecule occupies the axial coordination site of the molybdenum center, and a second thiol radical (ΔG = +24.4 kcal/mol from **E**), from which homo-coupling of the thiyl radicals and dissociation of water from the molybdneum center yield the molybdenum (IV) monooxo species, water, and product disulfide (ΔG = -36.3 kcal/mol). This overall process for formation and homo-coupling of two thiyl radicals from the thiol and oxo-Mo complex **1** has a ΔG of +4.0 kcal/mol.

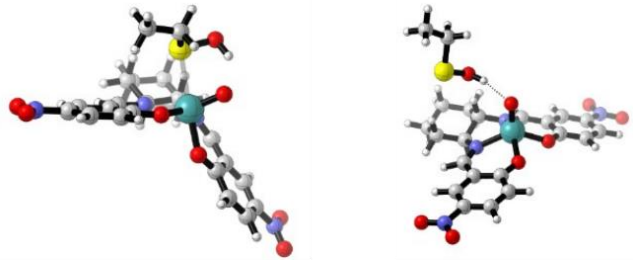

G ΔG = +20.1 **H** ΔG = +12.0

Figure 4-12. Optimized structures of intermediates for 2-electron reduction of ethane thiol with complex **1.** ΔG is given in kcal/mol relative to the starting materials (ethanethiol and complex **1**)

Modeling an attack of thiyl radical on the molybdenum hydroxyl group yields complex **G**, an S-ligated sulfenic acid molybdenum (IV) species (ΔG = +15.6 kcal/mol versus A), which could then dissociate to yield complex **H** (ΔG = -8.1 kcal/mol versus **G**), in which the sulfenic acid is hydrogen-bonded to the oxo moiety of the molybdenum (IV) monooxo complex. This pathway approximates the 2-electron reduction pathway of thiol to sulfenic acid. Comparison of the two modeled pathways shows that the 1-electron oxidation intermediate **D** is stabilized by 4.0 kcal/mol compared to the isomeric 2-electron reduction intermediate **G**, suggesting that the 1-electron pathway may be favored over the 2-electron pathway. Although complex **H** is stabilized relative the radical products (**E** + EtS$^{\bullet}$), the radical-forming pathway is the most favorable of the three modeled reaction pathways. That being said, the high energy of the products of the second HAT products (**F** + EtS$^{\bullet}$) indicates that this pathway may not proceed as modeled here. The

formation of disulfide from oxidation of dodecane thiol at room temperature reported in Section 4.1.5 shows that this reaction is not prohibitively endergonic, which suggests that the actual pathway for formation of a second molecule of thiyl radical does not occur by reaction with a single dioxomolybdenum moiety. Instead, we suggest the possibility that the two thiyl radicals form by HAT reactions involving two dioxomolybdenum (VI) complexes **1**, and that the hydroxy-oxo molybdenum (V) complex **E** then disproportionates to form one dioxomolybdenum (VI) complex and one oxomolybdenum (IV) aquo complex. The intermediate species for all reaction pathways are all higher in energy than the starting materials, but the formation of water and disulfide—along with the disproportionation of the molybdenum (V) species—are sufficient as thermodynamic driving forces for the reaction ($\Delta G_{overall}$ = -9.0 kcal/mol, Figure 4-13). Transition states and activation energies were not calculated for the oxidation pathways, so discussion of rate differences between the pathways is not possible.

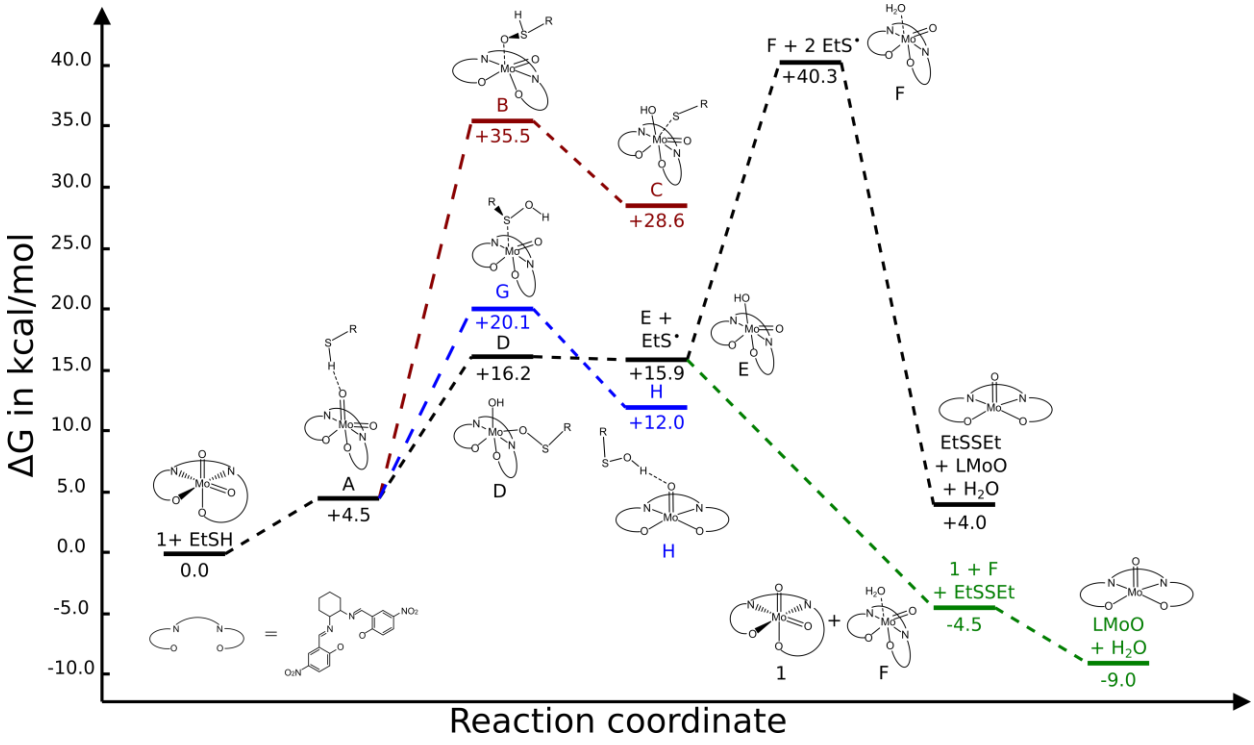

Figure 4-13. Reaction profile for modeled intermediate species for oxidation of thiols to disulfides by **1**.

4.2.3 Catalytic mechanism for formation of disulfide products

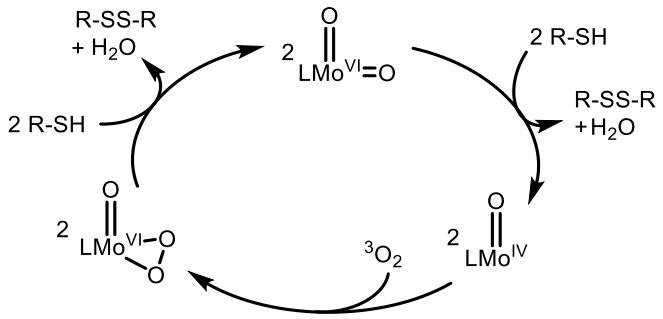

Figure 4-14. Possible catalytic cycle for generation of disulfides by dioxomolybdenum catalyst **1** under base-free conditions

Our experimental results suggest that the disulfide products are formed from both the dioxo- and oxoperoxo- molybdenum (VI) species, a process that may follow the catalytic cycle given in Figure 4-14. The first step of the oxidation proceeds by an atom-transfer process leading to the evolution of a sulfenic acid or thiyl radical intermediate [2,8], which is then able to form product disulfide and water by reaction with a free molecule of substrate thiol. The molybdenum (IV) monooxo species is then oxidized by dioxygen to the oxoperoxo species, which reacts with a molecule of thiol to produce another equivalent of thiyl radical intermediate through atom transfer from a peroxo moiety, regenerating the dioxomolybdenum species **1**.

The change in rate of conversion caused by addition of base is likely due to deprotonation of the thiol species (Figure 4-15). The thiolate ion is generally regarded to be a more reactive substrate towards 1-electron oxidation than the thiol, [37] reducing the thermodynamic barrier for the initial oxidation step. The decrease in conversion as the mol % of base increases may arise from a reaction step involving one thiol and one thiyl radical, or from a change in the pathway for regeneration of the dioxomolybdenum (VI) catalyst from either a molybdenum (V) 1-electron reduction product or a molybdenum (IV) 2-electron reduction product. The presence of thiolate in solution also gives another pathway for formation of disulfide bonds from the coupling of thiyl radical and thiolate to form a disulfide radical anion ($RSSR^{\bullet -}$), [2,38] a strong reductant that could then be oxidized either by dioxygen or an oxomolybdenum species.

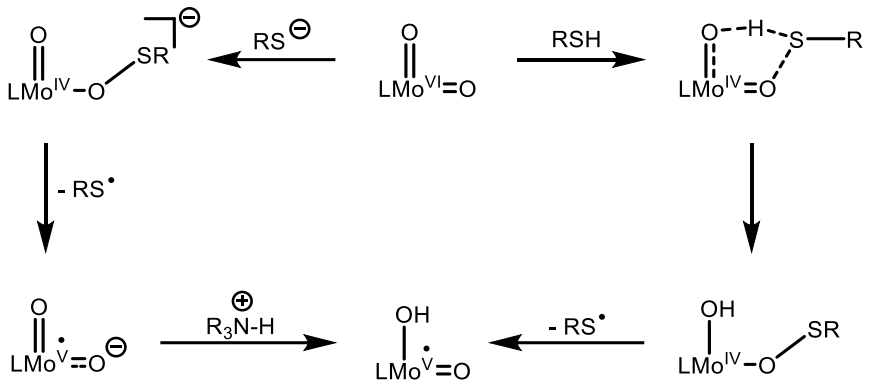

Figure 4-15. Possible oxidation pathways for base-promoted (left) and base-free (right) oxidation of thiol/thiolate to thiyl radical

4.2.4 Catalytic mechanism for formation of secondary products

The trisulfide product from benzyl thiol is suggested to form *via* a catalytic cycle (Figure 4-16) in which the molybdenum (VI) oxoperoxo species **11** carries out a multistep atom exchange and oxidation process with a molecule of the thiol substrate, yielding an aldehyde and the proposed oxo-sulfido species **1S**. Complex **1S** then reacts following the same pathway as complex **1**, forming disulfide, water, and a molybdenum (IV) monosulfido complex, which can react with dioxygen to form the molybdenum (VI) sulfidoperoxo complex **12**. This complex then reacts with a second molecule of thiol to produce the sulfenothiolate species **12b**, from which the trisulfide may be evolved by reaction with a molecule of thiol, yielding the trisulfide and water. The evolved oxomolybdenum (IV) species may then be oxidized to the oxoperoxo molybdenum (VI) by dioxygen. The increase in selectivity for the disulfide product as mol % of base increases demonstrates a change in the rate limiting step for formation of the trisulfide product, indicating that this step likely involves the protonated thiol substrate and the catalyst rather than the thiolate or thiyl radical.

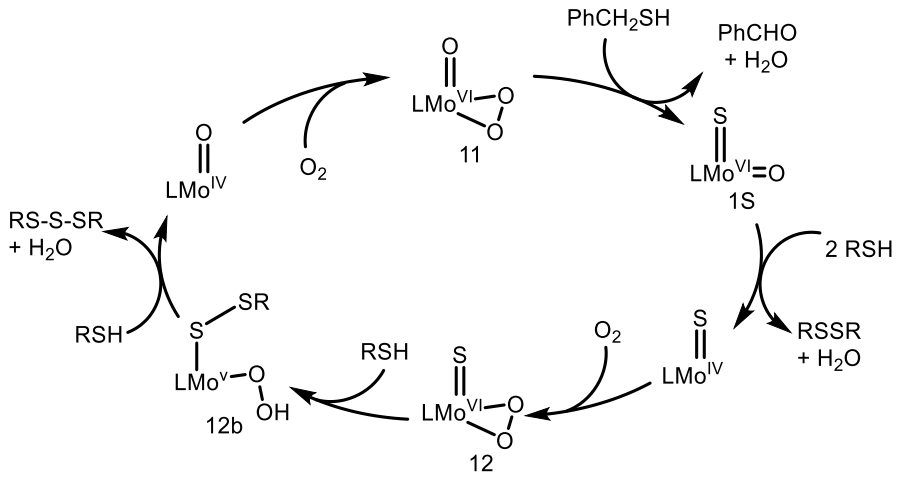

Figure 4-16. Possible catalytic cycle for formation of trisulfide by reaction with catalyst **1**

Molybdenum oxo-sulfido (or thio-oxo) molybdenum (VI) complexes are documented [39–42] as model complexes for reaction intermediates for xanthine oxidase and xanthine dehydrogenase, and can carry out sulfur atom transfer reactions with strong sulfur acceptors, such as triphenylphosphine. [43] While the formation of trisulfides by reaction with molybdenum (VI) sulfido complexes is not reported, the reverse reaction—abstraction of a sulfur atom from benzyl trisulfide by molybdenum species—is known for forming disulfido complexes. [43] Molybdenum (IV) oxo-sulfido intermediates are also invoked for the formation of thiiranes from olefin substrates. [44] Exchange reactions of oxo and sulfido groups have also been reported for strong sulfur donors, including hexamethyldisilathane, boron trisulfide, and Laweson's reagent (2,4-bis(p-methoxyphenyl)-1,3-dithiaphosphetane-2,4-disulfide). [43] As discussed in Chapter 3, molybdenum peroxo species are reported to oxidize benzylic alcohols to aldehydes, ketones and carboxylic acids, [45,46] though this has not been demonstrated to occur for aliphatic thiols until the current study. Outside of molybdenum catalysts, the oxidation of benzyl mercaptan to benzaldehyde has been demonstrated to occur with singlet oxygen as the oxidizing species, [47–49] using photocatalytic methods, as well as by atomic oxygen generated by photoexcitation of dibenzothiophene *S*-oxide. [50]

We suggest that the sulfenic anhydride product forms by a similar metal-centered mechanism to the trisulfide formation. There is no evidence in the literature for formation of the sulfenic anhydride by a condensation reaction of sulfenic acid species, as most small-molecule

sulfenic acid species are reported to undergo self-condensation to form thiosulfinates unless the sulfenic acid is made sterically or electronically stable. [2,51,52] Alternatively, we suggest radical coupling of thiyl and sulfenyl radicals could be the source of this product. The reactive intermediate species leading to formation of the sulfenic anhydride is proposed to be a metal-bound radical species analogous to the sulfenothiolate complex **12b**. Delocalization of the odd electron over the Mo-O bond serves to stabilize the forming sulfenyl moiety long enough for reaction with a molecule of thiol to occur, forming the sulfenic anhydride product and the molybdenum monooxo species.

This difference in reactivity and product from the two different thiols is suggested to be due to the reduced ease of oxidation for the α-methylene carbon in the dodecyl substrate, which prevents the oxo/sulfido exchange reaction described above for oxidation of benzyl mercaptan (Figure 4-16), thus preventing formation of aldehyde and trisulfide products with the dodecane substrate. The oxidative desulfurization of benzyl mercaptan has been previously investigated, with reports of formation of benzaldehyde by reaction with bases or peroxidic intermediates. [53] Metal-catalyzed C-S bond cleavage yielding alcohols has been reported for bimetallic cobalt and iron catalysts, [54,55] and a tungsten complex has been reported that is capable of completely cleaving sulfur from thiophenes by hydrodesulfurization. [56] The analogous molybdenum complex [57] is not capable of carrying out hydrodesulfurization of thiophene, though it is able to abstract selenium from selenophenes under the same conditions. There are, to the best of our knowledge, no reports of oxo-molybdenum or oxo-tungsten complexes performing oxidative desulfurization to either alcohol or aldehyde products.

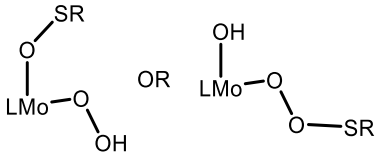

Figure 4-17. Possible molybdenum-bound sulfenate complexes leading to the formation of sulfenic anhydride

The lack of secondary products from the oxidation of N-acetyl cysteine may be explained by an increase in the ease of formation of the thiyl radical due to intramolecular hydrogen-bonding interactions, as mentioned in Section 4.1.2, [2,31] with the high availability of cysteine

thiyl species precluding the formation of either trisulfide or sulfenic anhydride secondary products *via* thiol-involved mechanisms.

4.3 Chapter Conclusions and Significance

To the best of our knowledge, this is the first report of molybdenum-catalyzed oxidation of thiols to disulfides using dioxygen as the stoichiometric oxidant. Further, this oxidation occurs catalytically in the absence of a base, and presumably produces only water as a byproduct, making it a greener option than the previously-reported molybdenum oxidations. We also report, to the best of our knowledge, the first formation of trisulfides from mercaptans without an additional source of sulfur. Finally, we report, with some caution, the first isolated sulfenic anhydride species.

Investigations of the molybdenum-catalyzed oxidative reaction forming disulfides from their respective thiols revealed several ways the reaction could be optimized towards formation of the target product. We find that the electronic character of the oxomolybdenum center has a key influence on the rate and product distribution, with more electron-rich complexes both accelerating the formation of disulfide and decreasing the relative yield of secondary products. Selectivity for disulfide and the rate of disulfide formation can be further increased by addition of sub-stoichiometric base, in keeping with other reports of oxo-metal catalyzed coupling of thiols to disulfides. Finally, our results with stoichiometric reactions and single-atom oxygen donors suggest that dioxomolybdenum complexes favor the formation of disulfide over the trisulfide and sulfenic anhydride secondary products. Taken together, these results indicate that the selectivity and rate of the catalytic oxidation can be optimized by using an electron-rich dioxomolybdenum catalyst (e.g. the *para*-methoxysalen complex **8**) with 5-10% added base and using N_2O. Similarly, the reaction conditions could be made to favor the secondary products by using an electron-poor dioxomolybdenum catalyst, such as complex **1** under reduced pressure of dioxygen without added base would favor the formation of benzyl trisulfide. Increasing catalyst loading beyond 1 mol% may also favor formation of trisulfide, though for this to be carried out on a practical scale, a more soluble catalyst would need to be developed, for which we suggest a *para*- or *ortho,para*-CF_3-functionalized salen ligand. We lack experimental evidence to make the

same proposal with regards to the sulfenic anhydride formed by oxidation of dodecane thiol, though the reaction pathway we suggest may imply that increasing the partial pressure of dioxygen could increase yield of the secondary product.

While we have clearly demonstrated the efficacy of the aerobic reaction for production of disulfides and the secondary oxidation products, and our computational results strongly suggest the reaction proceeds by a two-step HAT process, our experimental results do not directly illuminate the experimental pathway for either disulfide or secondary product formation. One of the key assumptions for the suggested mechanisms is that the ultimate fate of transferred oxygen atoms in the reaction is formation of water, which is also used to justify the otherwise endergonic pathway for formation of disulfide by reaction with the dioxomolybdenum species. The formation of water in the reaction could be assessed simply by running the reaction in a sealed system to allow for measuring of the stoichiometric relationship for the oxidized sulfur products and water. It would also be of interest to confirm that the disulfide formation reaction occurs *via* homo-coupling of thiyl radicals, which could be done using radical trapping experiments, and confirming which oxygen atoms are involved in the proposed hydrogen atom transfer steps of the catalytic oxidation. The latter study could be carried out using a sub-stoichiometric labeling experiment with ^{18}O-dioxygen as oxidant, with the ratio of labeled water yielding information about the oxidation pathway. Studies involving a radical trapping species could also be used to examine the possibility of radical quenching behavior for ground state oxygen under the studied reaction conditions. Beyond these primary mechanistic questions, there are several unresolved results relating to the oxidation products. The oxidation of *p*-chlorothiophenol is noted to form a mixture of products, of which the disulfide product is expected to be the major product, but trisulfides are not expected to be formed due to the difficulty of breaking a strong aromatic C-S bond. Determining the secondary product(s) for these substrates would contribute significant mechanistic knowledge for this oxidation process. Similarly, verification of the identity of the secondary product for oxidation of dodecane thiol, which we assign as the sulfenic anhydride, is important. As the formation of this product is proposed to be a result of the reduced ease of oxidation of the α-methylene carbon, a substrate survey could be carried out to determine which aliphatic thiols are oxidized to trisulfides and

which to sulfenic anhydrides. The involvement of sulfenic acid species in the formation of sulfenic anhydride products could be studied by using a reactive probe such as dimedone, which has been used to study cysteine sulfenic acids. [51]

4.4 Experimental

4.4.1 Catalytic reactions for disulfide/sulfenic anhydride/trisulfide formation

Typical reaction conditions:

To a round bottom flask was added 5.0 mg **1** (9.3 umol), 100 eq of thiol substrate (928.8 umol), and 16 mL chlorobenzene. The reaction flask was attached to an air condenser and heated to 130°C. Aliquots of the reaction mixture were taken between 20 and 24 hours of reaction time for analysis by No-D NMR and conversion was determined based on integration of the S-α-CH_2 peak.

Slow-addition reactions

To a 2-necked round bottom flask was added 32 mL chlorobenzene, 10 mg catalyst, and a stir bar. An equimolar mixture of thiol and 1,1,2,2-tetrachloroethane (as an internal NMR standard) was added by syringe pump at a rate of ~1 eq/h.

4.4.2 Purification of disulfides and sulfenic anhydrides

The reaction mixture from aerobic oxidation of thiol was concentrated under N_2 flow. The residue was redissolved in a small amount of DCM and adsorbed onto silica, then added to the top of a silica plug. The silica plug was washed with hexanes to isolate the oxidation products from the catalyst residue.

Dodecane thiol: The product mixture was purified using preparatory TLC with 3%EtOAc/hexane as the solvent. The disulfide was isolated from the band at R_f=0.7 and the putative sulfenic anhydride from the band at R_f=0.75. A later reaction was purified using High Performance Liquid Chromatography (HPLC) with a coupled Mass Spectrometer (MS) on a Shimadzu LCMS-2020 Single Quad/ESI ionization with a Luna C8(2) (5 µm, 100 Å, 250 mm x 10 mm) with MeOH (A)/water (0.1% formic acid) (B) as the eluent system [flow rate = 2.0 mL/min, 90% to 95% A over initial 20 min, 95% A for 60 min].

Dodecane disulfide: ^{1}H NMR (500 MHz, CDCl3) δ 2.74 – 2.62 (m, 4H), 1.68 (p, J = 7.5, 7.5, 7.4, 7.4 Hz, 4H), 1.39 (p, J = 6.8, 6.8, 6.5, 6.5 Hz, 4H), 1.35 – 1.22 (m, 32H), 0.89 (t, J = 6.9, 6.9 Hz, 6H). ^{13}C NMR (126 MHz, $CDCl_3$) δ 39.24, 31.92, 29.65, 29.60, 29.52, 29.35, 29.24, 28.54, 22.69, 14.12. (lit [30])

Bis-dodecyl sulfenic anhydride ^{1}H NMR (400 MHz, $CDCl_3$) δ 2.86 (t, *J* = 7.3, 7.3 Hz, 4H), 1.73 (p, *J* = 7.7, 7.7, 7.3, 7.3 Hz, 4H), 1.39 (p, *J* = 7.6, 7.5, 6.3, 6.2 Hz, 4H), 1.34 – 1.23 (m, 32H), 0.88 (t, *J* = 6.7, 6.7 Hz, 6H). ^{13}C NMR (101 MHz, $CDCl_3$) δ 38.88, 31.92, 29.66, 29.64, 29.59, 29.50, 29.36, 29.19, 28.82, 28.54, 22.70, 14.14. IR (KBr, cm^{-1}) UV-Vis (λ, nm) MS (DCM, ESI+) 419.34 (100%), 420.34 (22%), 421.34 (12%)

para-chlorophenyl disulfide: The product mixture from oxidation of p-chlorothiophenol was passed through a silica plug with hexane as the eluent. Solvent was removed under reduced pressure, yielding a light yellow powder (MP=67-70°C). Purity of the product was assessed by reverse phase HPLC on an Agilent series 1220 using a Gemini-NX C-18 (5 µm, 4.6 mm x 250 mm) column with H_2O (A) /acetonitrile (B) as the eluent system [flow rate of 1.0 mL/ min, gradient of 50% B to 65% B over 5 min, hold 65% B for 20 min, hold 100% B for 5 min]. Compounds elute at 28.26 and 28.96 min. ^{1}H NMR (500 MHz, $CDCl_3$) δ 7.49 – 7.37 (m, 1H), 7.36 – 7.27 (m, 1H). ^{13}C NMR (126 MHz, $CDCl_3$) δ 135.21, 133.73, 129.45, 129.29.

Benzyl thiol: The product mixture was passed through a silica plug with hexane as the eluent. Solvent was removed under reduced pressure, yielding a clear oil. The products were purified by reverse phase HPLC using a Bakerbond C-18 (10 µm, 150 Å, 21.2 mm x 250 mm) column with H_2O (A) /acetonitrile (B) as the eluent system [flow rate = 4 mL/min, 10 min at 76% B, gradient of 76% B to 92% B over 10 min, flow rate changed to 3.5 mL/min, hold 92% B for 15 min].

Benzyl disulfide was isolated as white needle-like crystals [monoclinic, *C2* (5), *a*=24.352(3), *b*=8.1284(12), *c*=13.4880(19) Å, *α*=*γ*=90°, *β*=114.255(5)°. *U*=2434.2(6) Å^3.] ^{1}H NMR (400 MHz, CDCl3) δ 7.38 – 7.20 (m, 10H), 3.60 (s, 4H). ^{13}C NMR (101 MHz, $CDCl_3$) δ 137.35, 129.43, 128.50, 127.45, 43.23. IR (KBr, cm^{-1}) υ_{max} = 1402 cm^{-1}.

Benzyl trisulfide was isolated as a white powder with no noticeable odor. ^{1}H NMR (500 MHz, $CDCl_3$) δ 7.35-7.26 (m, 10H), 4.03 (s, 4H). ^{13}C NMR (101 MHz, $CDCl_3$) δ 136.51, 129.46, 128.62, 127.59, 43.11. IR (KBr, cm^{-1}) υ_{max} = 1494 cm^{-1}.

N-acetyl cystine: Oxidation yielded a single product (>95% NMR yield), which was not isolated from the reaction mixture. ^{1}H NMR (500 MHz, PhCl) δ= 11.94 (s, 1H), 4.39 (tt, *J* = 8.4, 8.4, 1.7, 1.7 Hz, 2H), 3.02 (dd, *J* = 11.2, 8.4 Hz, 2H), 2.60 (dd, *J* = 11.2, 9.9 Hz, 2H), 1.46 (d, *J* = 1.6 Hz, 6H). lit [58] (400 MHz, D_2O) δ = 4.65 (dd, J = 4.4, 8.7 Hz, 2H), 3.24 (dd, J = 14.3, 4.4 Hz, 2H), 2.96 (dd, J = 14.3, 8.7 Hz, 2H), 1.98 (s, 6H)

4.4.3 Reaction condition variation studies

Reaction study for potential overoxidation of disulfides

To a round bottom flask was added 5.4 mg (10.0 µmol) of *p*-nitrosalCHXD dioxomolybdenum complex, 22.9 mg (93.0 µmol, 9 eq) of bisbenzyldisulfide, 15 mL chlorobenzene, and a stir bar. The flask was attached to a reflux condenser and placed in a 130°C oil bath. The reaction was monitored by No-D NMR of reaction aliquots.

Base-inclusive reaction conditions:

To a round bottom flask was added 5.0 mg MoO_2L^{5NO2} (9.3 umol), 100 eq of thiol substrate (930 µmol), 16 mL chlorobenzene, and diisopropylethylamine (1, 5, 25, and 100 eq, respectively). The reaction flask was attached to a jacketed condenser and heated to to 130°C. Aliquots of the reaction were taken between 20 and 24 hours of reaction time for analysis by No-D NMR and conversion was determined based on integration of the S-α-CH_2 peak.

General procedure for atmospheric variation studies of benzyl mercaptan oxidation

To a 50 mL round bottom flask was added 5 mg (9.29 µmol) of catalyst **1**, a stir bar, 16 mL chlorobenzene, and 9.8 µL of 1,1,2,2-tetrachloroethane (92.9 µmol) as an internal standard. The flask was sonicated to dissolve the catalyst and benzyl mercaptan (109 µL, 929 µmol) was added by Eppendorf pipette. The reaction flask was then attached to a manometer apparatus, which

was evacuated and backfilled with 1 atmosphere of the target gas (N_2, air, O_2, or N_2O). The reaction flask was placed in an oil bath at 130°C for 22 hours, at which point the reaction was removed from heat and conversion of substrate was measured by ^{1}H NMR based on integration of the α-methylene protons.

General procedure for catalyst variation studies of benzyl mercaptan oxidation

To a 50 mL round bottom flask was added catalyst, chlorobenzene, and a stir bar. The reaction mixture was sonicated to dissolve the catalyst and benzyl mercaptan was added by pipette. The flask was attached to a reflux condenser and placed in an oil bath at 130°C for 22h, at which point the reaction was removed from heat and conversion of substrate was measured by ^{1}H NMR based on integration of the α-methylene protons.

Table 4-4. reaction conditions for catalyst variation study

catalyst	µmol catalyst	mmol BnSH	Volume PhCl
MoO_2L^{5NO2}	9.29	0.929	16.0 mL
MoO_2L^{5OMe}	9.83	0.983	16.9 mL
MoO_2L^{5H}	11.2	1.12	19.2 mL
$MoO_2(acac)_2$	15.3	1.53	26.4 mL

4.4.4 Preparative reactions

Synthesis of authentic dodecyl disulfide by organic methodology

To a round bottom flask was added 5 mmol dodecane thiol and one equivalent sodium methoxide as 30% NaOMe in MeOH. The reaction mixture was stirred open to the atmosphere at RT for 20h. Once complete by TLC, the reaction mixture was concentrated under vacuum and the residue was redissolved in THF. To the solution was added saturated sodium thiosulfate (10 mL) and the mixture was agitated. The organic layer was removed and the aqueous layer extracted three times with EtOAc (10 mL). The combined organic layers were dried with sodium sulfate and concentrated under vacuum to isolate product as a waxy solid, MP=29-30°C.

^{1}H NMR (500 MHz, $CDCl_3$) δ 2.74 – 2.62 (m, 4H), 1.68 (p, *J* = 7.5, 7.5, 7.4, 7.4 Hz, 4H), 1.39 (p, *J* = 6.8, 6.8, 6.5, 6.5 Hz, 4H), 1.28 (d, *J* = 7.0 Hz, 32H), 0.89 (t, *J* = 6.9, 6.9 Hz, 6H). ^{13}C NMR (126 MHz, $CDCl_3$) δ 39.24, 31.92, 29.65, 29.60, 29.52, 29.35, 29.24, 28.54, 22.69, 14.12. (lit [30])

Preparation of (±)-*trans*-5-methoxycyclohexylsalen ligand

The p-OMe salen ligand was synthesized by a modification to literature procedure. [59] To a pear-shaped flask was added 5 mmol salicylaldehyde (0.758 g, 5.0 mmol), (±)-*trans*-cyclohexanediamine (0.299 g, 2.5 mmol), and 50 ml of ethanol. A magnetic stir bar was added and the flask was connected to a Soxhlet extractor containing a thimble of sodium sulfate and a condenser. The flask was heated to reflux for 6 hours. The product was isolated *via* vacuum filtration (718.6 mg) and recrystallized from methanol (487.4 mg, 1.3 mmol, 99% pure by NMR), yielding yellow-green rod-shaped crystals. Concentration of the supernatant provided a further 157.6 mg, 0.4 mmol, >95% pure by NMR). Total yield was 675 mg with 93% recovery and 70% yield.

^{1}H NMR (300 MHz, $CDCl_3$) δ 13.76 (s, 2H), 8.09 (s, 2H), 7.00 (d, *J* = 8.6 Hz, 2H), 6.37 (d, *J* = 2.5 Hz, 2H), 6.31 (dd, *J* = 8.5, 2.3 Hz, 2H), 3.77 (s, 6H), 3.28 – 3.16 (m, 2H), 1.96 (d, *J* = 13.4 Hz, 2H), 1.91 – 1.82 (m, 2H), 1.68 (d, *J* = 10.9 Hz, 2H), 1.46 (q, *J* = 10.8, 10.8, 10.5 Hz, 2H).

Preparation of (±)-*p*-methoxycyclohexylsalen dioxomolybdenum (**9**)

The dioxomolybdenum *p*-methoxycyclohexylsalen complex was synthesized by modification of a literature procedure [60] by placing 200 mg of p-OMe ligand (0.5 mmol) and 170.6 mg (0.5 mmol) of bis(acetylacetonato)-dioxomolybdenum in a 250 ml round bottom flask. A stir bar and 100 ml of ethanol was added to the flask. The flask was then connected to an air-cooled condenser and placed in a heating bath. The solution was heated to reflux, initially becoming rust-colored, and changing to yellow as the reaction progressed. Reaction progress monitored by TLC. After a total of 13 hours of reaction time, the solution was reduced *in vacuo* to 50 ml. The product was isolated by vacuum filtration as a yellow solid with total yield of 132.5 mg (0.3 mmol, 55% yield) and >95% pure by NMR.

^{1}H NMR (500 MHz, $CDCl_3$) δ 8.31 (s, 1H), 8.31 (s, 1H), 7.33 (d, *J* = 8.6 Hz, 1H), 7.29 (d, *J* = 9.0 Hz, 1H), 6.68 (d, *J* = 2.4 Hz, 1H), 6.63 (dd, *J* = 8.6, 2.5 Hz, 1H), 6.43 (d, J = 2.4 Hz, 1H), 6.40 (dd, J = 8.8, 2.4 Hz, 1H), 4.15 (td, *J* = 10.8, 3.2 Hz, 1H), 3.88 (s, 3H), 3.81 (s, 3H), 2.79 (tdd, J = 10.8, 4.1, 2.0 Hz,

1H), 2.52 (dtd, J = 11.9, 6.9, 2.9 Hz, 1H), 2.38 (dtd, J = 10.7, 5.5, 2.1 Hz, 1H), 2.07 (d, *J* = 13.0 Hz, 2H), 1.71 (qt, J = 11.9, 3.2 Hz, 2H), 1.55 (qt, J = 12.9, 3.2 Hz, 1H), 1.40 (qt, J = 13.5, 3.3 Hz, 1H). ^{13}C NMR (126 MHz, $CDCl_3$) δ 170.68, 167.58, 165.24, 161.84, 159.93, 159.84, 135.60, 134.30, 117.54, 114.93, 109.63, 109.53, 103.21, 101.99, 72.61, 70.94, 55.66, 55.48, 30.04, 28.72, 24.64, 23.92. IR (KBr, cm^{-1}): 2929, 2854, 1608, 1612, 1541, 1521, 1384, 1224, 910 ($MoO_{2\ sym}$), 873 ($MoO_{2\ asym}$), 590, 518.

4.4.5 Computational methods

All calculations were carried out using Gaussian 09. Structures were optimized using the B3LYP hybrid functional and the basis sets: Mo, LANL2DZ; S, 6-311++G(d,p); C, H, O, N, 6-311G(d) using Gaussian 09's ultrafine integration grid. The free energy correction to the energy was taken from the B3LYP frequency calculation. Reaction profiles were generated using the mechaSVG program. [61]

CITATION FOR GAUSSIAN 09

Gaussian 09, Frisch, M. J.; Trucks, G. W.; Schlegel, H. B.; Scuseria, G. E.; Robb, M. A.; Cheeseman, J. R.; Scalmani, G.; Barone, V.; Mennucci, B.; Petersson, G. A.; Nakatsuji, H.; Caricato, M.; Li, X.; Hratchian, H. P.; Izmaylov, A. F.; Bloino, J.; Zheng, G.; Sonnenberg, J. L.; Hada, M.; Ehara, M.; Toyota, K.; Fukuda, R.; Hasegawa, J.; Ishida, M.; Nakajima, T.; Honda, Y.; Kitao, O.; Nakai, H.; Vreven, T.; Montgomery, Jr., J. A.; Peralta, J. E.; Ogliaro, F.; Bearpark, M.; Heyd, J. J.; Brothers, E.; Kudin, K. N.; Staroverov, V. N.; Kobayashi, R.; Normand, J.; Raghavachari, K.; Rendell, A.; Burant, J. C.; Iyengar, S. S.; Tomasi, J.; Cossi, M.; Rega, N.; Millam, J. M.; Klene, M.; Knox, J. E.; Cross, J. B.; Bakken, V.; Adamo, C.; Jaramillo, J.; Gomperts, R.; Stratmann, R. E.; Yazyev, O.; Austin, A. J.; Cammi, R.; Pomelli, C.; Ochterski, J. W.; Martin, R. L.; Morokuma, K.; Zakrzewski, V. G.; Voth, G. A.; Salvador, P.; Dannenberg, J. J.; Dapprich, S.; Daniels, A. D.; Farkas, Ö.; Foresman, J. B.; Ortiz, J. V.; Cioslowski, J.; Fox, D. J. Gaussian, Inc., Wallingford CT, 2009.

Table 4-5. B3LYP calculated free energies (gas phase, Hartrees) for initial species involved in oxidation of thiols by complex **1**

Species	G
1	-1661.05061
EtSH	-478.00941
A	-2139.29474
B	-2139.24526
C	-2139.25623
D	-2139.27612
E	-1661.89453
$EtS^{\bullet}$	-477.38203
F	-1662.48304
G	-2139.26983
H	-2139.28275
$LMo^{IV}O$	-1586.05986
EtSSEt	-954.81483
H_2O	-76.43026

4.5 Works Cited

[1] D.D. Link, J.P. Baltrus, K.S. Rothenberger, P. Zandhuis, D.K. Minus, R.C. Striebich, Class- and Structure-Specific Separation, Analysis, and Identification Techniques for the Characterization of the Sulfur Components of JP-8 Aviation Fuel, Energy Fuels. 17 (2003) 1292–1302.

[2] M. Trujillo, B. Alvarez, R. Radi, One- and two-electron oxidation of thiols: mechanisms, kinetics and biological fates, Free Radical Research. 50 (2016) 150–171.

[3] H. Golchoubian, F. Hosseinpoor, Aerobic oxidation of thiols to disulfides catalyzed by a manganese(III) Schiff-base complex, Catalysis Communications. 8 (2007) 697–700.

[4] N.S. Panina, A.V. Eremin, A.N. Belyaev, Effect of metal nature (Ni, Pd, Pt) on the catalytic oxidation of aliphatic thiols: Quantum-chemical DFT modeling of separate steps of the catalytic cycle, Russ J Gen Chem. 85 (2015) 1655–1660.

[5] U. Burner, C. Obinger, Transient-state and steady-state kinetics of the oxidation of aliphatic and aromatic thiols by horseradish peroxidase, FEBS Letters. 411 (1997) 269–274.

[6] T. Nauser, W.H. Koppenol, C. Schöneich, Protein thiyl radical reactions and product formation: a kinetic simulation, Free Radical Biology and Medicine. 80 (2015) 158–163.

[7] S.P. Mezyk, Rate Constant Determination for the Reaction of Hydroxyl and Glutathione Thiyl Radicals with Glutathione in Aqueous Solution, J. Phys. Chem. 100 (1996) 8861–8866.

[8] A. Zeida, R. Babbush, M.C. González Lebrero, M. Trujillo, R. Radi, D.A. Estrin, Molecular Basis of the Mechanism of Thiol Oxidation by Hydrogen Peroxide in Aqueous Solution: Challenging the SN2 Paradigm, Chem. Res. Toxicol. 25 (2012) 741–746.

[9] D. Witt, Recent Developments in Disulfide Bond Formation, Synthesis. 2008 (2008) 2491–2509.

[10] T.J. Wallace, A. Schriesheim, The base-catalysed oxidation of aliphatic and aromatic thiols and disulphides to sulphonic acids, Tetrahedron. 21 (1965) 2271–2280.

[11] J.A. Fernández-Salas, S. Manzini, S.P. Nolan, Efficient ruthenium-catalysed S–S, S–Si and S–B bond forming reactions, Chemical Communications. 49 (2013) 5829–5831.

[12] C.F. Cullis, J.D. Hopton, C.J. Swan, D.L. Trimm, Oxidation of thiols in gas-liquid systems. II. Reaction in the presence of added metal catalysts, Journal of Applied Chemistry. 18 (1968) 335–339.

[13] S. Shinkai, S. Yamada, R. Ando, T. Kunitake, A flavoenzyme model: Facile oxidation of thiols by a flavin immobilized in cationic polyelectrolytes, Bioorganic Chemistry. 9 (1980) 238–247.

[14] A. Dhakshinamoorthy, M. Alvaro, H. Garcia, Aerobic oxidation of thiols to disulfides using iron metal–organic frameworks as solid redox catalysts, Chemical Communications. 46 (2010) 6476–6478.

[15] T.J. Wallace, Reactions of Thiols with Metals. I. Low-Temperature Oxidation by Metal Oxides1, Journal of Organic Chemistry. 31 (1966) 1217–1221.

[16] T. Nakaya, H. Arabori, M. Imoto, The Oxidation of Thiols to Disulfides with Manganic Tris (acetylacetonate), BCSJ. 43 (1970) 1888–1889.

[17] A. Corma, T. Ródenas, M.J. Sabater, Aerobic oxidation of thiols to disulfides by heterogeneous gold catalysts, Chem. Sci. 3 (2012) 398–404.

[18] G.F. Pavelko, Reactions of thiols and organic disulfides with iron and its oxides, Russ Chem Bull. 55 (2006) 1436–1439.

[19] M. Kirihara, K. Okubo, T. Uchiyama, Y. Kato, Y. Ochiai, S. Matsushita, A. Hatano, K. Kanamori, Aerobic Oxidation of Thiols to Disulfides Catalyzed by Trichlorooxyvanadium, Chemical and Pharmaceutical Bulletin. 52 (2004) 625–627.

[20] T.V. Rao, B. Sain, P.S. Murthy, T.S.R.P. Rao, G.C. Joshi, A.K. Jain, Iron(III)–Ethylenediaminetetraacetic AcidMediated Oxidation of Thiols to Disulfides with MolecularOxygen†, J. Chem. Res. (S). (1997) 300–301.

[21] S.M.S. Chauhan, A. Kumar, K.A. Srinivas, Oxidation of thiols with molecular oxygen catalyzed by cobalt(II) phthalocyanines in ionic liquid, Chemical Communications. (2003) 2348–2349.

[22] H. Firouzabadi, M. Naderi, A. Sardarian, B. Vessal, The Facile Oxidation of Thiols to Disulfides with Bis(2,2′-Bipyridyl) Copper-(II) Permanganate, Synthetic Communications. 13 (1983) 611–615.

[23] R. Mishra, R. Banerjee, S. Mukhopadhyay, Cu(II)-catalyzed oxidation of thiols by superoxide ligated to CoIII2, Journal of Physical Organic Chemistry. 25 (2012) 1193–1197.

[24] K. Tanaka, K. Ajiki, Cationic rhodium(I)/PPh3 complex-catalyzed dehydrogenation of alkanethiols to disulfides under inert atmosphere, Tetrahedron Letters. 45 (2004) 25–27.

[25] E.W. Harlan, J.M. Berg, R.H. Holm, Thermodynamic fitness of molybdenum(IV,VI) complexes for oxygen-atom transfer reactions, including those with enzymic substrates, J. Am. Chem. Soc. 108 (1986) 6992–7000.

[26] R. Sanz, R. Aguado, M.R. Pedrosa, F.J. Arnáiz, Simple and Selective Oxidation of Thiols to Disulfides with Dimethylsulfoxide Catalyzed by Dichlorodioxomolybdenum(VI), Synthesis. 2002 (2002) 856–858.

[27] M.N. Sheng, J.G. Zajacek, Oxidation of thiols to thiolsulfonates and sulfonic acids, US3670002A, 1972.

[28] W. Li, S.K. Chen, Z.H. Huang, S.X. Fang, C. Li, Trichloromonoxomolybdenum(V): An Efficient Catalyst for the Preparation of Symmetrical Disulfides from Thiols, Advanced Materials Research. 233–235 (2011) 62–65.

[29] A. Kertmen, S. Lach, J. Rachon, D. Witt, Novel and efficient methods for the synthesis of symmetrical trisulfides, Synthesis. (2009) 1459–1462.

[30] M. Kirihara, Y. Asai, S. Ogawa, T. Noguchi, A. Hatano, Y. Hirai, A Mild and Environmentally Benign Oxidation of Thiols to Disulfides, Synthesis. 2007 (2007) 3286–3289.

[31] H.-K. Woo, K.-C. Lau, X.-B. Wang, L.-S. Wang, Observation of Cysteine Thiolate and -S···H–O Intermolecular Hydrogen Bond, J. Phys. Chem. A. 110 (2006) 12603–12606.

[32] H. Arzoumanian, D. Nuel, J. Sanchez, Oxygen atom transfer from dimethyl sulfoxide and N2O to triphenylphosphine mediated by a cyanooxomolybdate(IV) anion, Journal of Molecular Catalysis. 65 (1991) L9–L11.

[33] K. Severin, Synthetic chemistry with nitrous oxide, Chem. Soc. Rev. 44 (2015) 6375–6386.

[34] Th. Zincke, J. Baeumer, II. Über Arylschwefelchloride. Über p-Chlor-o-nitrophenylschwefelchlorid. Überführung in Thiazinderivate, Justus Liebigs Ann. Chem. 416 (1918) 86–112.

[35] E. Vinkler, Investigations in the field of organic sulfur compounds, Acta Chimica. 15 (1958) 385–388.

[36] A.L. Moguin, Intramolecular Bifunctional Catalysis of the Racemization of Phenyl Benzenethiolsulfinate, Masters' Thesis, Oregon State University, 1969.

[37] A. Mirzahosseini, B. Noszál, Species-Specific Standard Redox Potential of Thiol-Disulfide Systems: A Key Parameter to Develop Agents against Oxidative Stress, Sci Rep. 6 (2016) 37596.

[38] A.D. Leu, D.A. Armstrong, Thiyl radical oxidation of copper(I): formation and spectra of oxidized copper thiolates, J. Phys. Chem. 90 (1986) 1449–1454.

[39] J.H. Enemark, C.G. Young, Bioinorganic Chemistry of Pterin-Containing Molybdenum and Tungsten Enzymes**Dedicated to Professor R. C. Bray on the occasion of his retirement and in recognition of his elegant and stimulating research on molybdenum enzymes, particularly his EPR studies of their molybdenum centers., in: A.G. Sykes (Ed.), Advances in Inorganic Chemistry, Academic Press, 1993: pp. 1–88.

[40] C.G. Young, L.J. Laughlin, S. Colmanet, S.D.B. Scrofani, Oxygen Atom Transfer, Sulfur Atom Transfer, and Correlated Electron−Nucleophile Transfer Reactions of Oxo- and Thiomolybdenum(IV) Complexes: Synthesis of Oxothiomolybdenum(VI) and (Hydroxo)oxomolybdenum(V) Species, Inorganic Chemistry. 35 (1996) 5368–5377.

[41] E. Hofer, W. Holzbach, K. Wieghardt, Configurational Isomerization of N,N-Disubstituted Hydroxylamido(1-)-O,N-Molybdenum(VI) Complexes, Angewandte Chemie International Edition in English. 20 (1981) 282–283.

[42] J.W. Faller, Y. Ma, A mononuclear oxosulfidomolybdenum(VI) complex and other oxo, sulfido, and .eta.2-S2O derivatives of (pentamethylcyclopentadienyl)molybdenum and -tungsten, Organometallics. 8 (1989) 609–612.

[43] J.P. Donahue, Thermodynamic Scales for Sulfur Atom Transfer and Oxo-for-Sulfido Exchange Reactions, Chemical Reviews. 106 (2006) 4747–4783.

[44] W. Adam, R.M. Bargon, W.A. Schenk, Direct Episulfidation of Alkenes and Allenes with Elemental Sulfur and Thiiranes as Sulfur Sources, Catalyzed by Molybdenum Oxo Complexes, J. Am. Chem. Soc. 125 (2003) 3871–3876.

[45] K. Jeyakumar, D.K. Chand, Aerobic oxidation of benzyl alcohols by MoVI compounds, Applied Organometallic Chemistry. 20 (2006) 840–844.

[46] S. Das, T. Bhowmick, T. Punniyamurthy, D. Dey, J. Nath, M.K. Chaudhuri, Molybdenum(VI)-peroxo complex catalyzed oxidation of alkylbenzenes with hydrogen peroxide, Tetrahedron Letters. 44 (2003) 4915–4917.

[47] E. Baciocchi, T. Del Giacco, O. Lanzalunga, A. Lapi, Singlet Oxygen Promoted Carbon−Heteroatom Bond Cleavage in Dibenzyl Sulfides and Tertiary Dibenzylamines. Structural Effects and the Role of Exciplexes, Journal of Organic Chemistry. 72 (2007) 9582–9589.

[48] A. Guerrero-Corella, A.M. Martinez-Gualda, F. Ahmadi, E. Ming, A. Fraile, J. Alemán, Thiol–ene/oxidation tandem reaction under visible light photocatalysis: synthesis of alkyl sulfoxides, Chemical Communications. 53 (2017) 10463–10466.

[49] B. Hong, A. Lee, Visible-light-mediated oxidative C–S bond cleavage of benzyl thiols through in situ activation strategy, Org. Biomol. Chem. 20 (2022) 5938–5942.

[50] S.M. Omlid, M. Zhang, A. Isor, R.D. McCulla, Thiol Reactivity toward Atomic Oxygen Generated during the Photodeoxygenation of Dibenzothiophene S-Oxide, Journal of Organic Chemistry. 82 (2017) 13333–13341.

[51] L.J. Alcock, M.V. Perkins, J.M. Chalker, Chemical methods for mapping cysteine oxidation, Chem. Soc. Rev. 47 (2018) 231–268.

[52] V. Gupta, K.S. Carroll, Sulfenic acid chemistry, detection and cellular lifetime, Biochimica et Biophysica Acta (BBA) - General Subjects. 1840 (2014) 847–875.

[53] T.J. Wallace, H. Pobiner, A. Schriesheim, Mercaptan Oxidations. VII. Oxidative Desulfurization of Benzyl Mercaptan, Benzyl Disulfide, and Related Species, Journal of Organic Chemistry. 29 (1964) 888–891.

[54] T. Ganguly, A. Das, M. Jana, A. Majumdar, Cobalt(II)-Mediated Desulfurization of Thiophenes, Sulfides, and Thiols, Inorganic Chemistry. 57 (2018) 11306–11309.

[55] T. Ganguly, A. Das, A. Majumdar, Iron(II) Mediated Desulfurization of Organosulfur Substrates Produces Nonheme Diiron(II)-hydrosulfides, Inorganic Chemistry. 58 (2019) 9998–10011.

[56] A. Sattler, G. Parkin, Carbon−Sulfur Bond Cleavage and Hydrodesulfurization of Thiophenes by Tungsten, J. Am. Chem. Soc. 133 (2011) 3748–3751.

[57] D. Buccella, K.E. Janak, G. Parkin, Reactivity of Mo(PMe3)6 towards Benzothiophene and Selenophenes: New Pathways Relevant to Hydrodesulfurization, J. Am. Chem. Soc. 130 (2008) 16187–16189.

[58] S. Nicolis, M. Zucchelli, E. Monzani, L. Casella, Myoglobin Modification by Enzyme-Generated Dopamine Reactive Species, Chemistry – A European Journal. 14 (2008) 8661–8673.

[59] K. Ambroziak, Z. Rozwadowski, T. Dziembowska, B. Bieg, Synthesis and spectroscopic study of Schiff bases derived from trans-1,2-diaminocyclohexane. Deuterium isotope effect on 13C chemical shift, Journal of Molecular Structure. 615 (2002) 109–120.

[60] K. Ambroziak, New dioxomolybdenum(VI) complexes of tetradentate Schiff base as catalysts for epoxidation of olefins, Journal of Molecular Catalysis A: Chemical. 211 (2004) 9–16.

[61] Angnes, R. A. mechaSVG, GitHub repository, 2020, doi: 10.5281/zenodo.3970267.

CONCLUSIONS

The robust atom transfer activity of molybdenum complexes has been long-established, but the work presented here shows that there are avenues of exploration and details of molybdenum-catalyzed OAT to be investigated. Our study of kinetic resolutions of phosphines reveals that catalytic oxygen atom transfer is a potential practical method for resolution of racemic chiral monophosphines and that standard DFT methods are robust enough to predict trends in selectivity for enantioselective oxygen atom transfer. The development of more selective catalyst for this resolution will need to focus on the steric environment of the transferred oxo group, with special attention paid to coordination geometries and, in Schiff-base systems, focus on the level of steric control enforced by the diimine backbone. Our investigation of dioxygen coordination to and transfer from molybdenum (IV/VI) centers reveals significant mechanistic detail and answers previously unaddressed questions about the differences in substrate scope for dioxomolybdenum and Mimoun-type catalysts (or reactions involving dioxomolybdenum complexes with peroxidic reagents). This work demonstrates that in order for catalytic aerobic oxidation of electrophilic substrates to become accessible, dioxomolybdenum complexes capable of oxidizing these compounds in absence of peroxidic oxygen atom donors must be developed. The unusual cleavage of a peroxo group by a molybdenum center following oxo group transfer to nucleophilic phosphine substrate is also reported. Aerobic oxidation of thiols to disulfides under base-free conditions is reported for the first time with a homogeneous molybdenum catalyst, and this reaction is found to be promoted by electron-donating *para*-substituents on the salen ligand. The oxidation is discovered to produce unexpected additional oxidation products for aliphatic thiol substrates (with aryl substrates suggested but not confirmed to also result in a mixture of products). The more-easily oxidized benzyl mercaptan is discovered to undergo C-S bond cleavage, followed by an unusual sulfur atom transfer reaction, resulting in formation benzyl trisulfide. Oxidation of dodecane thiol is found to form the hitherto-unreported sulfenic acid compound (R-S-O-S-R), which is also the secondary product suggested for oxidation of thiophenol substrates. The substrate scope for formation of this new functional group is in need of further exploration, as is the chemistry of the sulfenic anhydrides themselves.

APPENDIX A: SPECTRAL DATA FOR CHARACTERIZATION OF COMPOUNDS IN CHAPTER 2

IR Data

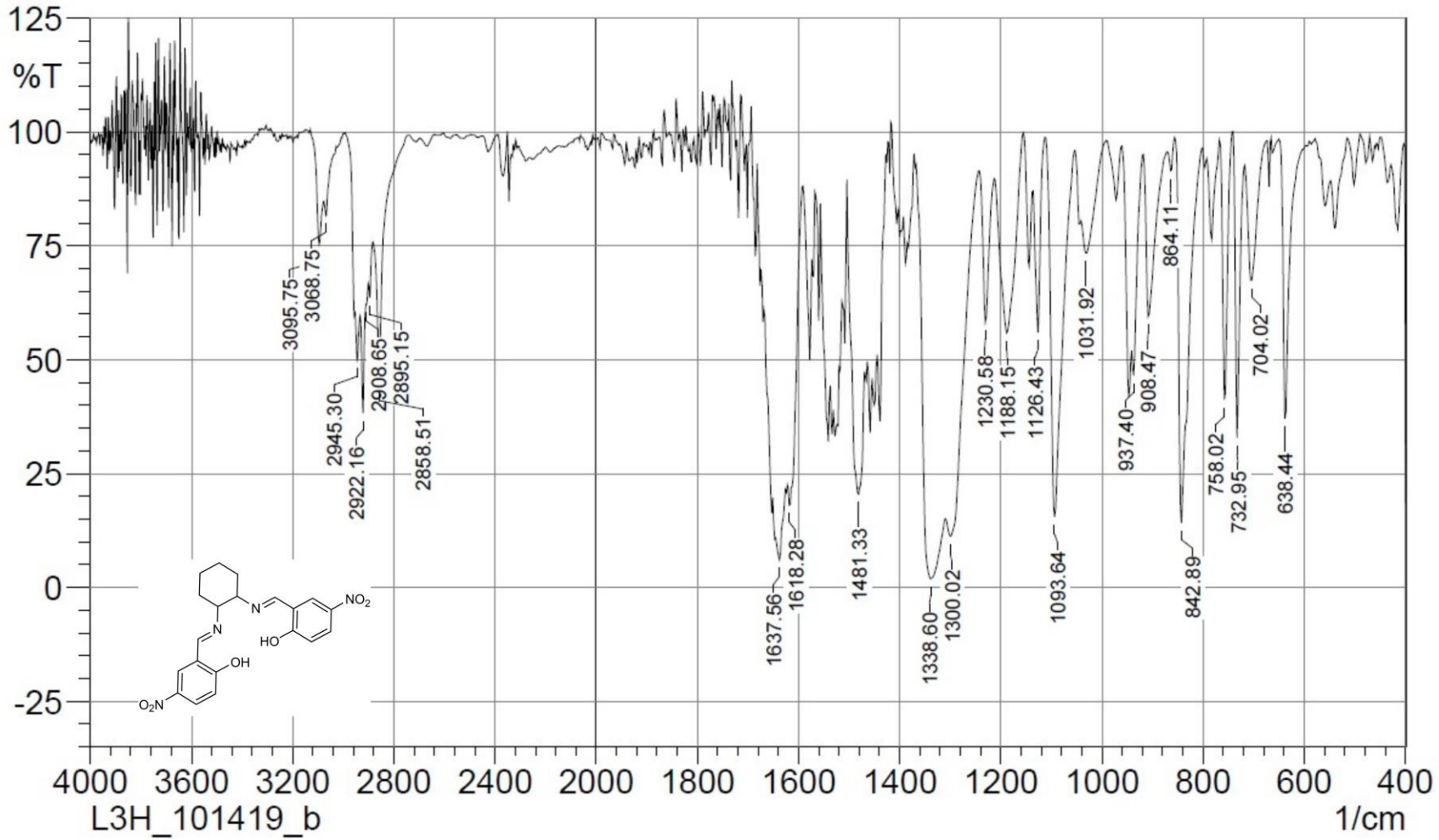

Figure A-1: IR spectrum of **2,** KBr pellet, cm^{-1}

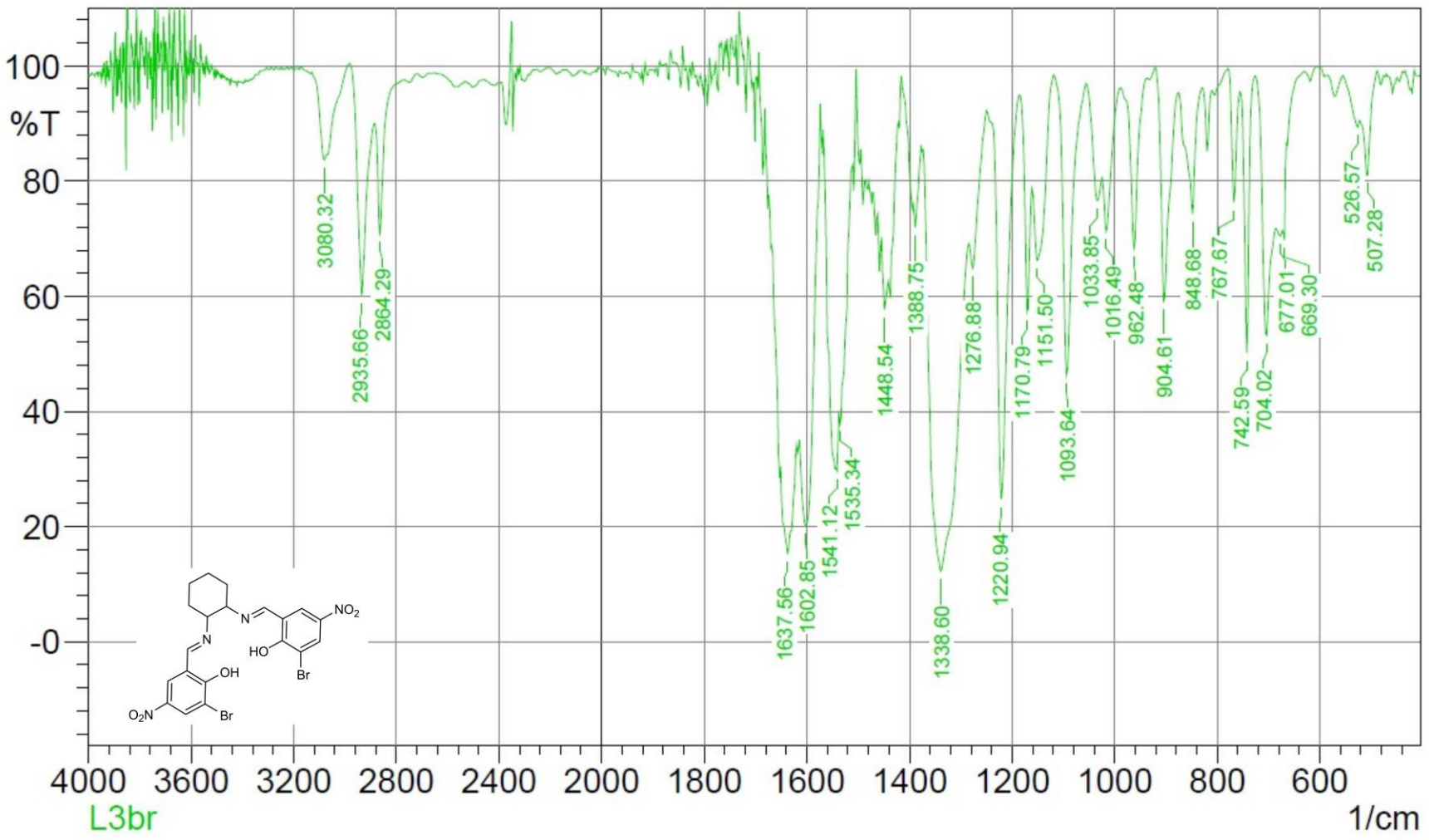

Figure A-2: IR spectrum **3**, KBr pellet, 1/cm

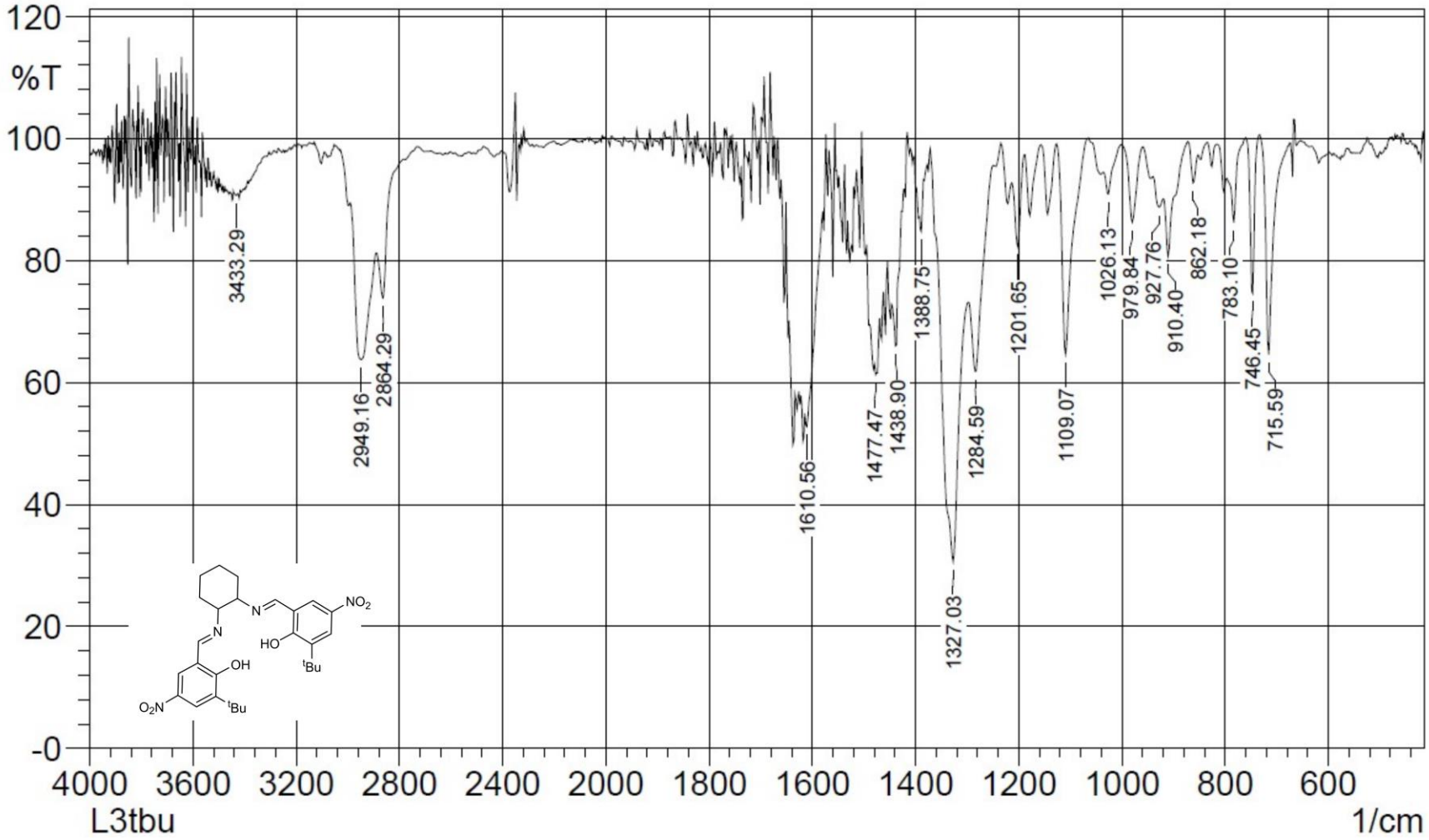

Figure A-3: IR spectrum of **4**, KBr pellet, 1/cm

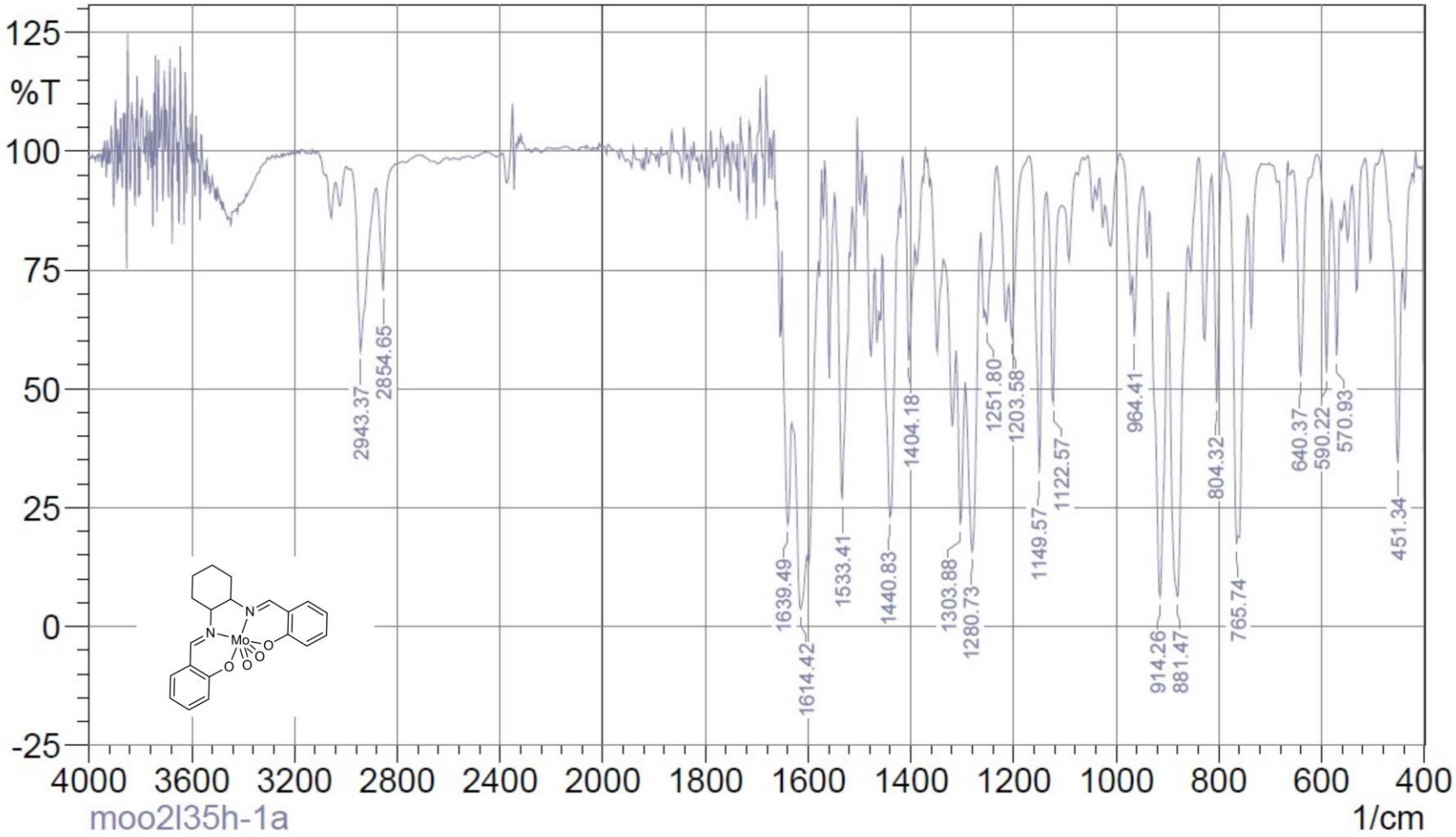

Figure A-4: IR spectrum of **6**, KBr, 1/cm

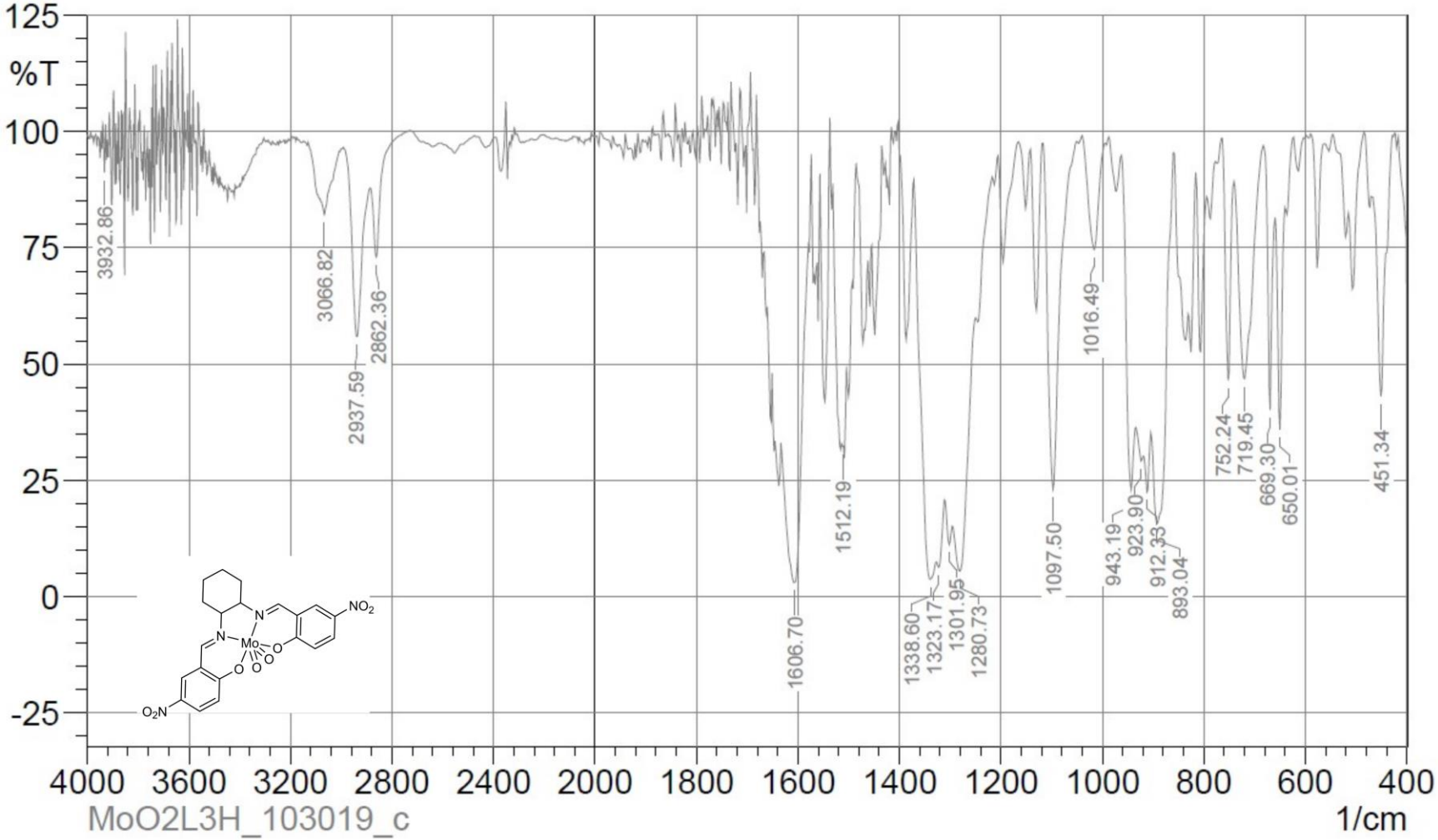

Figure A-5: IR spectrum of **7**, KBr, 1/cm

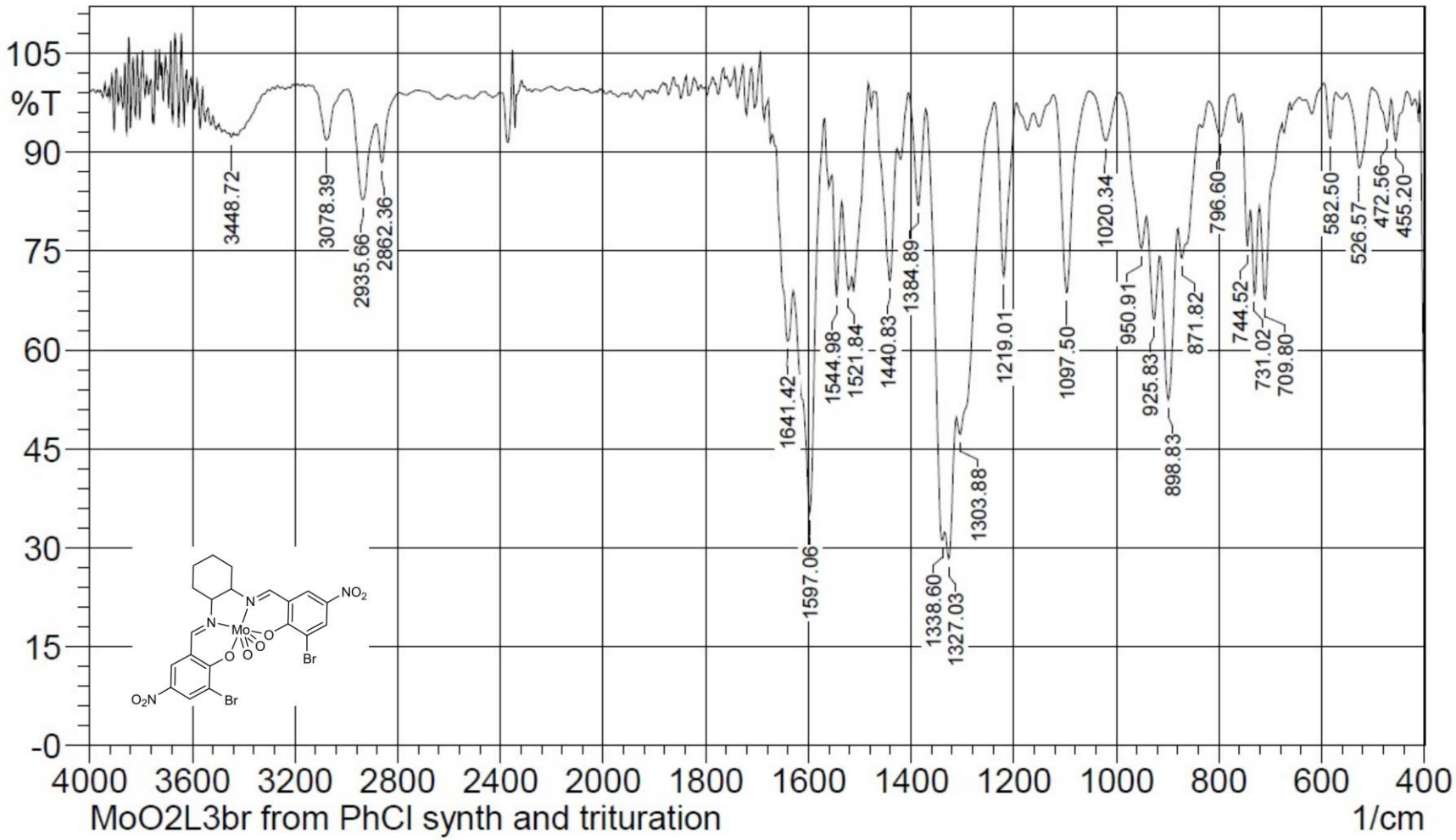

Figure A-6: IR spectrum of **8**, KBr, 1/cm

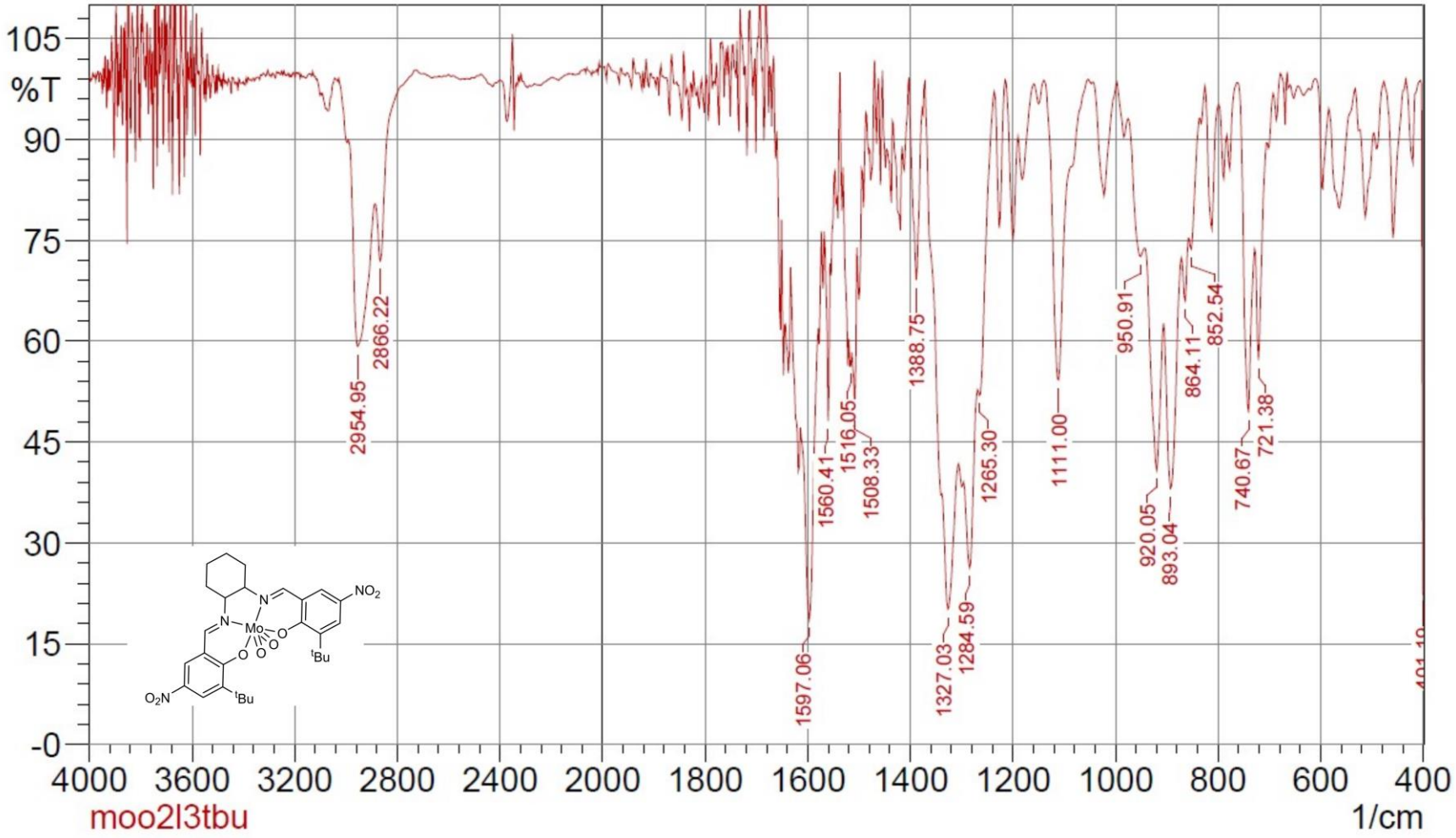

Figure A-7: IR spectrum of **9**, KBr, 1/cm

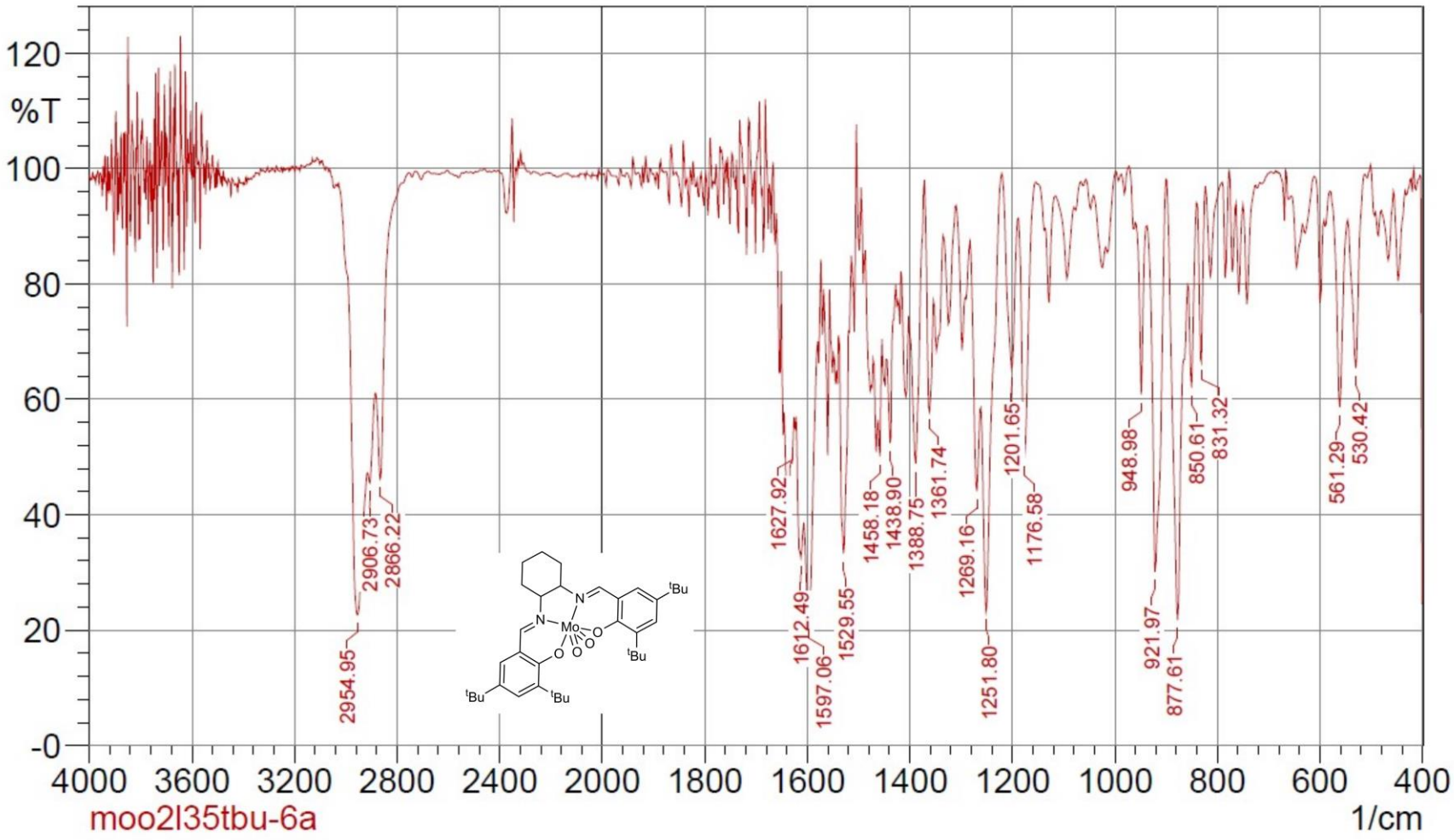

Figure A-8: IR spectrum of **10**, KBr, 1/cm

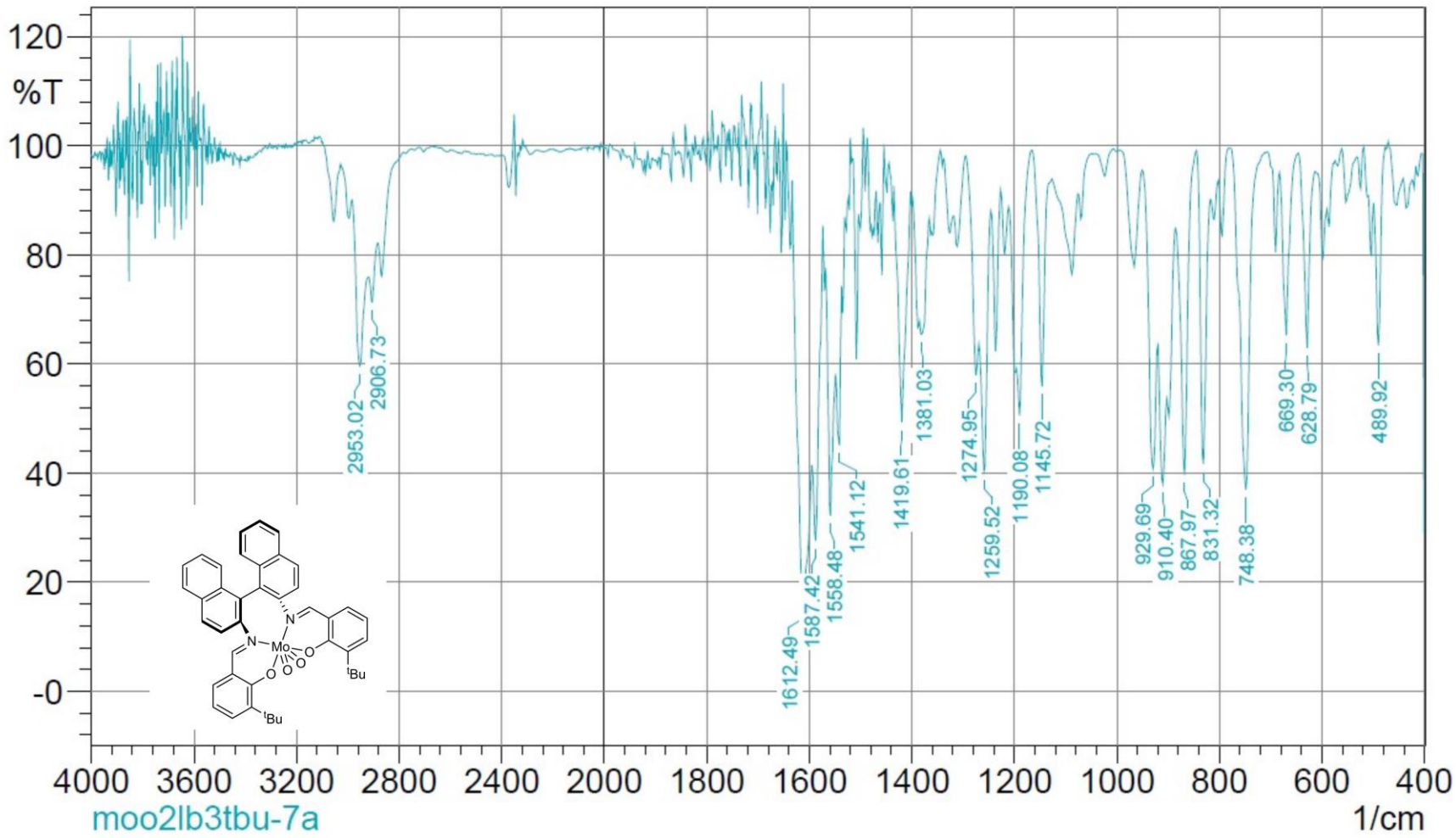

Figure A-9: IR spectrum of **12**, KBr, 1/cm

NMR Data

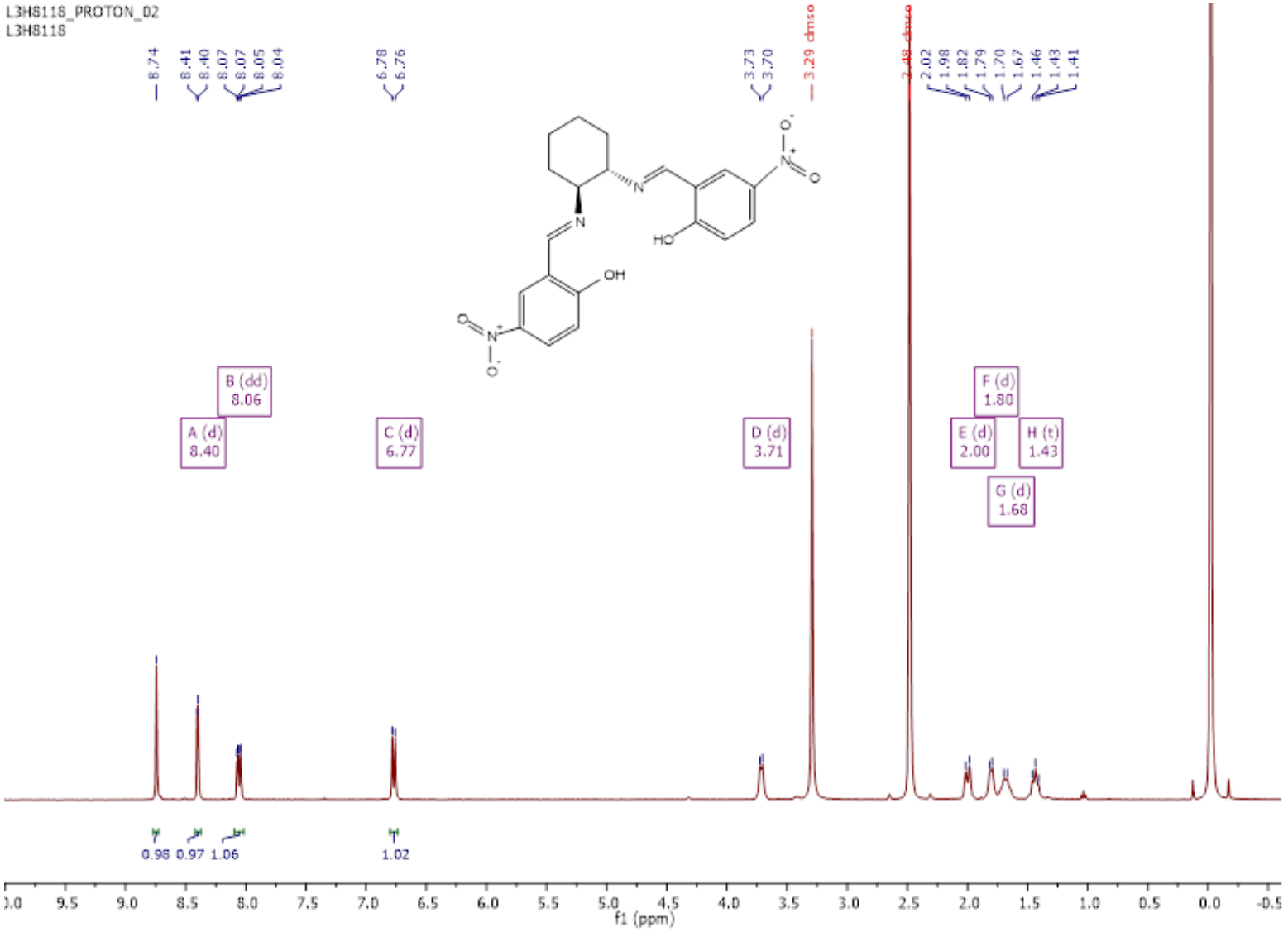

Figure A-10: 1H NMR of **2** (d_6-DMSO)

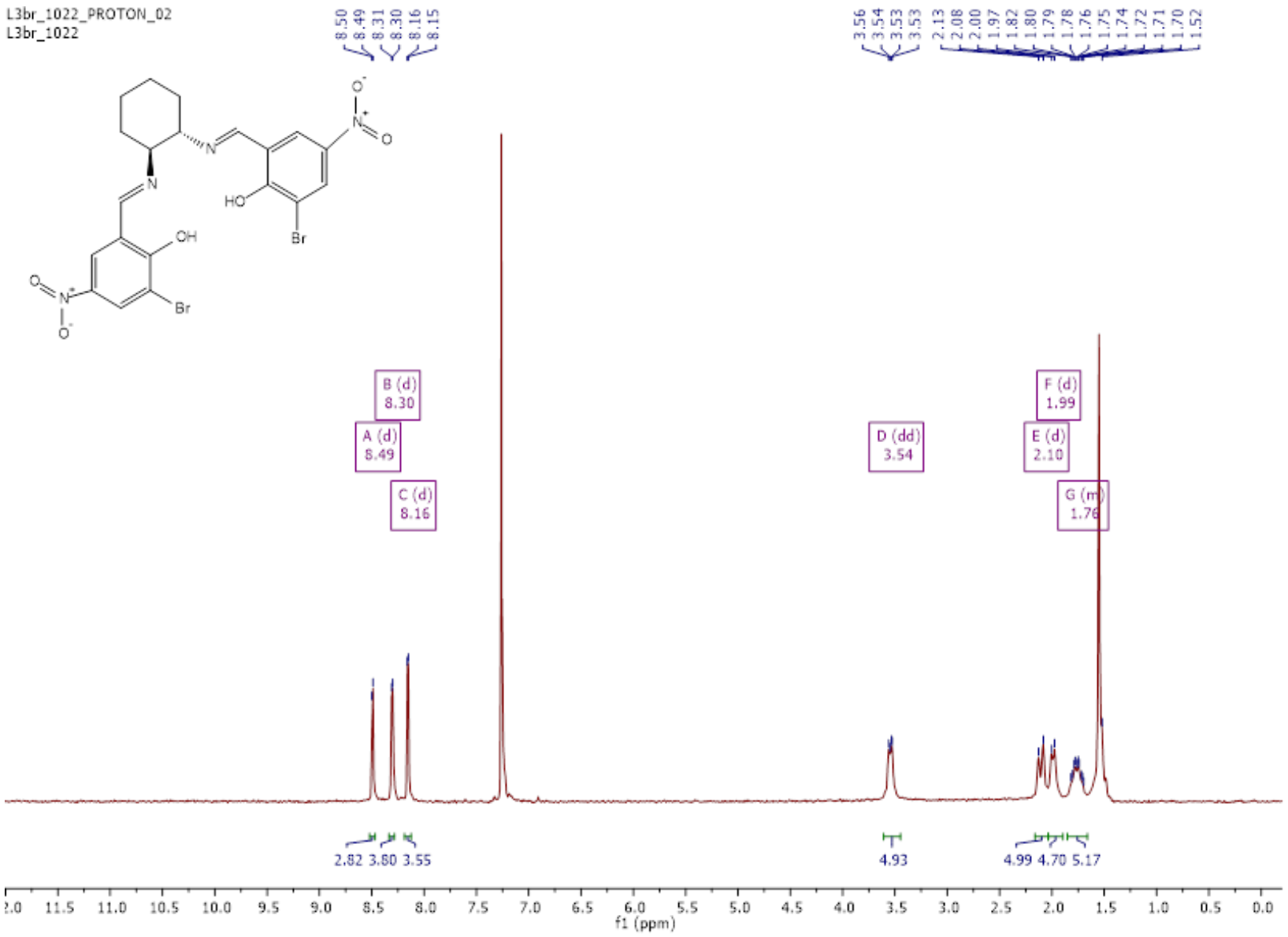

Figure A-11: 1H NMR of **3** ($CDCl_3$)

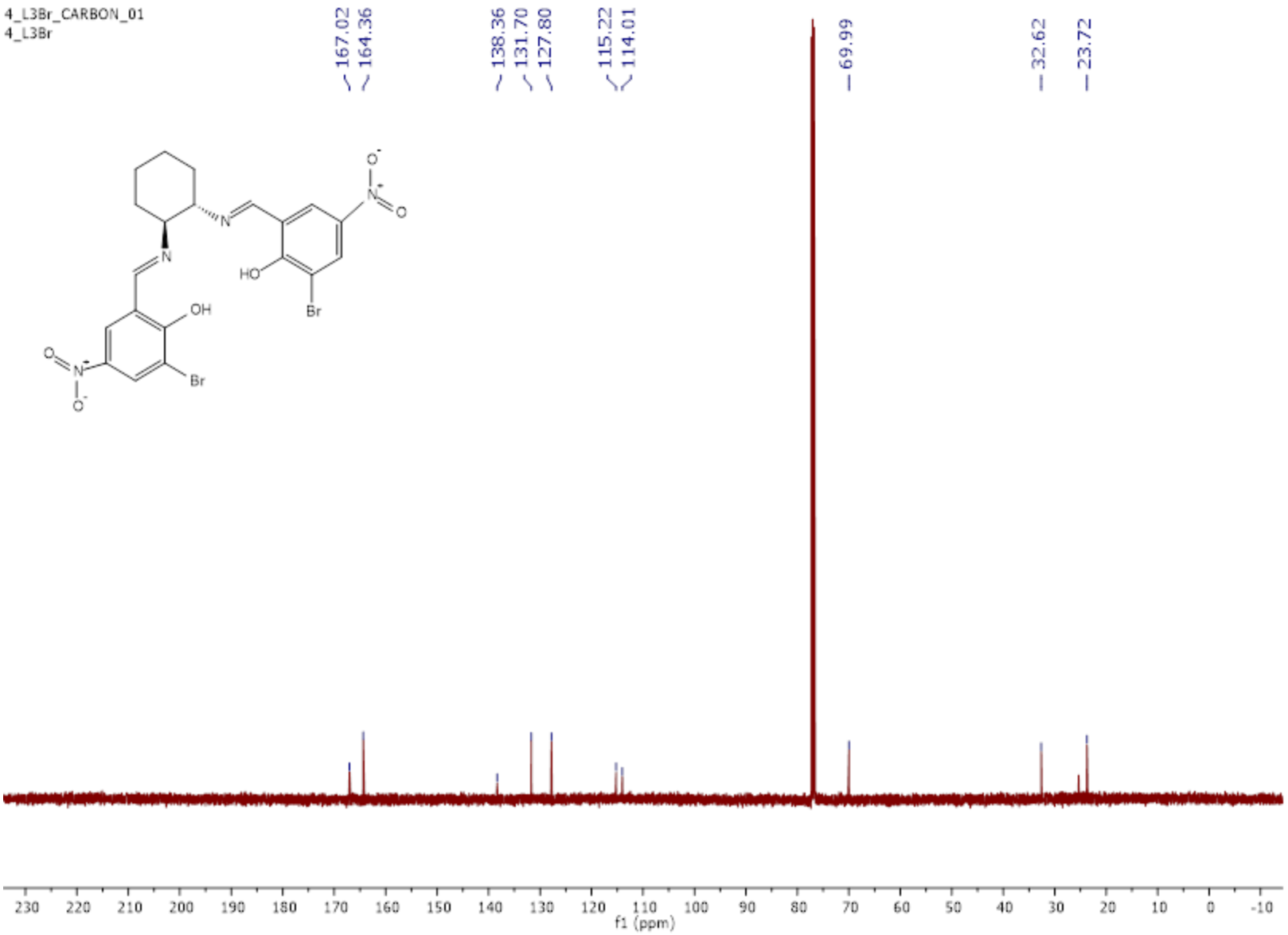

Figure A-12: 13C NMR of **3** ($CDCl_3$)

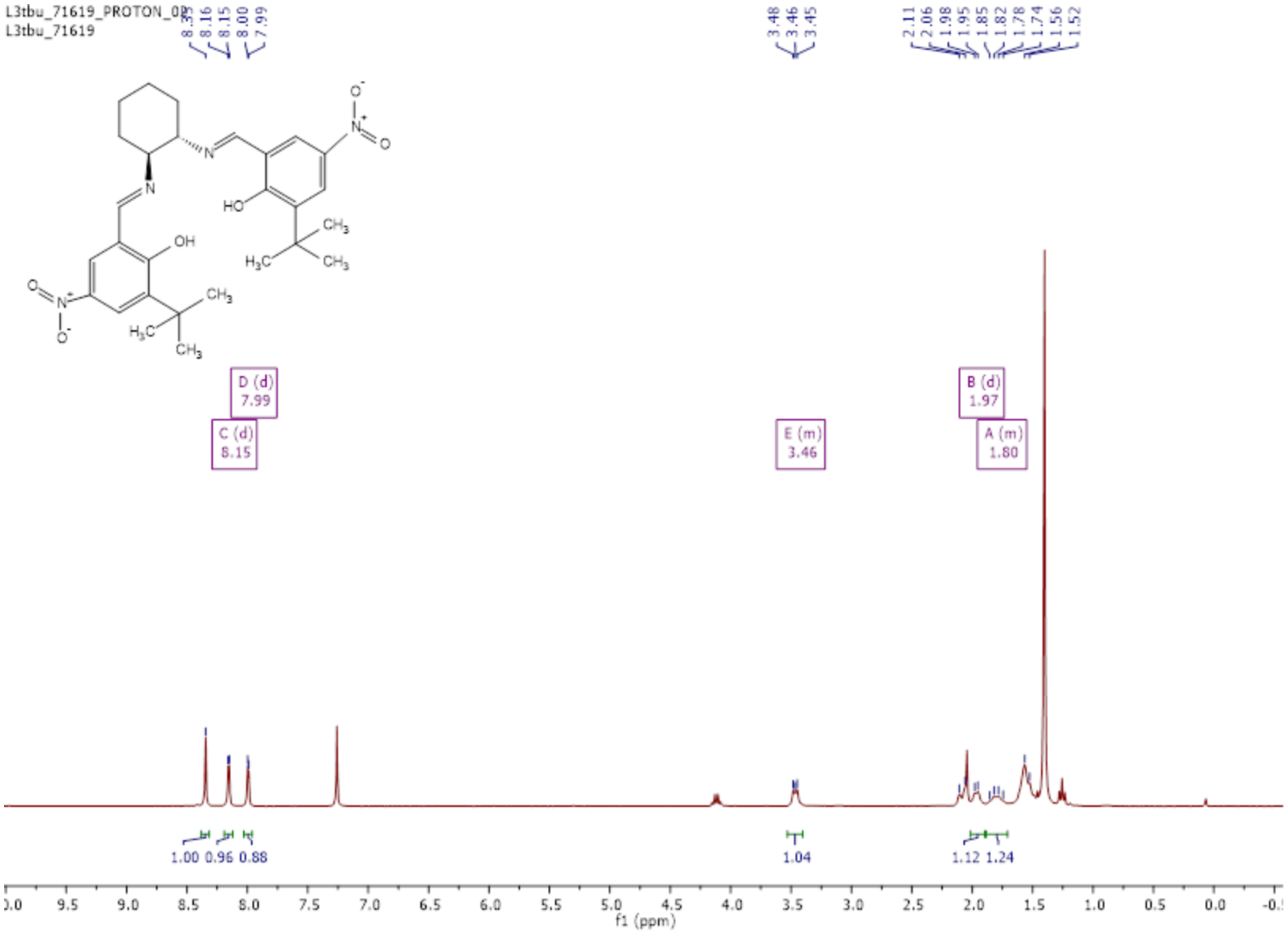

Figure A-13: 1H NMR of **4** ($CDCl_3$)

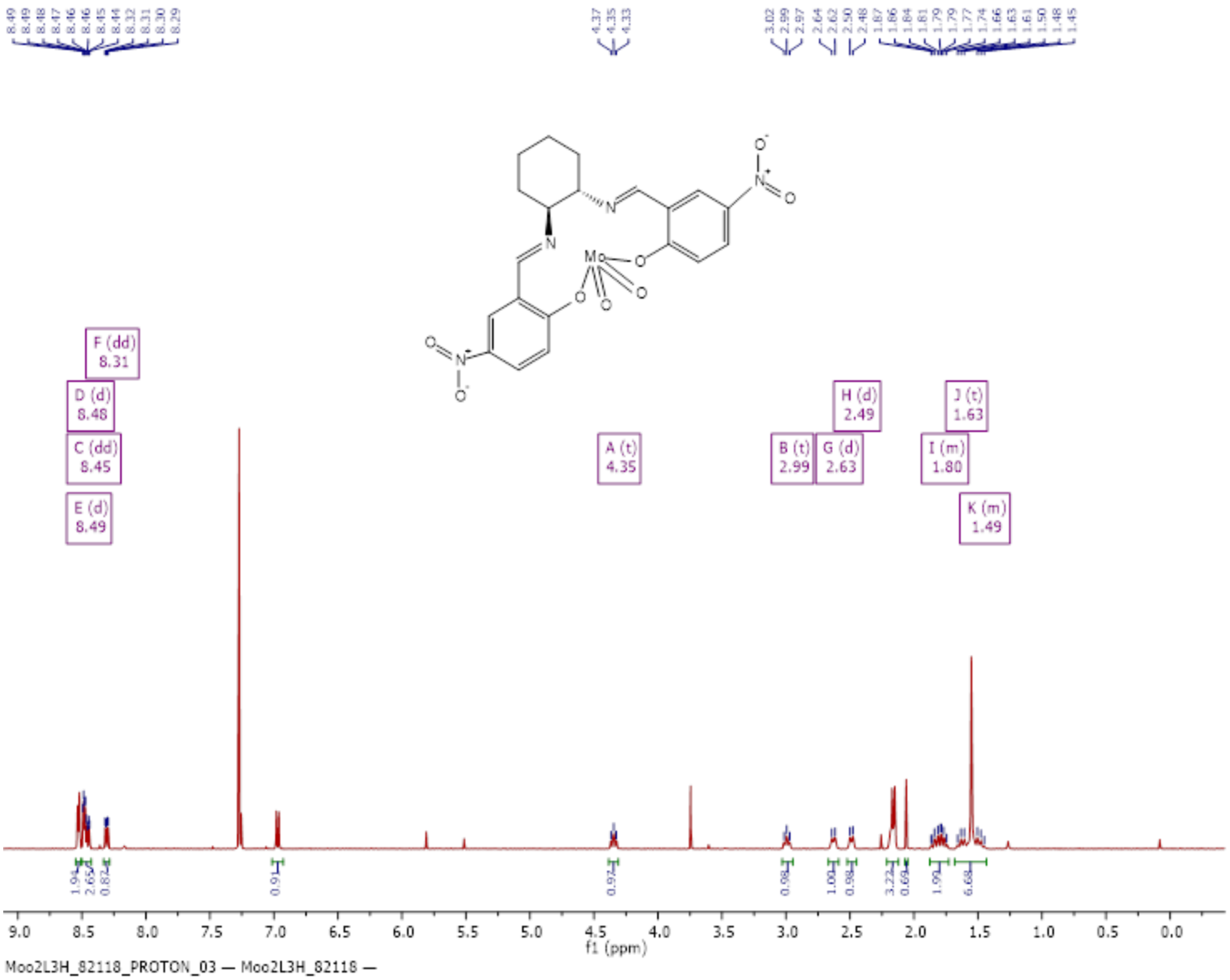

Figure A-14: 1H NMR of **7** ($CDCl_3$)

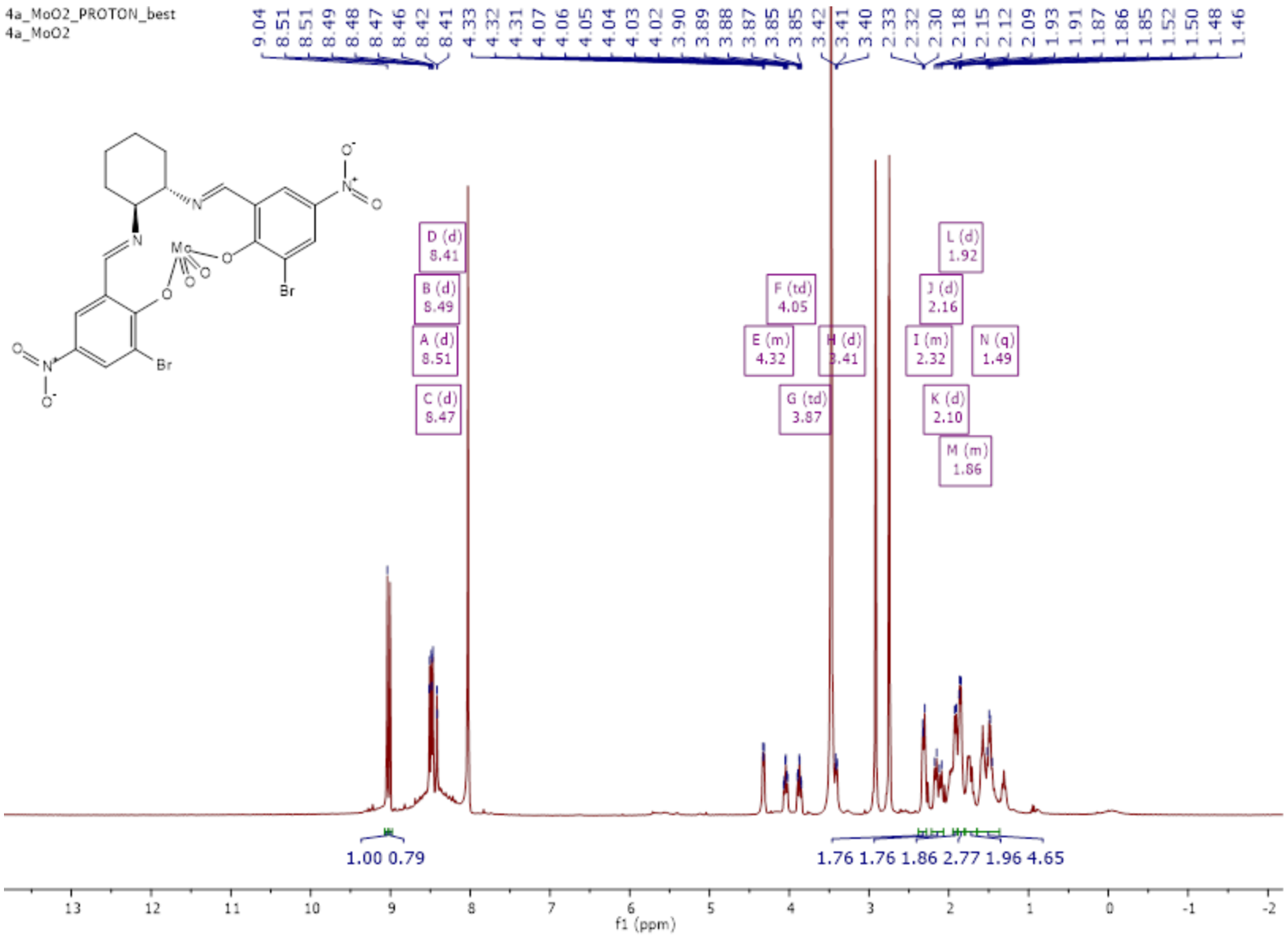

Figure A-15: 1H NMR of **8** (d_6-DMF)

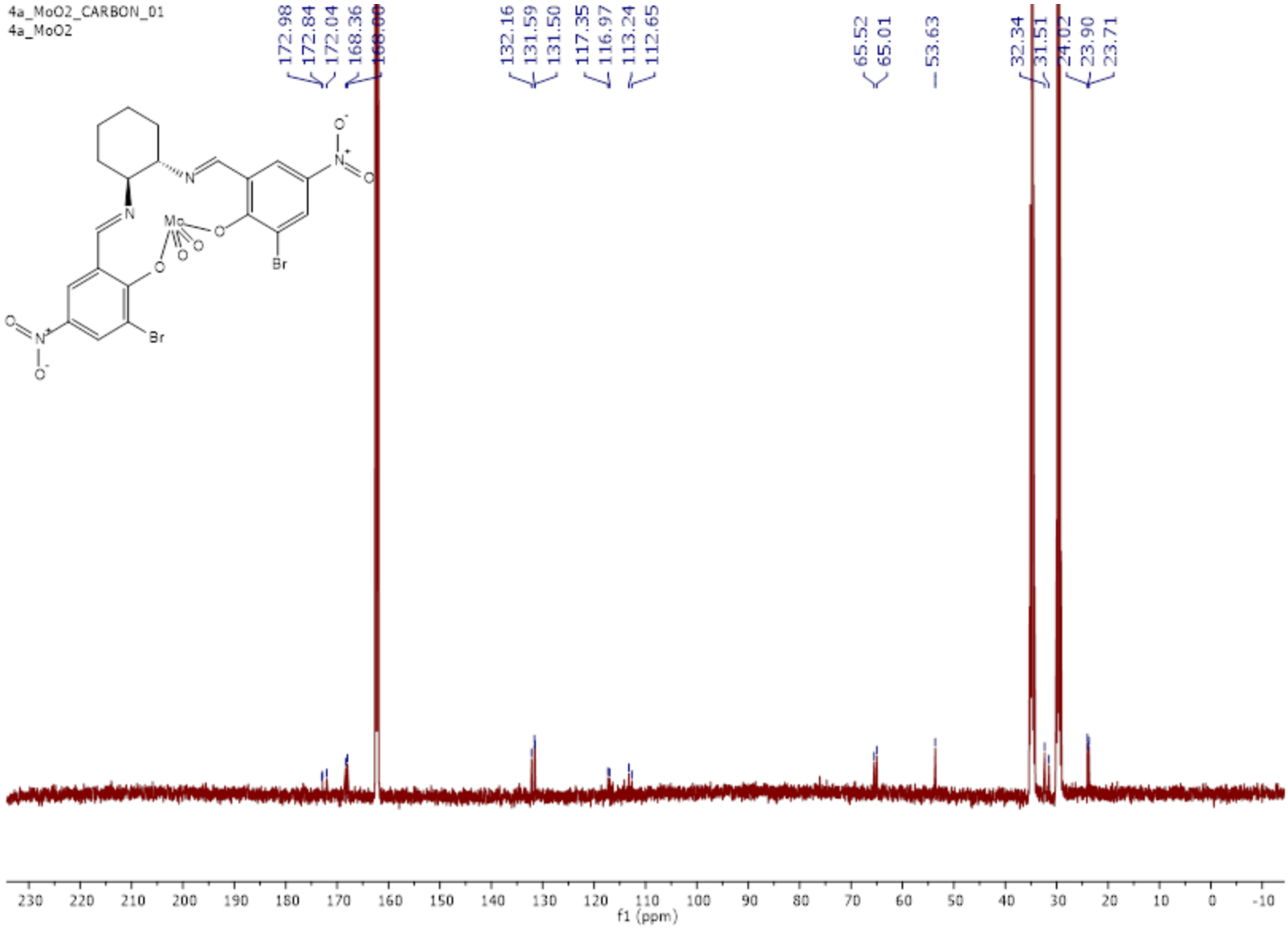

Figure A-16: 13C NMR of **8** (d_6-DMF)

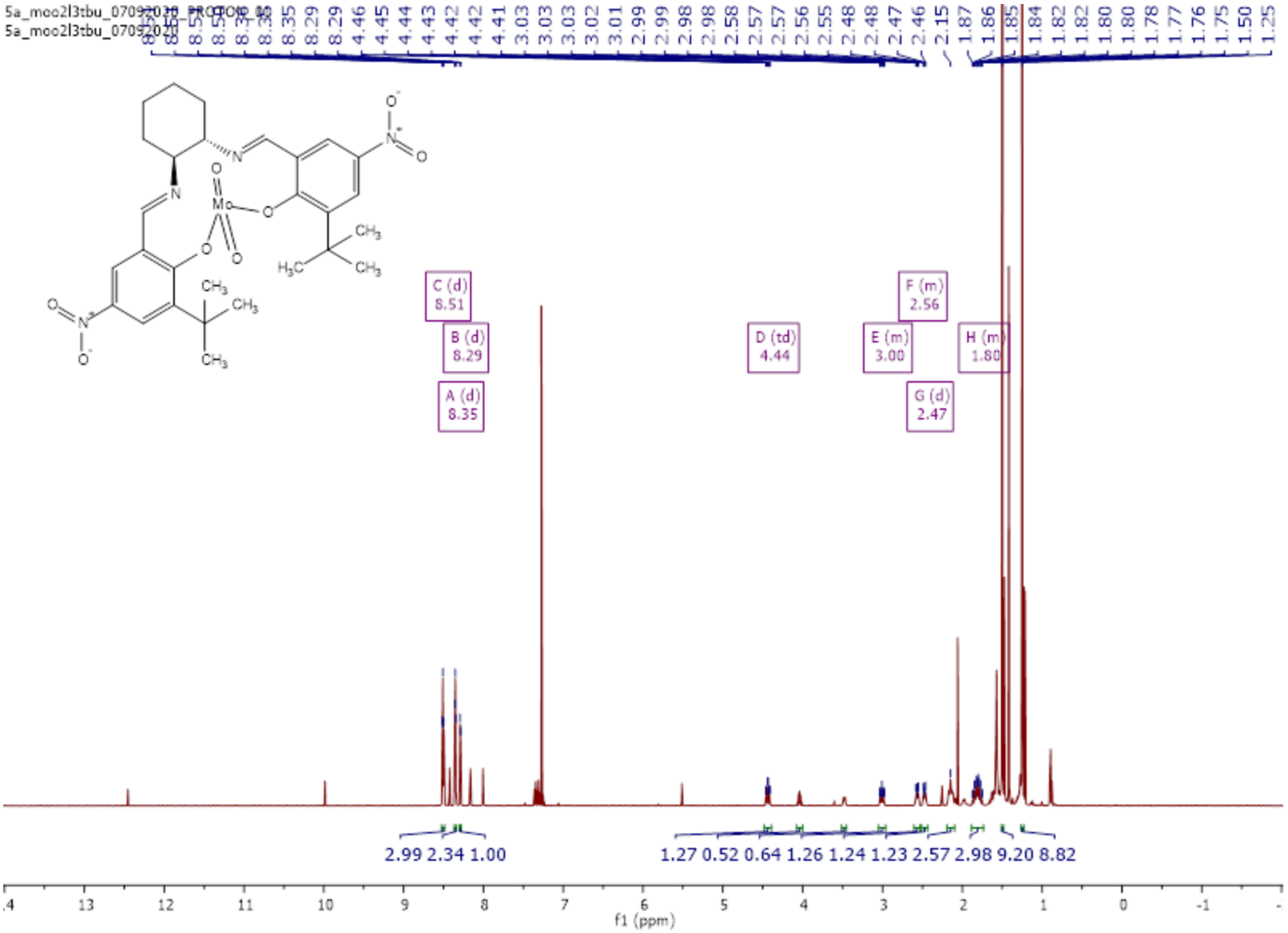

Figure A-17: 1H NMR of **9** ($CDCl_3$)

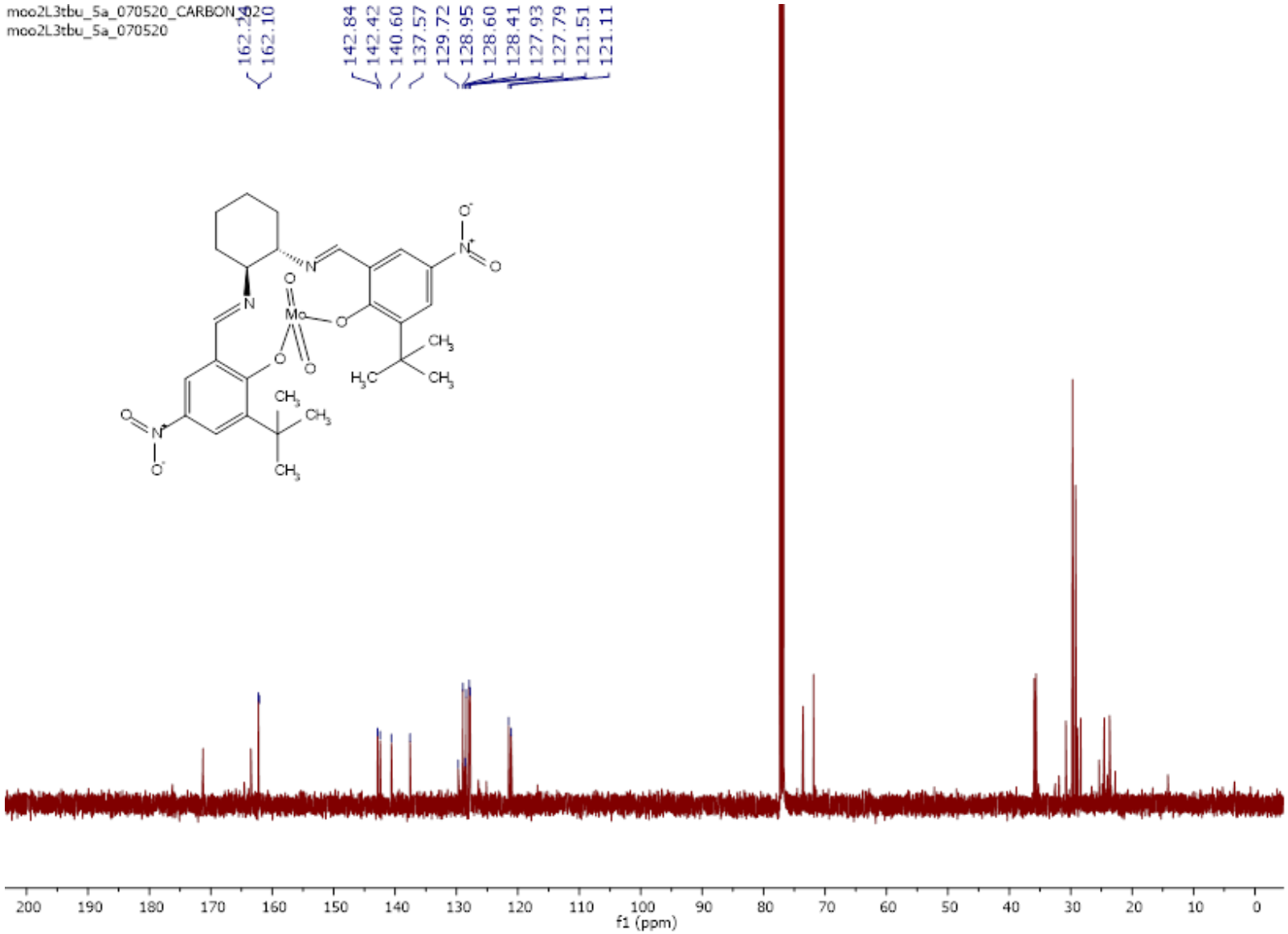

Figure A-18: 13C NMR of **9** ($CDCl_3$)

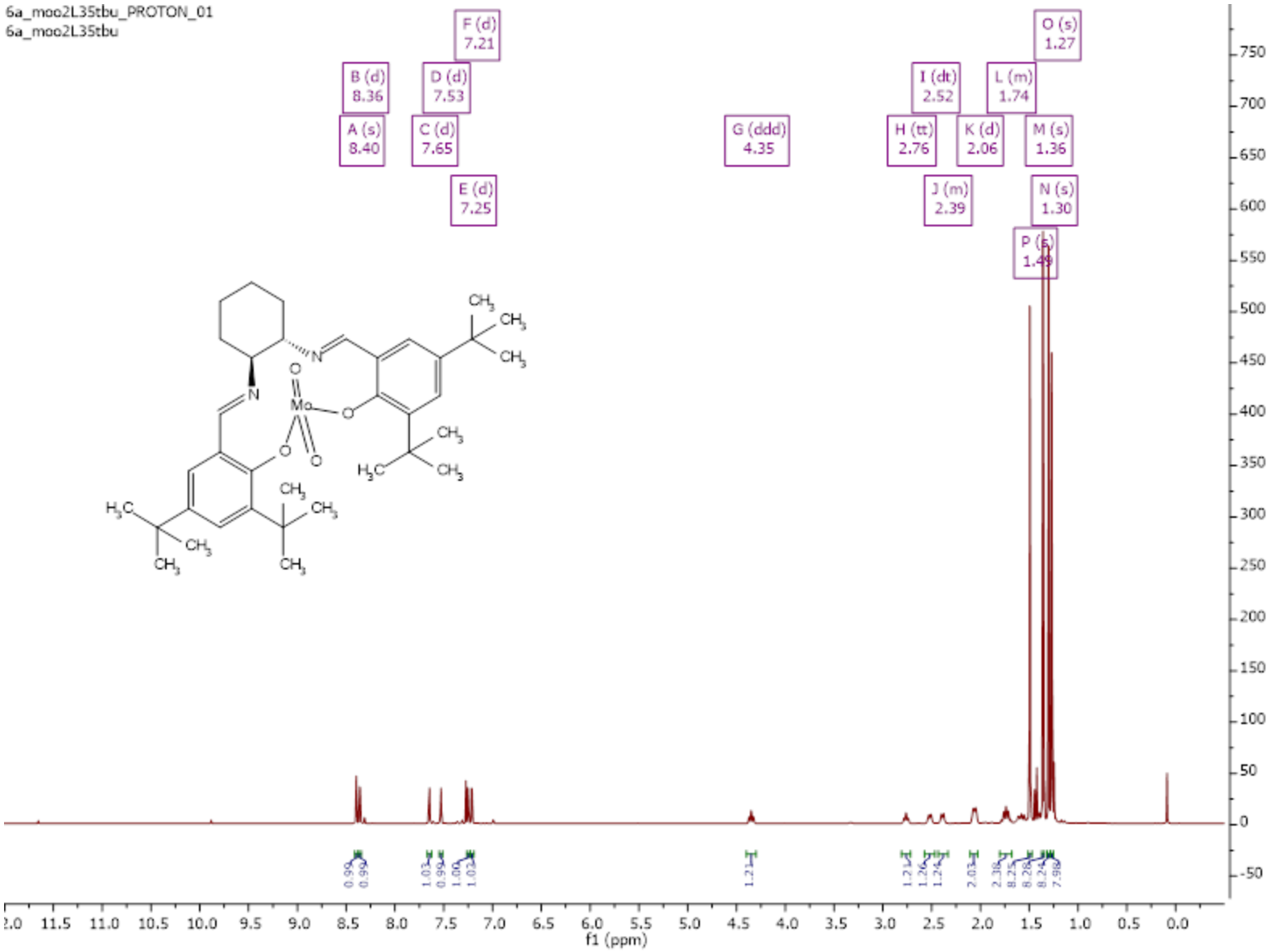

Figure A-19: 1H NMR of **10** ($CDCl_3$)

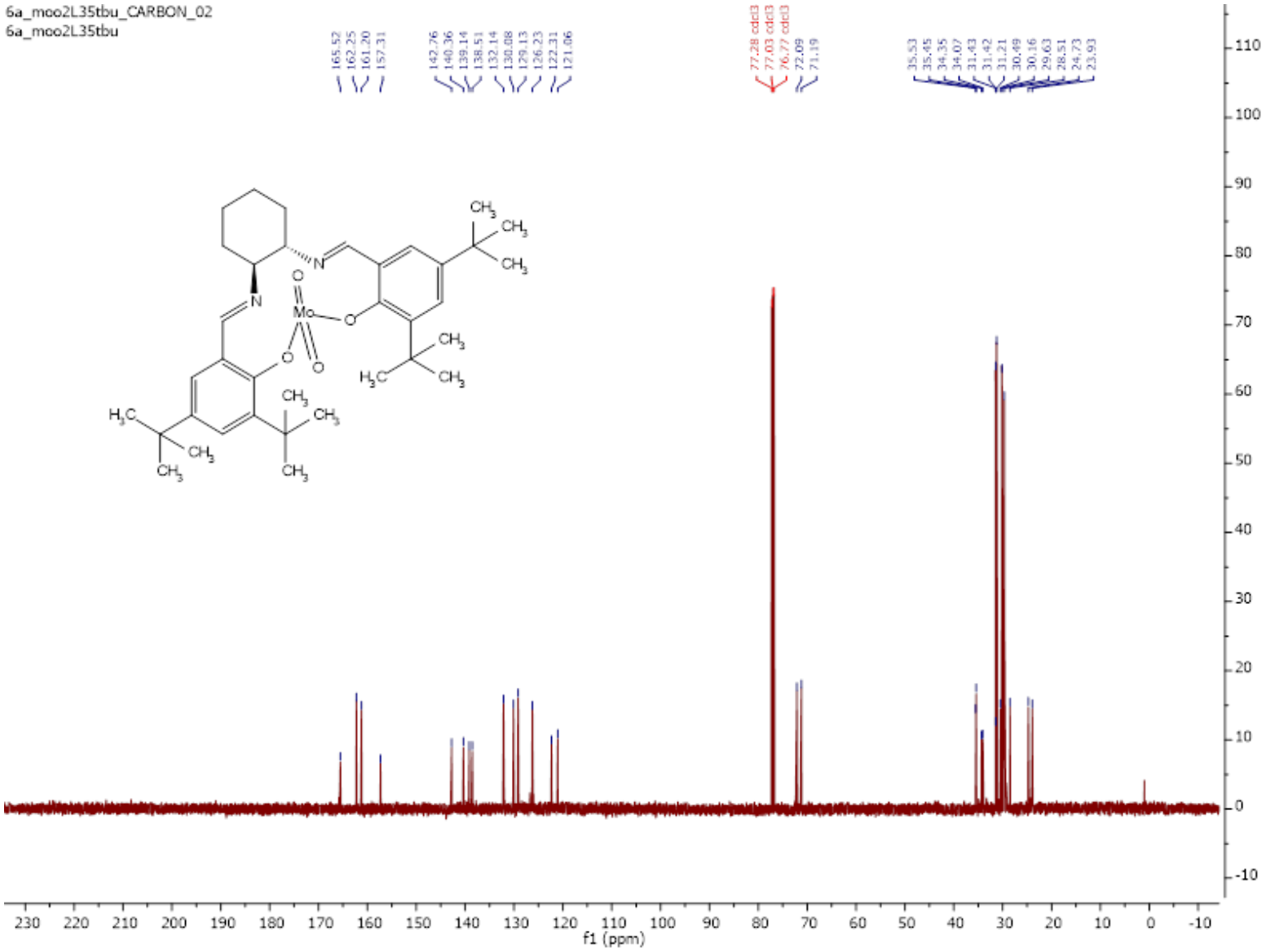

Figure A-20: 13C NMR of **10** ($CDCl_3$)

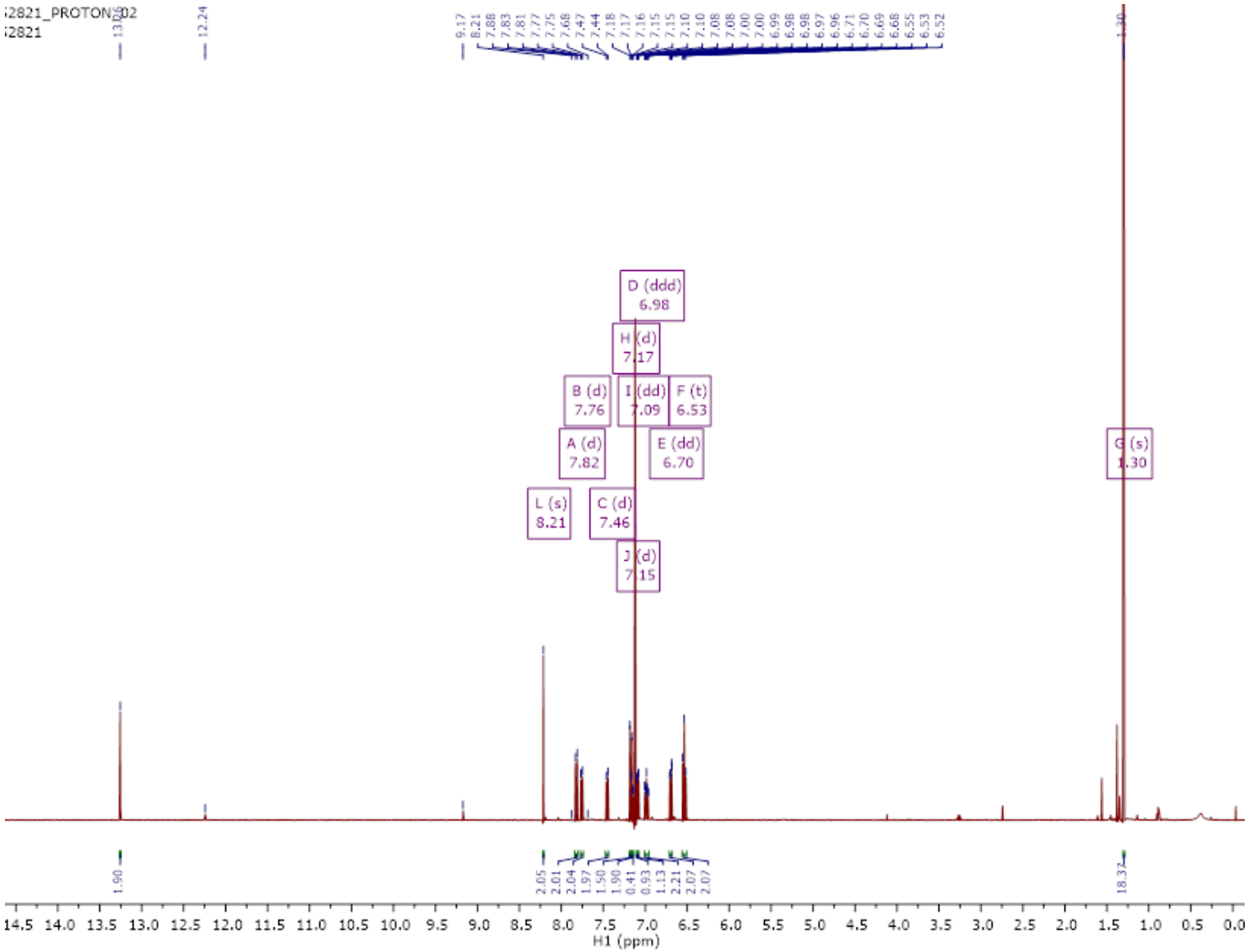

Figure A-21: ^{1}H NMR spectrum of 11 (C_6D_6)

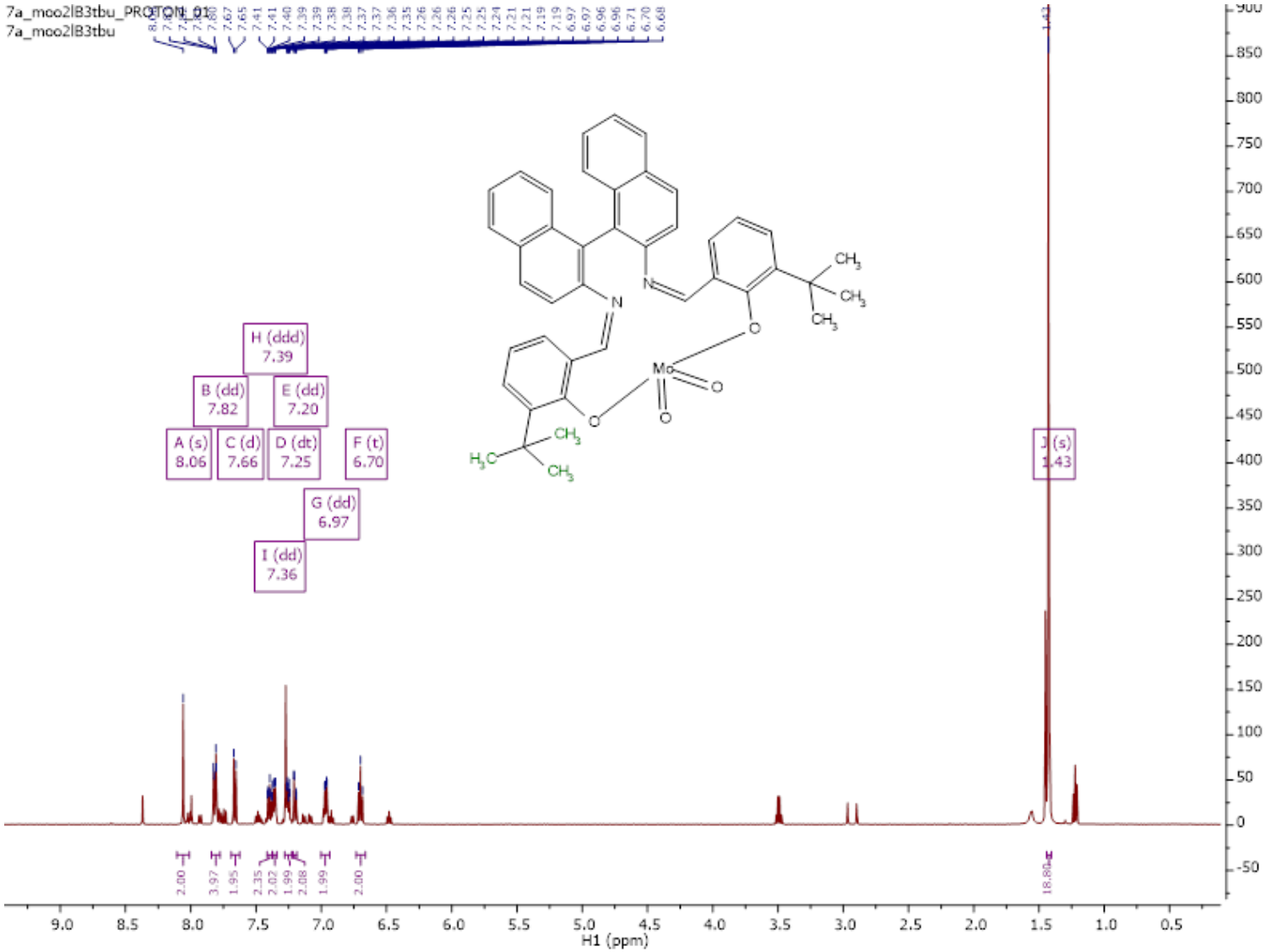

Figure A-22: 1H NMR of **12** ($CDCl_3$)

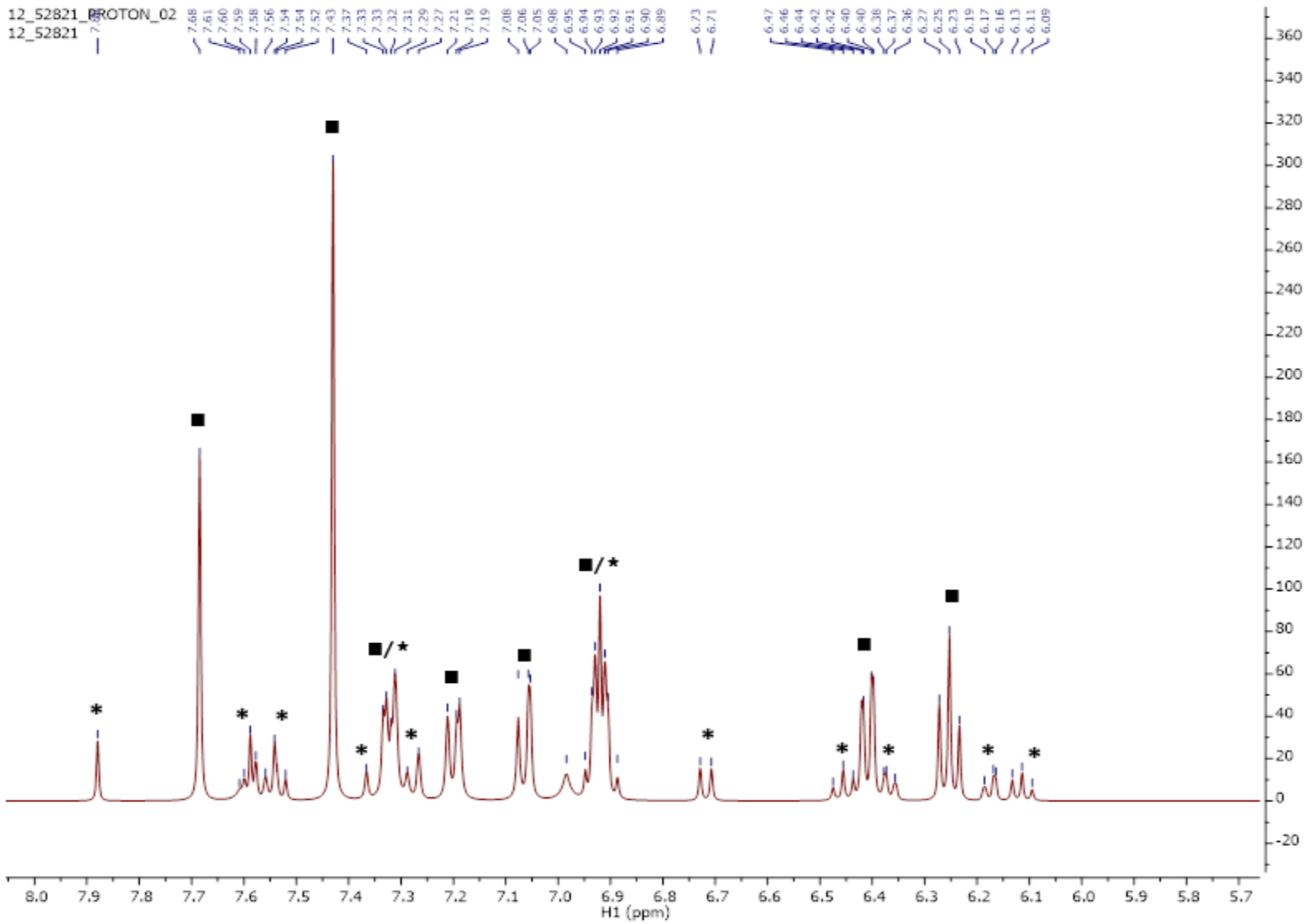

Figure A-23: Expanded aromatic region for ^{1}H NMR of 23 ($CDCl_3$) to show coordination isomers (3:1 C_2:C_1 by integration). C_1 isomer peaks are marked with a * and C_2 isomer with a ■

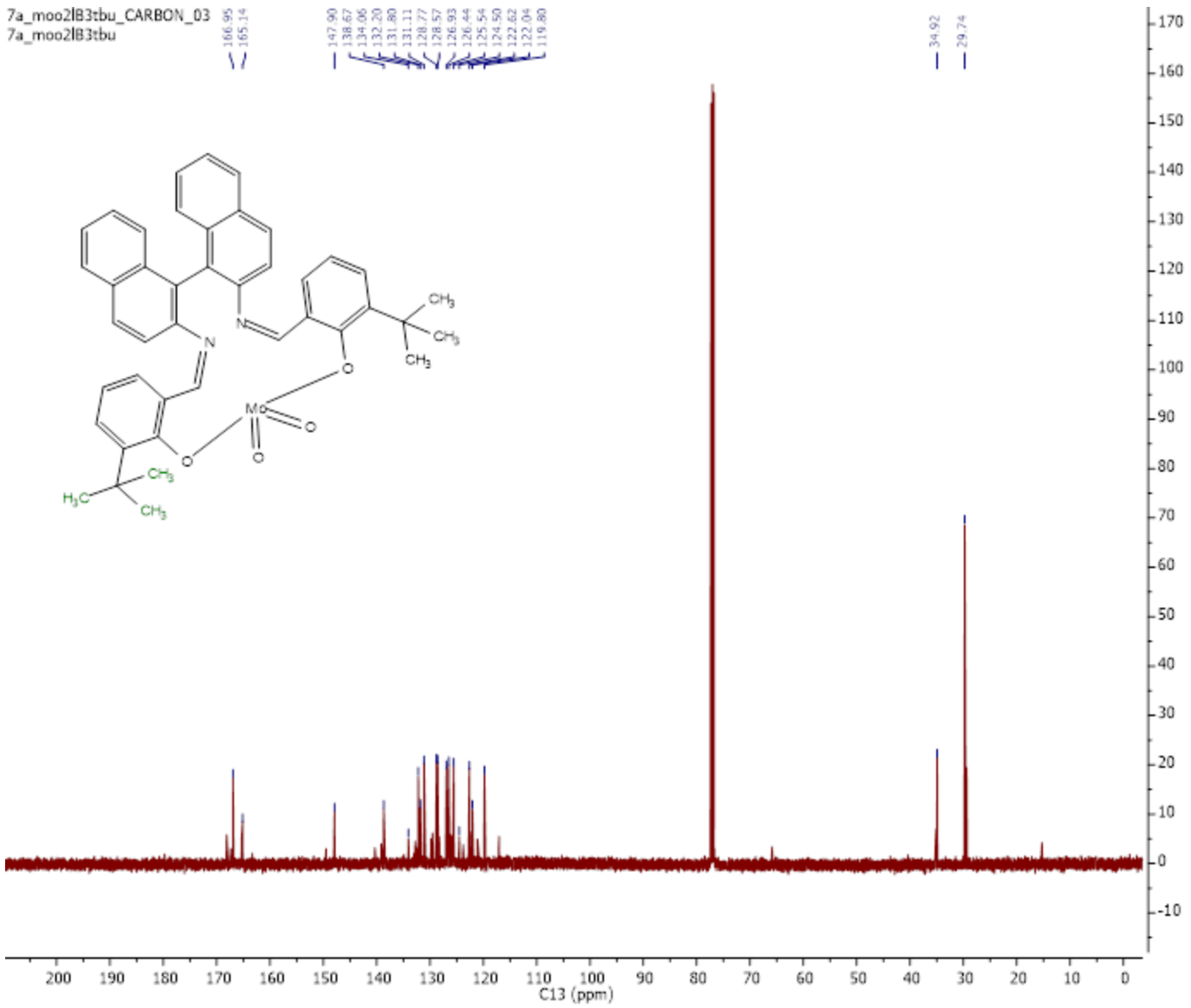

Figure A-24: 13C NMR of **12** ($CDCl_3$)

Mass Spectrometry Data

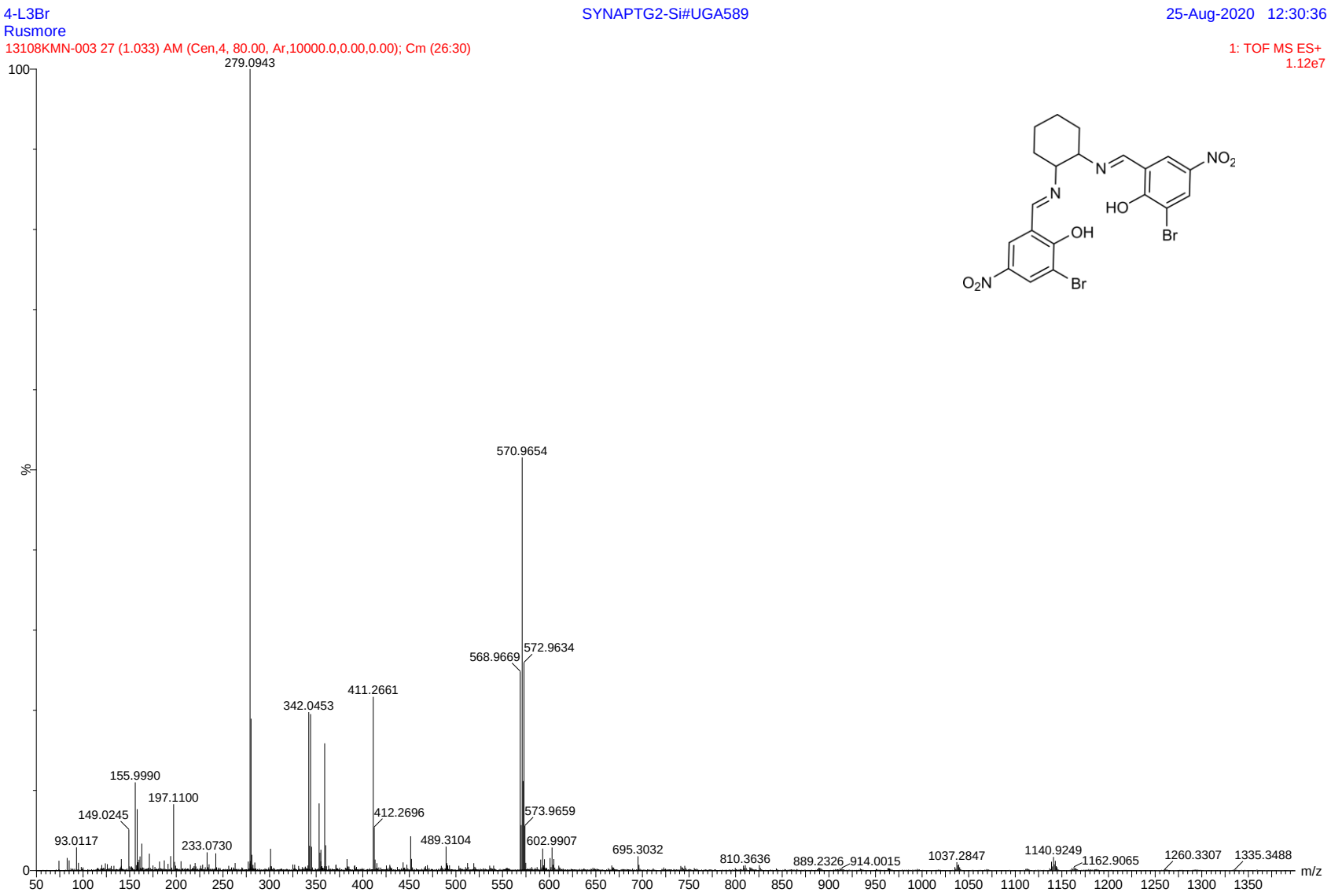

Figure A-25: ESI+ MS of **3**

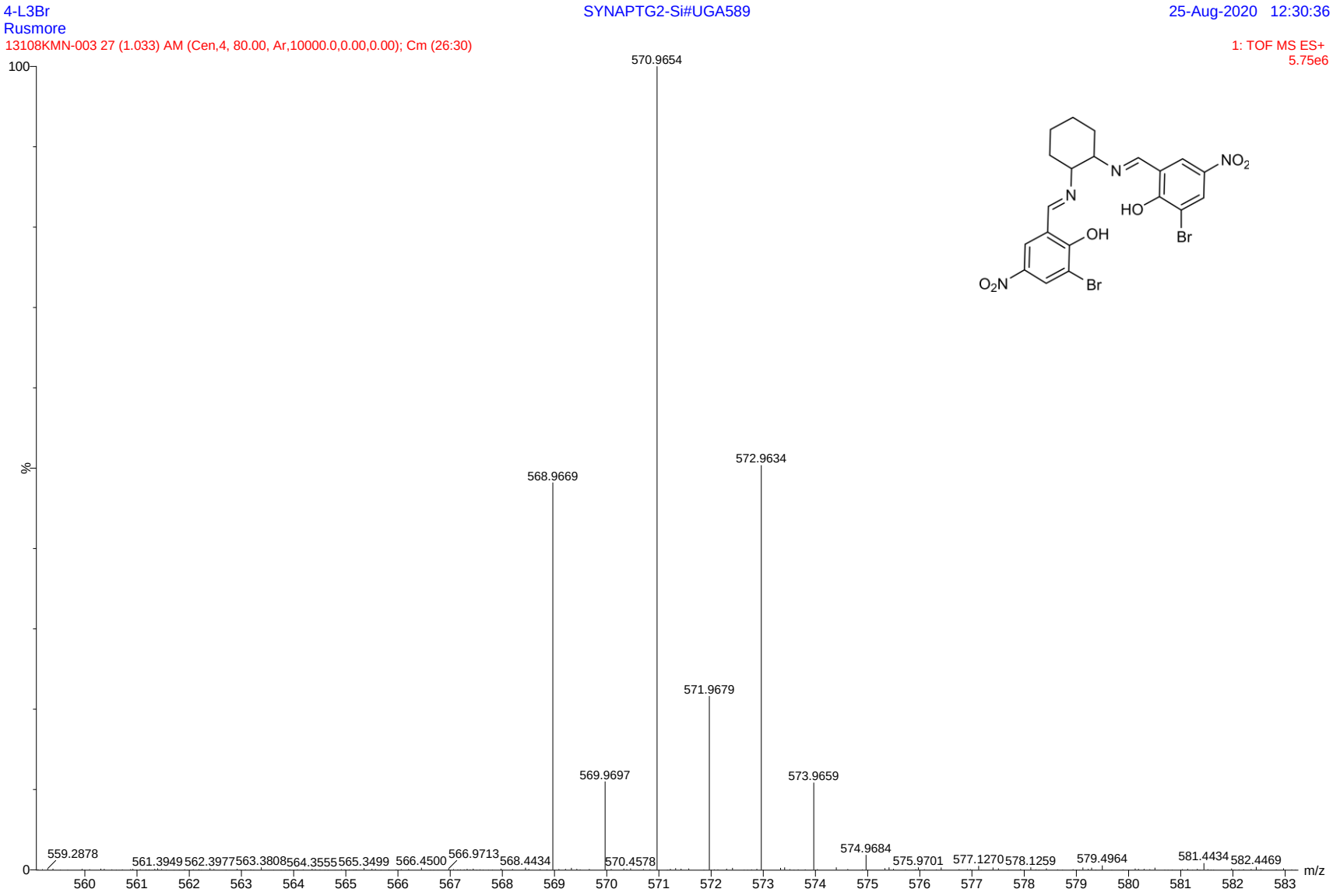

Figure A-26: Molecular ion peaks for ESI+ MS of **3**

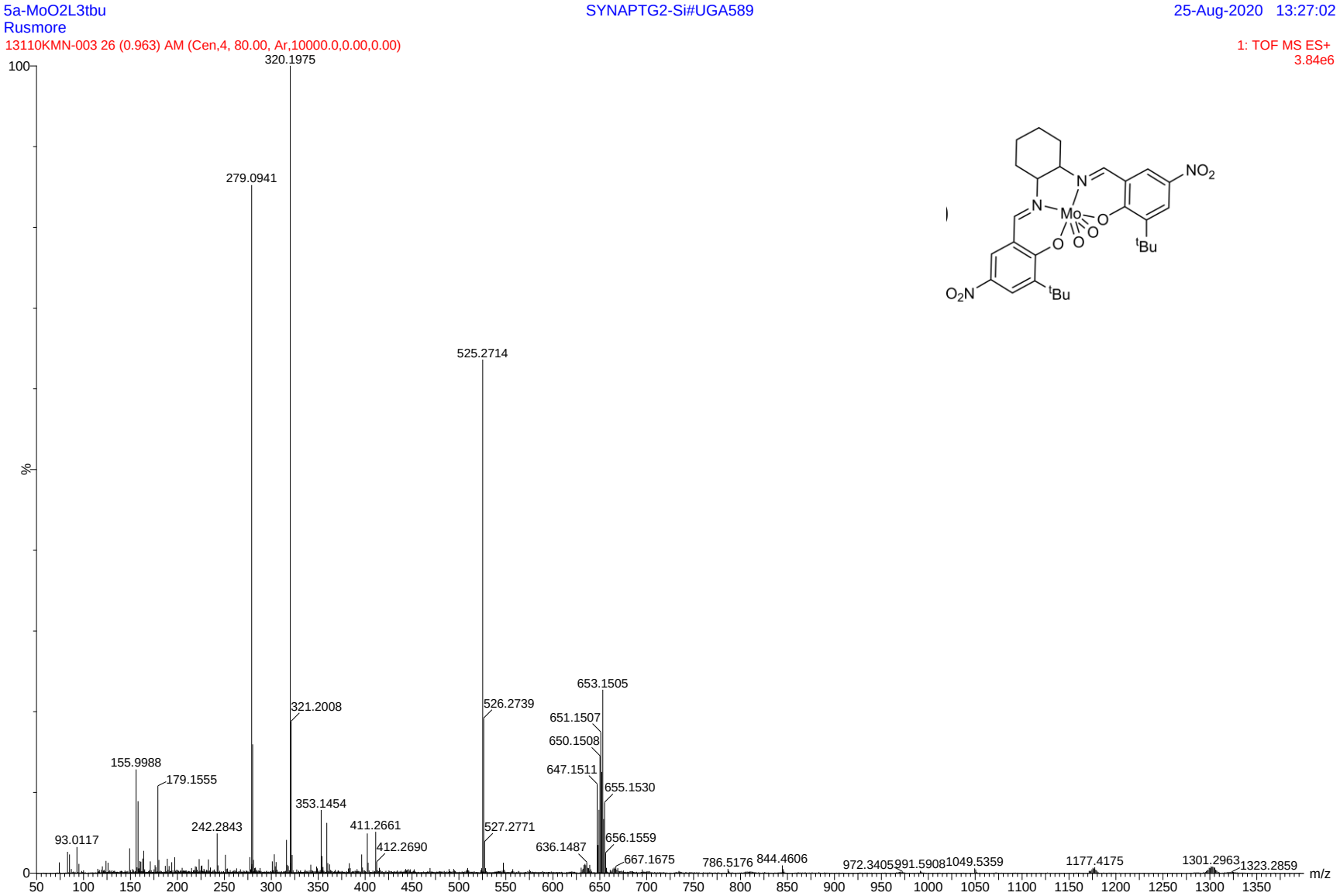

Figure A-27: ESI+ MS of **9**

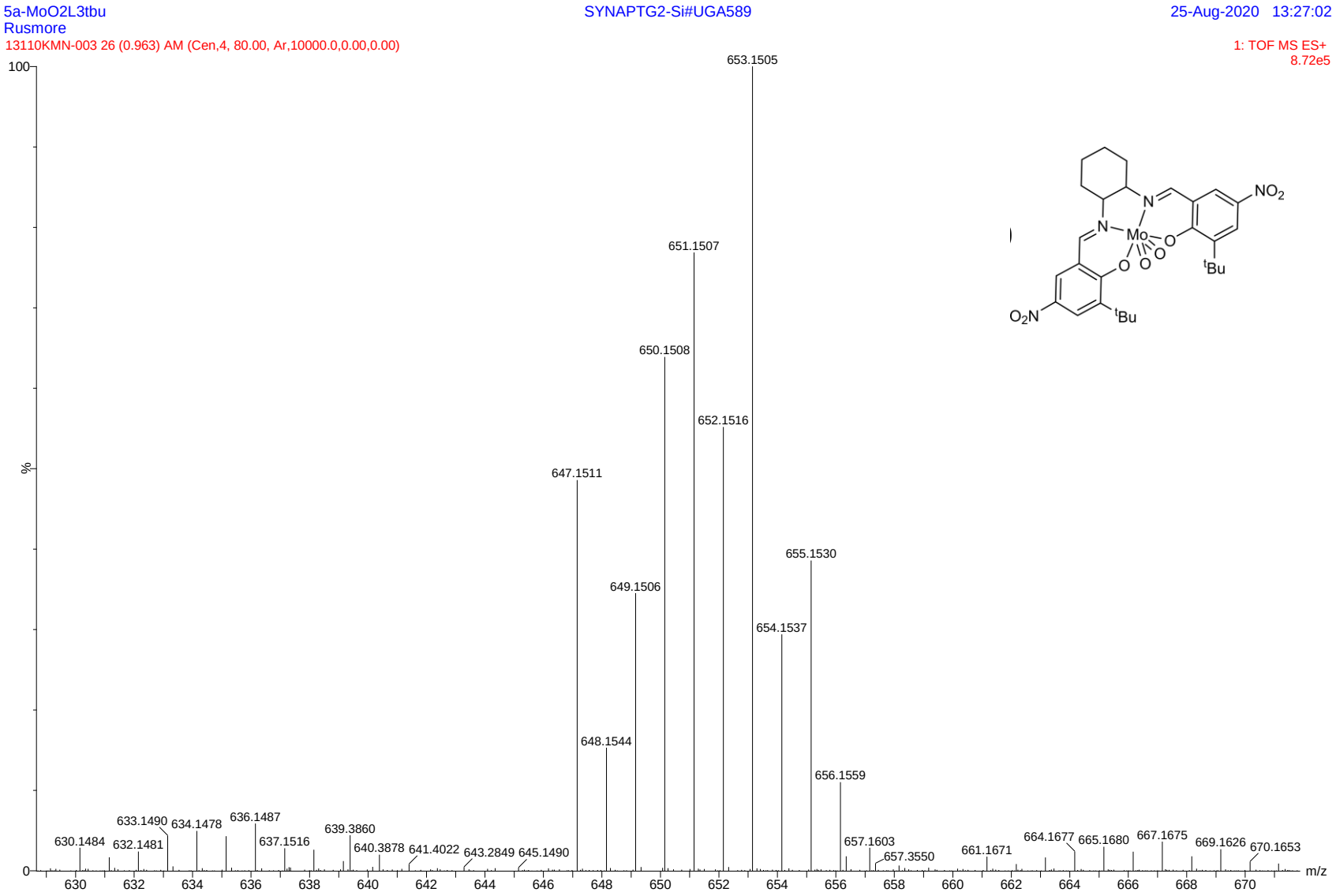

Figure A-28: Molecular ion peaks for ESI+ MS of **9**

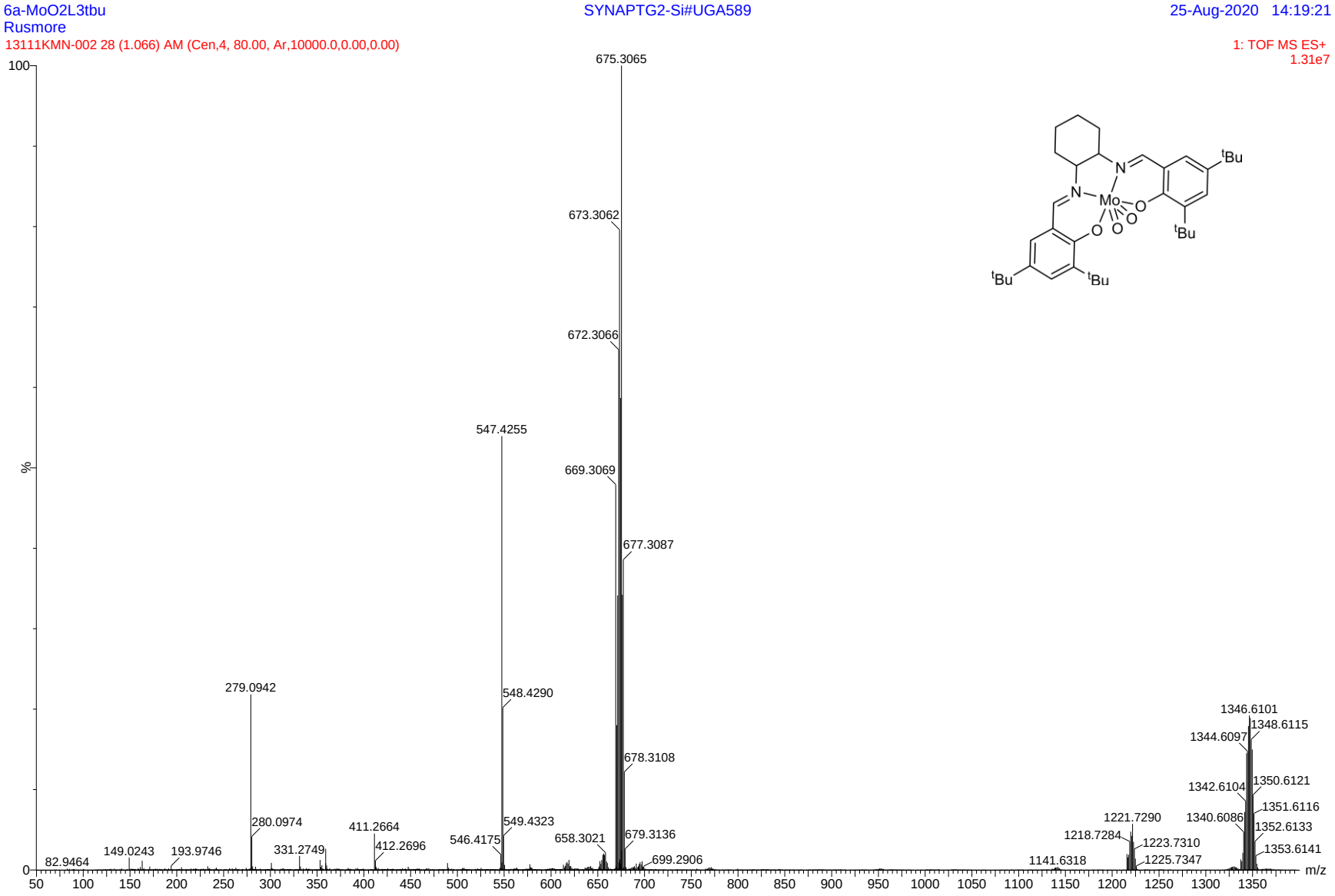

Figure A-29: ESI+ MS for **10**

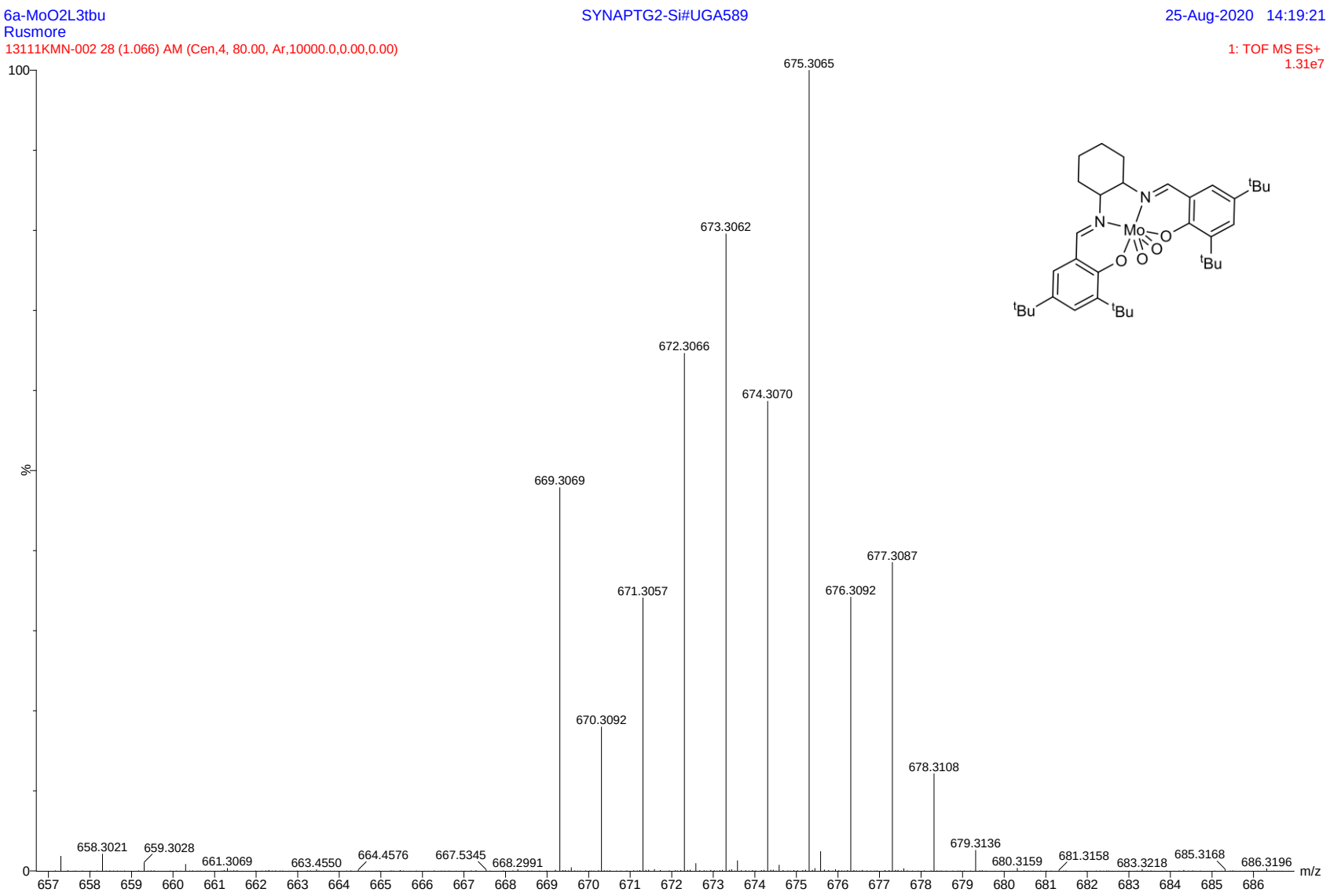

Figure A-30: Molecular ion peaks for ESI+ MS of **10**

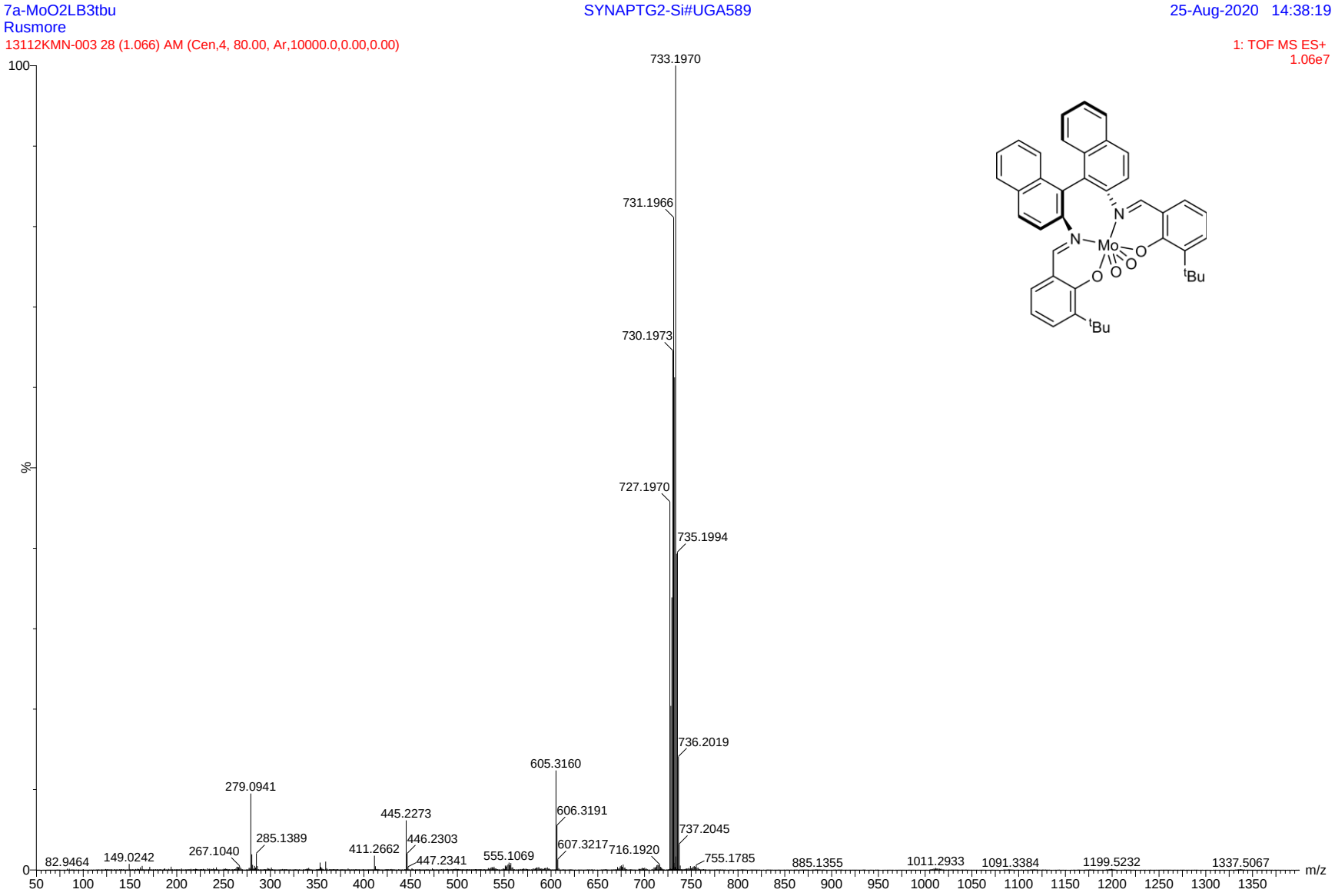

Figure A-31: ESI+ MS for **12**

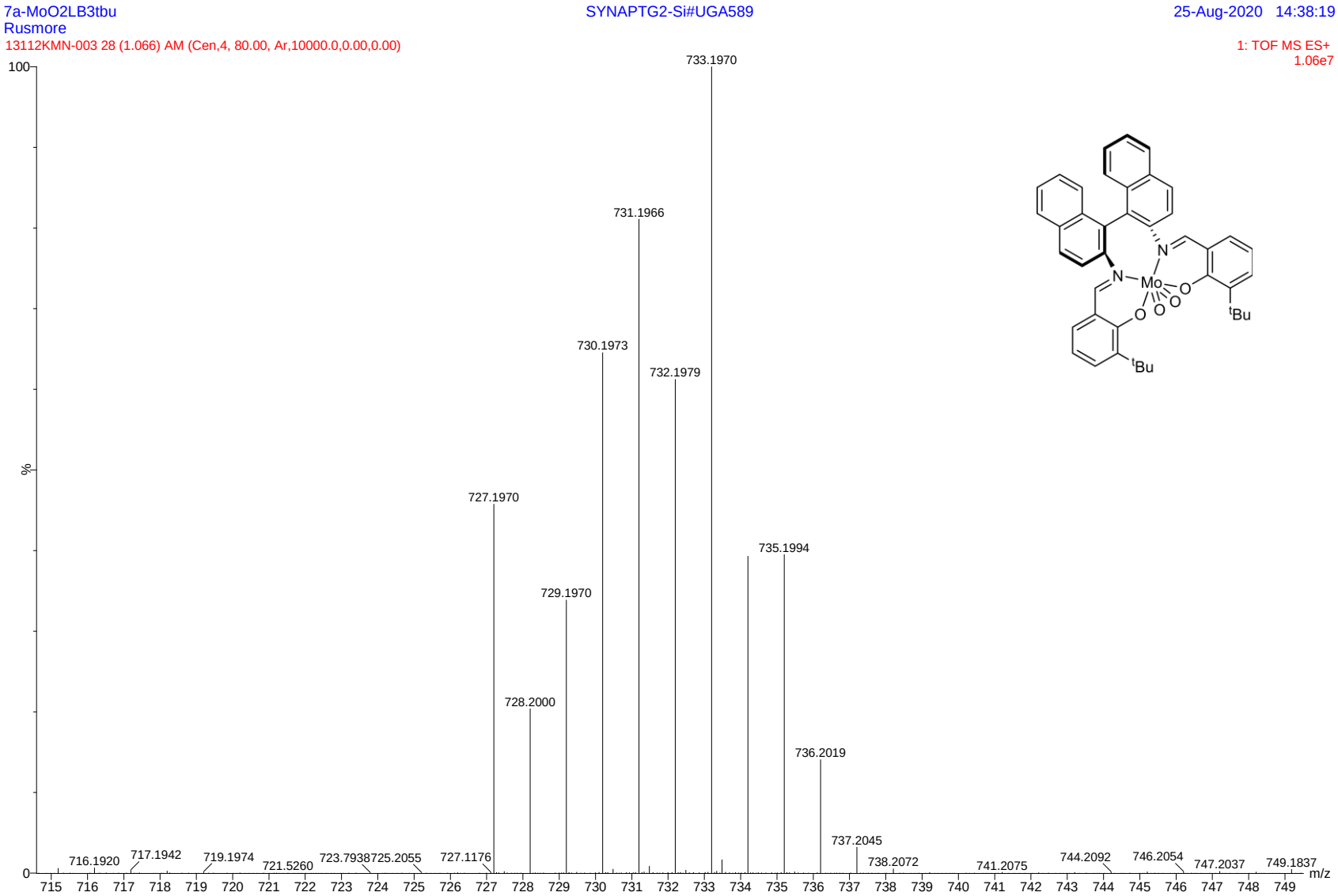

Figure A-32: Molecular ion peaks for ESI+ MS of **12**

APPENDIX B: CHARACTERIZATION DATA FOR SULFENIC ANHYDRIDE SPECIES

Spectral data for dodecyl sulfenic anhydride

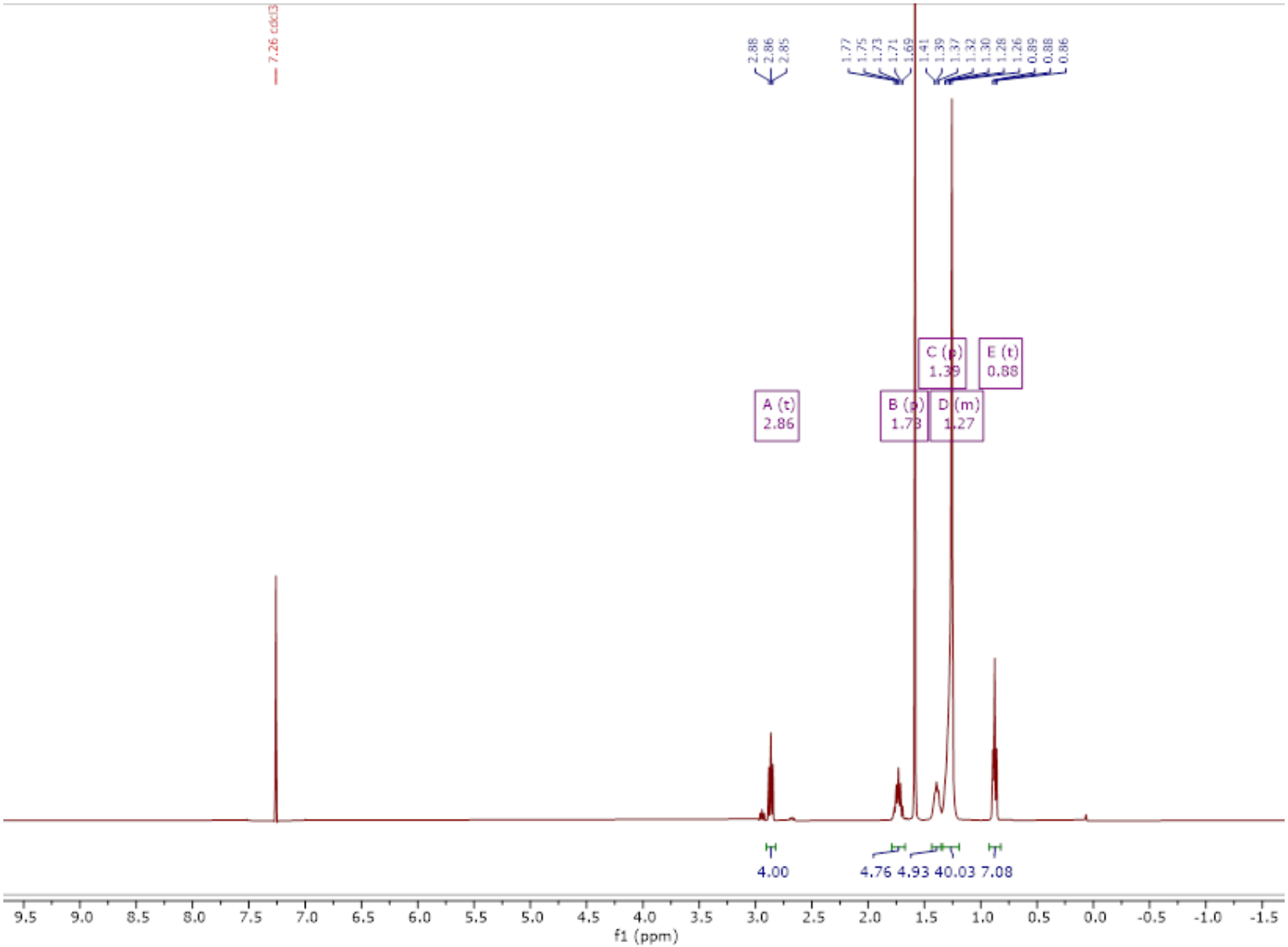

Figure B-1. ^{1}H NMR of dodecane sulfenic anhydride (~85% purity)

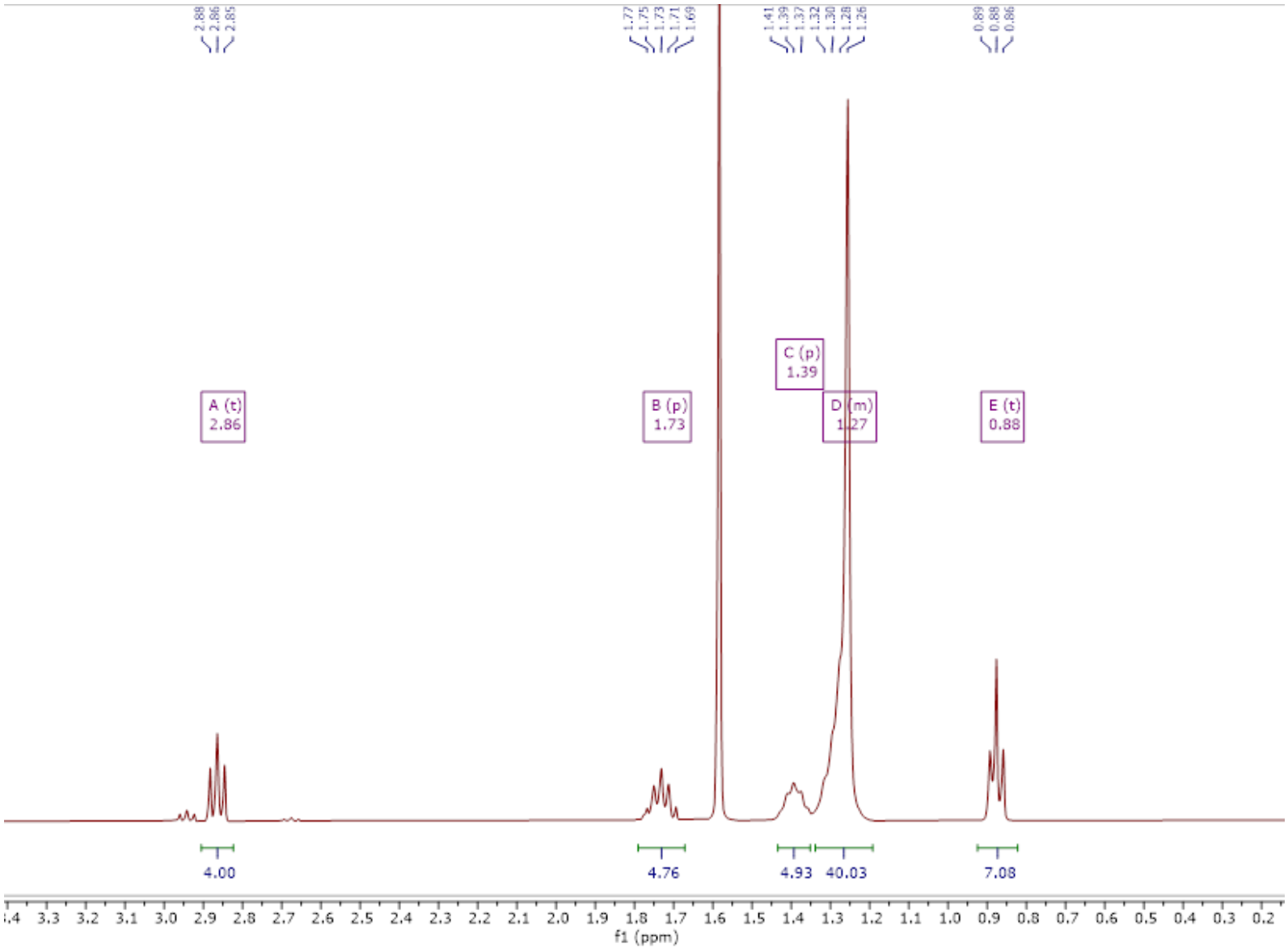

Figure B-2. Enlargement of aliphatic region for ^{1}H NMR of dodecane sulfenic anhydride (~85% purity)

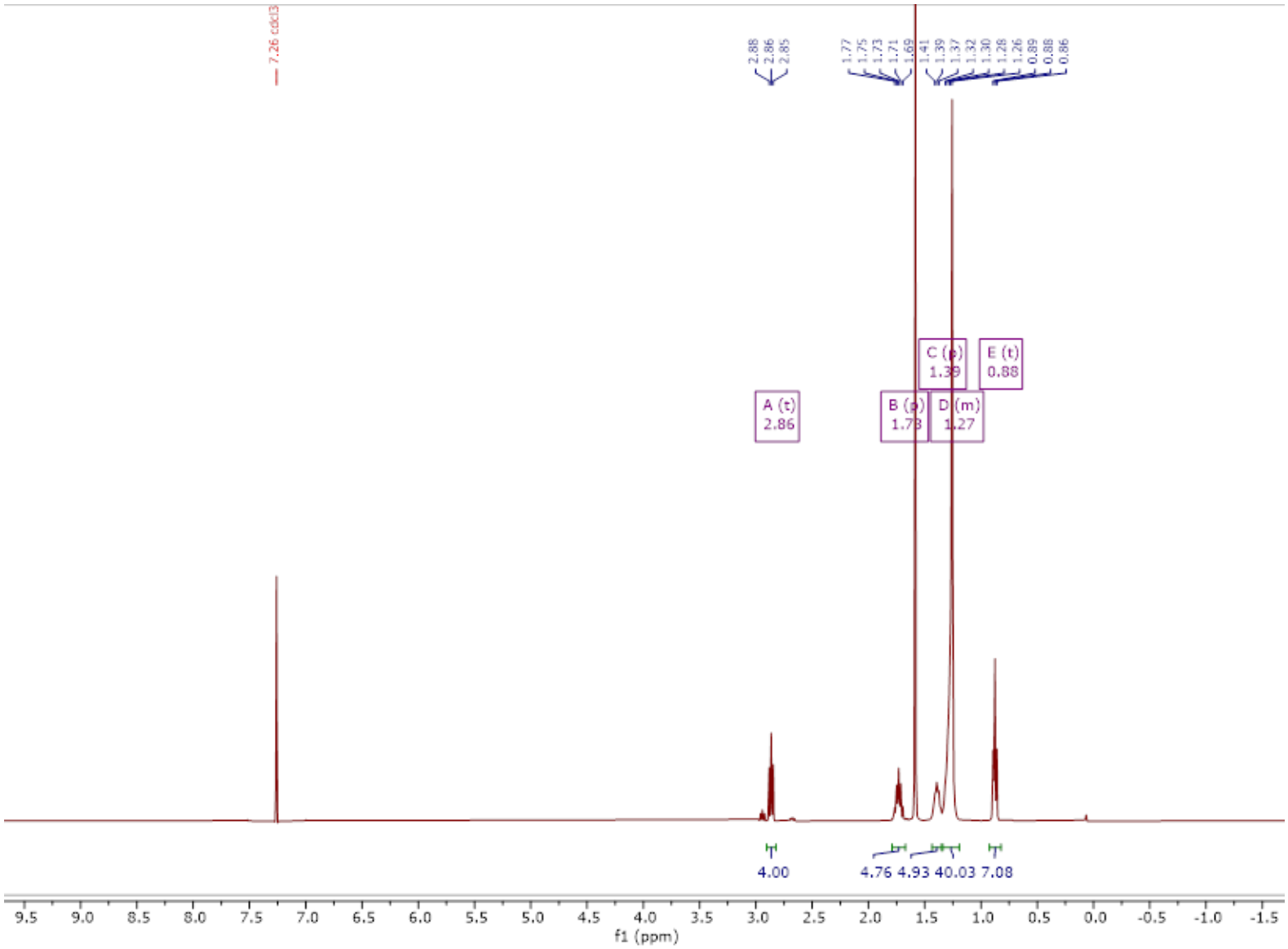

Figure B-1. ^{1}H NMR of dodecane sulfenic anhydride (~85% purity)

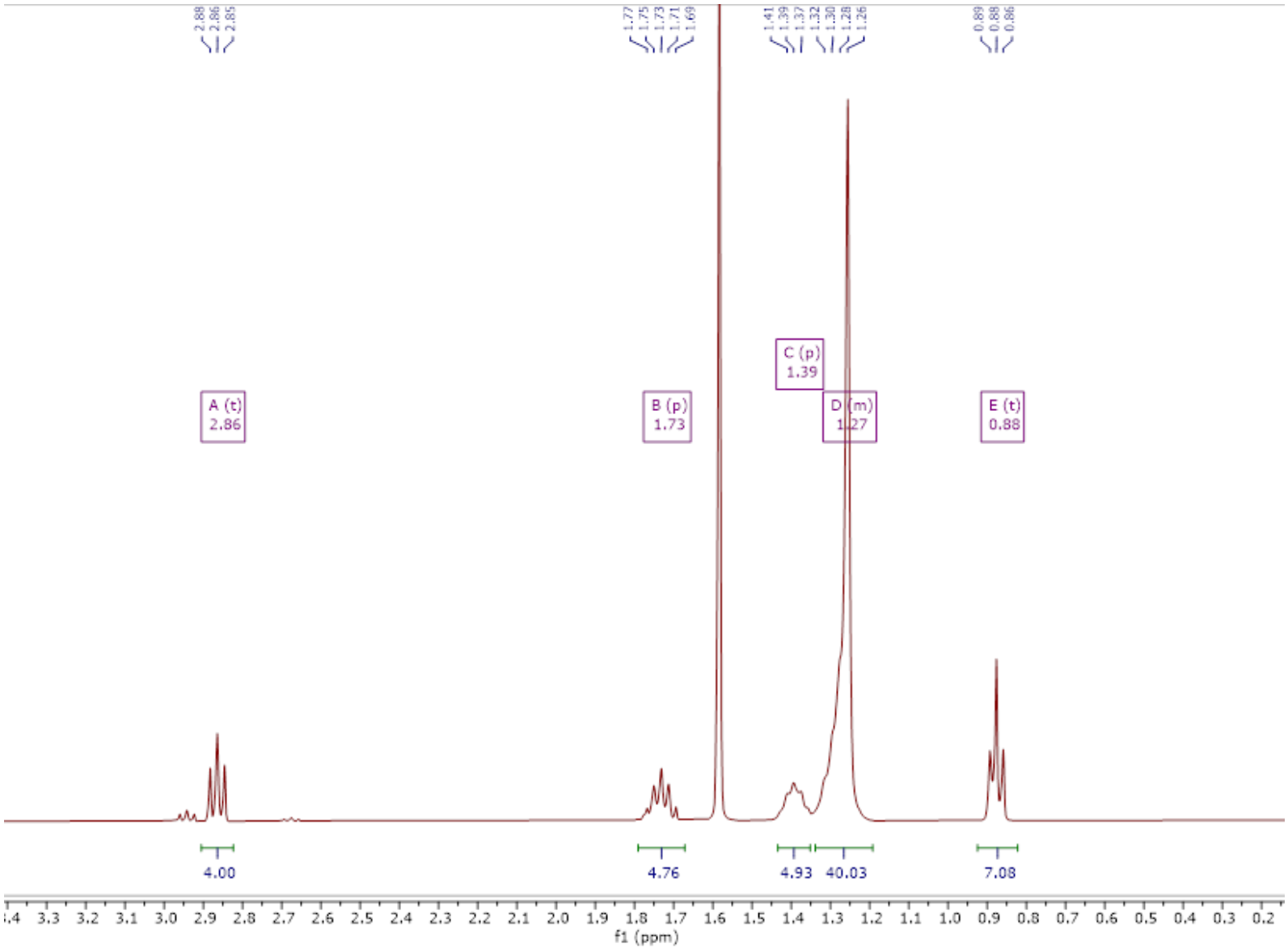

Figure B-2. Enlargement of aliphatic region for ^{1}H NMR of dodecane sulfenic anhydride (~85% purity)

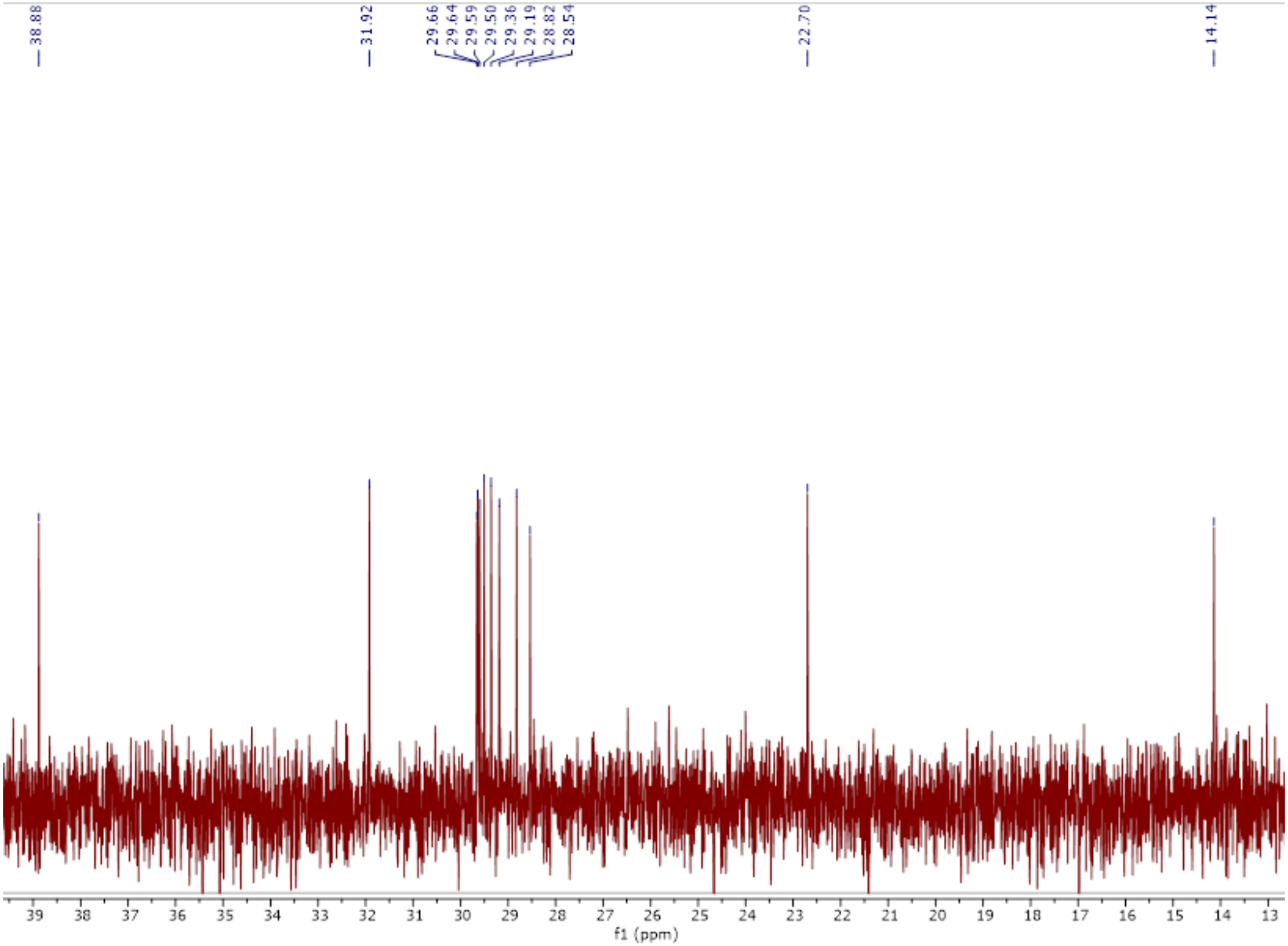

Figure B-3. ^{13}C NMR of dodecyl sulfenic anhydride

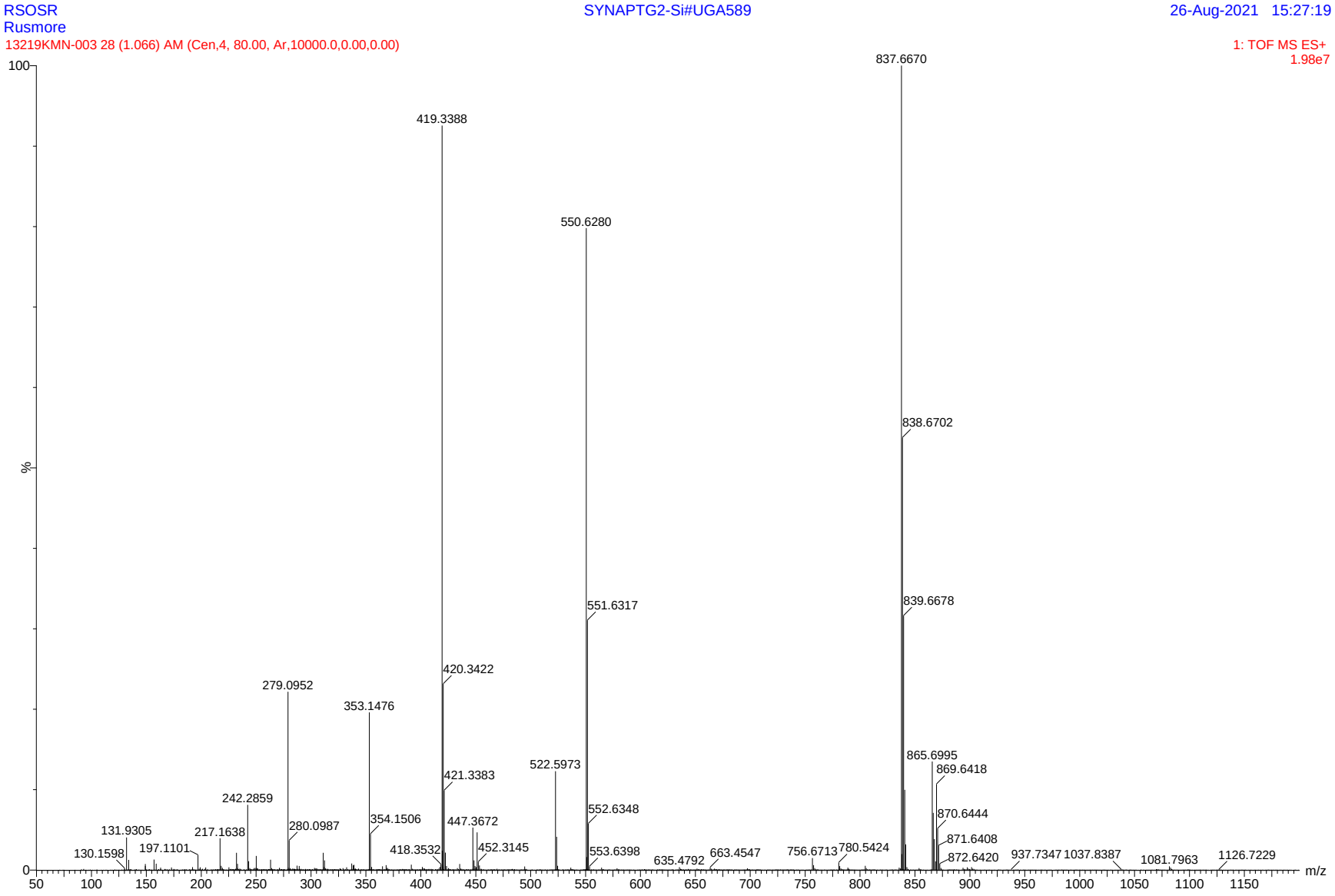

Figure B-4. ESI+ MS of dodecyl sulfenic anhydride

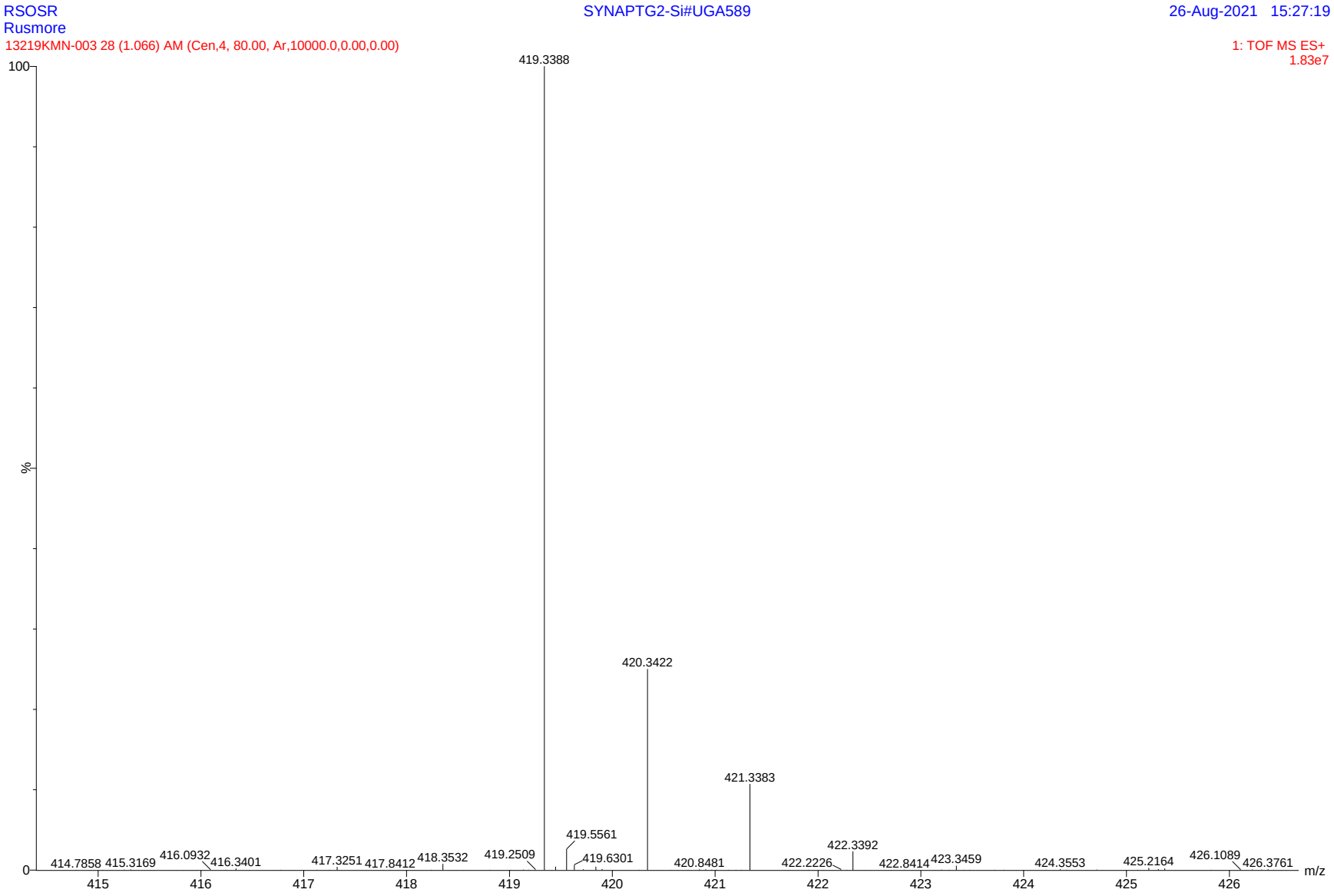

Figure B-5. Molecular ion peaks for ESI+ MS of dodecyl sulfenic anhydride

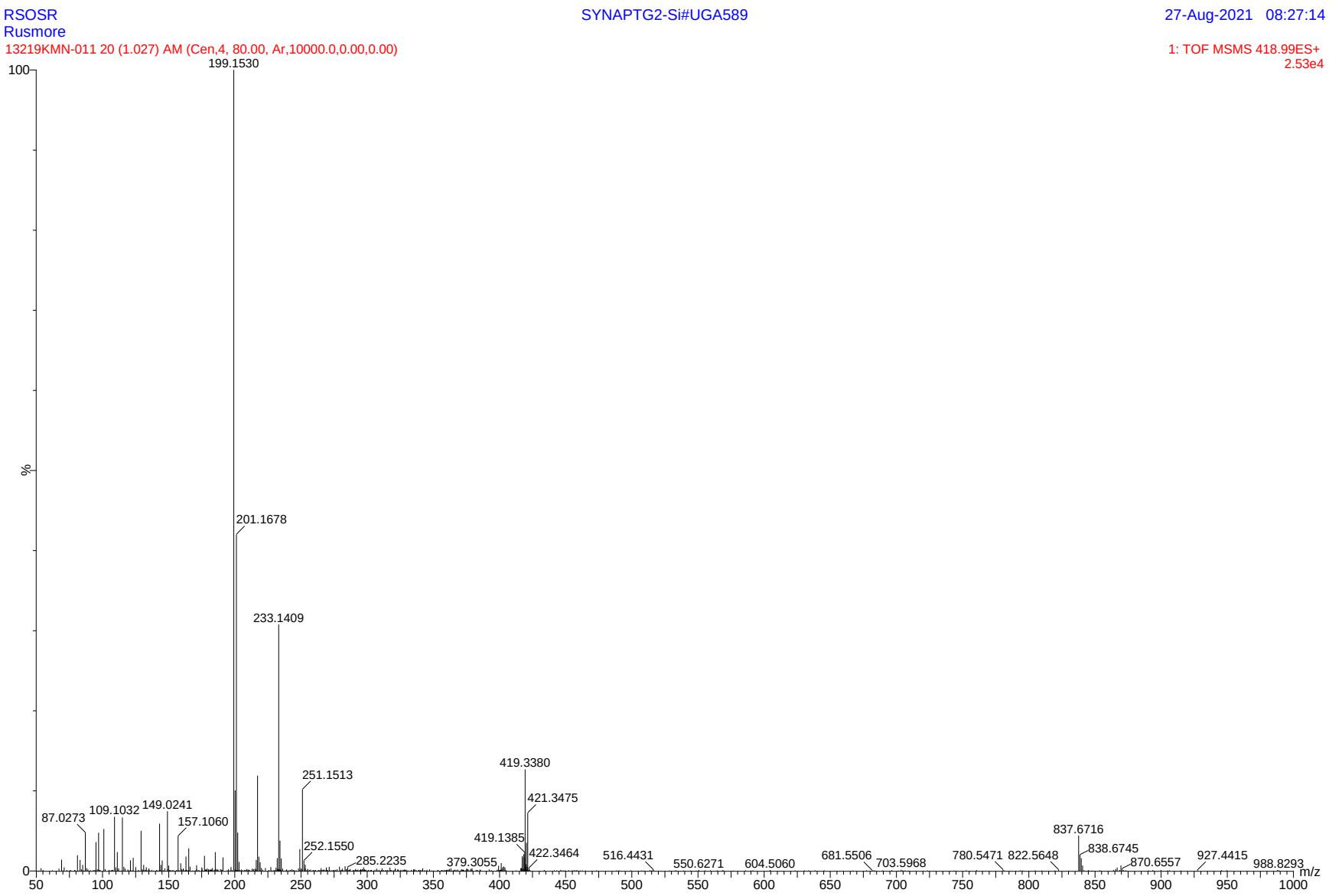

Figure B-6. TOF MSMS of dodecyl sulfenic anhydride

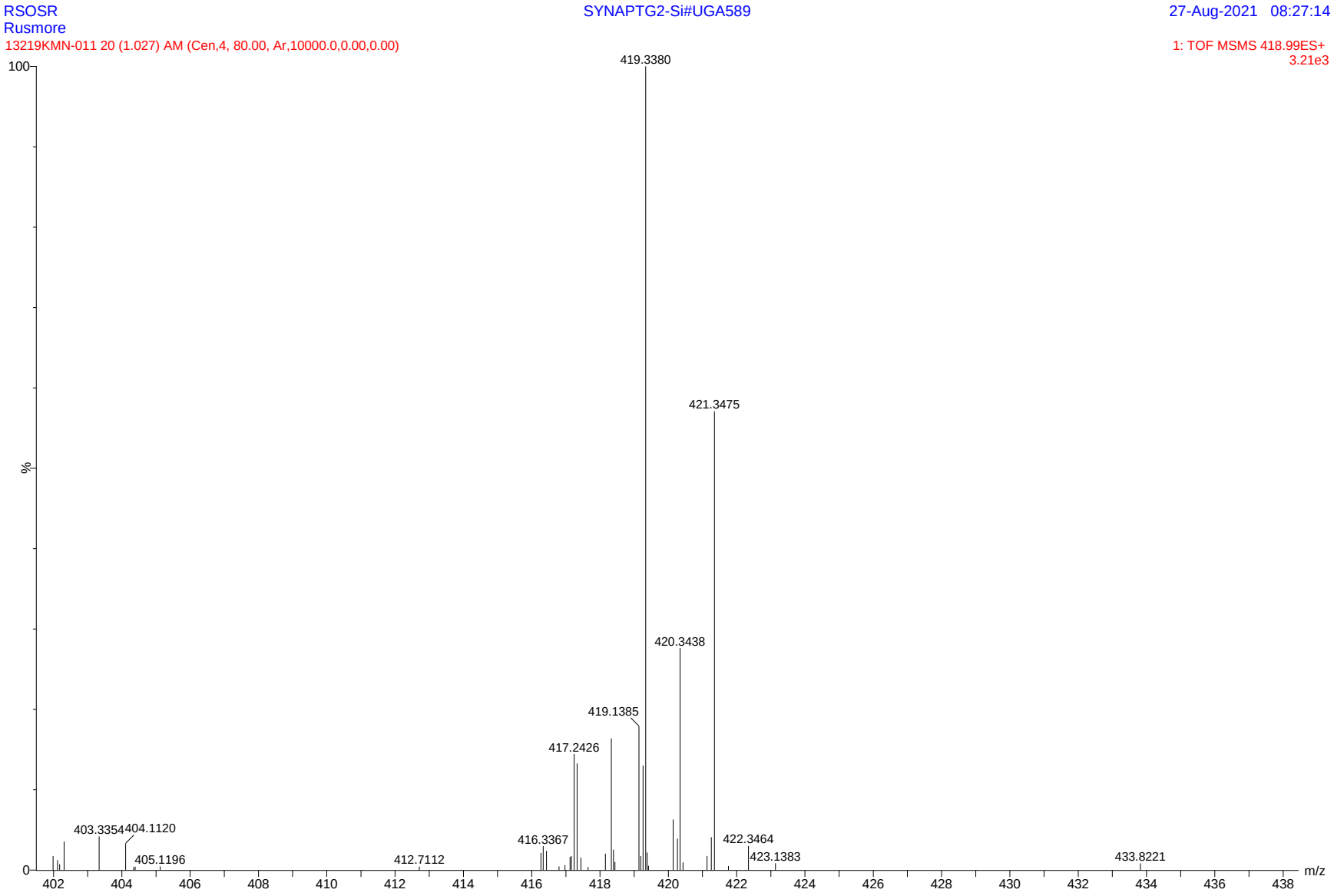

Figure B-7. TOF MSMS of dodecyl sulfenic anhydride $[M]^+$

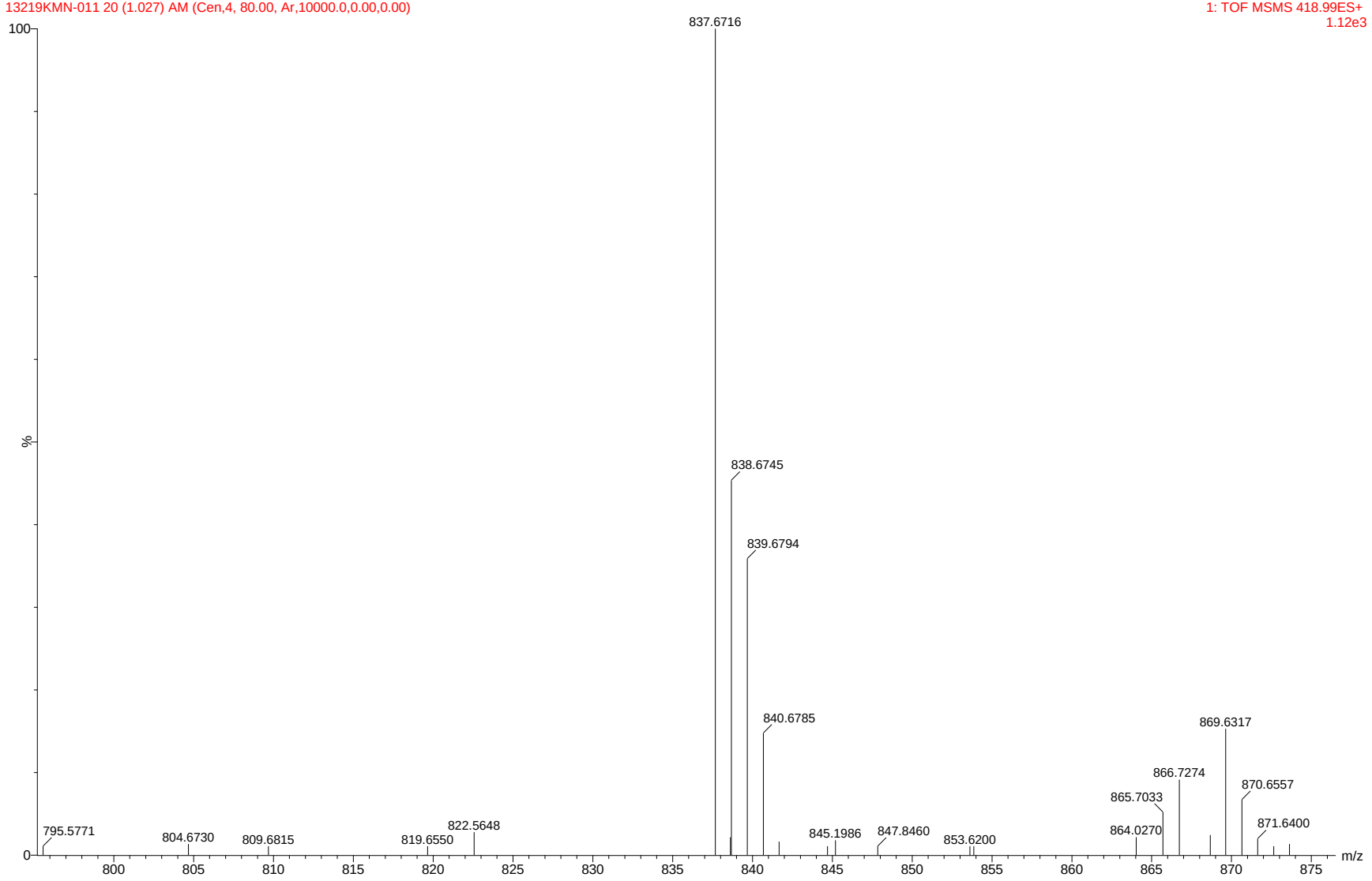

Figure B-8. TOF MSMS of dodecyl sulfenic anhydride $[2M]^+$

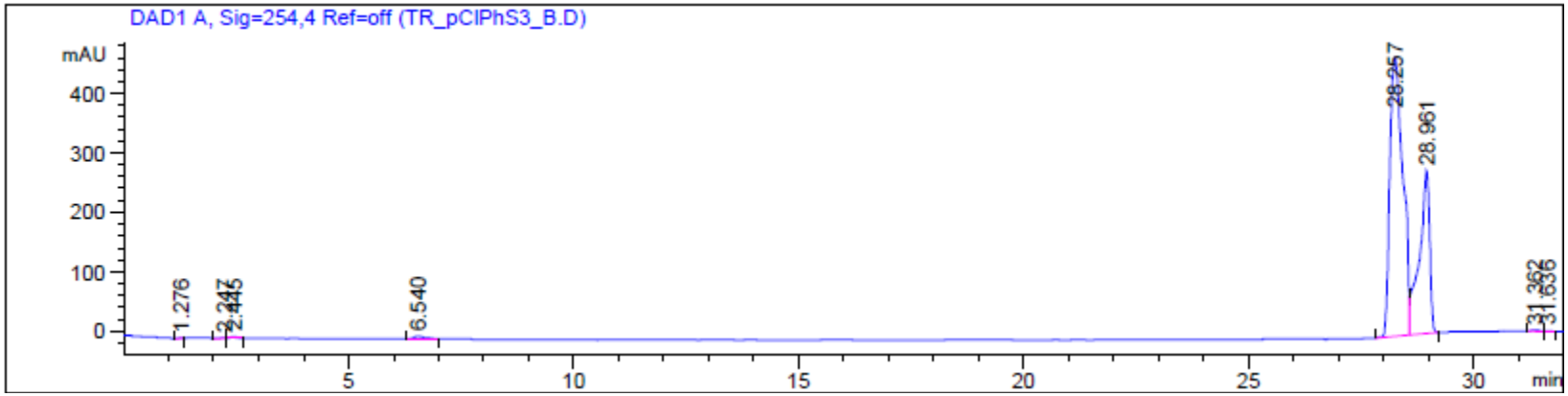

Signal 1: DAD1 A, Sig=254,4 Ref=off

Peak #	RetTime [min]	Type	Width [min]	Area [mAU*s]	Height [mAU]	Area %
1	1.276	BB	0.0836	7.01275	1.21007	0.0502
2	2.247	BV	0.1757	16.54366	1.16459	0.1185
3	2.445	VB	0.1946	29.48346	2.44679	0.2111
4	6.540	BB	0.2533	87.28867	4.96093	0.6251
5	28.257	BV	0.3002	9381.53223	471.34131	67.1825
6	28.961	VB	0.2258	4406.52100	273.74255	31.5557
7	31.362	BV	0.1927	25.45510	1.91941	0.1823
8	31.636	VB	0.1306	10.41126	1.16105	0.0746

Figure B-9. HPLC trace (λ = 254 nm) and peak data for *para*-chlorothiolphenol product mixture

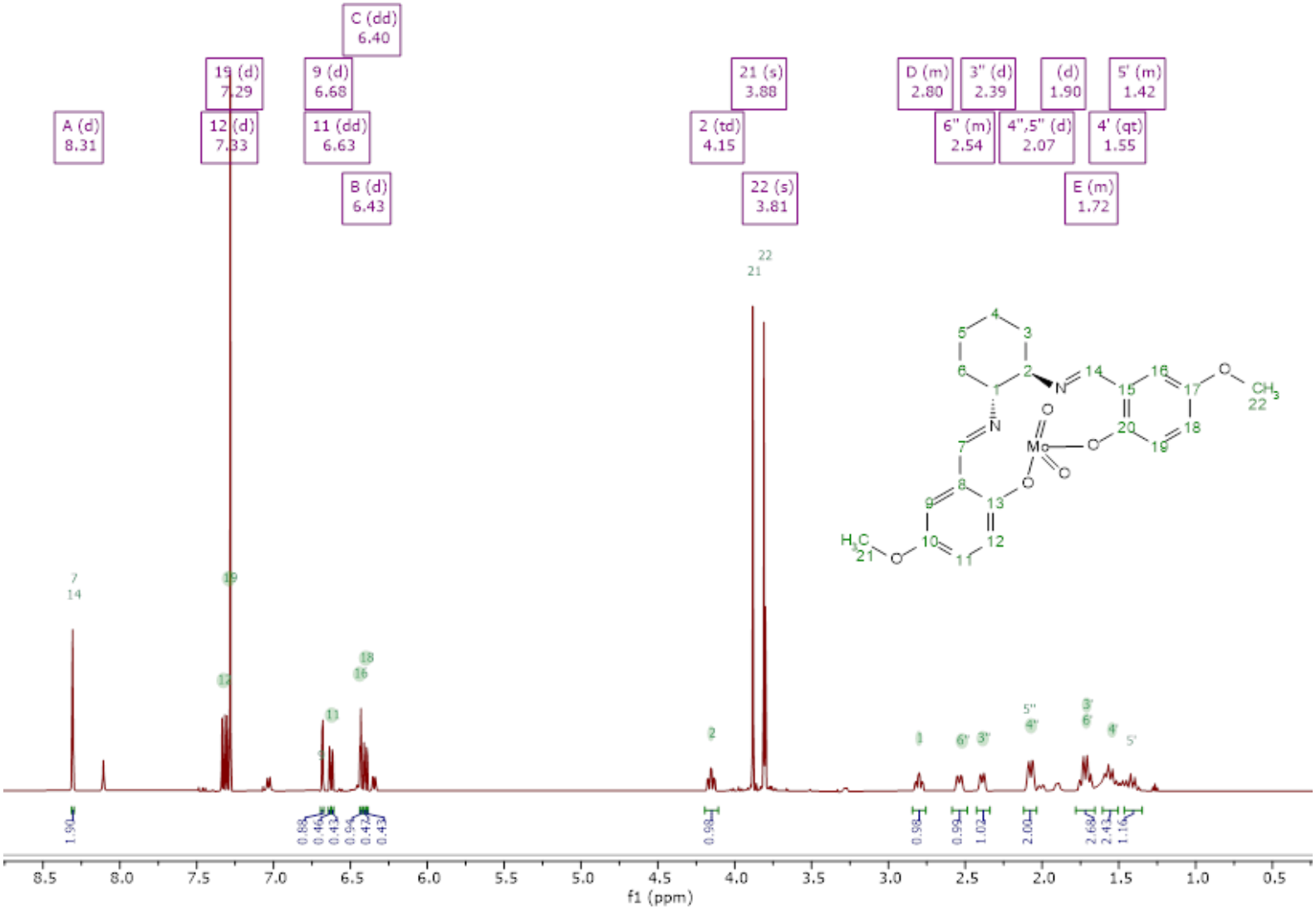

Figure B-10. ^{1}H NMR of *para*-methoxysalen dioxomolybdenum complex **9**

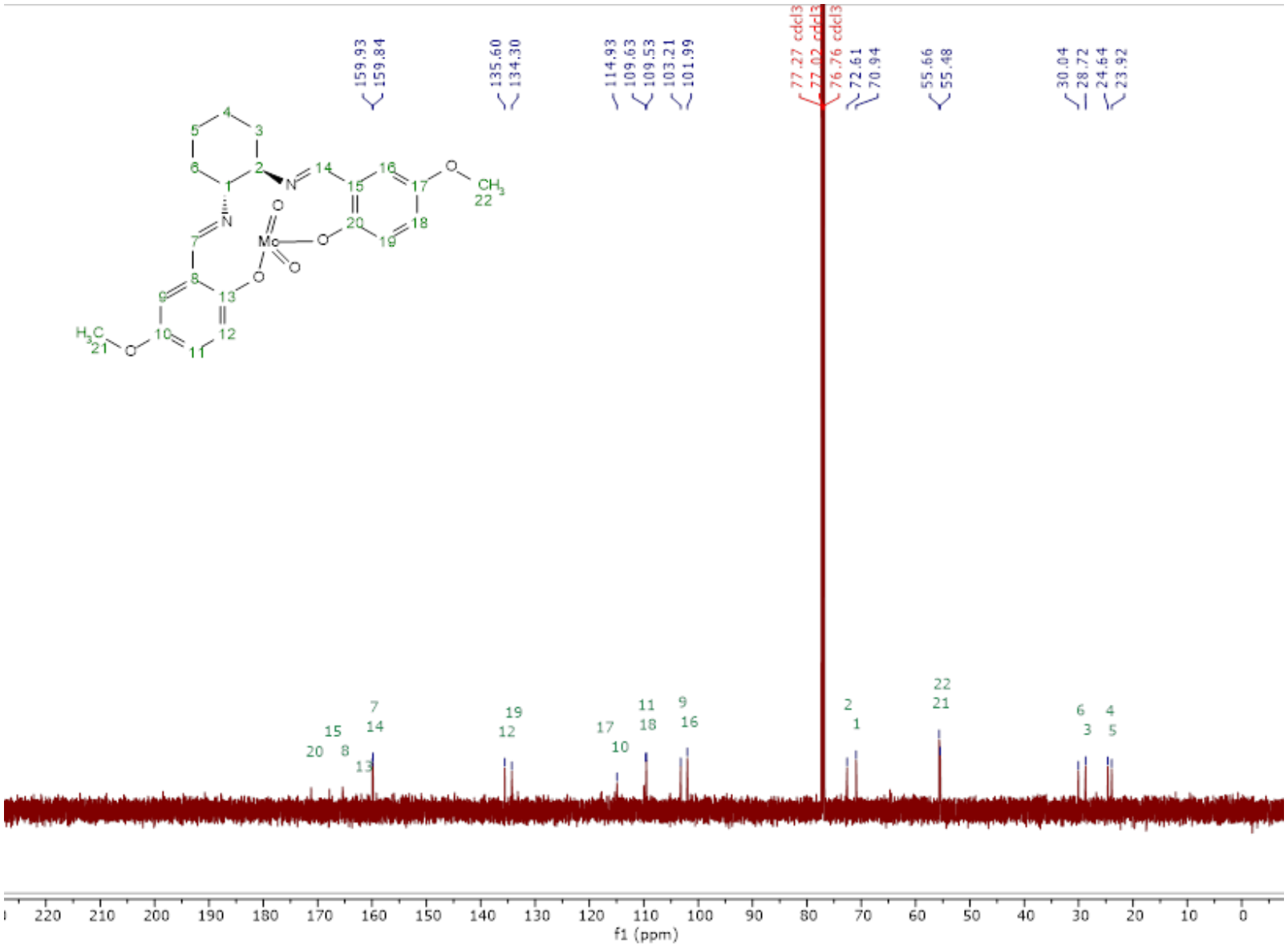

Figure B-11. ^{13}C NMR of *para*-methoxysalen dioxomolybdenum complex **9**